



**HAL**  
open science

# Asymptotic regimes of rotating flows driven by mechanical forcing in planetary cores: turbulent saturation and large-scale organisation

Thomas Le Reun

► **To cite this version:**

Thomas Le Reun. Asymptotic regimes of rotating flows driven by mechanical forcing in planetary cores: turbulent saturation and large-scale organisation. Fluid Dynamics [physics.flu-dyn]. Aix Marseille Université (AMU), 2019. English. NNT: . tel-02933056

**HAL Id: tel-02933056**

**<https://theses.hal.science/tel-02933056>**

Submitted on 8 Sep 2020

**HAL** is a multi-disciplinary open access archive for the deposit and dissemination of scientific research documents, whether they are published or not. The documents may come from teaching and research institutions in France or abroad, or from public or private research centers.

L'archive ouverte pluridisciplinaire **HAL**, est destinée au dépôt et à la diffusion de documents scientifiques de niveau recherche, publiés ou non, émanant des établissements d'enseignement et de recherche français ou étrangers, des laboratoires publics ou privés.



AIX-MARSEILLE UNIVERSITÉ  
ED 353: SCIENCES POUR L'INGÉNIEUR  
INSTITUT DE RECHERCHE SUR LES PHÉNOMÈNES HORS-ÉQUILIBRE

Thèse présentée pour obtenir le grade universitaire de docteur

Discipline: mécanique et physique des fluides

Thomas LE REUN

Régimes asymptotiques des écoulements en rotation excités par forçage  
mécanique dans les noyaux planétaires : saturation turbulente et  
organisation à grande échelle

Soutenance prévue le 17 septembre 2019 devant le jury composé de:

Thierry DAUXOIS	ENS Lyon	Rapporteur
Stephan FAUVE	ENS Paris	Rapporteur
Béregère DUBRULLE	CEA Saclay	Examinatrice
Fabien CODEFERD	LMFA	Examinateur
Jérôme NOIR	ETH Zürich	Examinateur
Joël SOMMERIA	LEGI	Examinateur
Benjamin FAVIER	IRPHE	Co-directeur de thèse
Michael LE BARS	IRPHE	Directeur de thèse



## Remerciements

Je souhaiterais tout d'abord remercier Michael Le Bars et Benjamin Favier qui ont dirigé mes travaux de thèse au cours de ces trois dernières années. J'ai bénéficié grâce à eux de conditions exceptionnelles pour mener à bien l'ensemble de mes recherches. En me laissant une grande liberté, ils m'ont donné l'opportunité d'explorer mes propres idées à un rythme qui me convenait, tout en se montrant toujours disponibles pour répondre à mes questions et discuter longuement les orientations à donner au projet de recherche présenté ici. Je tiens à les remercier de m'avoir chacun transmis une partie de leurs savoirs scientifiques et techniques, souvent différents entre Michael et Benjamin, mais finalement si complémentaires. Je leur suis également reconnaissant de m'avoir transmis leur expérience de la communication scientifique, en passant un très grand nombre d'heures à relire, annoter, corriger mes articles et mon manuscrit, ou encore à écouter et améliorer mes présentations. Enfin, je voudrais exprimer toute ma gratitude à mes deux directeurs pour m'avoir poussé à candidater à des bourses de recherches m'offrant des expériences différentes pendant ou après ma thèse. Ils m'ont épaulé dans la préparation de ces dossiers et ont largement contribué à les rendre convaincants et donc à même d'être sélectionnés. Grâce à Michael et Benjamin, j'ai donc passé trois belles années de recherches, et j'espère ne rien perdre de la formation que j'ai reçue d'eux dans le futur. Un seul regret subsiste cependant : comme l'a rappelé Benjamin le jour de la soutenance, nous n'avons jamais vu le Soleil se coucher derrière le Mont Canigou depuis Marseille, renforçant ainsi l'idée que ce n'est qu'une vaste légende étayée par des photos truquées.

J'ai consacré une partie de ma thèse à une expérience imposante de par ses dimensions et sa complexité. En extraire des résultats intéressants aurait été impossible sans les apports techniques décisifs de William Le Coz pour le montage du moteur de libration et le contrôle des caméras, ceux de Jean-Jacques Lasserre pour la métrologie des écoulements, ceux de Éric Bertrand, Hubert Ekongolo Nkake, Adrien Bavière et Mathieu Léger pour la conception et la fabrication des pièces constituant notre expérience.

Ma soutenance de thèse, le 17 septembre 2019, fut un moment très agréable malgré l'angoisse inhérente à cet exercice grâce à la bienveillance des membres du jury. J'en retiens finalement avant tout près de deux heures de discussions stimulantes. À cet égard, je voudrais remercier les deux rapporteurs du jury, Thierry Dauxois et Stephan Fauve, pour leur lecture minutieuse du manuscrit, pour le long commentaire qu'ils en ont donné, ainsi que pour leurs suggestions et questions au moment de la soutenance. Je suis également reconnaissant aux autres membres du jury, Bérengère Dubrulle, Fabien Godeferd, Jérôme Noir et Joël Sommeria de s'être plongé-e-s dans mes travaux pour en donner des éclairages différents et complémentaires lors de la soutenance au travers des nombreuses questions et discussions qui s'y sont tenues.

Une thèse est un travail de longue haleine et intellectuellement envahissant. Rares ont été les moments où j'ai pu oublier un peu mes recherches et où leurs progrès n'avaient pas mon humeur. Je suis heureux d'avoir eu Anne tout près de moi au cours de ces trois années (et avant, et après). Elle est souvent parvenue à dissiper les tensions, angoisses et doutes grâce à ses conseils et son écoute. Parmi de nombreuses contributions à mes recherches, Anne a cousu, décousu et recousu de ses mains un pouf confortable sur lequel j'ai assemblé les derniers morceaux de théories. Cette clairvoyance soudaine dans l'organisation de mes résultats n'aurait peut-être pas été possible sans ce coussin de couleur jaune moutarde rempli de billes de polystyrène, et donc sans Anne.

Je souhaiterais également remercier ma famille pour son soutien inconditionnel. Ce qui est sans doute un lieu commun n'en est pas moins vrai : elle a contribué à ce travail bien avant qu'il ne commence. Autrement dit, pour une multitude des raisons, commencer, poursuivre et terminer une thèse n'aurait jamais été possible sans chacun de ses membres. Au cours de ces trois dernières années, j'ai reçu de leur part de nombreux et précieux encouragements qui m'ont donné beaucoup de confiance. Ma famille m'a aussi apporté une aide matérielle et logistique dès que j'en ai eu besoin. Ils diront qu'elle était normale et acquise, mais cela ne diminue pas ma gratitude. Enfin, parmi les nombreux apports de ma famille à cette thèse, ce sont eux qui ont eu l'idée du festin mémorable de crêpes et de galettes qui a suivi la soutenance.

Ces trois années ne se sont pas limitées au huis-clos du laboratoire et de la thèse. Grâce au soutien de Michael et Benjamin, j'ai beaucoup voyagé, en Europe et ailleurs, et j'ai notamment pu réaliser un séjour de recherche à l'Institut Océanographique de Woods Hole au sein du programme Geophysical Fluid Dynamics durant l'été 2018. Cette sorte de colonie de vacances pour scientifiques, idéalement située à la pointe sud de Cape Cod, a été l'occasion de nombreuses rencontres et discussions avec des scientifiques intéressé·e·s par la géophysique et la mécanique des fluides. J'ai eu l'opportunité d'y rencontrer des chercheur·e·s ayant des expertises dans des domaines très différents, et donc de m'ouvrir à des thèmes parfois éloignés de ceux explorés au cours de ma thèse. Si ce séjour devait être une parenthèse dans le déroulement de ma thèse, il se trouve que les travaux détaillés plus loin en ont grandement bénéficié. C'est en effet au cours de ce séjour que j'ai pu longuement discuter avec Basile Gallet de mes récents résultats expérimentaux. En remettant en cause la compréhension que j'en avais, ces discussions nous ont amenés à explorer théoriquement des mécanismes d'interaction entre ondes inertielles et modes géostrophiques que je n'avais pas sérieusement envisagés. Même si leur contenu diffère de celui de nos discussions, les parties théoriques présentées ici (et qui ont depuis été étendues) ont été largement inspirées par ces recherches menées brièvement avec Basile à Woods Hole. Je voudrais donc exprimer ici toute ma gratitude envers d'une part Basile, et d'autre part le programme GFD qui a rendu possible cet échange fructueux.

De manière plus régulière, mon service annuel d'enseignement m'a également permis de sortir de temps à autre la tête de la thèse pour me consacrer à la préparation de TD. Je remercie Marc Georgelin qui m'a donné l'opportunité d'enseigner en première et deuxième année de la licence MPC1. J'ai pris beaucoup de plaisir à enseigner la mécanique, la physique ondulatoire et l'optique à ces promotions d'étudiant·e·s vifs·ves et intelligent·e·s . La préparation de ces TD, mais aussi les nombreuses interventions et questions des étudiant·e·s ont été stimulantes et m'ont donné l'occasion de réfléchir à des problèmes gravitant hors de mes recherches. Chaque semestre, lorsqu'il touchait à sa fin, j'ai regretté la perte de cette respiration hebdomadaire qu'était l'enseignement. Je suis finalement reconnaissant aux étudiant·e·s de MPC1 de s'être montré·e·s intéressé·e·s par mes interventions, mais aussi d'avoir fait preuve d'une indulgence très humaine lorsque je me suis trouvé dans des situations difficiles et imprévues, ou encore lorsque j'étais débordé par la rédaction de ce manuscrit.

Cela ne se sait pas vraiment, mais j'ose enfin l'avouer ici : je passe beaucoup trop de temps sur Twitter. Si ce réseau a été une source de distraction et de procrastination, je pense qu'il a aussi contribué à mon travail de recherche. Je suis, en effet, heureux d'y avoir trouvé une communauté bienveillante de scientifiques. J'y ai reçu de nombreux conseils, à la fois directement et indirectement, qui m'ont aidé à améliorer mes méthodes d'étude, mais aussi mes présentations et ma rédaction. Enfin, j'ai trouvé sur Twitter des personnes ayant traversé les mêmes expériences que moi et dont le soutien fut précieux, autant dans les moments difficiles que dans les succès.

Je voudrais remercier également les doctorant·e·s et post-doctorant·e·s de l'IRPHÉ pour m'avoir accompagné et souvent aidé pendant ces trois années : Daphné (qui aura donc survécu à un an et demi dans le même bureau que moi), Pierre, J-B, Giulio, Sandeep, Louis, Ludovic, Florence, Romain, Fabien, Fatma, Eduardo, Sarah, Keshav, Baptiste, Basile, Émilie et Teri. Je remercie tout particulièrement Amélie pour son souci constant des autres et les très nombreux services qu'elle m'aura rendus ces trois dernières années.

Enfin, je voudrais remercier les ondes, ces objets physiques à la fois si élégants, si complexes et si riches sur lesquels j'ai grandement apprécié travailler, bien que je ne m'en sois rendu compte que tardivement.

## Summary

Many terrestrial bodies, including the Earth, are surrounded by a magnetic field protecting them from high energy stellar particles. It originates from the turbulent motion of the liquid, conducting iron core of these planets and moons. The complex motion of liquid iron in planetary cores is often thought to be driven by thermal and solutal convection instabilities, but the presence of convection is sometimes hard to reconcile with the heat budget of terrestrial planets, especially the smaller ones. To explain the existence of magnetic fields surrounding small moons such as Ganymede and Io, mechanical forcing induced by tides has been proposed as an alternative source of turbulence in planetary cores.

Tidal interaction between a terrestrial body and a companion results in a distortion of the shape of the body, a deformation that remains mostly directed towards the companion and which may rotate at a different rate compared to the planet or the moon spinning rate. This is the case for instance of the Earth-Moon system: the Earth tidal bulge rotates at the Moon orbiting rate (in approximately 27 days) whereas the Earth spinning rate is much larger (1 day). Another effect of tidal interaction is to force periodic variations of the length of the day, an oscillation called libration.

These two effects (differential rotation and libration) have been shown to excite parametric resonance of inertial waves, the latter being spontaneous oscillations of rotating fluid interiors induced by the restoring action of the Coriolis force. This resonance is called the elliptical instability. The inertial waves grow exponentially and eventually collapse into turbulence. Although the saturation of the instability is the most important state for dynamo action and orbital evolution of planets, it remains poorly understood.

The work presented throughout this dissertation aims at better characterising the turbulence resulting from the elliptical instability, in particular in regimes that are relevant to geo- and astrophysics where both the tidal forcing amplitude and the viscous dissipation are weak. The investigation of the non-linear saturation of this parametric resonance is carried out with experiments and idealised numerical simulations.

In the experiment, we reveal that two regimes exist in the saturation of the instability. The first one, which is typical of turbulence in rotating fluids, is dominated by strong vortices invariant along the rotation axis, or geostrophic. We exhibit a new regime which is dominated by inertial waves in non-linear resonant interaction, a state called inertial wave turbulence. To extend our understanding of these two states and to fully characterise the inertial waves interaction, we proceed to idealised numerical simulations in local cartesian model of tidal flows. It allows producing the two regimes of saturation and exploring the weak forcing and dissipation regime. With this ideal model, we show that the transition between the two regimes mentioned earlier is caused by an instability that vanishes below a finite forcing amplitude. We also explore the possibility for direct forcing of strong geostrophic motion by the resonant waves directly, but our simulations suggest that they should not dominate in the geophysical limit. We therefore conclude that the superposition of inertial waves type of saturation is the relevant one for planetary cores.

We finally investigate the stability of stably stratified planetary cores undergoing tidal distortion. Similarly to the elliptical instability, we exhibit a resonance of internal waves, which are oscillations caused by the stable density stratification. We show with idealised numerical simulations that the resonant waves give rise to internal wave turbulence in the non-linear saturation of the instability.

# Contents

---

Introduction . . . . .	9
<b>1 Tidal forcing, inertial waves and the elliptical instability</b>	<b>15</b>
1 Tidal forcing in planetary cores: the primary response to tides . . . . .	15
2 Parametric sub-harmonic resonance of a pendulum . . . . .	22
3 Parametric excitation of inertial oscillations by mechanical forcing . . . . .	26
<b>2 Introduction to the non-linear saturation of the elliptical instability</b>	<b>35</b>
1 Simple scalings for the saturation flow . . . . .	35
2 Non-linear wave interactions . . . . .	37
3 Waves, vortices and the elliptical instability . . . . .	45
<b>3 Experiments on the non-linear saturation of the elliptical instability</b>	<b>53</b>
1 Design of the experimental set-up . . . . .	53
2 The experimental set-up . . . . .	58
3 Base flow and frames of reference . . . . .	62
4 The non-linear saturation at low forcing amplitude: waves in interaction . . . . .	64
5 Large forcing amplitudes: a geostrophic-dominated regime . . . . .	72
6 Discussion: the origin of the secondary transition . . . . .	79
7 Another forcing frequency, $f = 2.5$ . . . . .	79
8 Conclusion . . . . .	84
<b>4 Finite wave amplitude instabilities</b>	<b>87</b>
1 Introduction: the geostrophic problem . . . . .	87
2 Investigating a single wave instability . . . . .	88
3 Simulations of instabilities driven by an inertial wave . . . . .	91
4 The low wave amplitude case: direct forcing of geostrophic modes . . . . .	93
5 The finite wave amplitude instability mechanism . . . . .	96
6 Conclusions . . . . .	100
<b>5 Direct forcing of geostrophic modes in the saturation of the elliptical instability</b>	<b>105</b>
1 Deriving a low order model . . . . .	106
2 The upper bound on the wave-dominated regime . . . . .	114
3 Conclusion on the direct forcing of geostrophic modes by waves . . . . .	121
<b>6 A local model to investigate the saturation of the elliptical instability</b>	<b>125</b>
1 The idealised local model . . . . .	126
2 The geostrophic-dominated regime . . . . .	130
3 Attempts to observe a wave-dominated regime with the local model . . . . .	136
4 A wave-dominated regime in the local model . . . . .	139
5 Exploring the stability of wave turbulence . . . . .	149
6 Conclusion: the contributions of the local model . . . . .	155
<b>7 Tidally driven parametric instability in stratified flows</b>	<b>157</b>
1 The relevance of stratification to tides in planetary cores . . . . .	157
2 Local study of the equilibrium tidal base flow . . . . .	161
3 Stability analysis . . . . .	167

4	Non-linear saturation of the instability . . . . .	173
5	Conclusion . . . . .	185
<b>Conclusion</b>		<b>189</b>
1	The saturation of the elliptical instability in planetary cores . . . . .	189
2	Ideas and directions for future works . . . . .	192
	References . . . . .	205

# Introduction

In addition to the Earth, several terrestrial bodies of the Solar System are known to be presently protected from solar radiation by an intense magnetic field, or present evidence of a past one. For instance, flybys operated by probes equipped with magnetometers have revealed the presence of a magnetic field surrounding Mercury as well as Ganymede and Io, two of Jupiter's largest moons (Ness et al., 1975; Kivelson et al., 1996a; Sarson et al., 1997; Showman and Malhotra, 1999; Kivelson et al., 2002). Magnetised rock samples from Mars and the Earth's Moon have also revealed the existence of a past intense magnetic field (Stevenson, 2001; Garrick-Bethell et al., 2009; Le Bars et al., 2011). A summary of what is presently known about magnetic fields of terrestrial planets in the Solar System is given in figure 1. Beyond the Solar System, magnetic fields are also expected in extra-solar planets, where they constitute one of the key ingredients for habitability.

As first conjectured by Larmor (1919), the magnetic field of a planet originates in the turbulent motion of its liquid conducting layers, presumably in most cases of the liquid iron core (Olson, 2015). Following the seminal works of Roberts (1968) and Busse (1970), it has been shown that buoyancy-driven flows such as thermal and solutal convection in cores provoke turbulent stirring and dynamo action (Glatzmaiers and Roberts, 1995). This convective motion is driven by the secular cooling of a planet, by radiogenic heating, and by latent heat and potential energy release during its core solidification. While the energy budget to sustain the present day magnetic field of the Earth is closed—even if still partly controversial, see e.g. Labrosse (2015)—, the Earth early dynamo prior to the inner crystallisation and the dynamo in smaller bodies remain largely unexplained.

As an illustration, let us assume that the main source for dynamo lies in the initial thermal energy of the body acquired during its formation. This initial thermal energy can be estimated assuming that it is roughly tantamount to the loss of gravitational potential energy from a dispersed cloud to an aggregated body. Let us consider for instance the case of a proto-planet with mass  $M$  and radius  $\rho$  (see figure 2) which is impacted by a body of mass  $dM$  coming from afar. As the impactor is brought to the surface of the planet, it loses a gravitational potential energy  $dE_p$  such that:

$$dE_p = -G \frac{M dM}{\rho} \quad (1)$$

where  $G$  is the gravitational fundamental constant. Assuming the impactor and the proto-planet have the same homogeneous density  $\mu$ , the radius increase to  $\rho + d\rho$  may be converted into a potential energy loss as  $dM = 4\pi\mu\rho^2 d\rho$  so that:

$$dE_p = -\frac{16\pi^2}{3} G \mu \rho^4 d\rho . \quad (2)$$

The increase of the radius of the proto-planet up to a body of radius  $R$  thus corresponds to a gravitational potential energy loss proportional to  $R^5$ . We assume that during the process of planet formation, this potential energy loss is transformed into thermal energy by collisions. This heat is then radiated away from the planet at a rate proportional to the surface, *i.e.* to  $R^2$ . We thus infer that a secular cooling time scale for the planet scales like  $R^3$ . As a consequence, the core of relatively small planetary bodies such as Ganymede, Mercury or the early Moon cools down very quickly compared to the age of the Solar System, and should not be able to sustain turbulent convective motion and long-term dynamo action. Even for larger planets

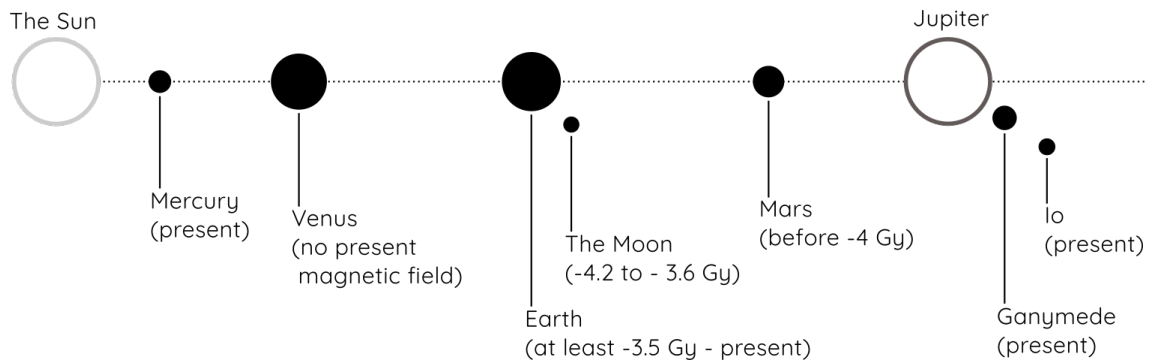


**Figure 1:** A summary of the terrestrial bodies (in black) of the Solar System known for having a past or present dynamo. The relative size of these planets and moons is respected (apart for Jupiter and the Sun). Venus is given for comparison as it is not surrounded by a magnetic field although it is of similar size to the Earth. It is not known whether Venus had a magnetic field in the past. We report the estimated period of existence of these fields when it is known (see the indications in brackets), based on Garrick-Bethell et al. (2009); Tarduno et al. (2010); Stevenson (2001).

such as the Earth, the initial temperature to maintain a dynamo all along their lifetime should be extremely hot, in possible contradiction with the presence of a solid mantle at the beginning of their existence (Andraut et al., 2016).

However, initial heat is not the only source of energy available to drive fluid motion. In particular, a huge amount of mechanical energy is stored in the rotational dynamics of planetary systems (Le Bars et al., 2015). If it is possible to convert this mechanical energy into turbulent kinetic energy inside a planetary core, it provides an interesting alternative to convective instabilities to drive planetary dynamos. In the ideal case of a perfectly spherical planet with uniform rotation, this conversion cannot happen: the liquid core follows the terrestrial planet in its solid-body rotation. However, tidal interactions between astrophysical bodies result in periodic alteration of their shape, of the direction of their rotation axis and of their rotation rate, which can then force fluid motion inside their cores.

The idea that tidal interactions could force core turbulence was first introduced by Malkus in three seminal articles (Malkus, 1963; Malkus, 1968; Malkus, 1989), but was largely dismissed by geophysicists for decades. As noted by Kerswell, this was mainly due to a misunderstanding regarding the nature of the flow excited by tides (Kerswell, 1996; Kerswell, 2002). Tidal interactions are of small amplitudes and their direct forcing only generates small departures from the solid-body rotation of the fluid core. Alone, these small perturbations are not powerful enough to sustain any magnetic field. However, these periodic perturbations are able to excite resonant instabilities which can then break down into bulk-filling turbulence.

While the flow directly created by tidal perturbations is purely laminar and of low amplitude in the first place, the excited instabilities are responsible for converting the huge rotational kinetic energy into turbulence, and possibly dynamo action. Flows driven by tidal instabilities in a geophysical context have benefited from extensive investigation over the past two decades. Theoretical and experimental studies have revealed that these instabilities, for the most part, rely on the interplay between inertial waves (which exist in any rotating fluid because of the restoring action of the Coriolis force) and the harmonic forcing. The underlying mechanism is a sub-harmonic resonance called the elliptical instability (Kerswell, 1993b; Le Dizès, 2000; Lacaze et al., 20050; Le Bars et al., 20070; Cébron et al., 20140; Grannan et al., 20140). This research has clarified the conditions for such an instability to develop in terms of tidal forcing

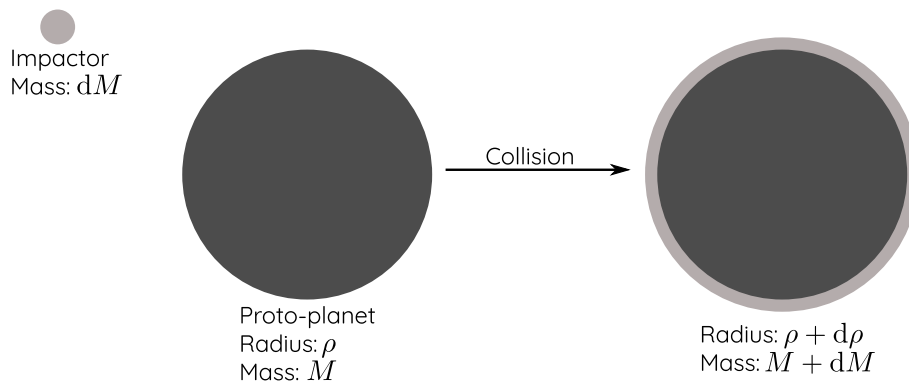


**Figure 2:** Schematic cartoon of the collision of a proto-planet with an impactor resulting in an increase of mass and radius of the proto-planet.

versus viscous damping inside planetary cores (see for instance Cébron et al. (2012a)). Yet, there is still much to understand about tidally-driven instabilities: the comprehension of their saturation into bulk-filling turbulence remains a challenging problem although of crucial importance to predict dynamo action. The turbulence driven by tidal instabilities is, indeed, very different from classical, homogeneous and isotropic turbulence. The forcing amplitudes due to tidal perturbations are weak, and yet, because of the massive size of astrophysical bodies, dissipation is sufficiently small for turbulence to develop. In such regimes, the turbulence is strongly influenced by planetary rotation. In addition, the weak forcing amplitude and dissipation regimes relevant for geo- and astrophysics is difficult to study as it is far beyond the reach of any numerical simulation or laboratory experiment; only extrapolations to planetary cores may be carefully drawn from present knowledge.

Nevertheless, significant steps have been made over the past few years, one of the most striking results being the evidence of a fully turbulent kinematic dynamo driven by tidal forcing in a planetary-relevant ellipsoidal geometry (Reddy et al., 2018). Although it was previously thought that the elliptical instability would lead to cycles of resonance, turbulent break-down and relaminarisation of the flow (Malkus, 1989; Eloy et al., 2003; Barker and Lithwick, 2013), Grannan et al. (2014), Favier et al. (2015) and Grannan et al. (2017) found that the resonance process also leads to sustained turbulence. In such a persistent saturation flow, they identified inertial waves in interaction, but also columnar vortices invariant along the rotation axis, called geostrophic modes. However, all these experiments and simulations have been carried out under relatively high dissipation and forcing amplitude, *i.e.* regimes that are far from with the conditions encountered inside planetary cores or stellar interiors.

The work presented throughout this dissertation aims at exploring regimes that are closer to geo- and astrophysical conditions. We explore with an experiment and a numerical idealised model the nature of the turbulence excited by the elliptical instability in weak forcing amplitude and weak dissipation regimes that have remained beyond the reach of any previous study. Because of their key role in the saturation process, our study focuses more particularly on non-linear processes involving inertial waves and geostrophic vortices. The main result overall is identify two regimes in the saturation of the elliptical instability, one which is dominated by inertial waves in weakly non-linear interaction and the other where strong geostrophic vortices take over the flow. We characterise the boundary between these two regimes in terms of dissipation and forcing amplitude, and strive to model theoretically the transition between them in order to extrapolate the expected type of saturation to the extreme geo- and astrophysical

regimes.

In addition, a significant part of the present work is targeted at the existence and the saturation of the tidally driven parametric instability in stably-stratified planetary cores. We show that very similarly to the elliptical instability, the tidal forcing excites resonance of internal gravity waves which are oscillations induced by a competition between inertia and gravity. In the non-linear saturation, the turbulent flow excited by the resonance is always a superposition of internal waves in non-linear interaction in the regimes of weak to moderate forcing amplitude and dissipation.

This dissertation is organised as follows.

- **Chapter 1** is a general introduction on mechanical forcing in geo- and astrophysical fluid interiors. We present the basic response of fluid bodies to tidal distortion, in particular the case where a planet is surrounded by an orbiting moon creating a rotating tidal bulge, and the case where tidal interaction forces oscillations of the rotation rate called librations. Prior to introducing the elliptical instability, a section is devoted to the fundamentals of parametric resonance illustrated in the case of a length-varying pendulum. The elliptical instability is presented in close analogy with the pendulum resonance.
- **Chapter 2** is a continuation of the introduction chapter where we introduce the main non-linear processes occurring between inertial oscillations, *i.e.* three-waves resonance, and between waves and geostrophic vortices. We present the challenges raised by the non-linear saturation of the elliptical instability and the goals of the work presented in this dissertation.
- **Chapter 3** is an experimental study of the saturation of the elliptical instability carried out in a librating ellipsoid, based on and extending the previous works of Noir et al. (2012), Grannan et al. (2014) and Grannan et al. (2017). We find two regimes of saturation. The first one occurs at low forcing amplitude and is dominated by inertial waves in triadic resonant interaction. The second is dominated by persistent geostrophic vortices emerging as the libration amplitude is increased. We focus on locating the secondary transition between the two regimes as a function of the libration amplitude and viscous dissipation.
- **Chapter 4** and **chapter 5** are two studies focusing on non-linear mechanisms transferring energy from waves to vortices. We first investigate numerically and theoretically the stability of a plane inertial wave. A finite amplitude instability leading to the exponential growth of a geostrophic mode is found to be driven by the wave. We prove the existence of a minimal wave amplitude below which the maintained wave transfers its energy to other inertial waves only. In the next chapter, we examine the role of direct forcing of geostrophic flows by non-linear self-interaction of inertial modes. Although the latter vanishes in inviscid fluids, self-interactions in boundary layers may be responsible for driving large amplitude geostrophic flow. We show with a numerical analysis of inertial modes in a sphere based on Tilgner (2007b), Lagrange et al. (2011) and Vidal and Schaeffer (2015) that this mechanism is unlikely to drive a geostrophic-dominated saturation of the elliptical instability.
- **Chapter 6** is an idealised numerical study of the saturation of the elliptical instability building on the previous work of Barker and Lithwick (2013). We bring to more extreme regimes the wave-dominated and the geostrophic-dominated regimes and further

analyse the detail of their content. We confirm that the wave-dominated regime is a superposition of inertial waves in non-linear resonant interaction, and give evidence that it should lead to inertial wave turbulence in geo- and astrophysical conditions. We also relate the transition between the two regimes to the finite Rossby number instability put forward in **chapter 4**.

- **Chapter 7** is a complementary investigation of the stability of stratified planetary interiors such as liquid iron core or sub-surface oceans. We investigate the strongly stratified limit where the effects of the Coriolis force are negligible compared to buoyancy. In close analogy with the study of **chapter 6**, we build a local model of tidally distorted stably stratified planetary layers and analyse its stability with Floquet analysis and numerical simulations. We find that internal gravity waves undergo a parametric resonance very similar to the elliptical instability in rotating fluids and closely related to the parametric subharmonic instability of internal waves studied by Joubaud et al. (2012). We then proceed to a systematic analysis of the saturation of the instability which happens to drive internal wave turbulence, a non-linear state that has been characterised for instance by Brouzet et al. (2016) in the different but closely related case of the break-down of an internal wave attractor. We characterise the spatio-temporal properties of this saturation state and quantify the associated turbulent mixing.



# Chapter 1

## Tidal forcing, inertial waves and the elliptical instability

### 1. Tidal forcing in planetary cores: the primary response to tides

The aim of this section is to review the basic effects of tides on planetary cores. We introduce the principal perturbations to the rotational motion of planets induced by tides and expose the method to infer the primary response of a fluid cavity to those perturbations.

#### 1.1 The shape of a planet undergoing tidal distortion

The gravitational interaction between two astrophysical bodies results in a force field distorting them called tides. For each body, it reflects the difference between the total gravitational attraction which drives its motion and the local attraction. Considering a planet  $T$  and a moon  $L$  separated by a distance  $d$  taken constant in first approximation (see figure 1.1), the tidal potential writes at lowest order:

$$U_{\text{tides}} = \frac{GM_T}{R_T^3} \frac{M_L}{M_T} \left( \frac{R_T}{d} \right)^3 (r^2 - (\mathbf{e}_X \cdot \mathbf{r})^2) \quad (1.1)$$

with  $r^2 = (X^2 + Y^2 + Z^2)$ ,  $\mathbf{r} = X\mathbf{e}_X + Y\mathbf{e}_Y + Z\mathbf{e}_Z$  and  $G$  the gravitational constant —the remaining variables are defined in figure 1.1. The tidal force field is represented in figure 1.1 and bears two important symmetries: it is invariant by rotation around the planet-moon axis ( $OX$ ) and by reflection relative to the ( $YOZ$ ) plane. The deformation induced by the tidal

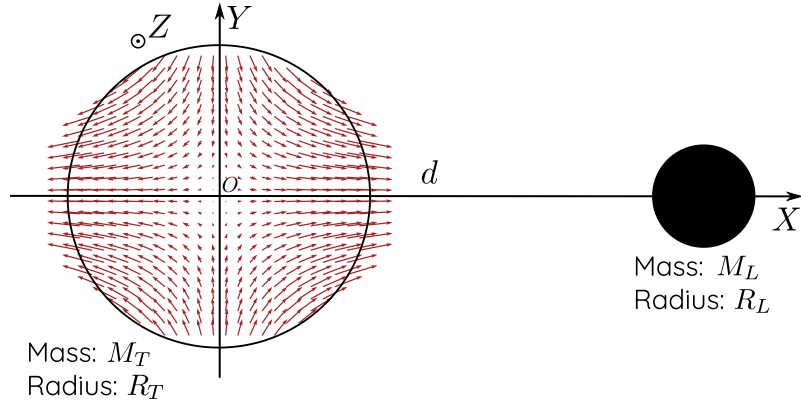


**Figure 1.1:** Schematic diagram of two astrophysical bodies such as the Earth and the Moon, assuming that they are perfectly spherical and homogeneous. The tidal force field induced by the Moon is represented by the red arrows in the Earth. This field is invariant under rotation around the  $X$  axis. Note that the Earth induces a similar field inside the Moon.

potential (1.1) can be analytically determined (Sridhar and Tremaine, 1992; Barker, 2016; Barker et al., 2016). At the lowest order, it can be shown that the planet adopts an ellipsoidal shape: the combination of the equatorial—or rotational—bulge, created by the centrifugal force, and of the tidal bulge force the three axes of this ellipsoid to have different lengths.

In the following, we assume that the outer boundary of a planetary cores is ellipsoidal. For simplicity's sake, we do not take into account the possible presence of a solid inner core. In a general context, as the mechanical properties and rigidities of a solid iron inner core and of the rocky mantle are different, the liquid iron domain would be a shell confined between two ellipsoids which are not necessarily homothetic. Such a geometry does not change the overall dynamics but makes its analysis more difficult—see for instance Lemasquerier et al. (2017). In addition, the case we consider is an actual situation encountered in young planets as solid inner cores only crystallise later after their formation. For instance, the Earth is known to have been surrounded by a magnetic field since at least 3.5 Gy although the inner core is only around 1 Gy old or less (Labrosse, 2015).

## 1.2 Flow modelling in planetary cores

The liquid iron of the outer core is a Newtonian fluid with a kinematic viscosity  $\nu$  similar to water,  $\nu \sim 10^{-6 \pm 2} \text{ m}^2 \cdot \text{s}^{-1}$ . (Olson, 2015). Apart from the last chapter of this dissertation, we discard any density variation in the fluid that may be induced by composition or pressure. The behaviour of a liquid core is therefore modelled by the incompressible Navier-Stokes equation.

As shown in the next sections, the rotation of the core is an important component of its dynamics. Unless it is specified, we study the velocity  $\mathbf{u}$  in the core in the rotating frame. Let us assume that the rotation rate vector is  $\boldsymbol{\Omega} = \Omega \mathbf{e}_z$ . The local acceleration of the fluid includes inertial pseudo-forces among which the centrifugal force  $\boldsymbol{\Omega} \times (\boldsymbol{\Omega} \times \mathbf{r})$ , which is included in the pressure gradient, and the Coriolis force  $2\boldsymbol{\Omega} \times \mathbf{u}$ . In the rotating frame, when  $\boldsymbol{\Omega}$  is constant in time, the incompressible dynamics of the flow  $\mathbf{u}$  writes:

$$\begin{cases} \partial_t \mathbf{u} + \mathbf{u} \cdot \nabla \mathbf{u} + 2\Omega \mathbf{e}_z \times \mathbf{u} &= -\nabla p + \nu \nabla^2 \mathbf{u} \\ \nabla \cdot \mathbf{u} &= 0 \end{cases} \quad (1.2)$$

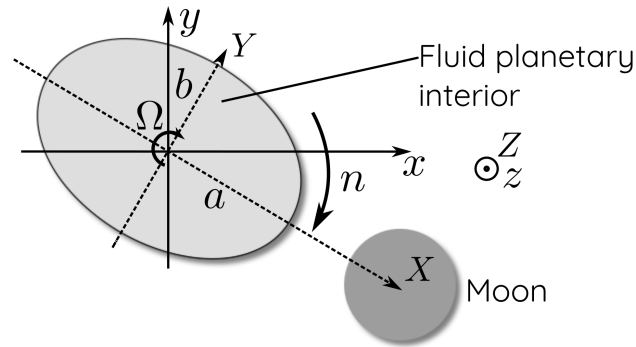


**Figure 1.2:** Schematic diagram of a moon orbiting around a planet. We define two systems of axes:  $(OXYZ)$  follows the revolution of the moon (hence of the ellipsoidal shape of the planet) and rotates at rate  $n\mathbf{e}_x$ ;  $(Oxyz)$  tracks the rotation of the planet and rotates (*i.e.* its solid mantle) at rate  $\Omega\mathbf{e}_z$ . We assume that the two rotation motions occur in the same plane for simplicity's sake. The fluid envelop is ellipsoidal: its axes have lengths  $a$  and  $b$  in the equatorial plane, and  $c$  along the axis of rotation.

where  $\nu$  is the kinematic viscosity of liquid iron and  $p$  is a modified pressure divided by the—constant—density and including the centrifugal acceleration. In the case where the rotation vector varies over time, a Poincaré acceleration  $\dot{\Omega} \times \mathbf{r}$  must be included in the left hand side of the first equation in (1.2). In what follows, we also refer to the Euler equation as the equation obtained in the limit  $\nu = 0$  of (1.2). These governing equations will be used in the following to determine the flows driven by tidal excitation.

### 1.3 Flow driven by differential spin and orbit

In a configuration similar to the Earth-Moon system, the spin of the Earth is not synchronised with the orbit of the Moon. Because the Earth rotates every day, but the Moon's orbit is 27 days long, and because of the symmetry of the tidal field, the solid part of the Earth is subject to slightly less than two tidal rises per day. Focusing on the core, while the liquid iron rotates at the same rate as the Earth, its outer shape bears a tidal bulge which follows the orbiting motion of the Moon.

Let us assume a simple case where those two rotations take place in the same plane, the corresponding situation being depicted in figure 1.2. In such a configuration, the flow inside the core is not a solid body rotation. We aim at determining the inviscid flow created by the differential rotation of the planet and its moon; it must satisfy the Euler equation and the non-penetration boundary conditions at the edge of the ellipsoidal container. We use the method introduced by Hough (1895). First we note that the derivation is facilitated when carried out in the frame of reference in which the boundary shape does not change over time, that is the frame  $(OXYZ)$  with axes aligned along the main axes of the ellipsoid with lengths  $a$ ,  $b$  and  $c$  (see figure 1.2). Then, we look for a uniform vorticity solution which directly satisfies the boundary conditions. This is achieved by first using a rescaled system of coordinates  $\tilde{\mathbf{X}} = (\tilde{X}, \tilde{Y}, \tilde{Z})$  which transforms the ellipsoid into a sphere, the velocity  $\mathbf{U} = (U, V, W)$  being also transformed accordingly:

$$\begin{cases} \tilde{X} = X/a \\ \tilde{Y} = Y/b \\ \tilde{Z} = Z/c \end{cases} \quad \text{and} \quad \begin{cases} \tilde{U} = U/a \\ \tilde{V} = V/b \\ \tilde{W} = W/c \end{cases} \quad (1.3)$$

and then looking for a vector  $\boldsymbol{\omega}(t)$  such that:

$$\tilde{\mathbf{U}} = \boldsymbol{\omega}(t) \times \tilde{\mathbf{X}}. \quad (1.4)$$

With this ansatz, the transformed velocity field is at each time  $t$  a solid-body rotation which necessarily satisfies the non-penetration boundary condition in the sphere. As a consequence, the flow  $\mathbf{U}$  transformed back into the original coordinates also satisfies the boundary conditions. Such a flow is divergence-free and has a uniform vorticity  $\boldsymbol{\omega}$  which writes:

$$\boldsymbol{\omega} = \nabla \times \mathbf{U} = \begin{bmatrix} \left(\frac{c}{b} + \frac{b}{c}\right) \omega_x \\ \left(\frac{c}{a} + \frac{a}{c}\right) \omega_y \\ \left(\frac{a}{b} + \frac{b}{a}\right) \omega_z \end{bmatrix}. \quad (1.5)$$

We look for a steady solution in the frame orbiting with the Moon at a rate  $n\mathbf{e}_z$  (see figure 1.2). Taking into account the Coriolis acceleration due to the rotation of the frame of reference, the stationary vorticity equation derived from the Euler equation reads:

$$(\mathbf{U} \cdot \nabla) \boldsymbol{\omega} = ((\boldsymbol{\omega} + 2n\mathbf{e}_z) \cdot \nabla) \mathbf{U}. \quad (1.6)$$

As  $\boldsymbol{\omega}$  is space-independent, the left hand side of this equation vanishes. The equations on the components of the vorticity are therefore:

$$\begin{cases} \left[ \frac{1}{c} \left( \frac{a}{b} + \frac{b}{a} \right) - \frac{1}{b} \left( \frac{c}{a} + \frac{a}{c} \right) \right] \omega_y \omega_z + 2\frac{1}{c} n \omega_y = 0 \\ \left[ \frac{1}{a} \left( \frac{c}{b} + \frac{b}{c} \right) - \frac{1}{c} \left( \frac{a}{b} + \frac{b}{a} \right) \right] \omega_x \omega_z - 2\frac{1}{c} n \omega_x = 0 \\ \left[ \frac{1}{b} \left( \frac{c}{a} + \frac{a}{c} \right) - \frac{1}{a} \left( \frac{c}{b} + \frac{b}{c} \right) \right] \omega_x \omega_y = 0. \end{cases} \quad (1.7)$$

The last equation prescribes either  $\omega_x$  or  $\omega_y$  to be equal to 0. Let us assume  $\omega_y = 0$  (a similar reasoning is possible for  $\omega_x = 0$ ): the first equation is then directly satisfied. The second equation either prescribes a  $\omega_z$  proportional to  $n$  for a non-zero  $\omega_x$ , or a zero  $\omega_x$ . However, the former possibility does not account for the global rotation of the planet at rate  $\Omega$ , which must be part of the solution. The physical solution is therefore obtained for  $\omega_x = 0$ .<sup>1</sup> To constrain the value of  $\omega_z$ , we consider that the vorticity of the fluid must match the planetary vorticity (Sridhar and Tremaine, 1992; Goodman, 1993; Barker, 2016):

$$\left( \frac{a}{b} + \frac{b}{a} \right) \omega_z = 2(\Omega - n) \iff \omega_z = \frac{2ab}{a^2 + b^2} (\Omega - n) \quad (1.8)$$

which finally gives the following steady flow driven by tides:

$$\begin{bmatrix} U \\ V \\ W \end{bmatrix} = \frac{2ab}{a^2 + b^2} (\Omega - n) \begin{bmatrix} -\frac{a}{b} Y \\ \frac{b}{a} X \\ 0 \end{bmatrix}. \quad (1.9)$$

<sup>1</sup>This condition is in any case the only one when we consider the viscous problem where the flow solution of (1.7) must reconnect to the rotating solid mantle through a thin boundary layer, see for instance Tilgner (2007a).

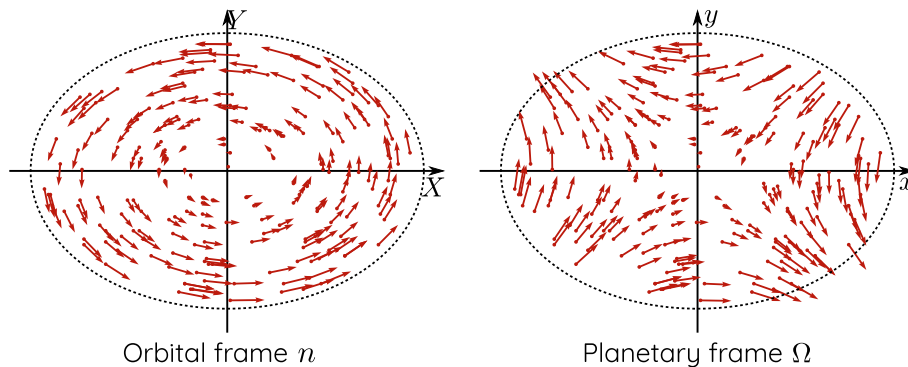


**Figure 1.3:** Tidal flow velocity field seen from the orbital frame rotating at rate  $n$  (left) and from the planetary frame rotating at rate  $\Omega$  (right). The arrows scale is not the same on the two figures.  $\Omega - n$  is positive: the fluid moves counter-clockwise in the orbital frame and the elliptical bulge moves clockwise when seen from the planetary frame. Planetary frame highlights the strain field which perturbs the solid-body rotation of the fluid.

Lastly, we can introduce the ellipticity of the deformation  $\beta = (a^2 - b^2)/(a^2 + b^2)$ ; the base flow then writes into a simpler and more compact form:

$$\mathbf{U} = (\Omega - n) \begin{bmatrix} 0 & -1 - \beta & 0 \\ 1 - \beta & 0 & 0 \\ 0 & 0 & 0 \end{bmatrix} \begin{bmatrix} X \\ Y \\ Z \end{bmatrix}. \quad (1.10)$$

Note that this last form is quite meaningful as it corresponds to the superposition of a circular vortex and a strain, which is a configuration known to be unstable (Pierrehumbert, 1986; Bayly, 1986; Waleffe, 1990). Moreover, in the frame rotating with the planet, the flow  $\mathbf{U}$ , denoted  $\mathbf{U}^\Omega$ , is:

$$\mathbf{U}^\Omega = -\beta\gamma \begin{bmatrix} \sin(2\gamma t) & \cos(2\gamma t) & 0 \\ \cos(2\gamma t) & -\sin(2\gamma t) & 0 \\ 0 & 0 & 0 \end{bmatrix} \begin{bmatrix} x \\ y \\ z \end{bmatrix} \quad \text{with: } \gamma = \Omega - n \quad (1.11)$$

which can be retrieved from (1.10) via a rotation of coordinates and a velocity composition. The two fields (1.10) and (1.11) are shown in figure 1.3. This last way of writing the tidal flow is even more meaningful as it highlights the time periodicity of the tidal excitation: the tidal frequency is twice the differential rotation between the planet and the moon, which reflects the symmetry of the tidal bulge respective to the plane  $(OYZ)$ . For  $n \ll \Omega$ , an observer bound to the rotating frame of reference undergoes two tidal rises a day as on the Earth where  $n/\Omega \sim 1/27$ . Besides, the tidal flow amplitude is proportional to the ellipticity of the deformation. Tidal excitation is a small perturbation to the planetary solid-body rotation, of relative amplitude  $10^{-7}$  on Earth for instance. Nevertheless, we show later in this chapter that this repetitive excitation, although of small amplitude, is able to excite turbulent flows.

## 1.4 Perturbation of the rotation rate: libration

In the previous section, we have introduced the tidal potential and its consequences on the shape of planetary cores. Tides not only induce distortion, they also alter the rotation of planets. We introduce in this section perturbations of the rotation rate, called librations, and combine them with the tidal distortion to derive the corresponding core flows.

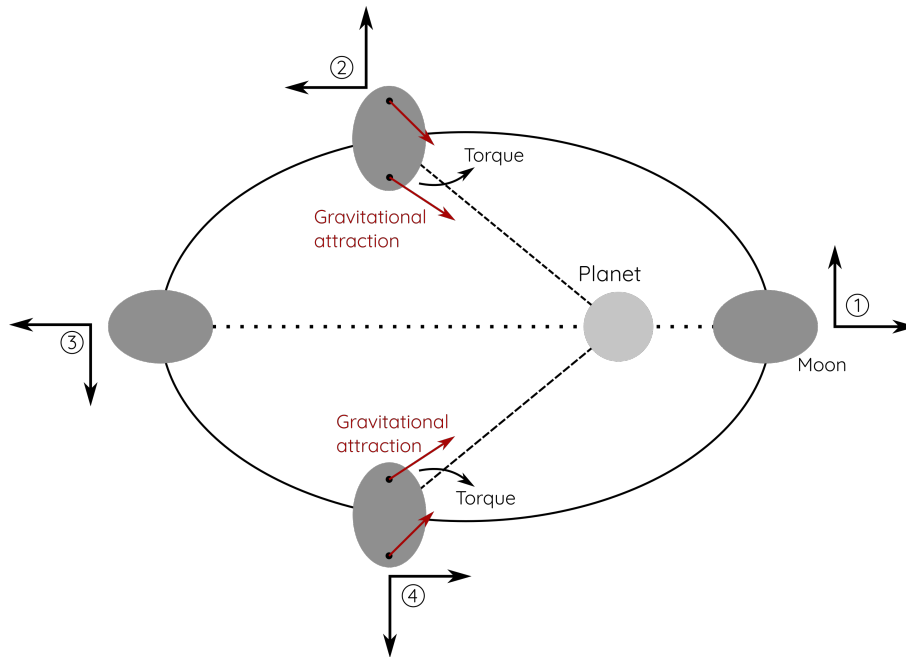


**Figure 1.4:** Schematic diagram of the excitation of libration on a moon with an eccentric orbit in spin-orbit resonance. Its bulge is frozen and follows the rotation of the moon instead of staying aligned towards the parent planet. The four snapshots separate the orbit and the rotation in four equal periods. Rotation is anti-clockwise.

### Libration of moons

Physical longitudinal libration, hereafter called libration, is the oscillation of the rotation rate of an astrophysical body without change in its rotation axis. This kind of motion is excited by tidal interaction between the considered body's tidal bulge and its parent planet or star. One common situation where libration is observed is presented in figure 1.4: a moon is synchronised in a spin-orbit resonance along an elliptical orbit, meaning that its orbital rate matches its mean rotation rate (like our Moon, which always shows us the same side). This is due to tidal dissipation inside the rocky mantle of such bodies which despins them from any initial rotation rate into this particular equilibrium (Rambaux and Castillo-Rogez, 2013). Moreover, because of the rigidity of the moon, its tidal bulge is in general not exactly aligned with the parent body. The figure 1.4 presents the extreme situation where the bulge is frozen and follows the rotation of the moon instead of staying aligned with the planet. This happens for instance in the case of the Earth's Moon which has a large fossil bulge which has not relaxed and is not induced by tidal interaction anymore but still persists. As depicted in figure 1.4, this misalignment and the difference of gravitational attraction between the two sides of the bulge create a torque which tends to accelerate the rotation rate at ② and to decelerate the rotation rate at ④. The rotation rate is therefore perturbed around a mean with the same period as the orbit.

The situation shown in figure 1.4 is not the only one leading to libration oscillations. In planetary systems with many satellites such as the Jovian and Saturnian systems, a body not only interacts with its parent planet but also with all the other moons. Some of them are in what is called a Laplace resonance, which is a stable situation where the orbit rates of several moons are multiples of one another (Rambaux and Castillo-Rogez, 2013). There also exists

length-of-day variations in non-synchronised planets like the Earth, corresponding to variation of their rotation rate

### Libration-driven flows

We now seek to determine the flow driven by libration and assume for simplicity's sake a purely rigid tidal bulge. The total rotation rate including libration can be written as:

$$\boldsymbol{\Omega} = \Omega_0 (1 + \varepsilon \sin(f \Omega_0 t)) \mathbf{e}_z \quad (1.12)$$

where  $\varepsilon$  is the relative variation of the rotation rate and  $f$  is the dimensionless libration frequency. Observed from the frame rotating at rate  $\Omega_0$ , the moon and its bulge oscillate with a frequency  $\omega_\ell \equiv f \Omega_0$  and with an amplitude angle  $\varepsilon \Omega_0 / \omega_\ell$ . Although in the example of spin-orbit synchronisation presented in figure 1.4  $\omega_\ell = \Omega_0$ , the libration frequency can take any value due to tidal interactions with many bodies as in the Jovian and Saturnian systems. To determine the libration-driven flow, we use the same method as for the tidal base flow: we look for a flow  $\tilde{\mathbf{U}} = \boldsymbol{\omega}(\mathbf{t}) \times \tilde{\mathbf{X}}$ —see definition (1.4)—in the frame where the boundary stands still, *i.e.* the librating frame. We use the same notation as before: in the frame  $(OXYZ)$  the boundary is still—therefore it is the librating frame—and  $(Oxyz)$  is the mean rotation frame. In the  $(OXYZ)$  frame the equation for the vorticity  $\boldsymbol{\omega}$  writes:

$$\partial_t \boldsymbol{\omega} + (\mathbf{u} \cdot \nabla) \boldsymbol{\omega} = ((\boldsymbol{\omega} + 2\boldsymbol{\Omega}) \cdot \nabla) \mathbf{u} - 2 \frac{d\boldsymbol{\Omega}}{dt} \quad (1.13)$$

where we include the time dependence of the flow—oscillating at the libration frequency—and a last term corresponding to the Poincaré's acceleration. In its expanded form, the equation (1.13) yields:

$$\begin{cases} \left( \frac{c}{b} + \frac{b}{c} \right) \dot{\omega}_x = \left[ \frac{a}{c} \left( \frac{a}{b} + \frac{b}{a} \right) - \frac{a}{b} \left( \frac{c}{a} + \frac{a}{c} \right) \right] \omega_y \omega_z + 2 \frac{a}{c} \Omega \omega_y \\ \left( \frac{c}{a} + \frac{a}{c} \right) \dot{\omega}_y = \left[ \frac{b}{a} \left( \frac{c}{b} + \frac{b}{c} \right) - \frac{b}{c} \left( \frac{a}{b} + \frac{b}{a} \right) \right] \omega_x \omega_z - 2 \frac{b}{c} \Omega \omega_x \\ \left( \frac{a}{b} + \frac{b}{a} \right) \dot{\omega}_z = \left[ \frac{c}{b} \left( \frac{c}{a} + \frac{a}{c} \right) - \frac{c}{a} \left( \frac{c}{b} + \frac{b}{c} \right) \right] \omega_x \omega_y - 2 \frac{d\Omega}{dt} . \end{cases} \quad (1.14)$$

Assuming  $\omega_x$  and  $\omega_y$  are zero, the last equation relates the temporal variation of  $\omega_z$  to the Poincaré acceleration:

$$\left( \frac{a}{b} + \frac{b}{a} \right) \dot{\omega}_z = -2\dot{\Omega} \iff \omega_z = -\frac{2ab}{a^2 + b^2} \Omega_0 \varepsilon \sin(f \Omega_0 t) + \text{cst} . \quad (1.15)$$

Considering a synchronised body in the librating frame, the constant component of the vorticity must be equal to zero. The resulting base flow can be written in the librating frame in terms of the axes' lengths or the ellipticity  $\beta$  defined earlier:

$$\begin{aligned} \mathbf{U} &= -\frac{2ab}{a^2 + b^2} \Omega_0 \varepsilon \sin(f \Omega_0 t) \begin{bmatrix} 0 & -a/b & 0 \\ b/a & 0 & 0 \\ 0 & 0 & 0 \end{bmatrix} \begin{bmatrix} X \\ Y \\ Z \end{bmatrix} \\ &= -\Omega_0 \varepsilon \sin(f \Omega_0 t) \begin{bmatrix} 0 & -1 - \beta & 0 \\ 1 - \beta & 0 & 0 \\ 0 & 0 & 0 \end{bmatrix} \begin{bmatrix} X \\ Y \\ Z \end{bmatrix} \end{aligned} \quad (1.16)$$

The libration flow written in the mean rotation frame—which requires doing velocity composition and coordinates change— writes, at the lowest order in  $\varepsilon$ :

$$\mathbf{U}^\Omega = \Omega_0 \varepsilon \beta \sin(f \Omega_0 t) \begin{bmatrix} 0 & 1 & 0 \\ 1 & 0 & 0 \\ 0 & 0 & 0 \end{bmatrix} \begin{bmatrix} x \\ y \\ z \end{bmatrix}. \quad (1.17)$$

Note that at  $t = \pi/(2f \Omega_0)$  the structure of the flow (1.16) is exactly similar to (1.10): snapshots of the velocity in the libration case are the same as figure 1.3-left for the librating frame and figure 1.3-right for the mean rotation frame. Generally, seen from the frame where the bulge is stationary, a fluid particle rotates around elliptical streamlines in the tidal case and oscillates along elliptical streamlines in the libration case. Seen from the mean rotation frame, the strain field in the tidal case rotates with a constant amplitude, whereas the strain field in the libration case has a stationary spatial structure but an oscillating amplitude.

## 2. Parametric sub-harmonic resonance of a pendulum

Both tidally and libration-driven base flows are unstable and tend to force three-dimensional complex flows. In the next section, we show that the instability is a parametric, sub-harmonic resonance of inertial oscillations that couples the effects of tidal perturbations with rotation. Prior to delving into the stability analysis of these flows, we wish to introduce in the present section a simple example of parametric resonance in the case of a pendulum. We will later use analogies with the pendulum to present the stability of tidally perturbed planetary and stellar interiors.

### 2.1 O Botafumeiro

One of the most striking example of parametric resonance that can be found around the globe is probably *O Botafumeiro* in Santiago de Compostella's Cathedral. It is a 54 kg thurible (a metal censer) that hangs on the top of the cathedral's dome. The length of the rope can be changed over time around its mean length of 21.5 m by a group of holders. To spread incense in the cathedral, the holders first let the thurible swing with a small angle. Each time the censer goes up, *i.e.* twice per period, they slightly pull down the rope to shorten the swing length, and let it increase again as the swing reaches its highest position. With this twice per period excitation, they manage to swing the censer with very large amplitude in a short time, up to a height of 20.6 m. The velocity at the lowest point of the oscillation reaches 68 km/h.

### 2.2 Mechanical study of the length-varying pendulum

As shown in figure 1.5, we model *O Botafumeiro* by a pendulum whose length  $\ell$  varies over time:

$$\ell(t) = \ell_0(1 + \eta \sin(\omega t)) \quad (1.18)$$

where  $\eta$  is a small parameter accounting for the small modulation of the relative length of the swing. We study the motion of the point object  $M$  of mass  $m$  at the end of the rope of length  $\ell(t)$ . We assume that the referential bound to  $O$  is Galilean and that the rope is mass-less. The velocity  $\mathbf{v}$  of  $M$  writes:

$$\mathbf{v} = \ell \dot{\theta} \mathbf{e}_\theta + \dot{\ell} \mathbf{e}_r \quad (1.19)$$

and the angular momentum  $L_z$  of  $M$  with respect to axis  $(O, \mathbf{e}_z)$  is:

$$L_z = m\ell^2 \dot{\theta} . \quad (1.20)$$

As gravity applies a torque  $-m\ell g \sin \theta$ , the conservation of angular momentum yields:

$$\ddot{\theta} + \frac{2\dot{\ell}}{\ell} \dot{\theta} + \frac{g}{\ell} \sin \theta = 0 . \quad (1.21)$$

Introducing the ansatz (1.18) and  $\omega_0^2 = g/\ell_0$  finally leads to:

$$\ddot{\theta} + \eta \frac{2\omega \cos(\omega t)}{1 + \eta \sin(\omega t)} \dot{\theta} + \frac{\omega_0^2}{1 + \eta \sin(\omega t)} \sin \theta = 0, \quad (1.22)$$

where  $\eta$  and  $\omega$  are two control parameters, the relative variation of the rope length and the frequency of these variations.

We can already qualitatively predict at which frequency the length must be varied for optimal oscillations by looking at equation (1.21): indeed, comparing to the classical pendulum equation where  $\ell$  is constant, but still accounting for  $\dot{\ell}$ , the second term in (1.21) appears in place of a viscous damping of type  $\nu \dot{\theta}$ . Here however the sign of the viscosity  $\nu$  depends on the sign of  $\dot{\ell}$ . In particular, shortening the length of the rope—*i.e.*  $\dot{\ell} < 0$ —corresponds to a “negative viscosity”, which encourages the motion;  $\dot{\ell} > 0$  corresponds to a classical positive damping. For the holders to input maximum energy into the system, the length must thus be shortened when the angular velocity  $|\dot{\theta}|$  is maximum, *i.e.* when the pendulum is at its lowest position, and increased when  $\dot{\theta} = 0$ , *i.e.* when it is at its highest position. Therefore, two antagonistic moves must be operated during half the period of the pendulum: the frequency of the excitation must be the double of the free oscillation. This will be formally proved in the following.

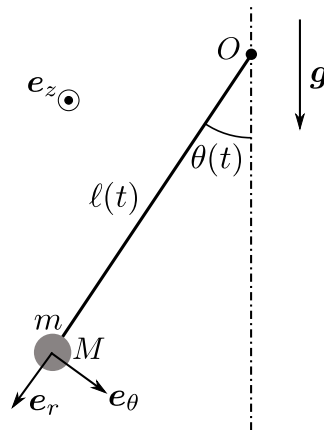


**Figure 1.5:** Model for *O Botafumeiro*: a length varying pendulum. The function  $\ell(t)$  is prescribed to periodically vary around a mean length  $\ell_0$  according to (1.18).

## 2.3 Asymptotic analysis

To analytically study the length-varying pendulum described by (1.22) and get the main physical properties of this system, we carry out an asymptotic study in the limit of small length variations  $\eta \ll 1$  and small angle  $\theta \ll 1$ . The equation (1.22) can then be expanded into:

$$\ddot{\theta} + \omega_0^2 \theta = \eta [-2\omega \cos(\omega t) \dot{\theta} + \omega_0^2 \sin(\omega t) \theta] \quad (1.23)$$

where the length variation appears at order one as a forcing. The system has two typical time scales. The first one is  $1/\omega_0$ , the natural or free period of pendulum oscillation. This is the fast timescale of the system. We further assume here that the forcing period  $1/\omega$  is of the same order of magnitude as  $1/\omega_0$ , because as seen just before, this is where interesting physics is expected. Then because of the forcing, the system also evolves over a slow timescale  $1/(\eta\omega_0)$ . We thus look for a first-order accurate- solution to (1.23) with respect to the small parameter  $\eta$ , where these two timescales are included and decoupled, *i.e.* a function  $\theta$  which depends on  $\tau = t$  and  $T = \eta t$  such that:

$$\theta(\tau, T) = (f_0(\tau) + \eta f_1(\tau)) F(T). \quad (1.24)$$

In this two-timing framework, the total time derivatives are expanded as partial derivatives according to:

$$\begin{cases} \frac{d}{dt} = \frac{\partial}{\partial \tau} + \eta \frac{\partial}{\partial T} \\ \frac{d^2}{dt^2} = \frac{\partial^2}{\partial \tau^2} + 2\eta \frac{\partial^2}{\partial T \partial \tau} \end{cases} \quad (1.25)$$

where we have kept only the terms up to order 1. Taking into account the ansatz (1.24) and (1.25) yields to an order zero and an order one equations such that:

$$\begin{cases} \frac{d^2 f_0}{d\tau^2} + \omega_0^2 f_0 = 0 \\ \frac{d^2 f_1}{d\tau^2} + \omega_0^2 f_1 = -2\omega \cos(\omega\tau) f_0' + \omega_0^2 f_0 \sin(\omega\tau) - 2 \frac{f_0' F'}{F}. \end{cases} \quad (1.26)$$

The solution to the first equation is straightforward, and using complex solutions:

$$f_0(\tau) = A e^{i\omega_0\tau} + B e^{-i\omega_0\tau}. \quad (1.27)$$

We then input this solution in the right hand side (RHS) of the second equation in (1.26) and expand it to find the following Fourier decomposition:

$$\begin{aligned} \frac{d^2 f_1}{d\tau^2} + \omega_0^2 f_1 &= e^{i(\omega_0+\omega)\tau} \left[ -Ai\omega_0\omega + A \frac{\omega_0^2}{2i} \right] \\ &+ e^{i(\omega_0-\omega)\tau} \left[ -Ai\omega_0\omega - A \frac{\omega_0^2}{2i} \right] \\ &+ e^{i(-\omega_0+\omega)\tau} \left[ Bi\omega_0\omega + B \frac{\omega_0^2}{2i} \right] \\ &+ e^{-i(\omega_0+\omega)\tau} \left[ Bi\omega_0\omega - B \frac{\omega_0^2}{2i} \right] \\ &+ e^{i\omega_0\tau} \left[ -2iA \frac{F'}{F} \omega_0 \right] + e^{-i\omega_0\tau} \left[ 2iB \frac{F'}{F} \omega_0 \right]. \end{aligned} \quad (1.28)$$

The frequency of the two terms appearing in the last line is the same as the eigen frequency of the harmonic oscillator in the left hand side (LHS) of (1.28) and should give rise to divergence of  $f_1$ . Those contributions to the LHS are called “secular terms” as they excite a long term growth of the solution. However, the Taylor expansion in the ansatz (1.24) requires  $f_1$  to remain bounded over time for the calculation to remain valid: secular terms must therefore be cancelled.

In general, a first possibility is to impose  $F' = 0$ , but this cannot explain the amplitude increase observed in the case of *O Botafumeiro*. A more interesting solution arises when the excitation frequency  $\omega$  is adequately chosen. When

$$\omega = 2\omega_0$$

the second and third lines then also have a frequency of  $\pm\omega_0$  and give a more complex condition for  $f_1$  to remain bounded. With this particular condition, cancelling the secular terms leads to

$$\begin{cases} -\frac{3}{2}\omega_0 A + 2\frac{F'}{F}B = 0 \\ -2\frac{F'}{F}A + \frac{3}{2}\omega_0 B = 0. \end{cases} \quad (1.29)$$

In order to avoid the simple solution  $A = B = 0$  which does not model the amplitude growth, the determinant of the above system must be zero. Cancelling the determinant imposes:

$$F(T) \propto e^{\pm\frac{3}{4}\omega_0 T}. \quad (1.30)$$

Under these conditions, it is straightforward that for the exponentially growing branch  $A = B$ . The total solution at lowest order, in terms of time  $t$  and only considering the growing solution for a pendulum released at  $t = 0$  from angle  $\theta_0$  with no initial velocity, is therefore:

$$\theta(t) = \theta_0 \cos(\omega_0 t) \exp\left(\frac{3}{4}\eta\omega_0 t\right). \quad (1.31)$$

Such a resonance process is called “parametric sub-harmonic resonance” as it happens when the excitation frequency is twice the free oscillation frequency. From a tiny perturbation, provided it is repetitive and has the adequate frequency, it leads to a drastic increase of the oscillations’ amplitude. This solution is represented in figure 1.6 left and superimposed to the fully nonlinear solution obtained via numerical resolution of equation (1.22) in figure 1.6 right. The two solutions are in very good agreement at early time, but our linear approach does not capture the collapse of the amplitude observed in the numerical solution. As we show in the following paragraph, this is due to non-linear effects which are not accounted for in our theoretical approach.

## 2.4 Saturation of the resonance

As noted in figure 1.6 right, the exponential growth computed in the preceding paragraph must come to an end. Here, the non-linearity—the  $\sin \theta$  term in (1.21)—causes a collapse of the oscillations. Indeed, the period of free pendulum oscillations then depends on the amplitude: it increases as the amplitude increases. At second order in  $\theta$ , the relation between period  $P$  and amplitude  $\theta_m$  is given by Borda’s formula:

$$P(\theta_m) = \frac{2\pi}{\omega_0} \left(1 + \frac{\theta_m^2}{16}\right). \quad (1.32)$$

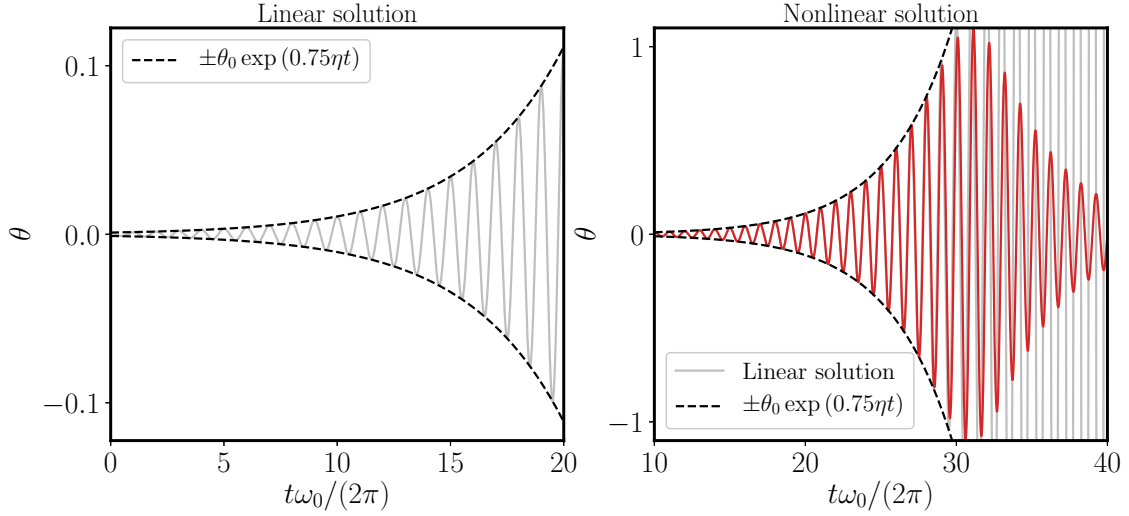


**Figure 1.6:** **Left:** linear solution corresponding to the expression (1.31) for  $\eta = 5 \times 10^{-2}$ ,  $\omega_0 = 1$ ,  $\omega = 2$  and  $\theta_0 = 1 \times 10^{-3}$ . **Right:** fully non-linear solution of equation (1.22) (in red) and comparison with the linear solution (in grey).

At early times, when the amplitude of the oscillations remains small, the excitation frequency  $\omega$  matches the resonance condition  $\omega = 2\omega_0$ . As the amplitude increases, the frequency of the pendulum decreases and the oscillator is detuned from the excitation. This reverses the energy transfer from the parametric excitation to the pendulum. As the excitation and oscillation are out of phase, energy is pumped back from the pendulum to the forcing—the negative viscosity effect becomes a positive viscosity. The consequence is the global decrease of the amplitude. Note lastly that in the case of *O Botafumeiro*, the holders can tune the excitation to the actual period of the thurible, hence maintaining large amplitude oscillations over a long time.

## 3. Parametric excitation of inertial oscillations by mechanical forcing

### 3.1 Oscillators in planetary cores: inertial waves

In the following, we draw an analogy between the length-varying pendulum and tidally-driven mechanical forcings in planetary cores. We identify what can be regarded as a pendulum inside planetary cores and what acts as a slight and repetitive perturbation.

The eigenmodes of rotating fluids are the so-called inertial waves. They are caused by the restoring action of the Coriolis force. This section is a short reminder of how to derive their governing equation and to infer their dispersion relation.

Let us derive a wave equation from the governing equations of incompressible rotating fluids. We consider the linear limit of the Euler equation for the velocity  $\mathbf{u}$  in the rotating frame of reference:

$$\partial_t \mathbf{u} + 2\boldsymbol{\Omega} \times \mathbf{u} = -\nabla p. \quad (1.33)$$

The equation governing the vorticity  $\boldsymbol{\omega} = \nabla \times \mathbf{u}$  reads:

$$\partial_t \boldsymbol{\omega} = 2(\boldsymbol{\Omega} \cdot \nabla) \mathbf{u} . \quad (1.34)$$

We assume  $\boldsymbol{\Omega} = \Omega \mathbf{e}_z$  and take the curl the vorticity equation (1.34) to obtain an equation on the velocity only:

$$\partial_t (\nabla \times (\nabla \times \mathbf{u})) = 2\Omega \partial_z \boldsymbol{\omega} . \quad (1.35)$$

We differentiate this last equation over time and then substitute (1.34) into (1.35) which gives:

$$\partial_{tt} (\nabla \times (\nabla \times \mathbf{u})) = 4\Omega^2 \partial_{zz} \mathbf{u} . \quad (1.36)$$

Taking into account the incompressibility condition  $\nabla \cdot \mathbf{u} = 0$ , we finally retrieve the Poincaré equation of rotating flows (Poincaré, 1885):

$$\partial_{tt} \nabla^2 \mathbf{u} + 4\Omega^2 \partial_{zz} \mathbf{u} = 0 . \quad (1.37)$$

Considering the divergence of the Navier-Stokes equation, one can easily find a similar equation on the pressure field  $p$ .

In an hypothetical infinite medium which satisfies translational invariance, the Poincaré equation admits plane waves solutions. Assuming that  $\mathbf{u}$  takes the form of a plane wave of vector  $\mathbf{k}$  and frequency  $\omega$  :

$$\mathbf{u}(\mathbf{r}, t) = \mathbf{u}_0 e^{i(\mathbf{k} \cdot \mathbf{r} - \omega t)}, \quad (1.38)$$

$\mathbf{r}$  being the position, the dispersion relation of inertial waves writes:

$$\omega^2 = 4\Omega^2 \frac{k_z^2}{k^2} \quad \text{i.e.} \quad \omega = \pm 2\Omega \cos \theta \quad (1.39)$$

where  $\theta$  is the angle between the rotation axis and the wave vector. Note that this dispersion relation is peculiar in the sense that wave frequency is not related to the wavelength but to the direction of the wavevector only. Moreover, the frequency of the waves is bounded between  $-2\Omega$  and  $2\Omega$ .

In the case of bounded geometry such as spheres or ellipsoids, the translational invariance is lost, but oscillatory solutions to the Poincaré equation can still be found. They are called inertial modes and their derivation for the special case of the sphere can be found in Greenspan (1968). Their frequencies remain bounded between  $-2\Omega$  and  $2\Omega$  (Greenspan, 1968). An example of inertial modes computed in an ellipsoidal container is given in figure 1.7. In the case of periodic mechanical forcing of planets, these inertial modes play the role of the excited oscillators.

### 3.2 Parametric excitation: the case of tidally-driven instabilities

In section 1.3, we derived the primary response of a fluid planetary interior to tidal distortion — see for instance the expressions (1.10) and (1.11); nothing has been said yet regarding the stability over time of this flow. This section shows that a tidal flow can excite a parametric resonance of inertial waves. We give the conditions under which a resonance can happen, and we later briefly present a few ideas on how to quantify its grow rate.

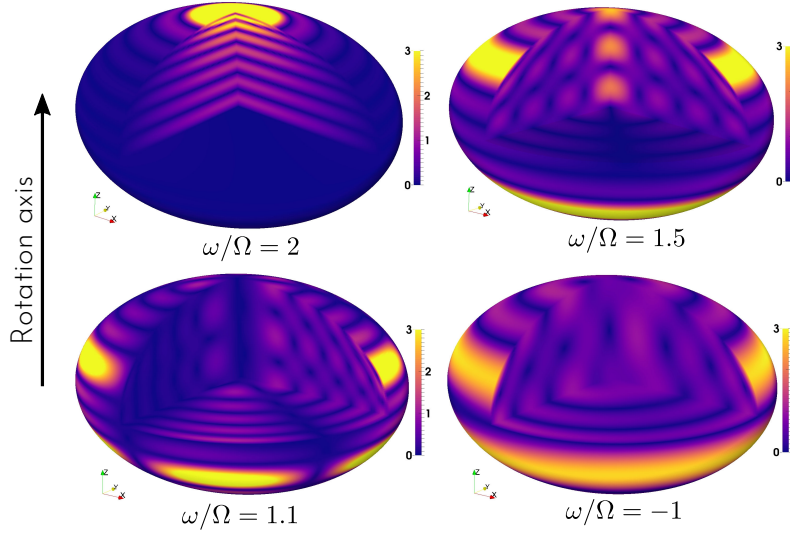


**Figure 1.7:** Four example of the velocity amplitude of inviscid inertial modes computed in an ellipsoid with axes  $a = 1$ ,  $b = 0.86$  and  $c = 0.57$  performed by Vidal and Cébron (2017). It shows equatorial and meridional cuts and the amplitude map at the surface of the ellipsoid. This figure is adapted from Vidal and Cébron (2017) figure 6.

We investigate the time evolution of perturbations to the tidal base flow, an instability being characterised by an exponential growth of these perturbations. In the frame rotating with the planet —see paragraph 1.3—, we write the total flow as :

$$\mathbf{U} = \mathbf{U}^\Omega + \mathbf{u} \quad (1.40)$$

where  $\mathbf{U}^\Omega$  is the tidal base flow (1.11) and  $\mathbf{u}$  is a perturbation —which is not necessarily small. As  $\mathbf{U}^\Omega$  is a non-linear, viscous solution to the flow in the bulk of the fluid, the Navier-Stokes equations (1.2) reduce to the following non-dimensional form:

$$\partial_t \mathbf{u} + \mathbf{U}^\Omega \cdot \nabla \mathbf{u} + \mathbf{u} \cdot \nabla \mathbf{U}^\Omega + \mathbf{u} \cdot \nabla \mathbf{u} + 2\mathbf{e}_z \times \mathbf{u} = -\nabla p + E \nabla^2 \mathbf{u} \quad (1.41)$$

$$\nabla \cdot \mathbf{u} = 0 \quad (1.42)$$

where lengths are scaled by the largest axis length  $a$ , time by  $1/\Omega$ , and where we have introduced the Ekman number  $E = \nu/(a^2\Omega)$  that compares the effects of viscous and Coriolis forces.

According to (1.11), the tidal base flow is proportional to the ellipticity of the tidal deformation  $\beta$ , and may therefore be written as

$$\mathbf{U}^\Omega = \beta \mathbf{A}(t) \mathbf{x}, \quad (1.43)$$

where  $\mathbf{A}(t)$  is a linear operator, harmonic in time with frequency  $2\gamma$ , acting on the position  $\mathbf{x}$ , representing the rotating strain field depicted in figure 1.3. We recall that  $\gamma$  is the difference between the planet's rotation rate and the moon's orbital rate, or equivalently the rotation rate of the tidal bulge in the rotating frame. In the linear, inviscid limit, the equation (1.41) can be recast as

$$\partial_t \mathbf{u} + 2\mathbf{e}_z \times \mathbf{u} + \nabla p = -\beta [\mathbf{A}(t) \mathbf{u} + \mathbf{A}(t) \mathbf{x} \cdot \nabla \mathbf{u}]. \quad (1.44)$$

This equation is very similar to the equation (1.23) governing the length-varying pendulum: eigenmodes of the system (*i.e.* inertial waves here), represented by the left hand side, are excited by a forcing which is harmonic in time, and depends on the amplitude of the eigenmodes.

From a qualitative point of view, the periodic stretching of waves by the tidal strain is able to convey energy from tides to waves.

The situation compared to the length-varying pendulum is here slightly enriched by the existence of an infinite number of oscillators: many pairs of inertial modes can cooperate and resonate with the tidal base flow. Let us consider a mode of frequency  $\omega_1$ : its non-linear interaction with the base flow corresponding to the RHS of (1.44) bears harmonic terms of frequencies  $\pm 2\gamma + \omega_1$  that can match a second mode oscillation, hence reinforcing it, provided its frequency  $\omega_2$  matches the following resonance condition:

$$|\omega_1 - \omega_2| = 2\gamma . \quad (1.45)$$

Reciprocally, mode 2 then reinforces mode 1. There is therefore a coherent effect of the tidal base flow and the two resonant waves in building the parametric resonance. Note that this resonance condition includes the single mode resonance for  $\omega_1 = -\omega_2 = \pm\gamma$ , which is reminiscent of the length-varying pendulum sub-harmonic resonance. Due to the nature of the base flow, this instability has been coined “elliptical instability”. Note also that the resonance condition and the bounded domain of the inertial frequencies implies that the tidally-driven resonance can be excited as long as  $|\gamma| \leq 2|\Omega|$ .

An illustration of the instability growth is given in figure 1.8. In both the experiment and the numerical simulation, the orbital and the spin rate are opposed, that is,  $\Omega = -n$ , such that  $\gamma = 2\Omega$ . The resonant modes are therefore at the limit of the inertial modes frequency domain. These modes are composed of horizontal layers of alternating horizontal velocity. They are reminiscent of plane waves in an unbounded domain as, at the frequency  $2\Omega$ , the wave vector is purely vertical. Lastly, it is interesting to note that even if the ellipticity is quite small in the experiment shown in figure 1.8 — $\beta = 0.06$ —, the flow is fully turbulent at later times, once the instability has reached saturation.

### 3.3 Quantifying the growth rate: a global approach

In this section, we detail a method to theoretically determine the growth rate of the parametric instability excited by the tidal base flow. We look for the long term evolution of the amplitude of the resonant modes, following the general process given in Tilgner (2007a). The perturbation flow  $\mathbf{u}$  can be written as a superposition of two eigenmodes with spatial structures  $\Psi_1(\mathbf{r})$  and  $\Psi_2(\mathbf{r})$ , that is:

$$\mathbf{u}(\mathbf{r}, t) = a_1(t)e^{i\omega_1 t}\Psi_1(\mathbf{r}) + a_2(t)e^{i\omega_2 t}\Psi_2(\mathbf{r}) , \quad (1.46)$$

where the  $a_j(t)$  are the amplitudes of the modes and the  $\omega_j$  their eigen frequencies. Noting  $\Pi_j$  the pressure field associated to the mode  $j$ ,  $\Psi_j$  and  $\Pi_j$  satisfy the following equation:

$$2\mathbf{e}_z \times \Psi_j + \nabla \Pi_j = i\omega_j \Psi_j , \quad (1.47)$$

that is,  $\Psi_j, \Pi_j$  are eigenmodes of the linearised, rotating Euler equation. Note that, in general, two modes satisfy an orthogonality relation (Greenspan, 1968):

$$\langle \Psi_j | \Psi_k \rangle \equiv \frac{1}{\mathcal{V}} \int_{\mathcal{V}} \Psi_j^* \cdot \Psi_k dV = \delta_{jk} , \quad (1.48)$$

where  $\mathcal{V}$  is the domain volume and  $\delta_{ij}$  is the Kronecker symbol.

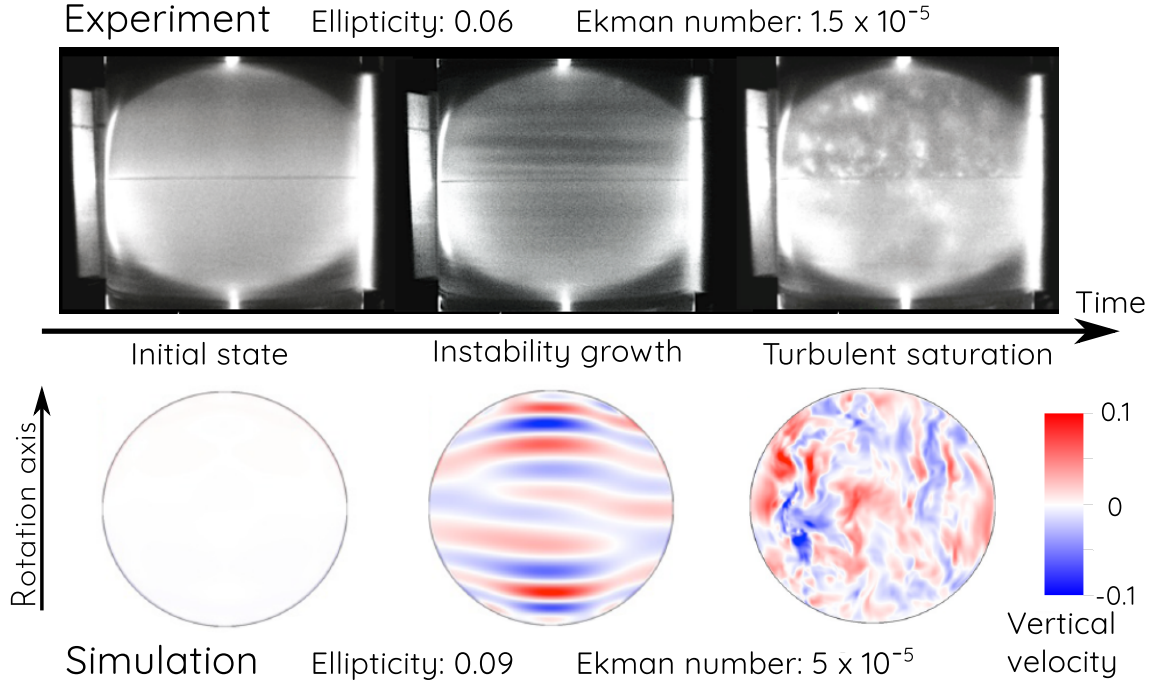


**Figure 1.8:** Time evolution of the tidally-driven flow inside an ellipsoid shown in a meridional cross-section. **Top:** experimental visualisation using flake-shaped particles materialising shear zones. **Bottom:** numerical simulation showing the vertical velocity. These pictures are adapted from Grannan et al. (2017), Figure 3.

Tidal distortion is always a small perturbation of the spherical shape of the container. The modes inside the slightly distorted container are therefore approximated here by the inertial modes of the sphere for simplicity (but see Vidal and Cébron (2017) for a more complete approach). Then we introduce an azimuthal wavenumber  $m$  such that the spatial structure of an inertial mode  $\Psi$  can be written as

$$\Psi(\mathbf{r}) = \Phi(r, z)e^{im\phi}$$

where  $(r, z, \phi)$  are the cylindrical coordinates (Greenspan, 1968). Two structures with different  $m$  are orthogonal, and the dot product between two modes can be specified as follows:

$$\langle \Psi_j | \Psi_k \rangle = \delta(m_k - m_j) \frac{2\pi}{\mathcal{V}} \int_{r,z} \Phi_j^* \cdot \Phi_k r dr dz = \delta(m_k - m_j) (\Phi_j | \Phi_k) . \quad (1.49)$$

where we have introduced a reduced dot product  $(\cdot | \cdot)$  that acts on the radial and vertical structure of the modes.

We introduce  $L(t)$  the linear operator associated to the RHS of equation (1.44), *i.e.* the linear operator which couples the modes with the tidal base flow. In general, for a field  $\mathbf{w}$ ,

$$L(t)\mathbf{w} = A(t)\mathbf{w} + A(t)\mathbf{x} \cdot \nabla \mathbf{w} . \quad (1.50)$$

With the orthogonality relation (1.48), the evolution of the amplitudes  $a_j$  are inferred from the ansatz (1.46) and the flow equation (1.44):

$$\begin{cases} \dot{a}_1 &= \beta \langle \Psi_1 | L(t)\mathbf{u} \rangle e^{-i\omega_1 t} \\ \dot{a}_2 &= \beta \langle \Psi_2 | L(t)\mathbf{u} \rangle e^{-i\omega_2 t} . \end{cases} \quad (1.51)$$

The RHS of (1.51) can be specified taking into account the temporal and spatial variations of the modes contained in  $\mathbf{u}$  and in the coupling operator  $L(t)$ . The tidal base flow is transformed into cylindrical coordinate as:

$$\mathbf{U}^\Omega = -\beta\gamma r [\sin(2\gamma t + 2\phi)\mathbf{e}_r + \cos(2\gamma t + 2\phi)\mathbf{e}_\phi] \quad (1.52)$$

showing that it contains the wave numbers  $m = 2$  and  $m = -2$ .  $L$  is therefore decomposed into:

$$L(t) = e^{i(2\gamma t + 2\phi)}L_0 + e^{-i(2\gamma t + 2\phi)}L_0^* \quad (1.53)$$

where  $L_0$  is independent of time and  $\phi$  and  $L_0^*$  is the complex conjugate of  $L_0$ . Using the orthogonality relation, the RHS of (1.51) is expanded as follows:

$$\begin{aligned} \langle \Psi_1 | L(t) \mathbf{u} \rangle e^{-i\omega_1 t} &= (\Phi_1 | L_0 \Phi_1) a_1 \delta(2 + m_1 - m_1) e^{i(\omega_1 + 2\gamma - \omega_1)t} \\ &+ (\Phi_1 | L_0^* \Phi_1) a_1 \delta(-2 + m_1 - m_1) e^{i(\omega_1 - 2\gamma - \omega_1)t} \\ &+ (\Phi_1 | L_0 \Phi_2) a_2 \delta(2 + m_2 - m_1) e^{i(\omega_2 + 2\gamma - \omega_1)t} \\ &+ (\Phi_1 | L_0^* \Phi_2) a_2 \delta(-2 + m_2 - m_1) e^{i(\omega_2 - 2\gamma - \omega_1)t} . \end{aligned} \quad (1.54)$$

and similarly for  $\langle \Psi_2 | L(t) \mathbf{u} \rangle e^{-i\omega_2 t}$ . When the resonance condition is satisfied, *i.e.*  $\omega_2 - \omega_1 = 2\gamma$ , the coupling between the modes 1 and 2 is effective provided the following selection rule applies:

$$m_2 - m_1 = 2 . \quad (1.55)$$

All the other coupling terms, whose frequency does not match the resonance condition, then vanish. A similar derivation for  $\langle \Psi_2 | L(t) \mathbf{u} \rangle e^{-i\omega_2 t}$  allows to prove that the system (1.51) reduces to:

$$\begin{cases} \dot{a}_1 &= \beta (\Phi_1 | L_0^* \Phi_2) a_2 \\ \dot{a}_2 &= \beta (\Phi_2 | L_0 \Phi_1) a_1 . \end{cases} \quad (1.56)$$

The growth rate  $\sigma$  is therefore given by the overlap between the tidal base flow and the two modes:

$$\sigma^2 = \beta^2 (\Phi_1 | L_0^* \Phi_2) (\Phi_2 | L_0 \Phi_1) . \quad (1.57)$$

The amplitude of the modes grows provided the overlap integrals have the same sign; the growth rate is then proportional to  $\beta$ . This is similar to the length-varying pendulum for which the growth rate was found to be proportional to the amplitude of the perturbation  $\eta$ .

Computing the growth rate is in this case rather difficult as it requires computing the overlap integrals between the modes and the tidal forcing. This is in general non-trivial: although the inertial modes in a sphere, or even a spheroid, are known, there is no analytical formula in the generic case of tri-axial ellipsoids. Computation of the overlap integrals therefore requires numerical solving of the eigenvalue problem of inertial modes, as done for instance in Vidal and Cébron (2017).

Lastly, the amplitude equations (1.56) may be refined accounting for the viscous damping of the modes. In the planetary limit of small Ekman number  $E$ , viscous dissipation is dominated by friction inside Ekman boundary layers, and yields a correction  $\mathcal{O}(\sqrt{E})$ ; as shown by Le Bars et al. (2010), the correction to the growth rate is then  $K\sqrt{E}$  with  $K$  a constant typically between 1 and 10 but see also Lemasquerier et al. (2017) for a discussion on the possible importance of bulk dissipation for finite Ekman numbers.

### 3.4 Quantifying the growth rate: short wavelength approximation

Although the derivation of the growth rate in the preceding paragraph is rather straightforward, it is quite difficult to extract quantitative information in complex geometries such as tri-axial ellipsoids. This approach requires knowing *a priori* the spatial structure of the inertial modes that must be computed numerically. Another approach that has proven efficient in past studies to make quantitative prediction (see e.g. Kerswell (2002) and references therein) consists in assuming a scale separation between short wavelength resonant modes and the large-scale tidal flow.

This approach, known as the Wentzel-Kramers-Brillouin (WKB) analysis, assumes that the perturbations take the form of a plane wave packet around a point that is advected by the base flow. The wave packet is affected by tidal distortion as it moves along with the Lagrangian point. This theoretical framework, which resembles the process to infer classical optics from light wave propagation, was formally introduced in the context of hydrodynamic instabilities by Lifschitz and Hameiri (1991). It is particularly suitable for the study of parametric instability of waves interacting with a base flow.

It was applied to the present case of the tidally driven elliptical instability in rotating flows by Le Dizès (2000). The WKB method allows to retrieve that the short wavelength growing perturbation corresponds to the superposition of two contrapropagating inertial waves of frequency  $\pm\gamma$  with an amplitude growth rate

$$\sigma = \frac{\beta\gamma}{16} (2 + \gamma)^2 . \quad (1.58)$$

Although this growth rate describes short wavelength perturbations under the form of inviscid plane waves in an infinite domain, it accounts very well for the growth of inertial modes in enclosed containers in the weak tidal distortion and low dissipation regime, *i.e.* the regime that is relevant for geophysics (Le Bars et al., 2010). A small correction due to boundary friction must then be considered, that is:

$$\sigma_v = \sigma - K\sqrt{E} \quad (1.59)$$

with  $K$  between 1 and 10 typically, as explained in the preceding section.

### 3.5 The elliptical instability in planetary cores

The preceding theoretical results have been used in past studies to evaluate the actual relevance of the tidally driven elliptical instability in natural systems, for instance by Cébron et al. (2012a). In the case of the Earth, the tidal distortion of the Moon (which induces a tidal bulge of ellipticity  $\beta \sim 10^{-7}$ ) is close but *a priori* not sufficient to overcome the viscous damping of resonant modes. Nevertheless, the study by Cébron et al. (2012a) also considered the early history of the Earth at times where the Moon was closer to its parent planet. Assuming the Earth-Moon distance is reduced by a factor 2, the core of the Earth becomes unstable to the elliptical instability. Mechanical forcings therefore provide an interesting alternative to drive magnetic field before the crystallisation of the inner core. Remember that the Earth is known to be surrounded by a magnetic field since at least 3.5 Gy (Tarduno et al., 2010) while the Earth's core only started to form around 1 Gy ago (Labrosse, 2015).

Following the same process as for the tidally-driven instability, librations have also been shown to drive parametric sub-harmonic instability of inertial waves with an inviscid growth rate proportional to  $\beta\varepsilon$ ,  $\varepsilon$  being the relative variation of the rotation rate (Kerswell and Malkus, 1998; Cébron et al., 2012b; Cébron et al., 2014). Kerswell and Malkus (1998) have in particular demonstrated that Io's core is unstable, thus providing a possible explanation to the magnetic field measured by the Galileo probe around the Jovian satellite (Kivelson et al., 1996b). Cébron et al. (2012a) have extended the preceding study to show that Europa's core may also be unstable. Note that Ganymede's core remains below the threshold of instability despite being surrounded by a magnetic field.



# Chapter 2

## Introduction to the non-linear saturation of the elliptical instability

The path from an initial tidal excitation to a fully turbulent flow is presented in figure 2.1. In the preceding chapter, we have focused on the first stage of the instability, *i.e.* the resonance mechanism where the differential rotation or the libration drives exponential growth of two inertial waves. We now develop the fundamental processes expected to take place in the non-linear saturation of the elliptical instability, building on previous studies devoted to rotating turbulence, and which are presented in the bottom panel of figure 2.1. After introducing simple scalings governing the saturation flow amplitude, we introduce the triadic resonant interaction which transfers energy from an inertial wave to two daughter inertial waves. A specific focus is made on geostrophic flows which are invariant and slowly evolving structures in rotating fluids, and correspond to the non-propagative limit of inertial waves. Geostrophic flows are ubiquitously observed in rotating turbulence; they are also observed in experiments and numerical simulations of the elliptical instability, although there is no resonant—and thus efficient—energy transfer from inertial waves to geostrophic flows, a theoretical result which is recalled in the following. Lastly, in the light of the introduced non-linear processes, we review the previous works that have been carried out on the non-linear saturation of the elliptical instability and detail the main goals of the work presented in this dissertation.

### 1. Simple scalings for the saturation flow

This short section is a simple scaling analysis of the Navier-Stokes equations in order to make simple predictions regarding the non-linear saturation of the elliptical instability. Consider the dimensionless equations (1.41) governing the perturbation  $\mathbf{u}$  to a tidal or libration

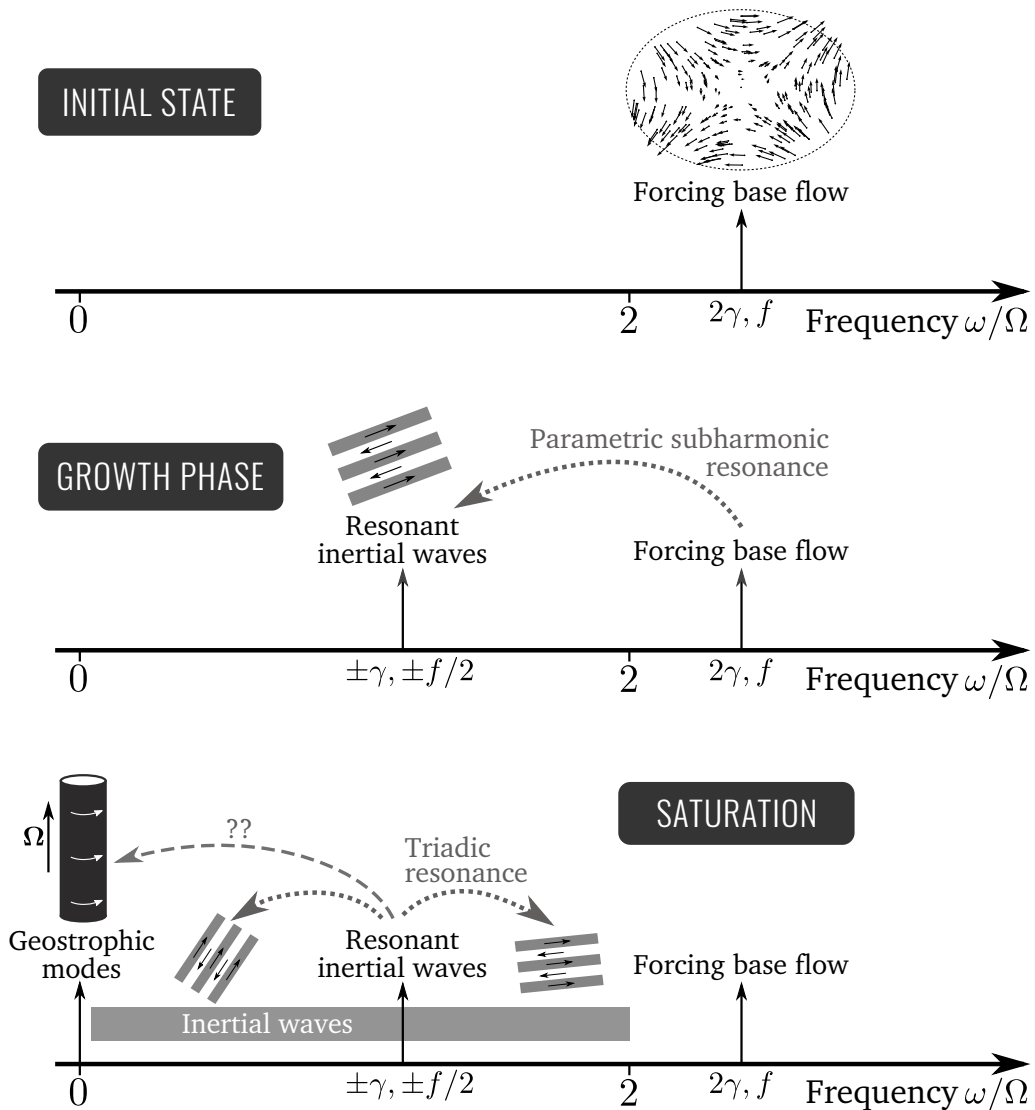


**Figure 2.1:** Schematic cartoon of the expected time evolution of the elliptical instability from the initial base flow driven by either differential rotation of the tidal bulge at frequency  $2\gamma$  or libration at frequency  $f$ . Energy is transferred first to resonant inertial waves through the mechanism detailed in chapter 1 section 3.2. In the non-linear saturation of the instability, a host of new structures are excited which include inertial waves excited by triadic resonant interaction and geostrophic flows. Although the latter are ubiquitous in rotating flows, the path from the resonant inertial waves to them is not fully elucidated.

base flow  $\mathbf{U}_b$  :

$$\begin{cases} \partial_t \mathbf{u} + \mathbf{U}_b \cdot \nabla \mathbf{u} + \mathbf{u} \cdot \nabla \mathbf{U}_b + \mathbf{u} \cdot \nabla \mathbf{u} + 2\mathbf{e}_z \times \mathbf{u} = -\nabla p + E \nabla^2 \mathbf{u} \\ \nabla \cdot \mathbf{u} = 0 \end{cases} \quad (2.1)$$

where time has been normalised by  $\Omega$  and length by  $a$ . We can first compare the effects of the base flow respective to the Coriolis force. The base flow is large scale, and its importance in the dynamics is simply measured by what we call an input Rossby number  $Ro_i$ , which is  $Ro_i = \beta\gamma$  in the case of differential rotation forcing ( $\gamma$  being the dimensionless differential rotation rate, normalised by the rotation rate  $\Omega$ ), and  $Ro_i = \beta\varepsilon$  in the case of libration.  $Ro_i$  quantifies the forcing amplitude and is a small control parameter in geophysical regimes.

It is then possible to estimate the saturation amplitude of the perturbation flow  $\mathbf{u}$  in equation (2.1). Consider that at saturation non-linear transfers balance the forcing terms. The typical length scale of the forcing base flow  $\mathbf{U}_b$  is the size of the planetary core ( $= 1$  in the dimensionless framework), whereas the resonant waves have a typical length scale  $\ell_f$ . The linear forcing terms are  $\mathbf{u} \cdot \nabla \mathbf{U}_b$  and  $\mathbf{U}_b \cdot \nabla \mathbf{u}$  are both proportional to the perturbation flow. Calling  $u^*$  a typical perturbation velocity scale, the dimensionless forcing terms scale like:

$$|\mathbf{u} \cdot \nabla \mathbf{U}_b| \sim u^* Ro_i \quad \text{and} \quad |\mathbf{U}_b \cdot \nabla \mathbf{u}| \sim \frac{u^*}{\ell_f} Ro_i. \quad (2.2)$$

The non-linear self-interaction  $\mathbf{u}$  scales likes:

$$|\mathbf{u} \cdot \nabla \mathbf{u}| = \frac{u^{*2}}{\ell_f}. \quad (2.3)$$

We therefore obtain either that  $u^* \sim Ro_i$  or  $u^* \sim \ell_f Ro_i$ , and Grannan et al. (2017) confirmed at least that  $|\mathbf{u}| \propto Ro_i$ . As a conclusion, the input Rossby number  $Ro_i$  roughly quantifies the expected amplitude of the saturation perturbation flow, and is therefore a quantification of the Rossby number comparing the importance of the Coriolis force to non-linear transfers.

## 2. Non-linear wave interactions

In this section, we introduce triadic resonances which are fundamental non-linear interactions between inertial waves. They are expected to play an important role in any non-linear transfer involving an inertial wave, and thus in the saturation of the elliptical instability, as summarised in the schematic of figure 2.1. We introduce the formalism of the triadic resonance in the particular context of an unbounded rotating fluid. This simplifying assumption allows explicitly computing the non-linear wave interaction terms, but does not alter the universal physics of three-modes interactions.

### 2.1 The helical modes

Prior to introducing the non-linear interaction between inertial waves, it is first required to determine the spatial structure of the latter. We dwell on the case of unbounded rotating fluids, and we look for plane wave solutions to the linearised rotating Euler equation. A first general solution is deduced from the Poincaré equation (1.37), derived in chapter 1 from

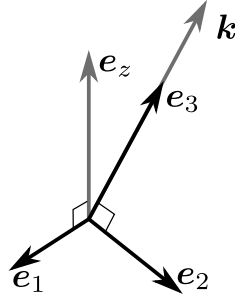


**Figure 2.2:** Schematic representation of the Craya-Herring basis ( $e_1, e_2, e_3$ ). The rotation axis is along  $e_z$ .  $k$  is the wave vector on which the basis is built.

the rotating, linearised Euler equation. This solution is specified using the incompressibility condition and the Euler equation to show that it is in general a linear combination of so-called “helical modes”.

Let us consider an unbounded rotating fluid. The dimensionless, rotating Euler equation on the velocity and pressure field ( $\mathbf{u}, p$ ) writes:

$$\partial_t \mathbf{u} + 2\mathbf{e}_z \times \mathbf{u} + \nabla p = \mathbf{u} \times (\nabla \times \mathbf{u}) \quad (2.4)$$

which can be linearised into the following:

$$\partial_t \mathbf{u} + 2\mathbf{e}_z \times \mathbf{u} + \nabla p = 0. \quad (2.5)$$

In an unbounded fluid, because of the invariance under spatial translation, the solutions to the equation (2.5) are plane waves  $\mathbf{u}_k = \mathbf{u}_0(t) \exp(i\mathbf{k} \cdot \mathbf{r})$  where  $\mathbf{k}$  is a wave vector and  $\mathbf{x}$  is the position vector. As explained in the preceding chapter (section 3.1), the linearised Euler equation (2.5) yields the Poincaré equation (1.37)

$$\partial_{tt} \nabla^2 \mathbf{u} + 4\partial_{zz} \mathbf{u} = 0.$$

The latter allows further specifying the function  $\mathbf{u}_0(t)$ :

$$\mathbf{u}_0(t) = \mathbf{a}_+ e^{-i\omega t} + \mathbf{a}_- e^{i\omega t} \quad \text{with} \quad \omega = 2 \frac{k_z}{|\mathbf{k}|}. \quad (2.6)$$

Because of the incompressibility condition, the vectors  $\mathbf{a}_{+,-}$  must be orthogonal to  $\mathbf{k}$ . To describe the structure of the mode, it is thus convenient to introduce an orthogonal basis ( $\mathbf{e}_1, \mathbf{e}_2, \mathbf{e}_3$ ) in which two vectors are orthogonal to the wave vector  $\mathbf{k}$ . It is built as follows:

- the third vector  $\mathbf{e}_3$  is given by the normalised wave vector itself, i.e.  $\mathbf{e}_3 = \mathbf{k}/k$ ;
- the first vector must be orthogonal to  $\mathbf{e}_3$ , it is also chosen to be orthogonal to the rotation axis  $\mathbf{e}_z$ , that is:  $\mathbf{e}_1 = (\mathbf{e}_3 \times \mathbf{e}_z)/|\mathbf{e}_3 \times \mathbf{e}_z|$ ;
- the second vector must be orthogonal to the two first:  $\mathbf{e}_2 = \mathbf{e}_z \times \mathbf{e}_1$ ;<sup>1</sup>
- in the special case where  $\mathbf{k}$  is parallel to  $\mathbf{e}_z$ ,  $\mathbf{e}_1 = \mathbf{e}_x$  and  $\mathbf{e}_2 = \mathbf{e}_y$ .

<sup>1</sup>The vectors  $\mathbf{e}_2$  and  $\mathbf{e}_3$  are orthogonal, therefore  $|\mathbf{e}_2 \times \mathbf{e}_3| = 1$  and no normalisation is required in the definition of  $\mathbf{e}_2$ .

This  $\mathbf{k}$ -dependent basis is often called the ‘‘Craya-Herring basis’’ (Craya, 1957; Herring, 1974). In the expression (2.6) of the function  $\mathbf{u}_0(t)$ , the two vectors  $\mathbf{a}_{+,-}$  are decomposed as a linear combination of the vectors  $\mathbf{e}_{1,2}$  of the Craya-Herring basis. As a consequence, an inertial plane wave solution  $\mathbf{u}_k$  may be written as follows:

$$\mathbf{u}_k(t) = (a_1^+ \mathbf{e}_1 + a_2^+ \mathbf{e}_2) e^{i(\mathbf{k} \cdot \mathbf{x} - \omega t)} + (a_1^- \mathbf{e}_1 + a_2^- \mathbf{e}_2) e^{i(\mathbf{k} \cdot \mathbf{x} + \omega t)}. \quad (2.7)$$

It fulfils the incompressibility condition by construction of the Craya-Herring basis.

The solution (2.7) may be further simplified by finding relations between the coefficients  $a_1^{+,-}$  and  $a_2^{+,-}$ . These relations are extracted from the linearised Euler equation (2.5). Plugging the plane wave  $\mathbf{u}_k = \mathbf{u}_0(t) \exp(i\mathbf{k} \cdot \mathbf{x})$  into the Euler equation yields

$$\frac{d\mathbf{u}_0}{dt} + 2\mathbf{e}_z \times \mathbf{u}_0 + i\mathbf{k}p_0 = 0 \quad (2.8)$$

where we have introduced  $p_0$  such that  $p_0 \exp(i\mathbf{k} \cdot \mathbf{x})$  is the pressure field corresponding to the velocity  $\mathbf{u}_0 \exp(i\mathbf{k} \cdot \mathbf{x})$ . The pressure is then eliminated from (2.8) by projecting this equation onto the sub-space orthogonal to the wave vector, *i.e.* by applying to both sides of (2.8) the linear operator

$$\mathbb{1} - \mathbf{e}_3 \mathbf{e}_3^T$$

where  $\mathbb{1}$  is the identity matrix and  $\mathbf{e}_3^T$  is the transposed of the vector  $\mathbf{e}_3$ . Using  $\mathbf{u}_0 \cdot \mathbf{e}_3 = 0$ , the result of projecting the linearised Euler equation on the plane orthogonal to  $\mathbf{k}$  equation is:

$$\frac{d\mathbf{u}_0}{dt} + 2(\mathbb{1} - \mathbf{e}_3 \mathbf{e}_3^T)(\mathbf{e}_z \times \mathbf{u}_0) = 0. \quad (2.9)$$

In order to derive relations between the coefficients  $a_1^{+,-}$  and  $a_2^{+,-}$ , the solution (2.7) to the Poincaré equation is plugged into (2.9). After some algebra, it is found that:

$$\begin{cases} 2(\mathbb{1} - \mathbf{e}_3 \mathbf{e}_3^T)(\mathbf{e}_z \times \mathbf{e}_1) = 2(\mathbf{e}_z \cdot \mathbf{e}_3) \mathbf{e}_2 = \omega \mathbf{e}_2 \\ 2(\mathbb{1} - \mathbf{e}_3 \mathbf{e}_3^T)(\mathbf{e}_z \times \mathbf{e}_2) = -2(\mathbf{e}_z \cdot \mathbf{e}_3) \mathbf{e}_1 = -\omega \mathbf{e}_1 \end{cases} \quad (2.10)$$

where we have used that  $\omega = 2k_z/|\mathbf{k}| = 2\mathbf{e}_z \cdot \mathbf{e}_3$ . The linearised, rotating Euler equation thus yields the following simple relations between the coefficients:

$$\begin{cases} a_2^+ = -ia_1^+ \\ a_2^- = ia_1^- \end{cases} \quad (2.11)$$

Finally, the plane wave solution (2.7) to the linearised Euler equation (2.5) simply writes as follows:

$$\mathbf{u}_k(t) = a_1^+ (\mathbf{e}_1 - i\mathbf{e}_2) e^{i(\mathbf{k} \cdot \mathbf{x} - \omega t)} + a_1^- (\mathbf{e}_1 + i\mathbf{e}_2) e^{i(\mathbf{k} \cdot \mathbf{x} + \omega t)}. \quad (2.12)$$

To conclude, in an unbounded rotating fluid, the linearised Euler equation has harmonic plane wave solutions which are the inertial waves introduced in the preceding chapter. From the Euler equation, we have shown that, for a wave vector  $\mathbf{k}$ , any plane wave solution is a linear combination of the two following functions:<sup>2</sup>

$$\mathbf{h}_k^s e^{i(\mathbf{k} \cdot \mathbf{x} - \omega_s t)} \quad \text{with} \quad \mathbf{h}_k^s \equiv \frac{1}{\sqrt{2}} (\mathbf{e}_1 - is\mathbf{e}_2), \quad \omega_s = s \frac{2k_z}{|\mathbf{k}|} \quad \text{and} \quad s = \pm 1. \quad (2.13)$$

<sup>2</sup>Note that the definition here given of  $\mathbf{h}_k^s$  is consistent with the definition of Smith and Waleffe (1999), provided that a factor  $is$  is applied to  $\mathbf{h}_k^s$ .

These two functions are in fact two orthogonal eigenmodes of the linear operator:

$$\mathbf{u} \mapsto 2(\mathbb{1} - \mathbf{e}_3 \mathbf{e}_3^T)(\mathbf{e}_z \times \mathbf{u})$$

which describes the inviscid, rotating dynamics of a plane wave (see equation (2.9)). The associated eigenvalues are the inertial modes frequencies  $\omega_s$ . The plane waves  $\mathbf{h}_k^s \exp(i\mathbf{k} \cdot \mathbf{x})$  are called helical modes, since the vorticity of these plane waves is parallel to  $\mathbf{h}_k^s$ . This can be simply shown by first computing the vorticity associated to a helical mode:

$$\nabla \times (\mathbf{h}_k^s e^{i\mathbf{k} \cdot \mathbf{x}}) = i\mathbf{k} \times \mathbf{h}_k^s e^{i\mathbf{k} \cdot \mathbf{x}} = -sk \mathbf{h}_k^s e^{i\mathbf{k} \cdot \mathbf{x}}. \quad (2.14)$$

The dot product of this expression with  $(\mathbf{h}_k^s e^{i\mathbf{k} \cdot \mathbf{x}})^*$  gives the helicity of the plane wave which is simply  $-sk$ , so that  $s$  is actually related to the sign of the wave helicity. Besides, the pressure mode  $\Pi_k^s$  corresponding to the helical mode  $\mathbf{h}_k^s$  is:

$$\Pi_k^s = -\frac{2}{k^2} s \mathbf{e}_z \cdot \mathbf{h}_k^s. \quad (2.15)$$

Lastly, it is interesting to note that the helical vectors  $\mathbf{h}_k^s$  may be used as alternatives to the vectors  $\mathbf{e}_1$  and  $\mathbf{e}_2$  of the Craya-Herring basis. For a given wave vector  $\mathbf{k}$ , it is indeed straightforward to show that:

$$\mathbf{e}_1 = \frac{\mathbf{h}_k^1 + \mathbf{h}_k^{-1}}{\sqrt{2}} \quad \text{and} \quad \mathbf{e}_2 = i \frac{\mathbf{h}_k^1 - \mathbf{h}_k^{-1}}{\sqrt{2}}. \quad (2.16)$$

Besides, the helical vectors with opposite helicity signs are orthogonal:

$$\mathbf{h}_k^{1*} \cdot \mathbf{h}_k^{-1} = \frac{1}{2} (\mathbf{e}_1 \cdot \mathbf{e}_1 + i^2 \mathbf{e}_2 \cdot \mathbf{e}_2) = 0. \quad (2.17)$$

As a consequence, the basis  $(\mathbf{h}_k^1, \mathbf{h}_k^{-1}, \mathbf{e}_3)$  is an adequate alternative to the Craya-Herring basis to describe incompressible plane waves.

## 2.2 Amplitude equations on the helical modes

In the present section, we aim at describing the dynamics of the rotating—non-linear—Euler equation. The velocity field is decomposed into a superposition of plane waves with time-varying amplitudes  $\mathbf{u}_k = \mathbf{u}_{k0}(t) \exp(i\mathbf{k} \cdot \mathbf{x})$ . Since the flow is incompressible, and according to the concluding remarks of the preceding section, the time-varying amplitude  $\mathbf{u}_{k0}(t)$  may be projected onto the helical vectors basis  $\mathbf{h}_k^s$  with  $s = \pm 1$ . Following Smith and Waleffe (1999), we propose to decompose the—real—flow  $\mathbf{u}$  as follows:

$$\mathbf{u} = \sum_q \sum_{s=\pm 1} b_q^s(t) \mathbf{h}_q^s e^{i(\mathbf{q} \cdot \mathbf{x} - \omega_q^s t)} + \text{c.c.} \quad (2.18)$$

with  $\omega_q^s = s2q_z/|\mathbf{q}|$ . The spatio-temporal evolution of the flow  $\mathbf{u}$  is thus described via the temporal variations of the amplitudes  $b_q^s(t)$ . The equations governing the helical modes amplitudes are derived in the following from the rotating Euler equation. Note that the temporal variations of the amplitudes  $b_q^s(t)$  are left unspecified at this stage, so that the decomposition (2.18) is not restricted to inertial waves with frequencies between  $-2$  and  $2$ .

To derive the helical modes amplitude equations, we first define a functional scalar product  $\langle \mathbf{u}_1 | \mathbf{u}_2 \rangle$  that acts on two complex flows  $\mathbf{u}_1$  and  $\mathbf{u}_2$  according to:

$$\langle \mathbf{u}_1 | \mathbf{u}_2 \rangle \equiv \int_{\mathbb{R}^3} \mathbf{u}_1^* \cdot \mathbf{u}_2 \, dV. \quad (2.19)$$

The helical modes are orthogonal with respect to the preceding scalar product, that is, for any wave vectors  $\mathbf{q}$  and  $\mathbf{p}$ :

$$\langle \mathbf{h}_q^{s_1} e^{i\mathbf{q} \cdot \mathbf{x}} | \mathbf{h}_p^{s_2} e^{i\mathbf{p} \cdot \mathbf{x}} \rangle = \delta(\mathbf{q} - \mathbf{p}) \delta(s_1 - s_2). \quad (2.20)$$

We use this dot product for projecting the equation (2.5) onto the helical modes to obtain the time evolution of their amplitudes.

We base the derivation of the amplitude equations on the curl of the rotating Euler equation:

$$\partial_t \nabla \times \mathbf{u} - 2\partial_z \mathbf{u} = \nabla \times (\mathbf{u} \times (\nabla \times \mathbf{u})). \quad (2.21)$$

Working with the latter equation avoids dealing with the pressure field. Since the pressure is a non-linear function of the velocity field, it cannot be decomposed into the superposition of the modes  $\Pi_k^s$  (defined in equation (2.15)) corresponding to the decomposition (2.18). To transcribe the space and time evolution of the flow in terms of amplitudes equations for the helical modes, we inject the decomposition (2.18) in equation (2.21). We first note that:

$$\partial_t \nabla \times b_q^s \mathbf{h}_q^s e^{i(\mathbf{q} \cdot \mathbf{x} - \omega_q^s t)} - 2\partial_z b_q^s \mathbf{h}_q^s e^{i(\mathbf{q} \cdot \mathbf{x} - \omega_q^s t)} = -sq \mathbf{h}_q^s e^{i(\mathbf{q} \cdot \mathbf{x} - \omega_q^s t)} b_q^s \quad (2.22)$$

where we have used the properties of helical eigenmodes and the eigen frequency definition  $sq\omega_q^s = 2q_z$ . The left hand side of equation (2.21) projected onto a helical spatial structure  $\mathbf{h}_k^s \exp(i\mathbf{k} \cdot \mathbf{x})$  thus writes:

$$\langle \mathbf{h}_k^s e^{i\mathbf{k} \cdot \mathbf{x}} | \partial_t \nabla \times \mathbf{u} - 2\partial_z \mathbf{u} \rangle = -sk b_k^s(t) e^{-i\omega_k^s t}. \quad (2.23)$$

With the helical modes decomposition, the non-linear term is expanded as (see Smith and Waleffe (1999), Smith and Lee (2005) or Bellet et al. (2006)):

$$\begin{aligned} \mathbf{u} \times (\nabla \times \mathbf{u}) &= \sum_{\mathbf{q}, \mathbf{p}} \sum_{s_1, s_2} \left( b_q^{s_1}(t) \mathbf{h}_q^{s_1} e^{i(\mathbf{q} \cdot \mathbf{x} - \omega_q^{s_1} t)} + b_q^{s_1}(t)^* \mathbf{h}_q^{s_1*} e^{-i(\mathbf{q} \cdot \mathbf{x} - \omega_q^{s_1} t)} \right) \\ &\quad \times \left( -s_2 p b_p^{s_2}(t) \mathbf{h}_p^{s_2} e^{i(\mathbf{p} \cdot \mathbf{x} - \omega_p^{s_2} t)} + s_2 p b_p^{s_2}(t)^* \mathbf{h}_p^{s_2*} e^{-i(\mathbf{p} \cdot \mathbf{x} - \omega_p^{s_2} t)} \right) \\ &= \sum_{\mathbf{q}, \mathbf{p}} \sum_{s_1, s_2} \left( -s_2 p b_q^{s_1} b_p^{s_2} (\mathbf{h}_q^{s_1} \times \mathbf{h}_p^{s_2}) e^{i((\mathbf{q}+\mathbf{p}) \cdot \mathbf{x} - (\omega_q^{s_1} + \omega_p^{s_2}) t)} \right. \\ &\quad \left. + s_2 p b_q^{s_1} b_p^{s_2*} (\mathbf{h}_q^{s_1} \times \mathbf{h}_p^{s_2*}) e^{-i((\mathbf{q}-\mathbf{p}) \cdot \mathbf{x} - (\omega_q^{s_1} - \omega_p^{s_2}) t)} \right) + \text{c.c.} \\ &= \frac{1}{2} \sum_{\mathbf{q}, \mathbf{p}} \sum_{s_1, s_2} \left( b_q^{s_1} b_p^{s_2} (s_1 q - s_2 p) (\mathbf{h}_q^{s_1} \times \mathbf{h}_p^{s_2}) e^{i((\mathbf{q}+\mathbf{p}) \cdot \mathbf{x} - (\omega_q^{s_1} + \omega_p^{s_2}) t)} \right. \\ &\quad \left. + b_q^{s_1} b_p^{s_2*} (s_2 p - s_1 q) (\mathbf{h}_q^{s_1} \times \mathbf{h}_p^{s_2*}) e^{-i((\mathbf{q}-\mathbf{p}) \cdot \mathbf{x} - (\omega_q^{s_1} - \omega_p^{s_2}) t)} \right) + \text{c.c.} \quad (2.24) \end{aligned}$$

where in the last line we have used reordering of  $\mathbf{q}$ ,  $\mathbf{p}$  and the corresponding  $s_1$ ,  $s_2$  permutation to symmetrise the expressions. This complicated non-linear term is reduced by the projection

onto one single helical mode, that is:

$$\begin{aligned}
& \langle \mathbf{h}_k^s e^{i\mathbf{k}\cdot\mathbf{x}} | \nabla \times (\mathbf{u} \times (\nabla \times \mathbf{u})) \rangle \\
&= \frac{1}{2} \sum_{\mathbf{q}+\mathbf{p}+\mathbf{k}=0} \sum_{s_1, s_2} b_q^{s_1*} b_p^{s_2*} (s_2 p - s_1 q) \mathbf{h}_k^{s*} \cdot \left[ -i(\mathbf{p} + \mathbf{q}) \times (\mathbf{h}_q^{s_1*} \times \mathbf{h}_p^{s_2*}) \right] e^{i(\omega_q^{s_1} + \omega_p^{s_2})t} \\
&= -\frac{1}{2} \sum_{\mathbf{q}+\mathbf{p}+\mathbf{k}=0} \sum_{s_1, s_2} b_q^{s_1*} b_p^{s_2*} (s_2 p - s_1 q) (\mathbf{h}_q^{s_1*} \times \mathbf{h}_p^{s_2*}) \cdot [i\mathbf{k} \times \mathbf{h}_k^{s*}] e^{i(\omega_q^{s_1} + \omega_p^{s_2})t} \\
&= -\frac{1}{2} \sum_{\mathbf{q}+\mathbf{p}+\mathbf{k}=0} \sum_{s_1, s_2} b_q^{s_1*} b_p^{s_2*} (s_2 p - s_1 q) (\mathbf{h}_q^{s_1*} \times \mathbf{h}_p^{s_2*}) \cdot [-s\mathbf{k}\mathbf{h}_k^{s*}] e^{i(\omega_q^{s_1} + \omega_p^{s_2})t} \quad (2.25)
\end{aligned}$$

where we have used the properties of the mixed product and the helical modes. The Euler equation is equivalent to the following amplitude equations for all wave vectors  $\mathbf{k}$ :

$$\dot{b}_k^s(t) = \frac{1}{2} \sum_{\mathbf{q}+\mathbf{p}+\mathbf{k}=0} \sum_{s_1, s_2} b_q^{s_1*} b_p^{s_2*} (s_2 p - s_1 q) \mathbf{h}_k^{s*} \cdot (\mathbf{h}_q^{s_1*} \times \mathbf{h}_p^{s_2*}) e^{i(\omega_k^s + \omega_q^{s_1} + \omega_p^{s_2})t}. \quad (2.26)$$

This equation may be shortened by defining a transfer coefficient:

$$C_{kqp}^{s_k s_q s_p} \equiv \frac{1}{2} (s_p p - s_q q) \mathbf{h}_k^{s_k*} \cdot (\mathbf{h}_q^{s_q*} \times \mathbf{h}_p^{s_p*}). \quad (2.27)$$

Note that to include viscous effects in the evolution equation, it is only required to introduce in the left hand side of the amplitude equation (2.26) the term  $k^2 E b_k^s$  where  $E$  is the Ekman number.

## 2.3 The mechanism of inertial wave triadic resonance

Building on the helical mode decomposition and the amplitude equations derived above, this section aims at exhibiting the mechanism by which one inertial wave gives rise to new waves with initially infinitesimal amplitudes. Consider three waves with wave vectors  $\mathbf{k}$ ,  $\mathbf{q}$  and  $\mathbf{p}$ , the first one being kept at constant amplitude  $b_0$ . The first necessary condition for interaction is that the waves have matching spatial structures, that is  $\mathbf{k} + \mathbf{p} + \mathbf{q} = \mathbf{0}$ . According to the amplitude equations (2.26), the two waves  $\mathbf{q}$  and  $\mathbf{p}$  with amplitudes  $b_q^{s_q}$  and  $b_p^{s_p}$  have the following time evolution equations:

$$\begin{cases} \dot{b}_q^{s_q} &= C_{qkp}^{s_q s_k s_p} b_0^* b_p^{s_p*} e^{-i(\omega_k^{s_k} + \omega_q^{s_q} + \omega_p^{s_p})t} = C_1 b_0^* b_p^{s_p*} e^{i\Delta\omega t} \\ \dot{b}_p^{s_p} &= C_{pkq}^{s_p s_k s_q} b_0^* b_q^{s_q*} e^{-i(\omega_k^{s_k} + \omega_q^{s_q} + \omega_p^{s_p})t} = C_2 b_0^* b_q^{s_q*} e^{i\Delta\omega t}, \end{cases} \quad (2.28)$$

where we have introduced  $C_{1,2}$ , to shorten the notation of the transfer coefficient, and the eigen frequency mismatch

$$\Delta\omega \equiv \omega_k^s + \omega_q^{s_1} + \omega_p^{s_2}.$$

From the set of equations (2.28), one may derive a single equation on either one of the two amplitudes  $b_q^{s_q}$  or  $b_p^{s_p}$ . Deriving the first equation of (2.28) with respect to time gives the following second order ordinary differential equation:

$$\ddot{b}_q^{s_q} - i\Delta\omega \dot{b}_q^{s_q} - |b_0|^2 C_1 C_2^* b_q^{s_q} = 0. \quad (2.29)$$

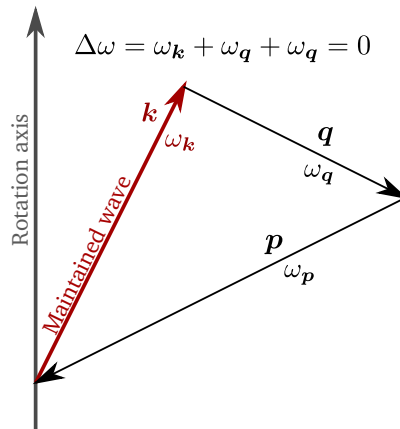


**Figure 2.3:** Schematic cartoon of three waves in exactly resonant triadic interaction, the amplitude of the wave  $k$  being maintained to a constant amplitude. This example of resonant triad is the one reported by Embid and Majda (1998) and Smith and Waleffe (1999), that is,  $k = [4, 0, 8]$  ( $\omega_k \simeq 1.79$ ),  $q = [6, 0, -3]$  ( $\omega_q \simeq -0.89$ ) and  $p = [-10, 0, -5]$  ( $\omega_p \simeq -0.89$ ).

To further our analysis of the three wave interaction, we first notice that the product  $C_1 C_2^*$  is real. This is rather straightforward as:

$$\begin{aligned} C_1 C_2^* &= \frac{1}{4} (s_p p - s_k k) \mathbf{h}_q^{s_q^*} \cdot (\mathbf{h}_k^{s_k^*} \times \mathbf{h}_p^{s_p^*}) \times (s_q q - s_k k) \mathbf{h}_p^{s_p} \cdot (\mathbf{h}_k^{s_k} \times \mathbf{h}_q^{s_q}) \\ &= -\frac{1}{4} (s_p p - s_k k) (s_q q - s_k k) \left| \mathbf{h}_p^{s_p} \cdot (\mathbf{h}_k^{s_k} \times \mathbf{h}_q^{s_q}) \right|^2 \\ &\equiv -\frac{C_0}{4} \end{aligned} \quad (2.30)$$

where we have introduced  $C_0$  a real coupling coefficient. The second order ODE (2.28) has exponential solutions of the form  $\exp(\sigma_T t)$  where  $\sigma_T$  is a complex quantity solution of:

$$\sigma_T^2 - i\Delta\omega \sigma_T - \frac{C_0}{4} |b_0|^2 = 0. \quad (2.31)$$

From this equation, it is straightforward to show that the daughter waves are exponentially growing—*i.e.*  $\text{Re}(\sigma) > 0$ —only when the following condition on the detuning  $\Delta\omega$  and the maintained wave amplitude  $b_0$  is satisfied:

$$\Delta\omega^2 = \left| \omega_k^{s_k} + \omega_q^{s_q} + \omega_p^{s_p} \right|^2 < C_0 |b_0|^2. \quad (2.32)$$

The triadic interaction thus leads to the growth of daughter waves when the coupling coefficient  $C_0$  is positive and the frequency detuning is sufficiently small compared to the dimensionless wave amplitude. When these conditions are met, the quantity  $\sigma_T$  may be decomposed into a real and imaginary part such that  $\sigma_T \equiv \sigma_r + i\sigma_i$  and a straightforward calculation gives (Vanneste, 2005):

$$\sigma_i = \frac{\Delta\omega}{2} \quad \text{and} \quad \sigma_r^2 = \frac{C_0}{4} |b_0|^2 - \frac{\Delta\omega^2}{4}. \quad (2.33)$$

The maximum growth rate of the two daughter waves is reached when the exact resonance condition is satisfied:

$$\omega_k^{s_k} + \omega_q^{s_q} + \omega_p^{s_p} = 0. \quad (2.34)$$

Near-resonances are allowed within a tolerance proportional to the amplitude of the wave or, in other words, to the Rossby number associated to the wave. An example of exactly resonant triad is depicted in figure 2.3.

The maximum frequency mismatch  $\Delta\omega$  tolerance derived here for near-resonance is also in agreement with the discussions of Smith and Lee (2005) regarding the importance of near-resonant triads between waves in rotating turbulence. Significant energy transfer between waves involved in quasi-resonant triads may occur over a non-linear time scale  $\ell_f/u^* \propto Ro_i^{-1}$  (see section 1 of this chapter) provided the mismatch between the eigen frequencies does not produce a significant phase change. In other words, significant energy transfer is ensured under the condition that the term  $\exp(i\Delta\omega t)$  does not significantly vary over the growth phase of the daughter waves. As discussed quantitatively in the close context of gravity wave resonant interaction by Bonnefoy et al. (2016), the decoherence brought by the frequency mismatch causes the non-linear transfer towards daughter waves to vanish over time scales larger than  $1/\Delta\omega$ .

## 2.4 The absence of growth of geostrophic modes under three-modes interaction

Geostrophic flows play a particular role in the dynamics of rotating fluids. They are solutions of the linearised, rotating Euler equation in the stationary limit and are thus associated to a balance between the Coriolis force and pressure, that is:

$$2\mathbf{e}_z \times \mathbf{u} = -\nabla p . \quad (2.35)$$

These modes are invariant along the rotation axis of the fluid, which is easily shown by taking the curl of the preceding equation:

$$2\nabla \times (\mathbf{e}_z \times \mathbf{u}) = 2\partial_z \mathbf{u} = \mathbf{0} . \quad (2.36)$$

Geostrophic flows may also be considered as the non-propagative limit of inertial modes. In unbounded fluids, because of the dispersion relation of inertial waves, their wave vector is perpendicular to the rotation axis ( $k_z = 0$ ) since their frequency is null. These particular structures are ubiquitous in rotating turbulence, but also in the saturation of the elliptical instability.<sup>3</sup> Turbulence excited by stochastic forcings tends to bi-dimensionalise and organise the flow in a set of vortices invariant along the rotation axis (see Godeferd and Moisy (2015) for a review). However, it is well-known that in the weakly non-linear and weakly dissipative limit of rotating fluids, inertial waves are unable to efficiently transfer energy to geostrophic modes with a three-modes resonance. This is a theorem proved by Greenspan (1969) in general, and we recall its proof in the special case of rotating unbounded fluids in the following.

Let us consider, as in the preceding section, a triad of waves  $\mathbf{k}$ ,  $\mathbf{q}$  and  $\mathbf{p}$  such that  $p_z = 0$ . The wave  $\mathbf{k}$  is maintained to a constant amplitude and we seek the growth rate of the two daughter waves. The eigen frequency of the two-dimensional mode is  $\omega_p^{s_p} = 0$ . The interaction condition on the wave vector  $\mathbf{k} + \mathbf{q} + \mathbf{p} = \mathbf{0}$  forces  $q_z = -k_z$ . The exact resonance condition  $\omega_k^{s_k} + \omega_q^{s_q} + \omega_p^{s_p} = \omega_k^{s_k} + \omega_q^{s_q} = 0$  together with the dispersion relation compel the additional relation:

$$\frac{s_k k_z}{k} + \frac{s_q q_z}{q} = k_z \left( \frac{s_k}{k} - \frac{s_q}{q} \right) = 0 . \quad (2.37)$$

<sup>3</sup>A literature review of the role of geostrophic modes is given in section 3.1 and 3.2 of this chapter.

Since  $|s_k| = |s_q| = 1$  and  $q, k > 0$ , it is clear that the exact resonance condition leads to  $q = k$ , and that the sign of the helicity of the waves  $\mathbf{k}$  and  $\mathbf{q}$  is the same. Then, the coupling term (2.27) quantifying the energy transfer from  $\mathbf{k}$  and  $\mathbf{q}$  towards the geostrophic mode  $\mathbf{p}$  is proportional to

$$s_q q - s_k k = 0 .$$

To conclude, there is no triadic resonant interaction giving rise to geostrophic flows. Although this result is derived in the case of inertial modes in an unbounded fluid, it is a more general property of inertial waves and geostrophic modes that has been proved by Greenspan (1969).

### 3. Waves, vortices and the elliptical instability

This section is a review of the main results obtained in previous studies targeted at the non-linear saturation of the elliptical instability. We focus on the particular role of inertial waves and geostrophic vortices in the turbulent saturation of the parametric resonance and we draw connections with the many studies of rotating turbulence. Along with this literature review, we introduce the main goals of the work presented in this dissertation.

#### 3.1 Stationary or cyclic saturation — A historical overview

The first experimental observations of the non-linear saturation of the elliptical instability came with the seminal work of Malkus (1989). He implemented an experimental set-up comprising a rotating cylinder deformed by two fixed rollers imposing an elliptical deformation. This set-up, therefore, produces inside the cylinder the tidal base flow (1.10) in the frame of the laboratory or (1.11) in the frame of the cylinder, with orbital rate  $n = 0$ . The fluid motion inside the cylinder is tracked with flake-shaped particles that tend to materialise the areas with strong shear. Malkus (1989) first reported a violent non-linear break-down (or in his own words an “explosion”) into small-scale turbulence of the growing resonant waves. He observed that it was followed by relaminarisation of the flow before a new growth of the instability mechanism, thus leading to a cyclic behaviour. Malkus and Waleffe (1991) proposed a qualitative explanation of the violent collapse into smaller scale relying on triadic resonances: as each resonant wave grows, it becomes itself unstable to triadic resonance and excites a host of daughter waves. The amplitudes of the latter grow super-exponentially—because the mother wave growth exponentially—which explains the impression of the sudden “explosion” of the flow. In addition, to explain the relaminarisation process, they proposed that the superposition of resonant and daughter waves drives strong turbulence and shear which blurs the background rotation and tidal strain sustaining the waves, thus leading to a decrease in their amplitudes which shortly follows the non-linear collapse of the instability. Kerswell (1999) and Mason and Kerswell (1999) proposed a different mechanism causing the short-lived non-linear breakdown of the elliptical instability followed by relaminarisation based on geostrophic vortices. They proved that inertial waves are unstable to a secondary instability giving rise to exponentially growing geostrophic vortices. Their theory proposes that, as the elliptical instability saturates, strong geostrophic vortices emerge and alter the local rotation rate of the fluid and thus disrupt the primary parametric resonance.

Eloy et al. (2003) furthered the experiments of Malkus (1989) with the use of particle-image velocimetry (PIV), and focused in the cycles of resonance, collapse and relaminarisation.

The PIV measurements performed by Eloy et al. (2003) proved that the fluid inside the cylinder remained close to solid-body rotation even in the sudden non-linear break-down, thus discarding the hypothesis of Malkus and Waleffe (1991) based on strong turbulence and shear. They also found evidence for the emergence of daughter waves right before the non-linear saturation that they associated to triadic interaction involving the resonant waves. In large dissipation regimes, they identified the emergence of geostrophic modes seemingly in agreement with the theory of Mason and Kerswell (1999).

Later on, several studies were dedicated to the tidally driven elliptical instability in rotating, deformable ellipsoids with non-zero orbital rate (Lacaze et al., 2005; Le Bars et al., 2007; Le Bars et al., 2010). It has also been proven numerically (Cébron et al., 2012a) and theoretically (Cébron et al., 2014) that libration also drives inertial wave resonance with the elliptical instability. They all reported “explosive” behaviour as in the study of Malkus (1989).

To explore the details of the turbulent saturation of the elliptical instability, Barker and Lithwick (2013) performed numerical simulations in a local Cartesian model instead of modelling a full ellipsoid or cylinder.<sup>4</sup> They also reported cycles of resonances and collapse, and their idealised model allowed to identify the key role of geostrophic vortices in the saturation. A typical output of their simulations is shown in figure 2.4. The cyclic resonances clearly appear in the kinetic energy time series. Most interestingly, they reveal that the energy of three-dimensional modes decreases quickly as the resonance saturates. In the relaminarisation phase, only persistent geostrophic modes remain, and decay over a viscous time until the resonance takes place again. They proposed an alternative description of the relaminarisation phase to what Mason and Kerswell (1999) and Kerswell (1999) proposed. According to Barker and Lithwick (2013), the instability mechanism is disrupted not because the waves transfer their energy to geostrophic vortices, but because geostrophic vortices affect the frequency of the waves by advection and Doppler shifting. As energy transfer from the base flow is allowed at only one frequency, the interaction between tides and waves is interrupted by geostrophic-driven detuning of the latter’s frequencies.

With the improvement of PIV techniques, experiments of the non-linear saturation of the elliptical instability driven by tides and libration have been carried out in larger ellipsoids. This is the work of Grannan et al. (2014) and Grannan et al. (2017) complemented by the numerical simulations performed by Favier et al. (2015). They all revealed that both libration-driven and tidally driven elliptical instability sometimes also lead to stationary non-linear saturation, as illustrated in figure 2.5. The observation of cyclic or steady saturation depends on the control parameters such as the amplitude of the tidal distortion or of the libration, and the differential rotation rate of the bulge and the planet or the libration frequency.

Several questions remain despite the large number of studies preceding the present work. First, although several explanations have been proposed for the cyclic type of saturation, it is not clear why changing the control parameters such as the amplitude and the frequency of the forcing leads to a sustained turbulent regime. In addition, all the experiments and numerical simulations that have been carried out up to now are realisations of the elliptical instability in regimes that are very far from the conditions encountered in planetary and stellar interiors. In astro- and geophysical regimes, both the forcing amplitude and the dissipation are very small. The Rossby number associated with libration or tidal base flow are all below  $10^{-3}$  while the Ekman number is at most  $10^{-11}$  (Cébron et al., 2012a).

In the present work, we aim at exploring the weak dissipation and forcing regimes, and

---

<sup>4</sup>This idealised model is presented in details in chapter 6.

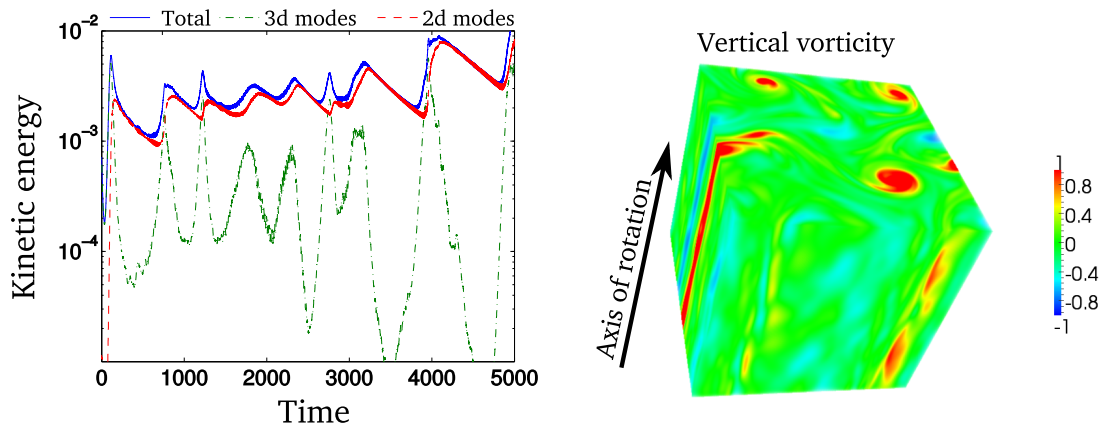


**Figure 2.4:** **Left:** time series of the kinetic energy of the flow driven by tidal elliptical instability simulated by Barker and Lithwick (2013) measured in the rotating frame of reference. The kinetic energy of the tidal base flow is removed, it has a typical dimensionless kinetic energy of  $10^{-2}$ . The flow is decomposed into two- and three-dimensional modes whose kinetic energy is also displayed for comparison. Two dimensional modes are invariant along the rotation axis and correspond to the slowly evolving geostrophic modes. **Right:** snapshot of the vertical vorticity of the perturbation flow simulated by Barker and Lithwick (2013) where two-dimensional modes appear clearly. This figure is adapted from Barker and Lithwick (2013).

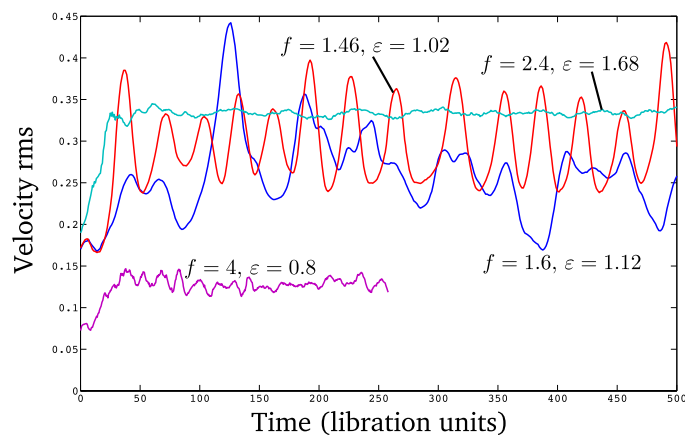


**Figure 2.5:** Time series of the root mean square value of the velocity perturbation to the base flow driven by the libration-driven elliptical instability. These experimental measurements have been performed by Grannan et al. (2014). Each curve corresponds to a different experiment: the libration frequency  $f$  and amplitude  $\varepsilon$  are given in the label of each curve (see section 1.4 and equation (1.12)). This figure is adapted from Grannan et al. (2014).

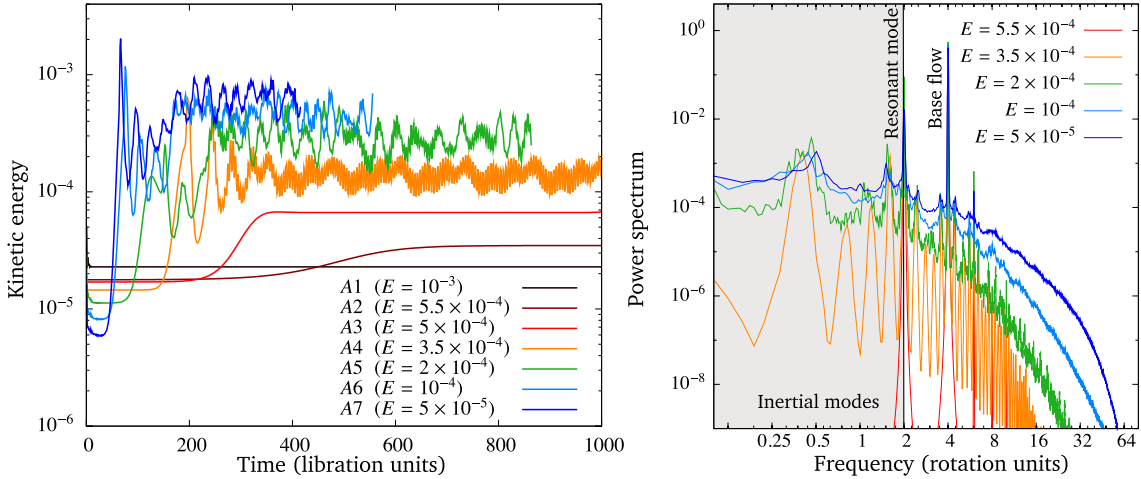


**Figure 2.6:** **Left:** time series of the total kinetic energy of the perturbation around the base flow in numerical simulations of the libration-driven elliptical instability performed by Favier et al. (2015). The libration frequency and amplitude are respectively  $f = 4$  and  $\varepsilon = 0.8$ . The time series are shown for decreasing Ekman number  $E$ . **Right:** corresponding temporal power spectra of the flow in the saturation of the instability. The frequency is given in rotation units so that the forcing libration flow appears at a frequency of 4. The resonant waves are at  $f/2$ . The inertial wave domain is materialised by the shaded area. This figure is adapted from Favier et al. (2015).

clarifying the nature of the non-linear saturation as a function of the control parameters. Gaining insight into the non-linear behaviour of the instability is necessary to fully understand dynamo action and tidal dissipation in planetary cores undergoing mechanical forcing.

### 3.2 Waves and vortices in the non-linear saturation of the elliptical instability

The recent improvement in experimental techniques and computing efficiency has allowed to delve deeper into the fluid structures excited in the saturation of the elliptical instability. This was already highlighted by the numerical work of Barker and Lithwick (2013) mentioned in the previous section which put forward the role of geostrophic modes in the re-laminarisation process. In their respective works, Grannan et al. (2014), Grannan et al. (2017) and Favier et al. (2015) measured the spectral content of the flow in order to characterise the presence of waves and geostrophic vortices in the saturation flow. This is illustrated in figure 2.6 where kinetic energy time series and the corresponding power spectra are shown for a simulation of the libration-driven elliptical instability in a case where the saturation is sustained. These simulations have clarified the evolution of the saturation flow as the Ekman number is decreased. Slightly above the threshold of the instability (the orange curve in figure 2.6-right), the resonant mode at frequency  $\omega = 2$  gives rise to 4 daughter waves via triadic resonant interaction. As the distance to the threshold is increased, the flow becomes more turbulent, and only two large peaks in the inertial modes domain are noticeable. It is unknown whether power spectra such as the blue ones in figure 2.6 are associated with a continuum of inertial modes, or to other structures. As it may also be noticed from figure 2.7, increasing the distance to the threshold of the instability (*i.e.* decreasing the Ekman number in this study) is also associated to the formation of a strong geostrophic anticyclone at the centre of the ellipsoid.

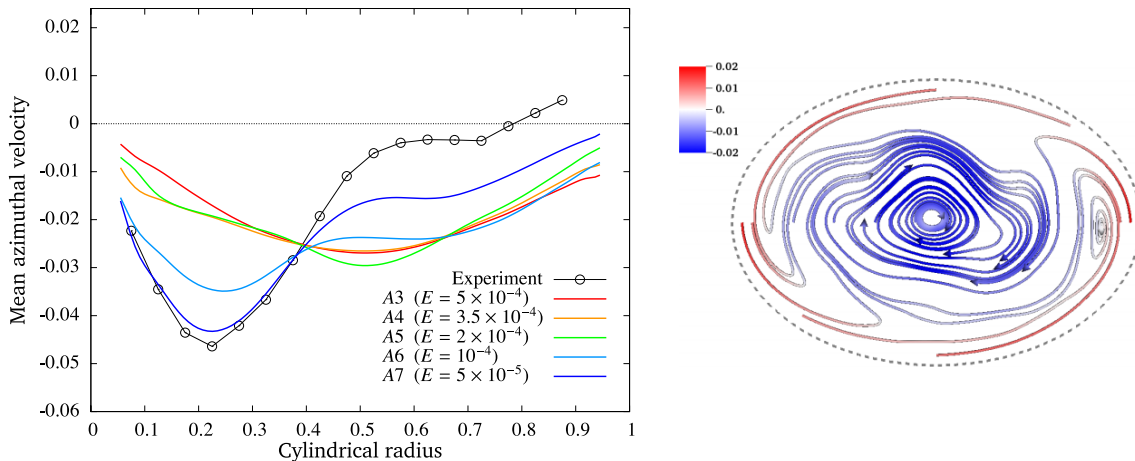


**Figure 2.7:** **Left:** azimuthal component of the mean flow measured in the same conditions as in figure 2.6, as a function of the distance to the rotation axis. It is averaged along this axis and over all azimuthal angles. The experimental curve corresponds to the work of Grannan et al. (2014). **Right:** a typical view of the mean flow in the equatorial plane of the ellipsoid. This figure is adapted from Favier et al. (2015).

Despite the clarification brought by these recent works and illustrated in the present section by the results of Favier et al. (2015), several questions remain. A regime with several inertial waves exists right above the threshold of the elliptical instability, but little is known about how it evolves as the distance to the threshold is increased. One possibility is that an increasing number of inertial modes is excited to form a continuum. However, larger distance to the threshold also leads to stronger geostrophic flows that are known to detune the waves (Barker and Lithwick, 2013) and thus to disrupt triadic resonant interaction. The work presented in this dissertation aims at clarifying the structures excited in the non-linear saturation of the elliptical instability. In particular, we will strive to elucidate the cause of the emergence of geostrophic vortices. It is already known that exact resonant triadic transfer from waves to geostrophic flow is impossible (Greenspan, 1969). Kerswell (1999) and Smith and Walleffe (1999) proposed four modes interactions to transfer energy from waves to geostrophic modes, but it is presently unknown whether such a mechanism is featured in the simulations of Barker and Lithwick (2013) and Favier et al. (2015), or in the experiments of Grannan et al. (2014); Grannan et al. (2017).

### 3.3 Waves and vortices in rotating turbulence

The turbulence excited by the parametric sub-harmonic resonance of inertial waves is expected to be strongly affected by rotation. This is already clear in the numerical results of Barker and Lithwick (2013) who observed the waves to give rise through non-linear processes to several geostrophic vortices. It is also suggested by the results of Favier et al. (2015); Grannan et al. (2014); Grannan et al. (2017) who observe triadic resonant interaction between inertial waves.

The duality between inertial waves and geostrophic vortices is also a defining feature of “classical” rotating turbulence, *i.e.* turbulence excited by random structures in rotating fluids. Although geostrophic vortices are ubiquitously observed in experiments and simulations (Godeferd and Moisy, 2015), inertial waves have also been detected in various set-ups using

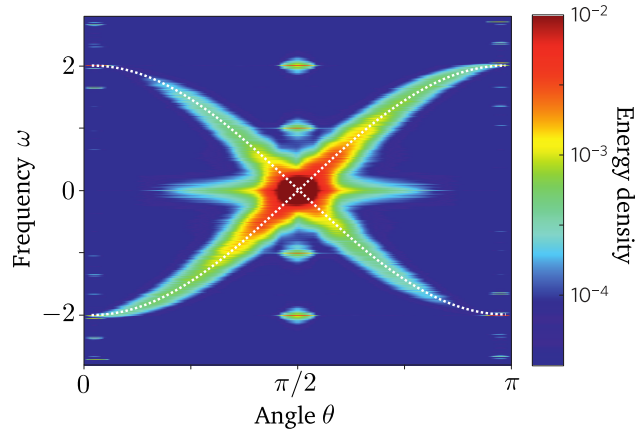


**Figure 2.8:** Left: A typical map of the kinetic energy of an experimental rotating turbulent flow (Yarom and Sharon, 2014) projected onto the dispersion relation spectral subset (see the relation (1.39)). The frequency  $\omega$  is given in rotation units. The dotted lines materialise the dispersion relation of inertial waves  $\omega = \pm 2 \cos \theta$ . The figure is adapted from Yarom and Sharon (2014).

sophisticated spectral techniques (Clark di Leoni et al., 2014; Yarom and Sharon, 2014; Yarom et al., 2017; Oks et al., 2017) or spatio-temporal correlations (Favier et al., 2010; Campagne et al., 2015). Several of these studies even quantify the detuning of the wave frequencies induced by the geostrophic vortices advection.

### The geostrophic issue

The reasons for the systematic emergence of strong geostrophic vortices and bi-dimensionalisation in rotating turbulence are not fully elucidated. Waleffe (1993) has proposed a qualitative argument to explain preferential non-linear transfers towards two-dimensional modes whose wave vector  $\mathbf{k}$  is such that  $k_z \rightarrow 0$ , but it does not explain the final transfer towards modes with  $k_z = 0$ . Smith and Lee (2005) suggested with numerical simulations that near-resonances of inertial waves (presented in section 2.3 of this chapter) involving geostrophic modes could be responsible for this finite transfer, but they did not propose a definitive mechanism. As explained earlier, four-modes interactions have been proposed but their relevance to rotating turbulence has not been tested.

Because the elliptical instability injects energy into waves only, we hope that such a specific forcing will shed light on interactions between waves and vortices in rotating turbulence.

### Inertial wave turbulence

In the asymptotic regime of vanishing Rossby and Ekman numbers, the energy transfers from three-dimensional modes towards geostrophic vortices should vanish, according to Greenspan (1969). Contrary to experimental and numerical realisations of rotating turbulence at moderate Rossby number, which systematically lead to bi-dimensionalisation and the formation of geostrophic vortices, one would therefore expect that the turbulence in the asymptotic regime of weak dissipation and weak forcing amplitude should remain three-dimensional. More precisely, in such a regime, the turbulence could be a superposition of linear inertial waves in weak triadic resonant interaction, a state called wave turbulence (Galtier, 2003; Bel-

let et al., 2006; Nazarenko, 2011).

Wave turbulence occurs in media in which dispersive waves propagate and exchange energy through resonant interactions (Nazarenko, 2011). It has been reported for instance in the case of surface capillary waves (Aubourg and Mordant, 2015), vibrating plates (Düring et al., 2006; Miquel and Mordant, 2011) and internal waves in stratified fluids (Brouzet et al., 2016). Yarom and Sharon (2014) claimed to find evidence of inertial wave turbulence in an experimental set-up of rotating turbulence at moderate Rossby number. The flow was excited with a series of alternating, random jets that input small-scale turbulence which then structures under the influence of rotation. They projected the energy in the subset of the spectral space associated with the dispersion relation of inertial waves, *i.e.* from a time series of the three-dimensional flow, they computed its kinetic energy as a function of  $\omega$  the frequency and  $\theta$  the angle between the wave vector and the axis of rotation. In this particular sub-space, they observed focusing of the energy along lines that correspond to the dispersion relation of inertial waves (see figure 2.8). However, Yarom and Sharon (2014) detected waves only at smaller scales, and most of the energy is located in geostrophic modes. Although it is clear that the flow they created features inertial waves, it is not clear whether they are generated through non-linear resonant interaction or if they stem from the random forcing that emits a continuum of waves. A convincing inertial wave turbulence in rotating fluid therefore remains to be observed.

### Non-universality of random forcing in rotating turbulence?

Experiments and numerical simulations of rotating turbulence are not adequate to fully understand the saturation of the elliptical instability. Instead of exciting random structures, the parametric resonance supplies energy to the fluid only through a small number of waves. Although Bordes et al. (2012) showed experimentally that maintaining a single wave in a rotating fluid gives rise to two daughter waves via triadic resonant interaction, as expected after the theoretical development presented in section 2.3, the response of the fluid as the dissipation is decreased remains poorly known. Favier et al. (2015) and Barker and Lithwick (2013) suggest that it could lead to other waves through a cascade of triadic resonances as well as strong geostrophic flows. In any case, the elliptical instability is a completely different approach to probe turbulence and the non-linear fate of waves in rotating fluids compared to standard stochastic forcing. In summary, it is another goal of the present work to explore how rotating turbulence depends on the nature of the forcing, and to determine whether wave excitation eventually leads to similar turbulent state as random forcing.

## 3.4 A summary of the thesis goals

To start with, the main goal of the work presented in this dissertation is to clarify the regimes of non-linear saturation of the elliptical instability via a large exploration of the space of control parameters. The control parameters comprise the forcing amplitude  $Ro_i$  as defined in section 1, dissipation quantified by the Ekman number  $E$  defined in chapter 2 section 3.2, but also the forcing frequencies,  $f$  in the case of libration and  $\gamma$  in the case of differential tidal bulge rotation. This investigation will be carried out with experiments, in continuation of the work of Grannan et al. (2014), and idealised numerical models, following the work of Barker and Lithwick (2013). These two models will complement each other in determining the nature

of the elliptical instability non-linear saturation. They will also be complemented with reduced theoretical models in order to explain the different observed regimes. This investigation will lead to extrapolated predictions for the expected type of turbulent saturation in weak forcing and dissipation regimes that are relevant to mechanical excitation in planetary cores and stellar interiors.

In characterising the different turbulent saturation states of the elliptical instability, we will in particular focus on the role of inertial waves and geostrophic vortices. We indeed aim at specifying their existence and origin with precise diagnostics, but also at quantifying non-linear processes between inertial waves, or between inertial waves and geostrophic flow.

Because the elliptical instability drives a turbulent flow by supplying energy in a small number of inertial waves (see figure 2.1), we also hope that this work will clarify some rather fundamental issues in rotating turbulence. Among them, we mention the universality of rotating turbulence with respect to the forcing: is the saturation state of the elliptical instability similar to classical, randomly-forced rotating turbulence? We also hope to clarify the nature of non-linear interactions leading to strong geostrophic flows. It is known from Greenspan (1969) that triadic interaction between inertial waves are unable to drive geostrophic flows, but Barker and Lithwick (2013) have shown that they may nevertheless take over the saturation of the elliptical instability. In identifying the origin of such strong vortices, we hope to shed light on the systematic emergence of strong geostrophic flows in classical, *i.e.* randomly-forced, rotating turbulence.

Lastly, although these two introduction chapters are focused on the interplay between mechanical forcing and inertial waves, we also explore in the last chapter of this dissertation the turbulence excited in a stably stratified planetary interior undergoing tidal distortion. As it will be explained later, stratified fluids sustain spontaneous oscillations under the restoring effect of buoyancy. They are called internal waves and bear properties similar to the inertial waves detailed in chapter 1 section 3.1. A substantial part of the present thesis work focuses on deriving an idealised model to study stratified planetary interiors undergoing tidal distortion, and on exploring the stability of these interiors as well as the turbulence that may result from instabilities.

# Chapter 3

## Experiments on the non-linear saturation of the elliptical instability

We present in the following an experimental study of the turbulence forced by the libration-driven elliptical instability. It builds on the experimental set-up of Noir et al. (2012) and is designed to explore more extreme regimes of weak forcing amplitude and dissipation that are relevant to the geo- and astrophysical contexts, but which have remained beyond the reach of previous experiments (Grannan et al., 2014) and simulations (Favier et al., 2015). In our set-up, a half-meter wide ellipsoid filled with water is brought to solid body rotation, and then undergoes sustained harmonic modulation of its rotation rate. This triggers the exponential growth of a pair of inertial waves that eventually collapse into turbulence. The flow is measured with Particle Image Velocimetry (PIV) performed in the equatorial plane of the ellipsoid. Depending on the amplitude of the rotation rate modulation, two different saturation states are observed. At large forcing amplitudes, the saturation flow main feature is a steady, geostrophic anticyclone. Its amplitude vanishes as the forcing amplitude is decreased while remaining above the threshold of the elliptical instability. Below this secondary transition, the saturation flow is a superposition of inertial waves which are in weakly non-linear resonant interaction, a state that could asymptotically lead to inertial wave turbulence. The transition between these two regimes and their relevance to geophysical applications are finally discussed at the end of this chapter.

### 1. Design of the experimental set-up

#### 1.1 The purpose of the experiments

The initial aim of the experimental part of the work presented throughout this dissertation is to achieve weak forcing and weak dissipation regimes to study the non-linear saturation

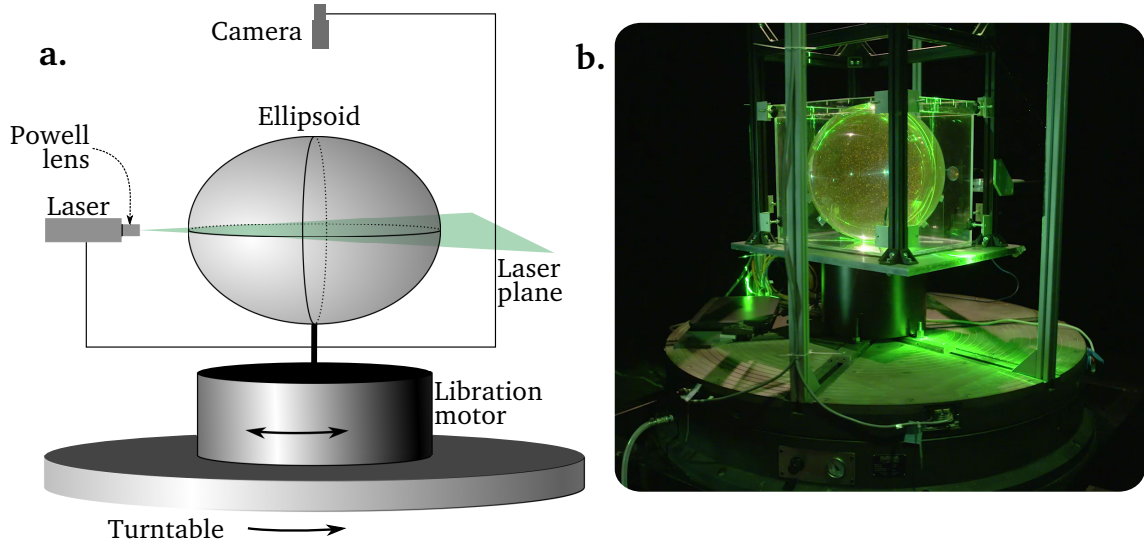


**Figure 3.1:** Schematic view (a) and photograph (b) of the experimental setup to carry out libration-driven elliptical instability. The ellipsoid is mounted on a turntable with a constant rotation rate  $\Omega_0$ , and an oscillating secondary motor to produce libration oscillations. The set-up to implement Particle Image Velocimetry is also shown. It comprises (in a) a laser and a Powell lens to create an equatorial light sheet illuminating particles that are observed with a camera. The ellipsoid is enclosed in a rectangular box filled with water, which limits refraction and ensuing image distortion, not depicted in (a) for clarity but visible in b.

of the instability in closer conditions to geo- and astrophysics, in a set-up of libration-driven elliptical instability extending the work of Noir et al. (2012) and Grannan et al. (2014). The overall design of the desired experiment, presented in figure 3.1, builds on the work of Noir et al. (2009) and Noir et al. (2012), and is identical to Grannan et al. (2014). An ellipsoid is mounted on a turntable rotating at a constant rate; the libration oscillation is imposed by a secondary motor so that the total rotation rate of the ellipsoid writes:

$$\Omega(t) = \Omega_0 (1 + \varepsilon \sin(f\Omega_0 t)) . \quad (3.1)$$

In order to determine the size and typical rotation rate of the new experiment, we may first examine the parameters that influence the typical dissipation rate, and the constraints that are imposed on them. Dissipation rate is quantified by the Ekman number  $E$  which compares the effects of viscosity to the Coriolis force and is defined as follows:

$$E = \frac{\nu}{a^2 \Omega_0} \quad (3.2)$$

where  $\nu$  is the kinematic viscosity of water,  $a$  is the half-length of the largest ellipsoid axis, and  $\Omega_0$  is the averaged rotation rate (see equation (3.1)). The values of these parameters used in Grannan et al. (2014) are recalled in table 3.1. To reach weaker dissipation regimes, it is clear that we must increase  $a$  and  $\Omega_0$  compared to this previous set-up.

In addition, to facilitate the comparison between our experimental study and the previous one, we prefer to keep the same ellipticity  $\beta = (a^2 - b^2)/(a^2 + b^2) = 0.34$  of the deformation in the horizontal plane (see section 1.3 in chapter 1). The two axes lengths  $a$  and  $b$  therefore remain in the same ratio as the experimental device is scaled up. The ratio of the third—vertical—axis length  $c$  with  $a$  and  $b$  is changed compared to Grannan et al. (2014) where

$b = c$ . In order to increase the inviscid growth rate of inertial modes excited by the elliptical instability, we chose  $c = (a + b)/2$  (C  bron et al., 2010); it lowers the viscous threshold of the instability and allows reaching weaker forcing regimes. In the design of the new experimental set-up, the only control parameter on the ellipsoid size is thus its largest—horizontal—axis half-length  $a$ , and we aim at increasing it by a factor 2 to 4 compared to Grannan et al. (2014).

## 1.2 Constraints on the secondary motor and the size of the set-up

Increasing both the size of the ellipsoid and the rotation rate of the turntable bears some consequences on the libration secondary motor, especially on the power it has to deliver. Let us call  $J$  the moment of inertia of all the set-up that is carried by the secondary motor with respect to its axis of rotation; the power  $\mathcal{P}$  needed to impose the time-varying rotation rate  $\Delta\Omega \equiv \Omega_0 \varepsilon \sin(f \Omega_0 t)$  writes:

$$\mathcal{P} = \frac{1}{2} J \frac{d\Delta\Omega^2}{dt} = \frac{1}{2} J \Omega_0^3 \varepsilon^2 f \sin(2f \Omega_0 t) . \quad (3.3)$$

$J \sim ma^2$  where  $m$  is the on-board mass carried by the secondary motor; assuming that the whole water-filled box is librating,  $m \propto a^3$ , so that  $J, \mathcal{P} \propto a^5$ . The energetic cost of increasing the size of the ellipsoid is *a priori* very high.

Another limitation on the secondary engine is the maximal torque it can develop. The instantaneous torque  $C$  is inferred from the power  $\mathcal{P}$  as follows:

$$\mathcal{P} = C(t)\Delta\Omega(t) = C(t)\Omega_0 \varepsilon \sin(f \Omega_0 t) , \quad (3.4)$$

so that:

$$C(t) = J\Omega_0^2 \varepsilon f \cos(f \Omega_0 t) . \quad (3.5)$$

We observe, as expected, that the secondary motor torque is in phase quadrature with respect to the rotation rate  $\Delta\Omega$ , the torque is maximal when the motor works against inertia to invert the rotation direction.

In order to design the experiment, we must quantitatively evaluate the maximal power and torque needed to impose a libration motion to an ellipsoid whose largest axis  $a$  remains to be defined. To carry out the calculation of the moment of inertia  $J$ , we assume that the water-filled box perfectly frames the ellipsoid, that is, the sizes of its sides are  $2a$ ,  $2b$  and  $2c$ . The ellipsoid's PMMA density difference with water is also neglected. The moment of inertia writes:

$$J = \frac{1}{6} \rho (a^2 + b^2) \times 8abc \quad (3.6)$$

Rotation rate (RPM)	$E$	$a$ (mm)	$b$ (mm)	$c$ (mm)	$\max \varepsilon (f = 4)$
30	$2 \times 10^{-5}$	127	89	89	1.6

**Table 3.1:** Table of the principal parameters of the experiments of Noir et al. (2012) and Grannan et al. (2014).  $a$ ,  $b$  and  $c$  are the half-lengths of the ellipsoid's axes.  $E$  is the Ekman number defined in (3.2) and  $\varepsilon$  is the relative variation of the rotation rate induced by libration, defined in (3.1).

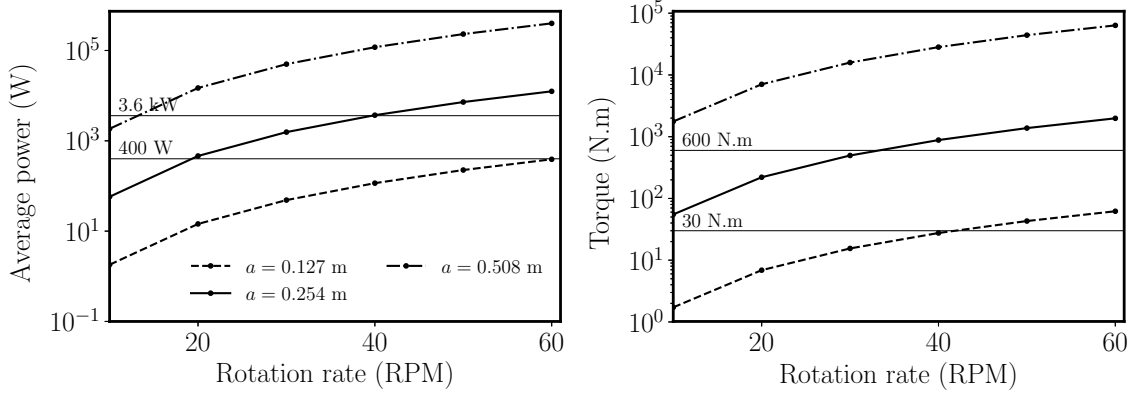


**Figure 3.2:** Calculation of the maximal power (left) and torque (right) needed to force the libration of an ellipsoid which has a major semi-axis increased by a factor 1, 2 and 4 compared to the one used in Grannan et al. (2014), which is given in the legend in meters. The calculation is done at  $\varepsilon = 1$ . The two horizontal lines materialise the maximal power produced by the motor used in the previous experiment (Yaskawa SGMCS-10C3B11, see Noir et al. (2009)), and by the most powerful motor of the same series (Yaskawa SGMCS-2ZN3A11).

where  $\rho$  is the density of water. This value of  $J$  is *a priori* over-estimated: the fluid inside the container is not expected to librate at the same velocity as the secondary motor—apart from the boundary layers—as it rather oscillates with a typical velocity reduced by a factor  $\beta$  inside the ellipsoid (see section 1.4 in chapter 1). Nevertheless, we have neglected here heavy equipment such as the aluminium structure supporting the ellipsoid, the camera and the laser that are on board of the secondary motor. To estimate a safety factor on the maximum power and torque, we rely on the experiment of Grannan et al. (2014). They used a Yaskawa ring-style servo-motor (Yaskawa SGMCS-10C3B11) that is able to deliver a maximum power and torque of 400 W and 30 N.m respectively. In their experiments, the maximum rotation rate was limited to 30 RPM, and a relative rotation rate  $\varepsilon = 1.6$  was reached at most for the libration frequency  $f = 4$  (see table 3.1). According to our crude estimates (3.3) and (3.5) based on the moment of inertia (3.6), this maximum parameters correspond to a power of  $\sim 10$  W and a torque  $\sim 2$  N.m, which is about an order of magnitude below the maximum values. This discrepancy between the estimate and the experiment is likely due to the heavy on-board equipment (laser, aluminium frame, etc.) and a factor 10 on both power and torque shall be taken as a safety margin in the design of our experiment.

With the lengths ratios detailed in the preceding section, the estimates of the maximum power (3.3) and torque (3.5) requested from the secondary motor is displayed in figure 3.2; they include a factor 10 as a safety margin. We assume for the estimates an extreme case where  $\varepsilon = 1$  and  $f = 4$ . These values are compared to the specifications of two Yaskawa ring-style servo-motors, the one used in the experiments of Grannan et al. (2014) and Noir et al. (2009), and the most powerful one which is able to develop a maximum power and torque of  $\sim 3.6$  kW and 600 N.m respectively.

The diagrams of figure 3.2 clearly indicate that it is impossible to force librations of a four times larger ellipsoid, even with the most powerful servo-motor (Yaskawa SGMCS-2ZN3A11). However, the latter seems adapted to our needs since it provides a sufficient torque to drive fast oscillations of a twice larger ellipsoid at a turntable rotation rate as high as  $\sim 30$  RPM, including the factor 10 safety margin.

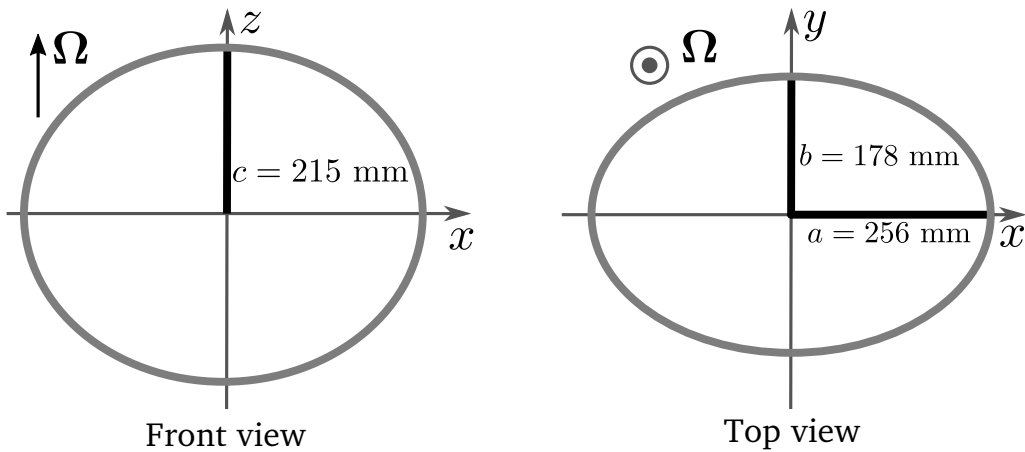


**Figure 3.3:** Views of the ellipsoid and its interior dimension. The thickness of the PMMA is of 7 mm. The rotation axis is materialised by the vector  $\Omega$ .

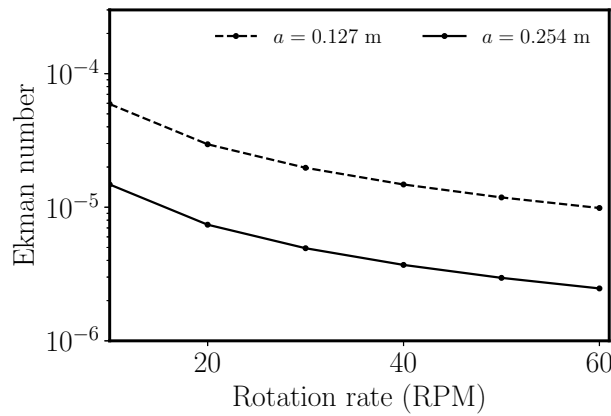


**Figure 3.4:** Computation of the Ekman number defined by the formula (3.2) for the ellipsoid of Grannan et al. (2014) ( $a = 0.127$  m) and the one chosen for our study ( $a = 0.254$  m).

We thus chose the most powerful Yaskawa servo-motor (SGMCS-2ZN3A11), and an ellipsoid with largest axis length  $a = 254$  mm. The physical dimensions of this ellipsoid in all three directions are shown in figure 3.3. At extreme libration amplitude and frequency ( $\varepsilon = 1$  and  $f = 4$ ), it is expected that the turntable can be brought to 30 RPM, and higher rotation rates may even be reached at lower forcing amplitudes. In addition, we provide in figure 3.4 the Ekman number as a function of the rotation rate for the ellipsoid used by Grannan et al. (2014) and the twice-larger ellipsoid chosen for our experiments. We notice that the Ekman number is decreased to  $E \sim 5 \times 10^{-6}$  in our set-up, which is about one order of magnitude lower than in previous experiments (Grannan et al., 2014) and recent numerical simulations Favier et al. (2015), for which  $E > 2 \times 10^{-5}$ .

### 1.3 Machining of the ellipsoid

In this section, we aim at specifying the needed manufacturing quality of the ellipsoid via determining the maximum tolerance on defect thickness. We estimate that a defect must not exceed the typical Ekman boundary layer size; beyond that point, defects might be able

to induce significant perturbations of the flow. The typical Ekman layer thickness is  $\delta = a\sqrt{E}$  and taking  $E \sim 3 \times 10^{-6}$  gives

$$\delta \sim 4 \times 10^{-4} \text{ m} .$$

The maximum tolerance on the machining of the ellipsoid is therefore about 0.1 mm.

The ellipsoid used in the present experimental study with the dimensions specified in figure 3.3 has been manufactured from two transparent, 22 cm-thick PMMA blocks. They have been reduced to the half-ellipsoids —cut in the  $(xOz)$  plane with thickness 7 mm, with a machining precision as low as 0.05 mm. The assembly of the two halves has been carried out with UV glue, which avoids the use of screws and the associated stress that usually results in cracks. The typical gluing line is about 0.1 to 0.2 mm thick, which is smaller than any dimension of the ellipsoid and smaller than the defect tolerance detailed above. Note however that the assembly process induces local modifications of the optical properties of the PMMA close to the gluing line, which may perturb the imaging quality. Access to the interior of the ellipsoid is only provided by a 5 mm-wide hole, chosen as small as possible to avoid perturbation of the shape of the container. This hole is located away from the rotation axis to avoid extra stress on the gluing line; it is therefore not located at the highest point of the ellipsoid. Filling and emptying thus require tilting of the container, which is however facilitated by the water-filled box in which the ellipsoid floats and is easily movable.

## 2. The experimental set-up

### 2.1 Choice of the libration frequency

In the present chapter, apart from section 7, we focus on the excitation frequency  $f = 4$ . At this frequency, the frequency of the resonant modes is  $\pm 2$ , at the high frequency end of the dispersion relation. These modes comprise several horizontal layers of alternating velocity, and are known to have the largest inviscid growth rate under the libration-driven elliptical instability (Cébron et al., 2012a). In addition, as shown by Grannan et al. (2014) and Favier et al. (2015), the expected number of layers is around 5 at an Ekman number  $E \sim 10^{-5}$ , and is probably larger at lower values of  $E$ . It ensures a reasonable scale separation between the size of the ellipsoidal container and the typical resonant wavelength. We thus choose to focus on the specific forcing frequency  $f = 4$  in order to facilitate the exploration of weaker forcing amplitude and dissipation regimes while keeping mostly horizontal velocities that are more easily measured with the equatorial laser plane (see figure 3.1). Note however that the last part of this chapter is targeted at the forcing frequency  $f = 2.5$  for completeness.

### 2.2 Rotation and libration

In the present experiment, the ellipsoid sits on a turntable whose rotation rate ranges from 10 RPM to 40 RPM. The modulation of the rotation rate  $\Omega$  is operated by a 3.1 kW ring-style, direct-drive, servomotor (YASKAWA SGMCS-2ZN3A11). The sinusoidal motion is controlled via a card (Servopack SGD7S) and is discretised on 2000 points per period. This motor is able to produce oscillations of a system weighting around 100 kg with lateral extent of 30 cm, with a rate ranging from 0 to 180 oscillations per minute. The typical amplitude of

Rotation rate	Ekman number	Libration angle range	$\varepsilon$ range	$Ro_i \times 10^2$ range
10 RPM	$1.5 \times 10^{-5}$	$2.64^\circ$ – $4.74^\circ$	0.185–0.331	6.31–11.2
20 RPM	$7.4 \times 10^{-6}$	$1.68^\circ$ – $4.22^\circ$	0.118–0.294	4.02–10.0
30 RPM	$5.0 \times 10^{-6}$	$1.07^\circ$ – $4.23^\circ$	0.0747–0.296	2.54–10.1
40 RPM	$3.7 \times 10^{-6}$	$1.41^\circ$ – $1.74^\circ$	0.0986–0.122	3.36–4.16

**Table 3.2:** Summary of the different input parameters used in the experiment at a forcing frequency  $f = 4$  and the corresponding dimensionless parameters. The rotation rate is in rotations per minute (RPM). The Ekman number is defined as  $\nu/(a^2\Omega_0)$ , where  $\nu$  is the viscosity of water, considered to be  $1.0 \times 10^{-6} \text{ m}^2.\text{s}^{-1}$  at room temperature. It compares the effects of viscosity to those of the Coriolis force. Note that the typical relative error on the value of the libration angle is about 1.5 %. Lastly, the input Rossby number quantifies the amplitude of the libration base flow measured in the rotating frame, that is,  $Ro_i = \beta\varepsilon$ .

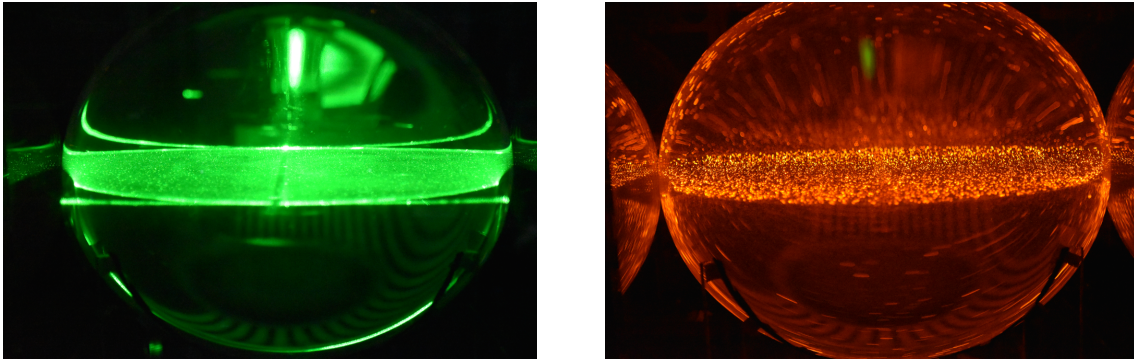


**Figure 3.5:** Photographs taken with (right) and without (left) an orange filter of the laser sheet lighting the fluorescent PIV particles. Using PIV particles absorbing the green light and emitting in red allows filtering out the reflections of the sheet on the surface of the ellipsoid, thus improving the overall quality of the images taken by the high-resolution camera. Note that there was no water in the outer box at the time the picture was taken.

the oscillations used in this study ranges from  $0^\circ$  to  $5^\circ$  at  $f = 4$ , although larger amplitudes can easily be reached at lower frequencies (the system has been tested up to  $25^\circ$  at one oscillation every two seconds). Relative variations of the rotation rate of the primary turntable due to the oscillations of the servo-motor do not exceed 0.4 %.

The typical libration amplitudes of the relative rotation rate variation  $\varepsilon$  and the associated libration angle and input Rossby number  $Ro_i = \beta\varepsilon$  (see sections 1 in chapter 2) are given in table 3.2 for the case  $f = 4$ . We note that the typical values of  $\varepsilon$  are below the upper bound  $\varepsilon = 1$  used in the experimental set-up design calculations. This is mainly due to the fact that all the interesting phenomena relevant to planetary cores and stellar interiors have been observed at weak forcing amplitudes. Lastly, we emphasise that our set-up allows reaching values of the Ekman number that are about an order of magnitude below those of Grannan et al. (2014). This is made possible by the increase in the size of the ellipsoidal container and the use of the most powerful servo-motor of its category.

## 2.3 Imaging and velocity measurements

To measure the velocity of the flow, we use Particle Image Velocimetry (PIV). A green laser beam is transformed into a 2 mm-thick homogeneous sheet with a Powell lens; the sheet cuts the ellipsoid through the equatorial plane (see figure 3.1) and lights PIV particles with a fluorescent coating (Cospheric UVPMS-BO-1.00, 53-63 $\mu$ m). The fluorescent coating is such that it absorbs the green light to emit in orange; filtering out the green light allows capturing only the particles getting rid of parasitic reflections of the sheet on the ellipsoid —see figure 3.5.

High resolution images (2560  $\times$  1600 pixels) of the laser plane are taken with a camera (DANTEC SpeedSense 341) placed above the ellipsoid, the CCD sensor being at a distance of 38.7 cm from the equatorial plane. It is mounted with a 28 mm Zeiss lens. The camera is attached to a structure bound to the secondary motor, so that a fixed-shape ellipsoid is seen through the camera, which limits periodic variations of the field of view due to optical distortions. The framerate used in our experiments ranges from 20 Hz for the lowest rotation rate, to 50 frame per second (fps) for the highest. Image acquisition is controlled by DANTEC’s software DynamicStudio. The same software is used to process the images into velocity fields, via an adaptive PIV algorithm. The PIV algorithm is performed on 78  $\times$  50 boxes of 64  $\times$  64 pixels size. Note that the number of PIV particles in the ellipsoid is such that there is always about 3 to 5 particles inside these boxes. Lastly, both the camera and the servomotor are controlled by a computer lying on the turntable, which is monitored remotely via WiFi.

## 2.4 Calibration of the field of view

As explained in section 1.3, the only access to the interior of the ellipsoid is a 5 mm-diameter hole. There is no straightforward option to perform a calibration with the use of a precise grid, as usual in PIV measurements. We have therefore implemented a non-invasive method, which is less accurate, but still gives a satisfying estimate of the scaling factor between the physical field and the camera images, plus a quantitative estimate of the optical distortion on the plane.

The set-up used for the calibration process is presented in figure 3.6. A shaded pattern (referenced as the “physical pattern”) is created in the Laser sheet with an opaque grid placed on the wall of the water box. This grid is printed on a transparent slide and is made of black and transparent stripes, all  $10.0 \pm 0.5$  mm wide. The geometry of the physical pattern is computed from ray path construction, knowing the geometry of all the interfaces and their refractive indices; it is shown in figure 3.7a. The camera saves a “recorded pattern” of light and shade revealed by the particles. We further enhance this pattern by taking 500 pictures as the ellipsoid spins up from 0 to 10 RPM and averaging the light pattern over this set of images. A typical result of this process is shown in figure 3.7b. The core of the calibration process is to produce a “theoretical pattern”, which is the shaded pattern as it should be seen from the camera location. It is computed from the “physical pattern” with ray path construction from the camera to the equatorial plane of the ellipsoid. The recorded and theoretical patterns are then related by a scaling factor.

The result of this process is shown in figure 3.7 where the physical and recorded patterns are presented in panel a. and b. respectively. The refractive indices of water and PMMA taken for the ray path construction are respectively  $n = 1.33$  and  $n = 1.49$  (Weber, 2018). The result

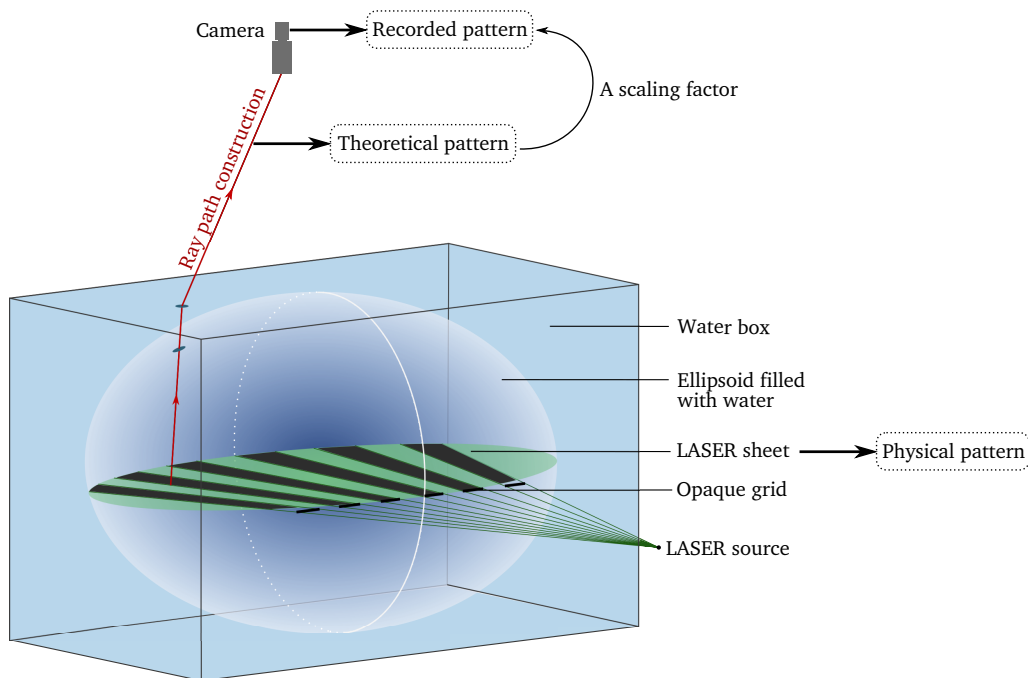


**Figure 3.6:** Schematic of the set-up used to calibrate the pictures of the LASER sheet. An opaque grid pattern placed on the wall of the water box is used to interrupt the Laser ray and create a shaded pattern—the “physical pattern”—inside the ellipsoid. The geometry of this physical pattern can be known by ray path construction. The camera records and “observed pattern” that is to be compared with a “theoretical pattern”. The latter is the result of ray path construction from the physical pattern to the camera.

of applying a scaling factor to the theoretical pattern to fit the recorded pattern is shown in figure 3.7c. Additional effects such as camera lens distortion or PMMA defects are within the error bar.

The theoretical mapping between the physical and theoretical patterns also reveals that the optical distortion of the physical pattern by the water box and the ellipsoid is merely isotropic, the relative discrepancy between the scaling in  $X$  and  $Y$  directions being below 2 %. The fitted scaling factor between the theoretical pattern (in meters) and the recorded pattern (in pixels) is  $5.69 \pm 0.08 \times 10^3 \text{ pixels.m}^{-1}$ . The error bar accounts for the uncertainty on the respective position of the laser sheet waist point and of the ellipsoid centre, the distance between them being  $42 \pm 0.5 \text{ cm}$ . In the processing of the PIV fields, we apply this scaling factor to the displacement measured in pixels by the PIV algorithm, and to the position of the points where the velocity is computed.

## 2.5 The experimental procedure

To study the non-linear saturation of the elliptical instability, we proceed as follows. We first turn on the turntable and wait for the fluid inside the ellipsoid to reach solid-body rotation. We then turn on the secondary motor which imposes oscillations at a dimensionless rate  $f$  with a desired amplitude  $\Delta\varphi = \varepsilon/f$  (see section 1.4 in chapter 1). Between two experiments carried out at the same rotation rate, the secondary motor is turned off and we wait for the remaining flow inside the ellipsoid to dissipate before starting a new run.

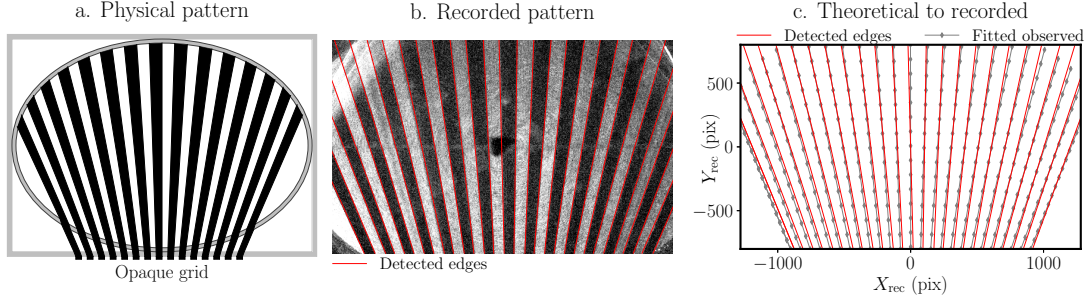


**Figure 3.7:** Panels **a.** and **b.** show respectively the shaded pattern created by the an opaque grid with a 10 mm step at the entrance of the water box. Panel **c.** shows the best fit between the detected edges (in red) and the observed pattern computed theoretically; the only fitting parameter is the scaling factor applied to the observe pattern to match the observed edges. In the computed shaded pattern depicted in **a.**, the PMMA containers, *i.e.* the ellipsoid and the outer box, are in grey, and all these containers are filled with pure water. The observed pattern of picture **b.** has been obtained by shining the LASER sheet to the particle-seeded ellipsoid while in a spin-up phase. It is the results of averaging 500 pictures spanning over about 15 s. The red lines are the result of an automated contour detection and a fit of the detected edges with lines. Note that averaging the light diffused by particles enhances the area where the two parts of the ellipsoid are glued together, materialised by an intermediate contrast horizontal line at mid-height. Heterogeneities in the diffused light caused by unavoidable parasitic reflections of the LASER sheet on the walls are also noticeable.

## 3. Base flow and frames of reference

### 3.1 Measuring the libration flow

In order to characterise each experiment and to quantify the flows excited by the elliptical instability, the amplitude and the phase of libration must be determined. This is done during the early phase of each experiment when librations are imposed but the instability has not yet significantly grown.

We recall from chapter 1 equation (1.16) that the libration base flow seen from the librating frame  $U_b^\ell$  with axes  $(X, Y, Z)$  writes

$$U_b^\ell = -[U, V, 0] = \frac{2ab}{a^2 + b^2} \Omega_0 \varepsilon \sin(\Omega_0 f t) \left[ -\frac{a}{b} Y, \frac{b}{a} X, 0 \right]. \quad (3.7)$$

In the rotating frame of reference with axes  $(x, y, z = Z)$ , the libration base flow  $U_b^\Omega$  writes (see equation (1.17)):

$$U_b^\Omega = -\Omega_0 \varepsilon \beta \sin(\Omega_0 f t) [y, x, 0]. \quad (3.8)$$

We also recall that the camera is in the libration frame while the dynamics of interest is in the rotating frame: an accurate determination of the libration amplitude is therefore needed to transform the experimental flow into the rotating frame.

From measurements performed in the librating frame, we first define a transformed base flow  $\tilde{U}_b^\ell = (\tilde{U}, \tilde{V})$  and a transformed position  $\tilde{X} = (\tilde{X}, \tilde{Y})$  such that:

$$\tilde{U} = U/a, \quad \tilde{V} = V/b, \quad \tilde{X} = X/a, \quad \tilde{Y} = Y/b \quad (3.9)$$

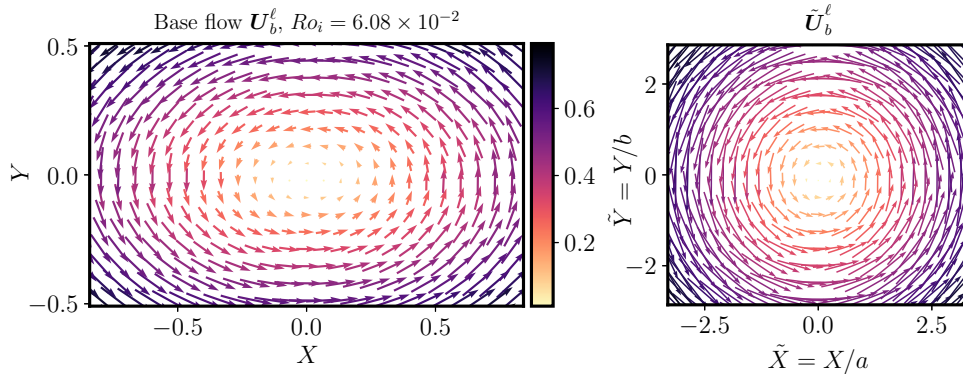


**Figure 3.8:** Experimental measurement of the libration base flow  $U_b^\ell$  (**left**) and the transformed base flow  $(\tilde{U}_b^\ell)^2$  (**right**) for an input Rossby number  $Ro_i = 6.01 \times 10^{-2}$ , an Ekman number  $E = 5.0 \times 10^{-6}$  and  $f = 4$ . Note that  $X$  and  $Y$  are normalised by  $a$ , and that the velocity is scaled by the typical libration velocity  $Ro_i a \Omega_0$ .

where  $U$  and  $V$  are the  $x$  and  $y$  components of the base flow velocity. Applying this transformation to the flow (3.7) yields:

$$\tilde{U}_b^\ell = \frac{-2ab}{a^2 + b^2} \Omega_0 \varepsilon \sin(\Omega_0 f t) [-\tilde{Y}, \tilde{X}, 0] = \frac{-2ab}{a^2 + b^2} \Omega_0 \varepsilon \sin(\Omega_0 f t) \tilde{r} \tilde{e}_\phi = -\tilde{\Omega}(t) \tilde{r} \tilde{e}_\phi \quad (3.10)$$

which is an oscillating solid-body rotation with effective maximum vorticity  $\tilde{\Omega}$ , and where we have introduced  $\tilde{r} = \sqrt{\tilde{X}^2 + \tilde{Y}^2}$  and  $\tilde{e}_\phi$  an orthoradial vector in the transformed coordinates. Experimental PIV fields of the base flow and the transformed flow are shown in figure 3.8, and are in good agreement with the theoretical expressions (3.7) and (3.10).

To determine the axis of rotation, the field  $(\tilde{U}_b^\ell)^2$  is fitted to an axisymmetric parabola with adjustable central position; the location of the centre is then averaged over the whole set of velocity fields. The same transformed field is used to determine  $\varepsilon$ : the position is sorted in 30 rings centred on the axis of rotation, on which the orthoradial transformed velocity is averaged. The result of this process is shown over half a libration period in the left panel of figure 3.9. Fitting the averaged orthoradial velocity with a line gives the effective vorticity  $\tilde{\Omega}(t)$  which is represented in the right panel of figure 3.9. The time series of  $\tilde{\Omega}$  is fitted to a sinusoidal function to measure the amplitude of libration  $\varepsilon$  and the phase. The agreement between the experimental data and the sinusoidal function is within 1.5 % relative error.

### 3.2 Transformation from the libration to the rotating frame

Although the camera is in the librating frame of reference for experimental convenience, the adequate frame to study the dynamics of the non-linear saturation of the elliptical instability is the rotating frame in which inertial waves and the geostrophic modes are well defined. The transformation of the PIV fields from one frame to another is performed in the post-processing phase. The position in the rotating frame is deduced from the position in the libration frame by a rotation of angle  $\theta_\ell = -(\varepsilon/f) \cos(\Omega_0 f t)$ , with an adequate choice of the initial time  $t = 0$ . The velocity at this rotating position is computed from interpolation of the

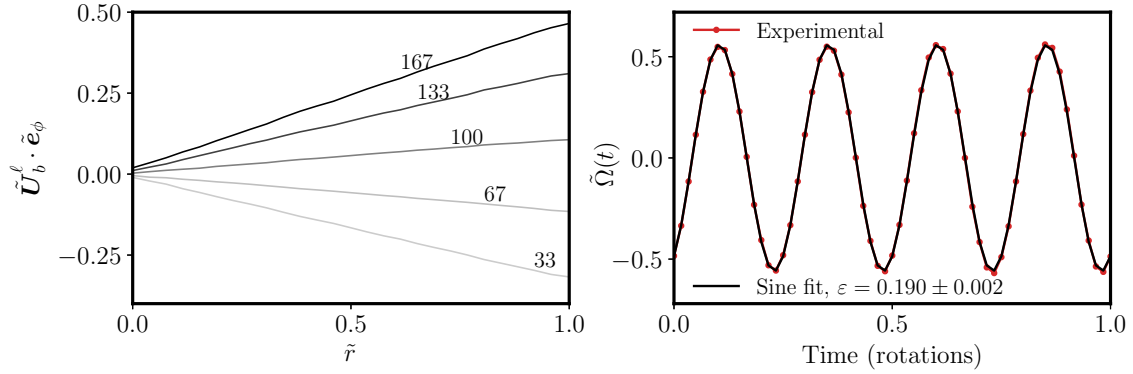


**Figure 3.9:** **Left:** experimental measurement of  $\tilde{U}_b^l \cdot \tilde{e}_\phi$  over half a period of libration, the time being given in milliseconds. **Right:** experimental measurement of the effective vorticity  $\tilde{\Omega}$  defined in equation (3.10) and best sinusoidal fit yielding  $\varepsilon = 0.190 \pm 0.002$  in this case. The fitting parameters are the phase and the amplitude of the sine. The agreement between the fit and the experimental data is within 1.5 %. For both panels, the Ekman number is  $E = 5.0 \times 10^{-6}$  and the libration frequency is  $f = 4$ .

PIV field with 3rd order two-dimensional splines using the `RectBivariateSpline` function of the PYTHON library `SciPy` (Jones et al., 2001). This transformation also includes a velocity composition: a solid body rotation associated to the rotation of varying angle  $\theta$  is removed from the measured velocity. A snapshot of the base flow transformed into the rotating frame is shown in figure 3.10. It is compared to the theoretical base flow at the same time and the overall agreement between the two fields is satisfactory. Discrepancies may be noticed around the line  $y = 0$  that are due to the line where the two parts of the ellipsoid are glued together and where the optical distortion is important. Other discrepancies may be noticed in the centre where the particles displacements are small and the direction of their motion is therefore difficult to determine from the PIV algorithm. Nevertheless, the relative error between the theoretical and the experimental base flow in the rotating frame computed with  $L^2$  norm is as low as 3 %.

## 4. The non-linear saturation at low forcing amplitude: waves in interaction

In the following, we focus on the non-linear saturation of the elliptical instability driven by libration at low forcing amplitudes and  $f = 4$ . For a fixed rotation rate, or Ekman number  $E$ , and libration frequency, the procedure described in paragraph 2.5 is repeated with increasing libration amplitude or input Rossby number  $Ro_i$ . We start with amplitudes that are below the threshold of the elliptical instability, which is approximately found at  $Ro_i \simeq 10\sqrt{E}$  (a similar value to Favier et al. (2015)), and then explore the non-linear regimes.

We first present time series of the saturation flow which indicate that despite the libration amplitudes being small, we observe a chaotic, if not turbulent, state. We then explore the spectral content of the flow and identify inertial waves that are in triadic resonant interaction with one another. What we mean by “low forcing amplitude” is left unspecified in this section, the boundaries of the regime we detail here will be explored afterwards.

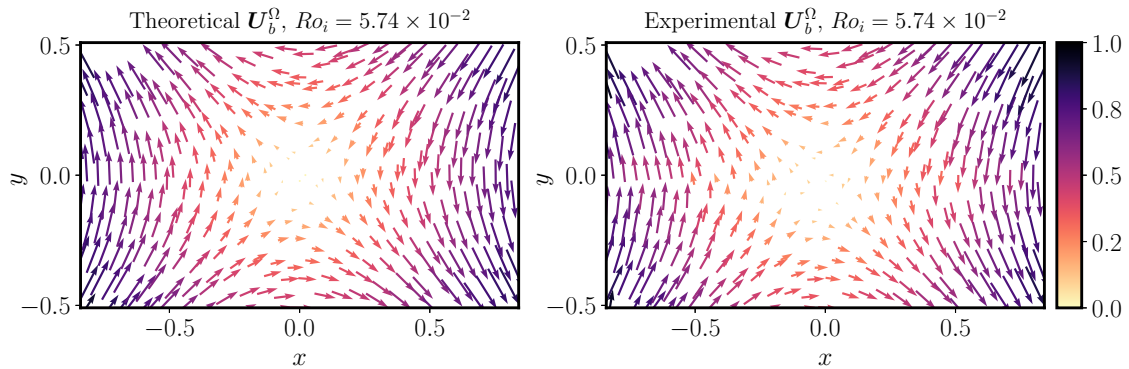


**Figure 3.10:** Snapshot of the theoretical (**left**) and experimental (**right**) libration base flow  $U_b^\Omega$  transformed into the rotating frame, for an input Rossby number  $Ro_i = 5.74 \times 10^{-2}$ , an Ekman number  $E = 5.0 \times 10^{-6}$  and a libration frequency  $f = 4$ . The theoretical base flow is given by formula (3.8). In this frame, the libration base flow is a strain field standing in space and oscillating in time. The velocity is normalised by a typical libration velocity  $Ro_i a \Omega_0$  and the distances are normalised by  $a$ . The agreement between the measured and theoretical base flows is overall satisfying, although some deviations can be spotted around the  $y = 0$  line and at the centre.

## 4.1 Kinetic energy time series

To describe in general the saturation of the libration-driven elliptical instability, we track the evolution of the kinetic energy over time. In particular, we focus on the kinetic energy of the fluctuations around the libration base flow. These fluctuations are measured directly in the libration frame, *i.e.* there is no need to proceed to a change of frame of reference to carry out this measurement. Let us call  $\mathbf{u}$  the fluctuations, such that the total flow in the libration frame of reference writes:

$$U(\mathbf{X}) = U_b^\ell(\mathbf{X}) + \mathbf{u}(\mathbf{X}) . \quad (3.11)$$

The flow in the rotating frame is deduced from (3.11) by a coordinate rotation  $\mathbf{X} \mapsto \mathbf{x}$  and a velocity composition  $U_{\text{rot}}$  such that:

$$U(\mathbf{x}) = U_b^\ell(\mathbf{x}) - U_{\text{rot}}(\mathbf{x}) + \mathbf{u}(\mathbf{x}) = U_b^\Omega(\mathbf{x}) + \mathbf{u}(\mathbf{x}) . \quad (3.12)$$

It is therefore equivalent to measure the kinetic energy of the fluctuations in these two frames. We therefore define a fluctuation kinetic energy  $\mathcal{E}$  and a base flow kinetic energy  $\mathcal{E}_b$ :

$$\mathcal{E} = \frac{1}{2} \langle \mathbf{u}^2 \rangle \quad \text{and} \quad \mathcal{E}_b = \frac{f \Omega_0}{2\pi} \int_0^{\frac{2\pi}{f \Omega_0}} \left\langle \frac{1}{2} (U_b^\Omega)^2 \right\rangle dt \quad (3.13)$$

where the operation  $\langle \cdot \rangle$  denotes a summation over all the locations in the PIV field.

The result of computing the ratio  $\mathcal{E}/\mathcal{E}_b$  is shown in figure 3.11 where we represent time series of this quantity and its mean value for several experiments at an Ekman number  $E = 5.0 \times 10^{-6}$  —see table 3.2.

The quantity  $\mathcal{E}$  undergoes fluctuations over time, be it at time scales as short as the rotation period or at very long times scales, similar to the slow non-linear time scale  $2\pi(Ro_i \Omega)^{-1}$  ranging from 60 to 200 rotation periods. In addition, the ratio  $\mathcal{E}/\mathcal{E}_b$  is of order 1, which indicates that the amplitude of the fluctuations is of order  $Ro_i$ , as expected from the simple scaling developed in chapter 2 section 1, and found in numerical simulations (Barker and

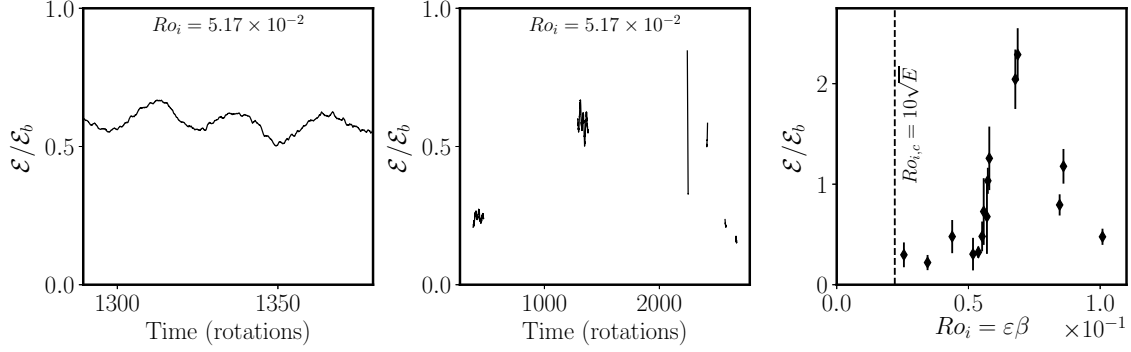


**Figure 3.11:** **Left:** kinetic energy variation over a hundred of rotation times at  $E = 5.0 \times 10^{-5}$ ,  $f = 4$  and  $Ro_i = 5.17 \pm 0.07 \times 10^{-2}$ . **Centre:** several measurements of the kinetic energy for the same experiment. The typical separation between two recordings is set by the time needed to transfer the data from the camera to the computer. This data set comprises long (5476 images) and short (500 images) recordings at 30 Hz. For both panels, the time series are low-pass filtered by a sliding average over one rotation period. **Right:** mean value of the kinetic energy in the saturation phase of the instability at 30 RPM and  $f = 4$  for all the experimented values of the input Rossby number  $Ro_i$ . The error bar corresponds to the standard deviation of kinetic energy considering all recordings of each experiment. The vertical dashed line materialises the approximate viscous threshold of the instability according to Le Bars et al. (2010) and Favier et al. (2015), which is  $Ro_{i,c} \sim 10\sqrt{E}$ , and below which the flow is experimentally observed to be stable

Lithwick, 2013; Grannan et al., 2017). These features of the kinetic energy attest that the saturation phase is dominated by non-linear transfers, and is potentially turbulent. Variations around the simple scaling  $\mathcal{E}/\mathcal{E}_b = \mathcal{O}(1)$  are noticeable in figure 3.11 but remain difficult to explain since our set-up only allows measuring horizontal motions in a plane. In particular, the vertical motions along the rotation axis and their dependence with  $Ro_i$  are not accessible. Lastly, although the typical velocity  $U^*$  scales like the forcing amplitude, the Reynolds number  $Re \equiv aU^*/\nu$  remains large. Given that  $U^* \sim Ro_i a \Omega_0$ , it is easily found that  $Re \sim Ro_i/E \sim 10^4$ .

In this section, we are interested in the saturation flow for forcing amplitudes that are above the threshold of the instability but which remain relatively small —typically  $Ro_i < 6 \times 10^{-2}$  at  $E = 5.0 \times 10^{-6}$ . The right panel of figure 3.11 proves that even close to the threshold the kinetic energy of the perturbation flow  $u$  reaches significant values ( $\mathcal{E}/\mathcal{E}_b > 0.3$ ) and undergoes temporal variability.

## 4.2 Spectral content of the flow: inertial waves in resonant interaction

### Temporal spectrum and triadic resonant interactions

To refine the analysis of the non-linear saturation flow we explore its spectral content in the temporal domain. It is a natural analysis to perform because many features of the flow have a specific frequency signature: the libration forcing appears at  $\omega = f = 4$ , and inertial waves are restrained to the domain  $[-2, 2]$  —time being normalised by the rotation time scale  $\Omega_0^{-1}$ .

To determine the spectral content of the flow, we randomly select a set of 300 locations in

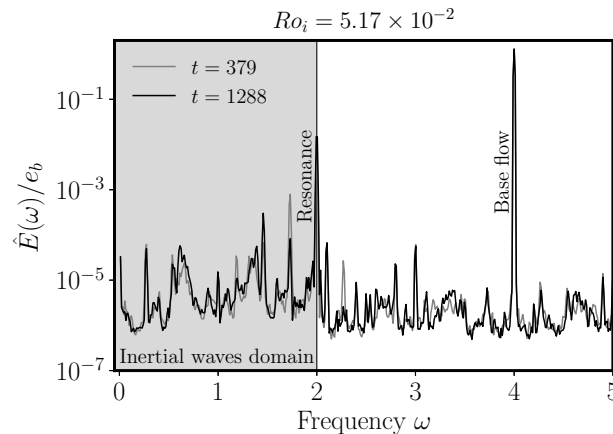


**Figure 3.12:** Ensemble average of temporal spectra at a forcing amplitude  $Ro_i = 5.17 \times 10^{-2}$ , a libration frequency  $f = 4$  and an Ekman number  $E = 5.0 \times 10^{-6}$ . The frequency  $\omega$  is given in rotation units, so that  $\omega = 1$  corresponds to a frequency of  $\Omega_0$ . Two different power spectra are displayed, they correspond to two different recordings around a time  $t$  indicated in rotation periods in order to enhance robust features. Among the clear peaks are the base flow at  $\omega = f = 4$  peaking at  $\hat{E}(f)/e_b \sim 1$ , and the resonant mode at  $\omega = f/2 = 2$ . The shaded area materialises the domain of existence of inertial waves. The typical frequency resolution is about  $1.1 \times 10^{-2}$ .

the rotating frame of reference where the two components of the velocity are recorded. They are then multiplied by a Hann windowing function<sup>1</sup> and Fourier transformed to compute their power spectra. Lastly, we perform an ensemble average over the set of 300 power spectra, yielding a quantity denoted as  $\hat{E}(\omega)$ . These power spectra are scaled by a typical local energy of the base flow  $e_b$  that is defined as the total base flow kinetic energy  $\mathcal{E}_b$  divided by the number of PIV boxes composing the field of view.

A typical result of this process for an Ekman number of  $E = 5.0 \times 10^{-6}$ , a libration frequency of  $f = 4$  and an input Rossby number  $Ro_i = 5.17 \times 10^{-2}$  is shown in figure 3.12. As anticipated, the peaks associated with the libration flow ( $\omega = f = 4$ ) and the resonant modes ( $\omega = f/2 = 2$ ) appear clearly in the power spectra. In addition, superposing power spectra for the same experiment but at different times reveals the overall reproducibility of this measurement.

The large number of peaks, in particular in the inertial modes range, and the low background noise together with the kinetic energy time series (figure 3.11), indicate that the saturation at low forcing is chaotic or weakly turbulent, and includes persistent inertial modes. Furthermore, we notice in figure 3.13a that the peak positions are not random but persist at different Ekman numbers provided the forcing remains small. Besides, the peaks can be paired together so that their frequencies  $\omega_1$  and  $\omega_2$  satisfy:

$$\omega_1 + \omega_2 = 2. \quad (3.14)$$

This suggests that the paired structures are inertial waves in triadic resonant interactions with the resonant mode, as explained in chapter 2 section 2.3 (see, in particular, relation (2.34))<sup>2</sup>.

<sup>1</sup>For a signal defined on the time interval  $[0, T]$ , the Hann windowing function is defined as

$$t \mapsto \frac{1}{2} - \frac{1}{2} \cos\left(\frac{2\pi}{T}t\right).$$

<sup>2</sup>Note that the relation (2.34) derived in chapter 2 was rather  $\omega_1 + \omega_2 + 2 = 0$  but since the field is real, all

The existence of triadic resonant interactions can be further assessed by determining from the local velocity measurements a bicoherence spectrum  $\mathcal{B}(\omega_1, \omega_2)$ , following in particular Favier et al. (2015); Brouzet et al. (2016). This quantity is determined from the—complex—temporal Fourier transform of the velocity local measurements  $\hat{u}_i$ , the index  $i$  referring to the index of the probe as well as the component. The bicoherence may be defined through the following formula:

$$\mathcal{B}(\omega_1, \omega_2) = \frac{|\langle \hat{u}_i(\omega_1) \hat{u}_i(\omega_2) \hat{u}_i^*(\omega_1 + \omega_2) \rangle|^2}{\langle |\hat{u}_i(\omega_1) \hat{u}_i(\omega_2)|^2 \rangle \langle |\hat{u}_i^*(\omega_1 + \omega_2)|^2 \rangle} \quad (3.15)$$

where the operation  $\langle \cdot \rangle$  here denotes an ensemble average over all the  $\hat{u}_i$ . The bicoherence depends on the relative phase between the Fourier component of the signal contrary to the second order power spectrum. It is maximal and reaches 1 when modes with frequencies  $\omega_1$  and  $\omega_2$  are locked over long times and everywhere in space to a structure oscillating at  $\omega_1 + \omega_2$ . It is, therefore, an adequate tool to look for the existence of triadic resonant interaction although it requires a large number of samples to converge. An example of bicoherence spectrum associated with the spectra of figure 3.12 is shown in figure 3.14, confirming the existence of triadic resonances involving the resonant modes, but also of some daughter modes.

### Spatial analysis of the modes in interaction

To further support our claim that the temporal power spectra present evidence for triadic resonant interactions, we extract from the PIV fields the structure at the peaked frequencies. The structure oscillating at frequency  $\omega$ , *i.e.* the Fourier component of the flow at this frequency  $\hat{\mathbf{u}}(\omega)$ , is extracted using the following operation:

$$\hat{\mathbf{u}}(\mathbf{r}; \omega) = \frac{1}{t_1 - t_0} \int_{t_0}^{t_1} \mathbf{U}(\mathbf{r}, t) e^{i\omega t} dt, \quad (3.16)$$

where  $t_0$  and  $t_1$  are the start and end times of a PIV recording and  $\mathbf{U}$  is the total velocity field measured in the rotating frame. The result of such a process is shown for several frequencies in figure 3.13. The spatial structures extracted at the peaked frequencies show a spatially periodic organisation which is typical of inertial modes. Comparison with theoretical structures remains nevertheless complicated because the viscous inertial modes of a tri-axial ellipsoid are not known theoretically and require complicated numerical computation (Vidal and Cébron, 2017; Vidal et al., 2017).

In addition, the ability of the paired modes to interact with the resonant one may be assessed by examining their principal azimuthal wave numbers. The latter is determined for a mode  $\hat{\mathbf{u}}(\mathbf{r}; \omega)$  by transformation into polar coordinates  $(r, \phi)$ , and Fourier transform along  $\phi$  to obtain the following decomposition of the mode:

$$\hat{\mathbf{u}}(r, \phi; \omega) = \sum_m \hat{\mathbf{u}}_m(r) e^{im\phi}. \quad (3.17)$$

Because the fluid container is not axisymmetric such decomposition necessarily comprises more than one wave number, but we can still identify the largest contributions to the azimuthal wave-number decomposition by computing the energy of the coefficients by radial

---

the frequencies  $\pm\omega_{1,2}$  and  $\pm 2$  are present so that a relation of the type  $\omega_1 + \omega_2 = \omega_0$  is also significant of triadic interaction.

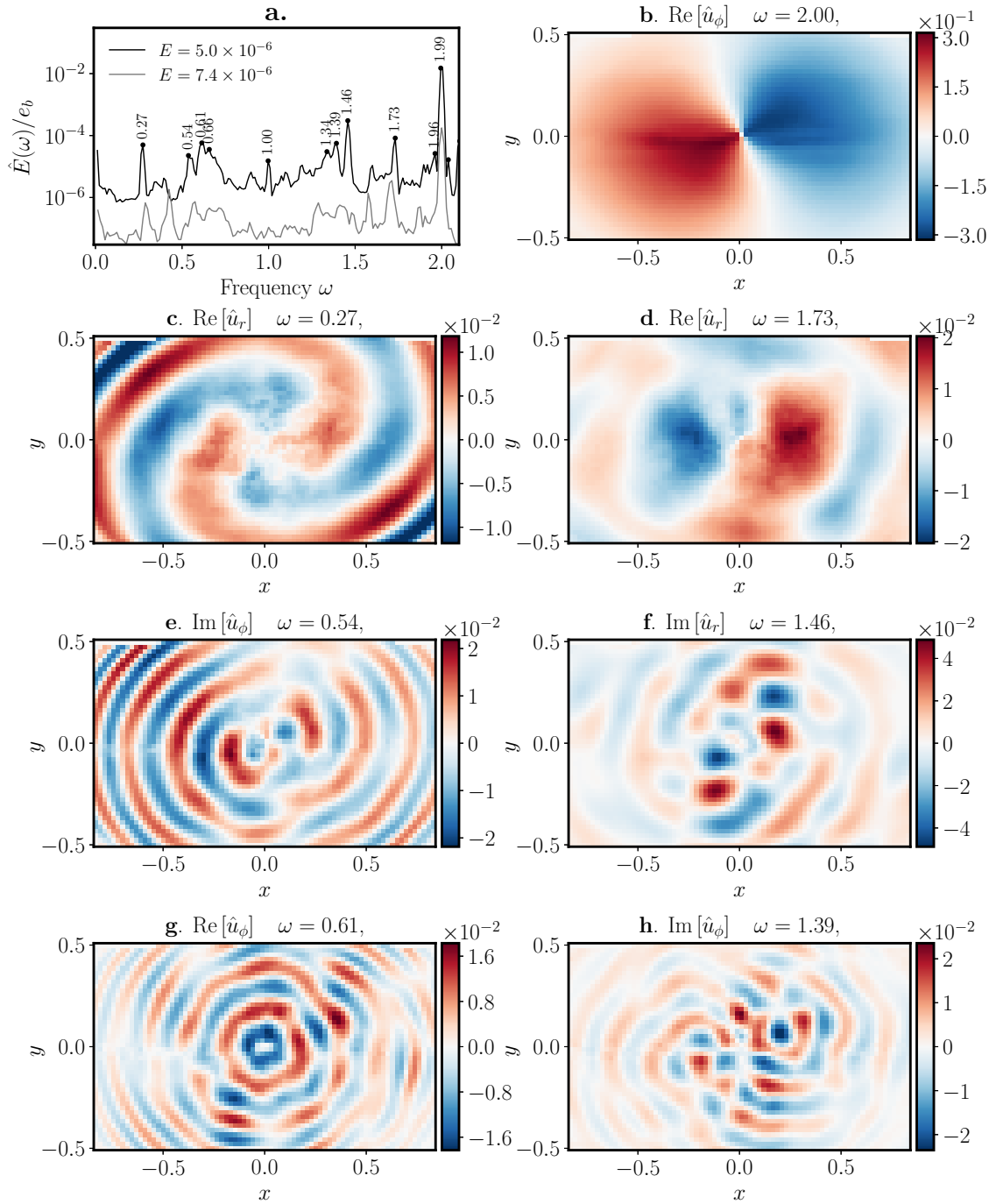


**Figure 3.13:** **a.** Power spectra with labelled peaks. The spectrum at  $E = 5.0 \times 10^{-6}$  is the same as in figure 3.12. The  $E = 7.4 \times 10^{-6}$  spectrum has been vertically shifted to facilitate the comparison. For the larger value of the Ekman number,  $Ro_i = 5.17 \times 10^{-2}$ . Several pairs of triadic resonance relation can be noticed, such as  $0.27 + 1.73$ ,  $0.54 + 1.46$ ,  $0.61 + 1.39$  and  $0.66 + 1.34$ . **b:** azimuthal component of the resonant wave in the horizontal plane accessible to PIV. **c to g:** pairs of structures  $\hat{\mathbf{u}}(\mathbf{r}; \omega)$  satisfying the triadic resonance condition on the frequency (relation (3.14)). For each frequency, including  $\omega = 2$ , we show the component which has the largest amplitude among the imaginary and real parts of the radial and azimuthal velocity. Lastly, in all velocity maps, distance is normalised by  $a$  and velocity by  $Ro_i a \Omega_0$ .

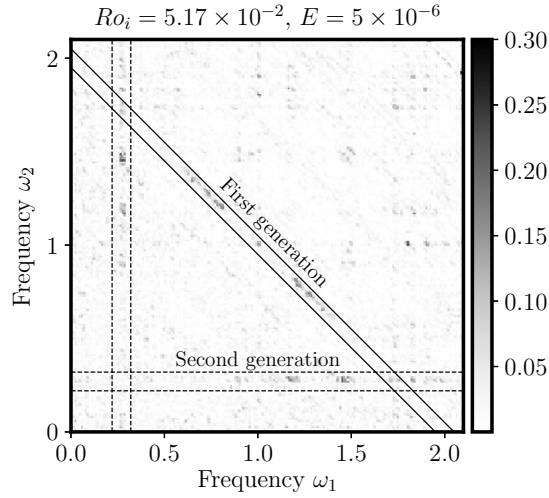


**Figure 3.14:** Bicoherence spectrum computed from local measurements in the saturation of the instability at a forcing amplitude  $Ro_i = 5.17 \times 10^{-2}$ , Ekman number  $E = 5.0 \times 10^{-6}$  and forcing frequency  $f = 4$ . It is computed using the formula (3.15). The plain lines frame the frequencies of the modes that are in resonant interaction with the unstable modes at  $\omega = 2$ . Other significant three mode interaction may be noticed between daughter modes for instance at frequencies  $\omega = 0.27$ ,  $\omega = 1.47$  and  $\omega = 1.73$  and are framed by dashed lines. Note that this map is symmetric under inversion of  $x$  and  $y$  coordinates.

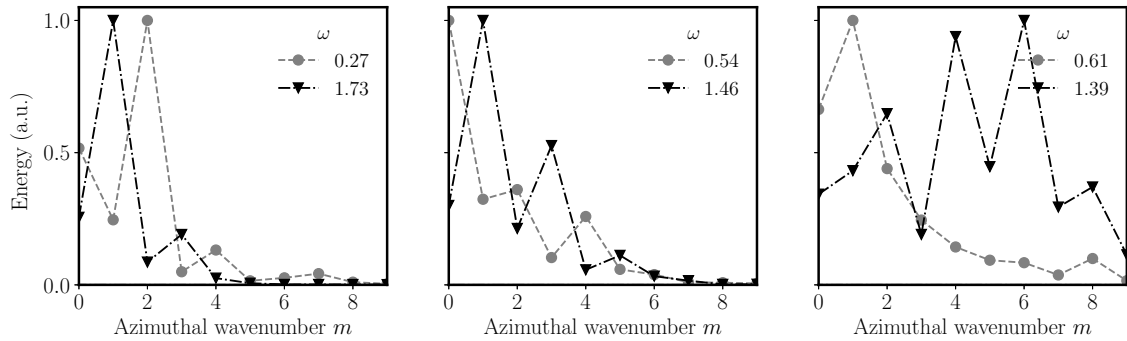


**Figure 3.15:** Computation of the azimuthal wavenumber decomposition —see formulae (3.17) and (3.18)— of the paired structures shown in figure 3.13. The energy contained in the wave numbers is shown in arbitrary units. Note that these maps are symmetric respective to  $m = 0$ , so that the energy contained in the  $m$  and  $-m$  modes is the same. For these structures to significantly interact with the resonant mode, the gap between the displayed principal wavenumbers numbers must be  $\pm 1$  —see relation (3.19)—, which is indeed observed for the first two pairs, but less obvious for the last one. Note that in the computation of the energy, the radial integration has been restricted to radii below  $0.25a$  although larger values do not change significantly the present decomposition.

integration, that is:

$$\int_{r < r_{\max}} |\hat{u}_m(r)|^2 r dr . \quad (3.18)$$

where  $r_{\max}$  is a maximum radius over which the integration is performed, here  $0.25a$ , which although larger values do not change significantly the mode decomposition. For instance, it is clear from figure 3.13b that the main azimuthal wave numbers of the resonant modes is  $m_i = \pm 1$ , in agreement with the selection rule (1.55) found in chapter 1 section 3.3. In three-modes interaction involving a mode with wave number  $m_i$  with two daughter modes with wave numbers  $m_{j,k}$ , a necessary condition for significant non-linear interaction is:

$$m_j + m_k = m_i \quad (3.19)$$

which is very similar to the condition on frequency (2.34). In the present case, the mode  $i$  is the resonant one, for which  $m_i = \pm 1$ , so that the difference between absolute value of the main wave numbers of paired modes should be  $\pm 1$ . The result of computing the azimuthal wave number decomposition is shown in figure 3.15, and is, at least for two pairs of modes, consistent with the relation (3.19).

Lastly, regardless of considerations on the azimuthal structures, it is striking in figure 3.13 that only modes with similar scales are observed to couple in triadic resonances. This is coherent with the fact that, as the resonant mode at  $\omega = 2$  has almost no horizontal variations, the two daughter modes must have matching horizontal wave numbers to ensure a significant overlap and efficient energy transfer.

### Inertial wave turbulence?

To conclude, the spatio-temporal analysis of the flow at low forcing amplitudes provides significant evidence that, in this regime, the non-linear saturation of the elliptical instability is a superposition of daughter waves that are in triadic resonant interaction with the unstable wave. This state is robust as the Ekman number is changed, provided the forcing remains small. It is reminiscent of the wave turbulence described in chapter 2 which occurs in media sustaining dispersive waves and allowing non-linear transfers between one another. Wave turbulence has been theoretically described for infinite, homogeneous media subject to a large-scale stochastic forcing in the vanishing forcing amplitude and dissipation regimes (Nazarenko, 2011). In this context, the forcing results in a continuum of waves in weakly non-linear resonant interactions translating in a cascade of energy through temporal and spatial scales.

One could argue that in the present set-up, some hypotheses of classical wave turbulence theory (Nazarenko, 2011) are not fulfilled. First, the flow is not statistically homogeneous in space, as we observe modes whose structures are influenced by boundaries. It is neither statistically homogeneous in time because the system is by essence forced at a single frequency. Lastly, as discussed above, dissipation is still too high and prevents energy cascade in a large range of scales. Some of these limitations are inherent to the experimental approach used here, but may be irrelevant in the asymptotic geophysical regime. The state we characterise in this section could be seen as discrete inertial wave turbulence (Kartashova, 2009), which may lead to inertial wave turbulence in the weak dissipation and forcing regime. Note also that none of the previous numerical or experimental set-ups studying rotating turbulence have yet reported a regime dominated by inertial waves only and without a dominant geostrophic

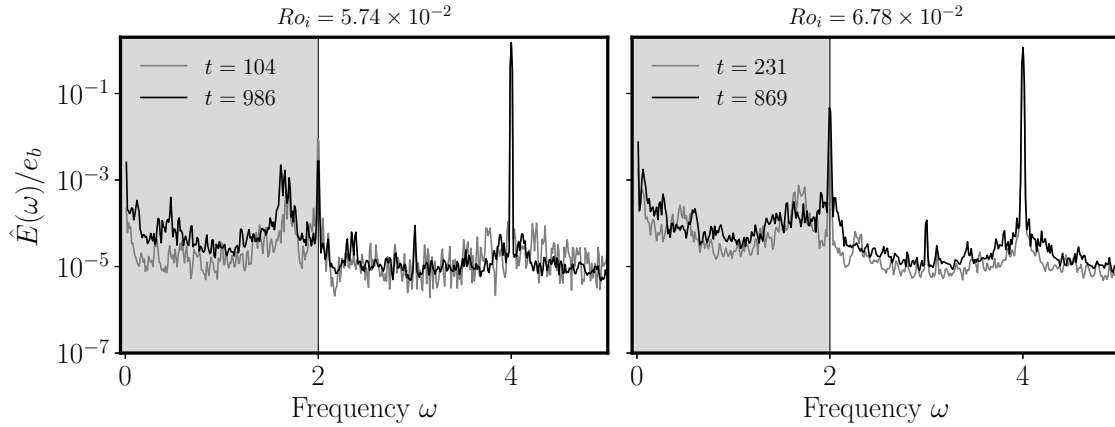


**Figure 3.16:** Temporal spectra of the saturation flow obtained at  $E = 5.0 \times 10^{-6}$  and  $f = 4$  with the same process as in figure 3.12, but with higher forcing amplitudes or  $Ro_i$  values. As earlier, the inertial wave domain is highlighted in grey, and the base flow and resonant peaks are clearly identifiable at  $\omega = 4$  and  $\omega = 2$  respectively.

component (see Godefert and Moisy (2015) for a review) as we observe here. We thus argue that this work is a first step towards reaching an inertial wave turbulence regime.

## 5. Large forcing amplitudes: a geostrophic-dominated regime

In this section, we detail our experimental finding that the wave-dominated regime vanishes at larger forcing amplitude and  $f = 4$ . This secondary transition is caused by the emergence of a strong geostrophic anticyclonic vortex that back-reacts on the structure of the waves. Our experimental set-up allows locating the secondary transition in the forcing-dissipation  $(Ro_i, E)$  plane and to find the existence domain of the wave-dominated regime. As earlier, our analysis starts by exploring the spectral content of the saturation flow. We then detail its shape and amplitude and how it affects the resonant modes.

### 5.1 Spectral content of the saturation flow at large forcing amplitude

We reproduce the temporal analysis of the saturation flow detailed in paragraph 4.2, now applied to the larger forcing experiments. Several striking changes appear in these power spectra displayed in figure 3.16 compared to what is obtained at lower forcing (see figure 3.12). First, the number of peaks in the inertial wave domain is reduced, and the remaining ones are wider. Moreover, the ratio between the background level and the forcing peak—at  $\omega = f = 4$ —increases with the forcing amplitude, thus suggesting that the flow becomes more turbulent. Lastly, the gap between the mean flow—at  $\omega = 0$ —and the resonant mode reduces from two to less than one order of magnitude between low (figure 3.12) and large forcing.

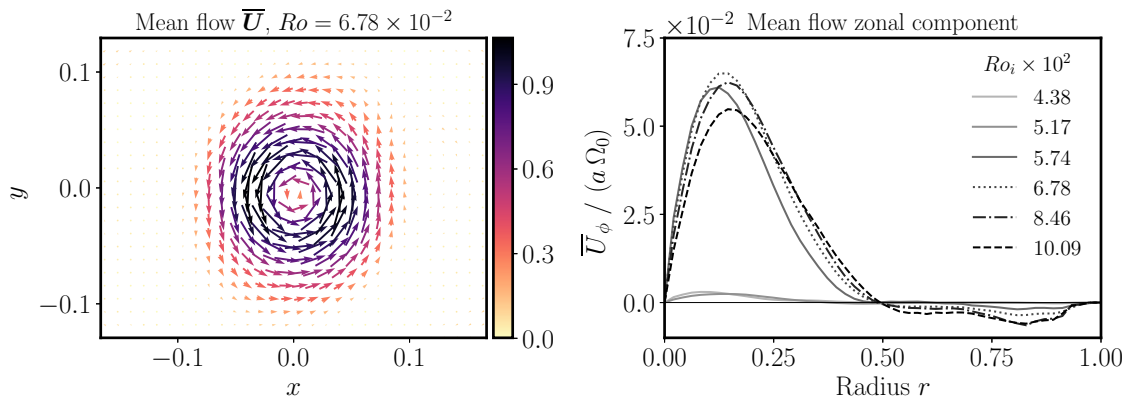


**Figure 3.17:** **Left:** mean flow  $\bar{\mathbf{U}}$  extracted by averaging the saturation flow observed for  $f = 4$  at an Ekman number  $E = 5.0 \times 10^{-6}$  and an input Rossby number  $Ro_i = 6.78 \times 10^{-2}$ . The colorscale of the arrows gives the norm of the velocity, normalised by the base flow velocity  $Ro_i\Omega a$ . The rotation of the turntable being clockwise, the observed vortex is an anticyclone. Lengths are normalised by  $a$ . **Right:** zonal average of the mean flow orthoradial velocity at the same Ekman number; it is normalised by  $a\Omega_0$ , independently of  $Ro_i$ , which enhances the dramatic change of mean flow.

It is thus clear that the saturation flow has transitioned towards another regime: the many triadic resonances that clearly appeared in the inertial modes domain in figures 3.12 and 3.13 are no longer present.

## 5.2 The emergence of a strong geostrophic anticyclonic vortex

The key to the transition out of the wave-dominated regime is the rise of the geostrophic mean flow amplitude, a feature noticed in figure 3.16. The aim of the present paragraph is to explain the properties of this particular component of the saturation flow and to quantify its evolution when the forcing amplitude, or equivalently  $Ro_i$ , is changed.

The geostrophic component of the flow is extracted by time averaging the velocity fields over a sufficiently long time period. It is found that 5 rotation periods are sufficient to average a representative mean flow, although we perform the averaging operation over the full length of a recording, which typically ranges from tens to about a hundred rotation periods.

A typical view of the mean flow is given in the left panel of figure 3.17. Regardless of the forcing amplitude and the rotation rate, the mean flow  $\bar{\mathbf{U}}$  always adopts the shape of an anticyclonic zonal wind, *i.e.* a stationary flow with mostly azimuthal velocity and which rotates counter-clockwise—while the rotation of the turntable is clockwise. To better quantify the structure and the amplitude of the meanflow  $\bar{\mathbf{U}}$ , we consider its zonal average  $\bar{U}_\phi(r)$ , defined as :

$$\bar{U}_\phi(r) = \frac{1}{2\pi} \int_{\phi=0}^{2\pi} \bar{\mathbf{U}} \cdot \mathbf{e}_\phi \, d\phi . \quad (3.20)$$

It is computed by dividing the PIV field in concentric rings of radius  $r$  and averaging the quantity  $\bar{\mathbf{U}} \cdot \mathbf{e}_\phi$  on each ring. This zonal average is pictured in figure 3.17 right. There exists a clear transition from the lowest values of the input Rossby number  $Ro_i \leq 5.28 \times 10^{-3}$  with very weak vortex amplitude to larger values where a strong mean flow develops. A similar strong anticyclonic vortex was also observed by Favier et al. (2015) and Grannan et al. (2014) in the

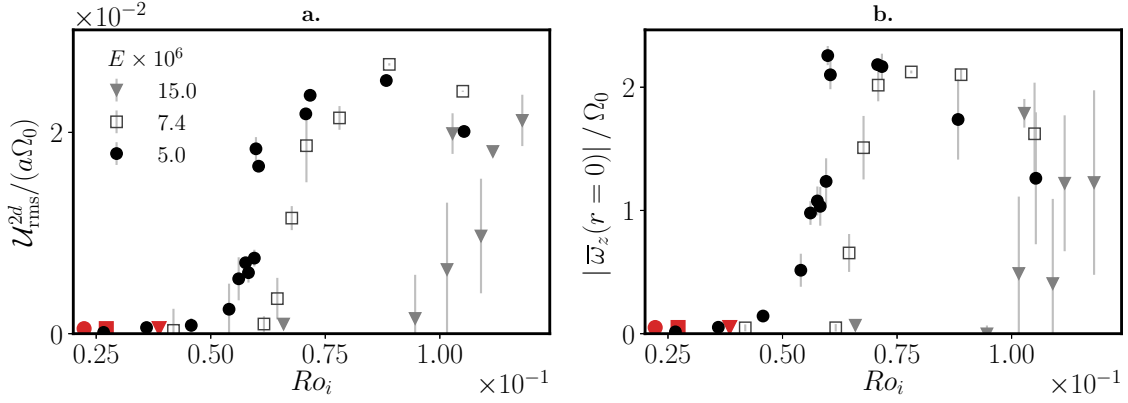


**Figure 3.18:** **a:** experimental measurements of the root mean square value  $\mathcal{U}_{\text{rms}}^{2d}$  of the mean flow, defined in equation (3.21), as a function of the input Rossby number  $Ro_i$ ; it is normalised by  $\alpha\Omega_0$  instead of  $Ro_i\alpha\Omega_0$  which is an independent of  $Ro_i$  quantity. The red symbols materialise the approximate critical Rossby number of the elliptical instability  $10\sqrt{E}$  at the Ekman number corresponding to the shape of the symbol. **b:** experimental measurements of the central vorticity of the mean flow  $\bar{\omega}_z(r=0)$ —see formula (3.22)—as a function of  $Ro_i$ . It is normalised by the rotation rate  $\Omega_0$ . Note the the mean flow is an anticyclonic vortex and has therefore a vorticity in the opposite direction to the rotation rate's. For both panels, the error bars indicate the typical variability in the saturation phase by computing the standard deviation of  $\mathcal{U}_{\text{rms}}^{2d}$  and  $\bar{\omega}_z(r=0)$  when more than one data set was available.

turbulent saturation of the libration-driven elliptical instability, at Ekman numbers ranging from  $5 \times 10^{-5}$  to  $10^{-4}$  and at a single input Rossby number  $Ro_i = 0.272$ .

To further quantify the existence of a transition, we introduce two diagnostic quantities. The first one is the root mean square value of the mean flow  $\mathcal{U}_{\text{rms}}^{2d}$  defined as:

$$(\mathcal{U}_{\text{rms}}^{2d})^2 = \langle \bar{U}^2 \rangle \quad (3.21)$$

where the brackets stand for average over the PIV field. The second one is the central vorticity of the mean flow to quantify the central rotation rate of the geostrophic vortex. The average radial vorticity profile  $\bar{\omega}_z(r)$  is computed as:

$$\bar{\omega}_z(r) = \frac{\bar{U}_\phi}{r} + \frac{d\bar{U}_\phi}{dr}. \quad (3.22)$$

Close to the centre, it is computed via fitting a 3rd order polynomial to the zonal velocity profile  $\bar{u}_\phi$  as those depicted in figure 3.17;  $\bar{\omega}_z(r)$  is then twice the first order coefficient of the polynomial fit.

The evolution of the mean flow rms and central vorticity is shown in figure 3.18. In both panels, a clear transition from a negligible amplitude mean flow to a strong mean flow is observed, with a critical Rossby number  $Ro_{i,c}$  depending on the Ekman number. It proves the existence of a secondary transition of the geostrophic anticyclone that builds on the turbulent saturation of the libration-driven elliptical instability.

Despite a regular increase below the secondary transition, after careful examination, the variations of the central vorticity with  $Ro_i$  do not match any scaling  $\bar{\omega}_z(r) \propto Ro_i^2$  that has been proposed and measured for mean flows driven by the viscous libration base flow alone (Busse, 2010; Sauret et al., 2010; Sauret and Le Dizès, 2013) or by non-linear self interaction of a single inertial waves in the laminar regime (Tilgner, 2007b; Sauret et al., 20140; Morize

et al., 20100). This shows the mean flow does not result from non-linear self-interaction in the boundary layer of simple structures such as the base flow or a single inertial mode.

For input Rossby numbers above the secondary transition, the central vorticity reaches a plateau at the value of  $\sim -2\Omega_0$ , meaning that the core of the vortex cancels out on average the rotation of the fluid. It is striking that the central vorticity saturates at this value for which anticyclones are marginally stable according to the Rayleigh criterion for centrifugal instability (Afanasyev and Peltier, 1998; Drazin and Reid, 2004). Such a saturation value emerging out of a turbulent saturation may be reminiscent of self-organised criticality (Bak et al., 1987), an idea that is for instance invoked in stratified turbulence where flows are thought to be maintained close to marginal stability respective to shear instability —see for instance Salehipour et al. (2018).

Beyond this plateau, a slight decrease of both the rms and the central vorticity of the mean flow is observed at higher  $Ro_i$ , at least for Ekman numbers  $E = 5.0 \times 10^{-6}$  and  $E = 7.4 \times 10^{-6}$ . It is possibly linked to a transition from rotating to isotropic turbulence as the input Rossby number draws closer to 1 (Yokoyama and Takaoka, 2017). As observed for instance by Barker and Lithwick (2013), increasing the amplitude of the forcing leads to the destabilisation of the strong vortices produced by the saturation of the elliptical instability. Nevertheless, in our set-up, the transition from a purely two-dimensional vortex to three-dimensional structures with possible vertical motion is difficult to further quantify and ultimately irrelevant for geophysical applications.

### 5.3 Building a regime diagram of the saturation flow

As noted in figure 3.18, the secondary transition between a wave-dominated and a geostrophic-dominated regimes is characterised by a sudden increase in the mean flow rms and vorticity. The critical value of  $Ro_i$  at which this transition occurs varies with the Ekman number. Our experiments therefore allow to propose a regime diagram of the saturation of the instability based on the mean flow diagnostic quantities.

We show in figure 3.19 the location of all the experiments that have been carried out at a forcing frequency of  $f = 4$  with different input Rossby numbers  $Ro_i$  and at different rotation rates or Ekman numbers —see table 3.2. The experiments below and above the secondary transition are discriminated by setting a threshold on  $\mathcal{N}_{rms}^{2d}$  to 15 % of the maximal value over all the experiments performed at the same rotation rate. This regime diagram reveals that the critical value of the input Rossby number for the secondary transition  $Ro_{i,c}$  follows a power law respective to the Ekman number, that is:

$$Ro_{i,c} \propto E^{1/2} \quad (3.23)$$

although a definitive power law would require a larger range of Ekman numbers. We also report for comparison in figure 3.19 the location of the control parameters explored by Grannan et al. (2014) and Favier et al. (2015) and the points at which they observed either a strong or weak vorticity mean flow. The location of the secondary transition they report is consistent with ours. Note however that the state they observed below the secondary transition could not convincingly be described as an inertial wave turbulence due to the larger values of the Ekman number and input Rossby number they explored: they barely saw one or two couples of daughter inertial waves; however, they definitely see a sharp transition in the amplitude of the mean flow.

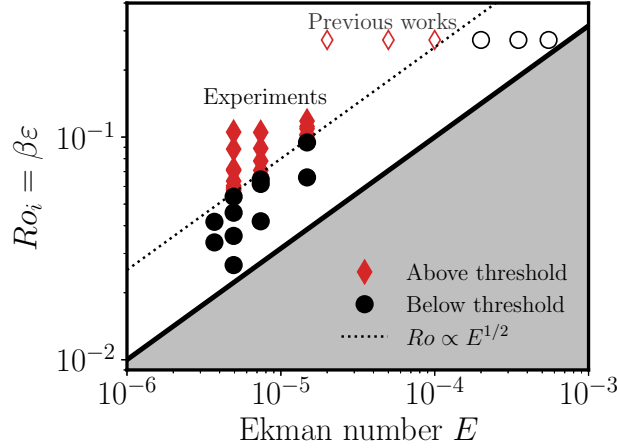


**Figure 3.19:** Experimental determination of the position of the secondary transition of the geostrophic vortex as a function of the Ekman number  $E$  and the input Rossby number  $Ro_i$ . The empty symbols stand for the control parameters of Favier et al. (2015) and Grannan et al. (2014) for which a central anticyclone similar to what is observed here is obtained in the non-linear saturation. As it can be noticed in the data of Favier et al. (2015) figure 5, there exists a sharp increase in the central vorticity; points below this transition are black and points above are red. To determine the location of the transition in our experiments, we consider that the threshold is reached when the energy of the mean flow is larger than 15 % of its largest value over a whole set of experiments carried out at the same Ekman number but different input Rossby numbers. Varying this threshold, say from 5% to 20 %, may change the nature of the points around the dashed line, but does not affect the overall trend for the separation between the two regimes.

## 5.4 Back-reaction of the geostrophic vortex on the resonant modes

As it may be noticed from the previous results, one of the striking consequences of the emergence of a strong geostrophic anticyclone is the loss of the numerous and well-defined triadic resonances detailed in the previous paragraph. The blurring of triadic resonances by geostrophic vortices is a well known feature of randomly-forced rotating turbulence: advection of inertial waves by these slowly evolving modes Doppler-shifts their frequencies and forces them out of resonant interaction (Campagne et al., 2015; Oks et al., 2017). Nevertheless, the present case is different from usual rotating turbulence since energy is only supplied to the system through a pair of inertial modes via the elliptical instability resonance. Besides, the vortex is persistent and drastically changes the local rotation rate of the fluid at the centre of the ellipsoid.

To better quantify the reaction of the waves to the existence of the strong anticyclone, we first consider the total vorticity  $2\Omega_0 + \bar{\omega}_z(r)$ , which is shown in figure 3.20, and where  $\bar{\omega}_z$  is determined with equation (3.22). There exists a radius below which the global vorticity remains significantly below  $2\Omega_0$ , at the core of the anticyclonic vortex. Once the secondary transition develops, the core of the anticyclone cannot sustain the resonant mode at  $\omega = 2$  since the maximal frequency cannot exceed the total vorticity. As a consequence, the radial structure of the resonant mode, which is constantly excited by the elliptical instability, changes as the secondary transition develops. This is illustrated in figures 3.20 and 3.21, where it appears clearly that the central amplitude of the resonant mode drops as the anticyclone emerges. Moreover, the spatial area affected by the drop in amplitude corresponds to the typical size of the vortex.

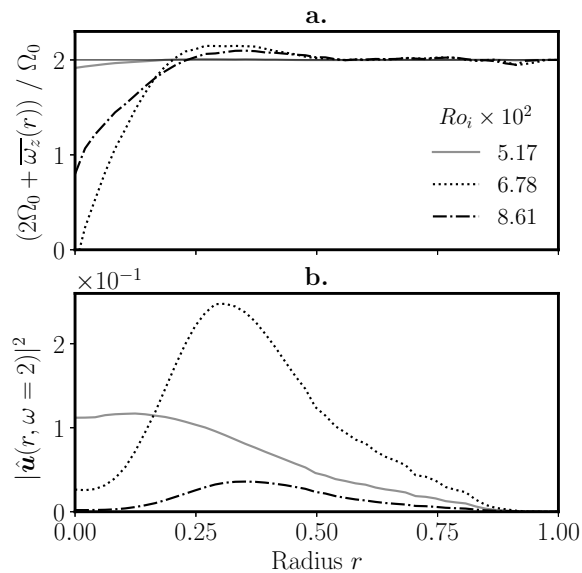


**Figure 3.20:** **a.:** Total vorticity  $2\Omega_0 + \bar{\omega}_z(r)$  of the fluid inside the ellipsoid as a function of the radius. **b.:** Local kinetic energy of the resonant mode at  $\omega = 2$  as a function of the radius. The energy is normalised by  $(Ro_i a \Omega_0)^2$  and the radius by  $a$ .

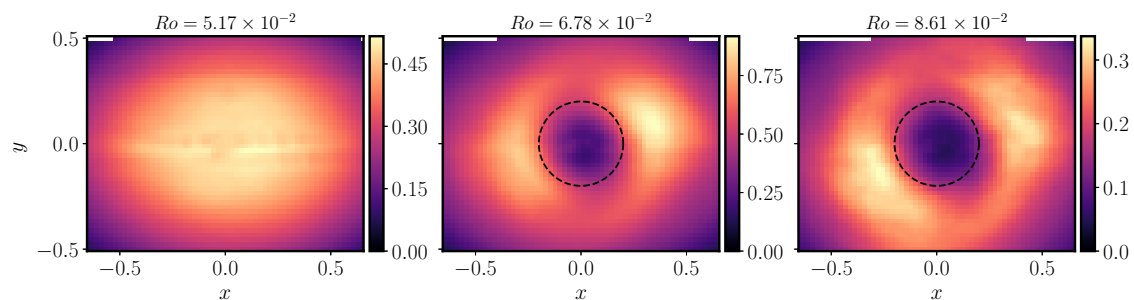


**Figure 3.21:** Resonant wave extracted by temporal filtering of the saturation field at  $\omega = 2$  below (**left**) and above (**centre and right**) the threshold of the secondary transition on the geostrophic anticyclone. The dashed circle materialises the radius at which the global vorticity is always below  $2\Omega_0$ , *i.e.*  $r/a \sim 0.2$  —see figure 3.20. The colorscale gives the norm of the velocity normalised by  $Ro_i a \Omega_0$ .

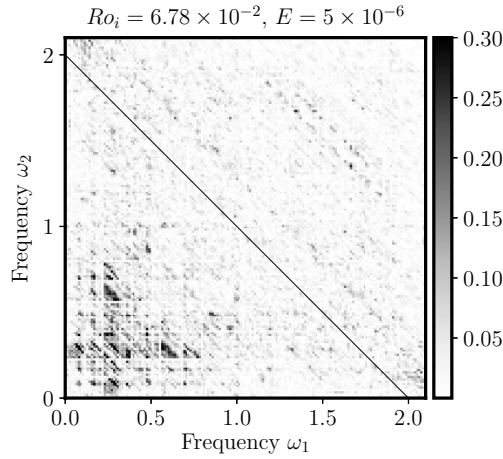


**Figure 3.22:** Bicoherence spectrum computed from local measurements in the saturation of the instability at a forcing amplitude  $Ro_i = 6.78 \times 10^{-2}$  and Ekman number  $E = 5.0 \times 10^{-6}$ . It is computed using the formula (3.15). The line materialises the frequencies of the modes that are in resonant interaction with the unstable modes at  $\omega = 2$ .

To conclude, the emergence of the secondary transition alters the spatial structure of the resonant modes. The strong anticyclone that emerges significantly alters the global vorticity, and hence the structure of inertial modes. If they still exist, triadic resonances cannot be the same as in the low forcing case since the structure of the modes has to account for the differential rotation introduced by the geostrophic flow. It is also interesting to note that despite the presence of the strong anticyclone, its localisation at the center of the ellipsoid ensures that the resonant mode persists outside the core of the vortex. As a consequence, the interaction between the libration base flow and the perturbation flow is maintained over time. For this reason, we do not observe cycles of growths and non-linear breakdowns provoked by the geostrophic flow detuning, as observed by Barker and Lithwick (2013) and discussed in chapter 2 section 3.1.

## 5.5 Triadic resonant interaction in the geostrophic saturation

The geostrophic anticyclonic vortex strongly affects the background rotation. Inertial modes with specific frequencies may still exist, but as proved in the previous section, their spatial structure must account for the presence of the strong mean flow. Non-linear three modes interactions could very well happen between these distorted modes, and we wish to investigate their existence using the bicoherence spectrum defined in relation (3.15). We show in figure 3.22 an example of bicoherence spectrum computed from local measurements in a typical experiment where geostrophic saturation is observed. Strong three modes interactions at lower frequencies are clearly revealed by this diagnostic quantity. The maxima of the bicoherence spectrum are rather widespread compared to the case of low forcing amplitudes (see figure 3.14). This larger spread of the interacting mode frequencies is not surprising: increasing the amplitude of the forcing and thus the amplitude of the modes leads to a larger number of near-resonant interactions, as it can be seen from the resonance condition (2.32) derived in chapter 2 section 2.3. We therefore show that the presence of the strong geostrophic flow does not disrupt the usual non-linear processes between modes, even though the structure of the modes has to account for the global modified rotation rate.

## 6. Discussion: the origin of the secondary transition

The spontaneous excitation of geostrophic structures by waves is a long standing issue in rotating fluid studies. As noted by Kerswell (1999), geostrophic vortices are always observed to emerge from non-linear interaction of waves in spite of the theorem proved by Greenspan (1969) stating that two inertial modes cannot transfer energy to vortices, at least in the asymptotic regime of low Rossby number. Direct and non-resonant excitation of strong zonal flows by non-linear self-interaction of inertial modes in the boundary layer have been characterised in simulations and experiments (Tilgner, 2007b; Sauret et al., 20140; Morize et al., 20100), but cannot be responsible for a sharp secondary transition, as the amplitude of the mean flow should be merely proportional to  $Ro_i^2$ . To explain the observation of strong geostrophic modes in rotating fluids, Kerswell (1999) and Smith and Waleffe (1999) proposed four-modes resonant instabilities. The inviscid growth rate of such instabilities is proportional to  $Ro^2$  where  $Ro$  is a Rossby number referring to the amplitude of the waves. As damping in a closed container is proportional to  $\sqrt{E}$ , the threshold Rossby number of the instability  $Ro_c$  follows a power law (Kerswell, 1999):

$$Ro_c \propto E^{1/4} . \quad (3.24)$$

Assuming that the saturated amplitude of the waves scales linearly with  $Ro_i$  in the non-linear regime of the elliptical instability, the threshold we observe in figure 3.19 for the secondary transition is inconsistent with the scaling (3.24). One possibility is that the dissipation of the mode in the range we explore is in  $E$  —*i.e.* volumic— instead of  $E^{1/2}$  —parietal—, a situation that has been reported for instance by Lemasquerier et al. (2017) but at slightly higher Ekman numbers and in the presence of a solid inner core. The scaling (3.24) would still apply in the planetary limit.

Another plausible way to explain the observed scaling may be that the secondary transition we detail in the present chapter is caused by finite Rossby effects. In particular, a helical wave structure under an insufficient rotation rate could be unstable to shear-driven instabilities since they contain inflection points (Drazin and Reid, 2004). The growth rate of such a secondary instability would then be proportional to the amplitude of the wave, *i.e.* to the Rossby number. Additional theoretical studies are needed to conclude on that matter, and will be carried out in the next chapters.

## 7. Another forcing frequency, $f = 2.5$

We wish to compare the results obtained in the previous sections at  $f = 4$ , and in particular to probe the existence of a secondary transition, at other forcing frequencies. It is, in general, a difficult task to find a frequency for which we observe a resonance of a mode with mostly horizontal velocities and which is not a large-scale mode.  $f = 4$  has all these characteristics, and although the horizontal structure of the resonant modes is large scale, it comprise  $\sim 5$  horizontal layers of alternating velocities in the vertical direction. Interesting behaviours were for instance observed at  $f = 1.53$  but because of large vertical velocities, the flow measured via the PIV algorithm in the equatorial plane was of unsatisfying quality. In this

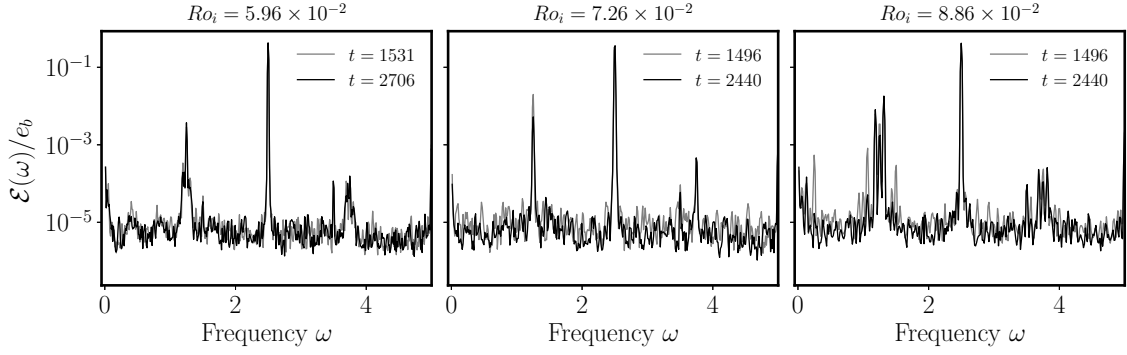


**Figure 3.23:** Ensemble average of temporal power spectra for a set of experiments at different  $Ro_i$  for a libration frequency  $f = 2.5$  and an Ekman number  $E = 5.0 \times 10^{-6}$ . The frequency  $\omega$  is given in rotation units. The construction and normalisation of these power spectra are identical to those used in figure 3.12. The principle peaks are  $\omega = f = 2.5$  corresponding to the forcing flow and the peaks around  $\omega = 1.25$  which correspond to resonant waves. Note that the precise frequency of the resonant waves at  $Ro_i = 8.86 \times 10^{-2}$  are specified in figures 3.24 and 3.25.

chapter we focus on the saturation observed at  $f = 2.5$  and an Ekman number  $E = 5.0 \times 10^{-6}$  which meets at least the horizontal velocity requirement.

## 7.1 Spatial and temporal analysis of the flow

### Temporal content of the saturation flow and variations with $Ro_i$

In order to draw comparisons with what has been obtained in the previous case  $f = 4$ , we first introduce the ensemble averaged temporal power spectra that are computed at three different input Rossby numbers; they are shown in figure 3.23. Sharp peaks corresponding to the forcing frequency  $\omega = f = 2.5$  and the resonant modes  $\omega \sim 1.25$  clearly appear in these power spectra. Nevertheless, several differences can be spotted compared to the case  $f = 4$ . First, apart from the peaks, the background noise level does not increase with the Rossby number as it has been previously observed. This means that turbulence and the associated creation of smaller scales does not develop as the input Rossby number  $Ro_i$  is increased. The second difference is that the spectra enrich in sharp peaks when  $Ro_i$  is increased, which is a reversed evolution compared to the case  $f = 4$ .

### Spatial structure of the resonant modes

To improve our understanding of the saturation flow, we extract in the case  $Ro_i = 8.86 \times 10^{-2}$  the different structures associated with a sharp peak in the inertial modes range, *i.e.* the temporal Fourier components  $\hat{u}(\mathbf{r}; \omega)$  of the velocity field at these specific frequencies. The result of such a process is shown in figure 3.24. Two main pairs of resonant modes are identified:

- $\omega = \pm 1.25$  such that  $2\omega = f$ ;
- $\omega_1 = 1.18$  and  $\omega_2 = 1.31$  such that  $\omega_1 + \omega_2 = 2.49$ .

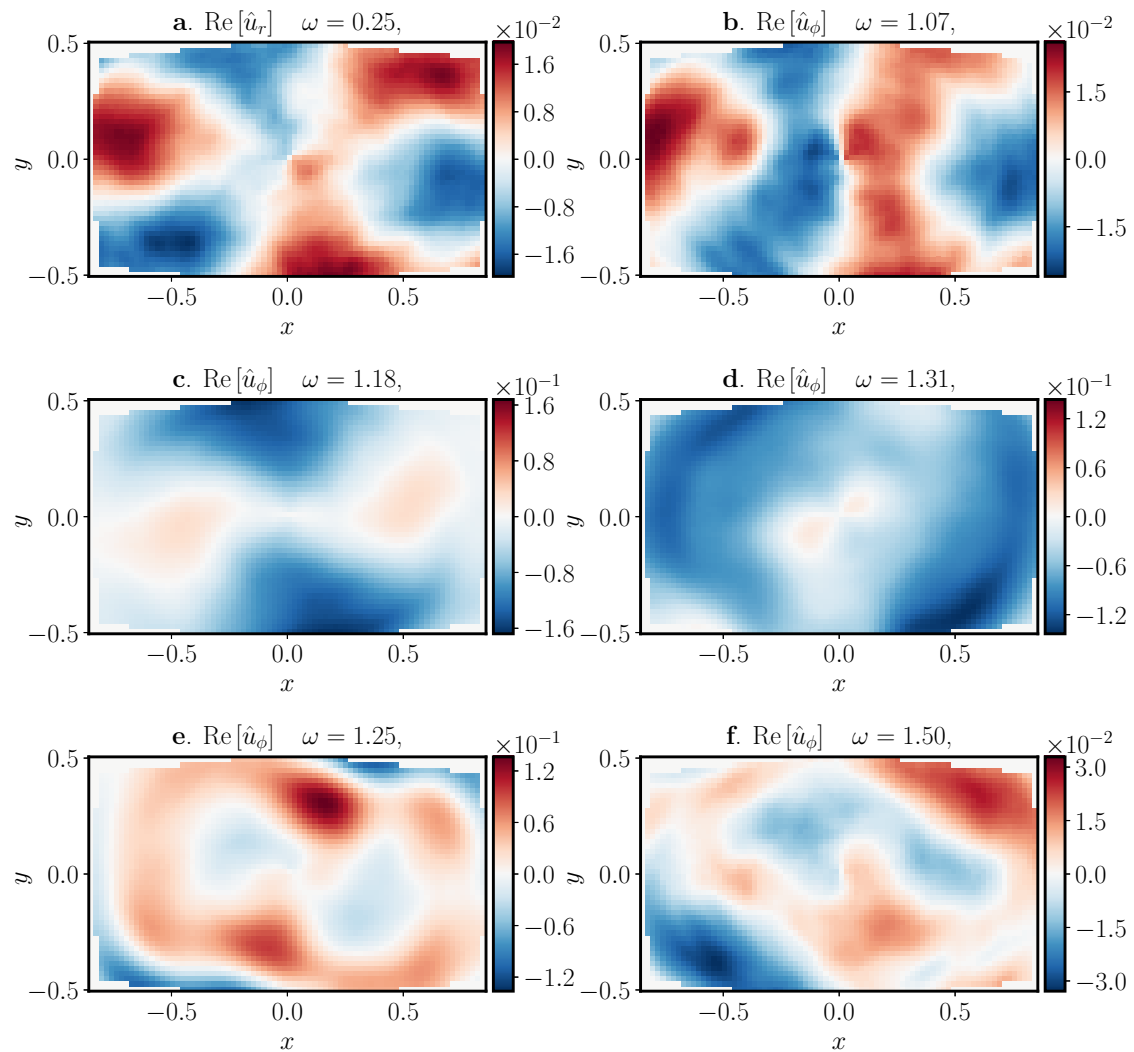


**Figure 3.24:** Result of the temporal filtering of the PIV fields at the peaked frequency observed in the temporal spectrum displayed in figure 3.23 for  $Ro_i = 8.86 \times 10^{-2}$ . The real part of either the azimuthal or radial component of the flow is pictured depending on which component is the largest, and it is scaled by the typical velocity  $Ro_i a \Omega_0$ , and lengths are scaled by  $a$ .

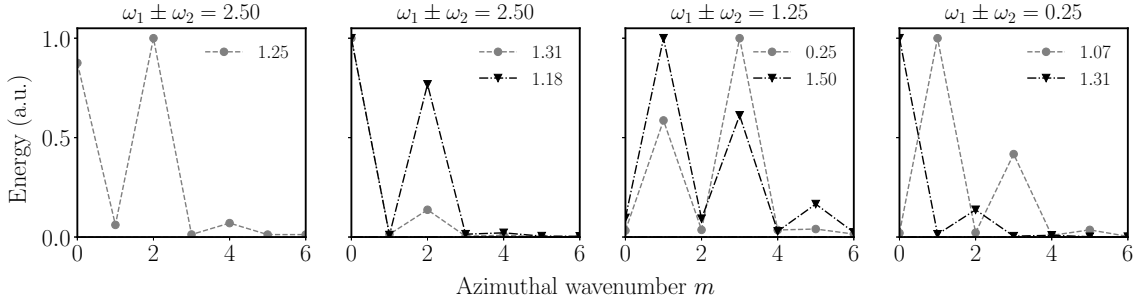


**Figure 3.25:** Azimuthal mode decomposition of pairs of modes in interaction with a third structure. The frequencies of the pair are given in the legend of the plots, and the frequency of the third structure, *i.e.* the sum of the frequencies of the two modes, is recall in the title of each plot. Note that these graphs are symmetric respective to  $m = 0$ . The two lefts panels are targeted at modes in resonance with the base flow. For the particular case where only the frequency 1.25 is given, the resonant structure (a superposition of  $m = 0$  and  $m = 2$  modes) interacts with itself and the  $m = 2$  libration flow. The two right panels are focused on daughter modes triadic interactions. We find that frequency combination  $1.50 - 0.25 = 1.25$  is consistent with wave number combination  $-1 + 3 = 2$ ; similarly frequency combination  $1.31 - 1.07 = 0.25$  is consistent with wave number combination  $0 - 1 = -1$  or  $0 - 3 = -3$ .

Computing their azimuthal wave number decomposition further supports that they are indeed in interaction with the libration flow with wave number  $m = 2$  (see figure 3.25). These primary modes are themselves involved in triadic resonant interaction with modes at frequencies  $\omega = 0.25, 1.07$  and  $1.50$ , which is also confirmed by their azimuthal wave number decomposition (see figure 3.25). We also note that all the extracted modes have large scale spatial structures, in particular the resonant modes. To explain the absence of turbulence attested in the temporal spectra (figure 3.23), one possibility is that the typical scale at which the energy is injected is too large to drive shear instability producing smaller scales. We observe instead the emergence of an increasing number of daughter modes via triadic resonances with increasing non-linearity, or equivalently  $Ro_i$ .

## 7.2 The mean flow

Using the same methods as in the preceding  $f = 4$  case, we compute the mean flow, its rms velocity and its central vorticity. The vector fields extracted for the three values of the input Rossby number are shown in figure 3.26. Although the core of the mean flow is again an anticyclonic vortex, its overall structure appears to be more complex than what has been observed at  $f = 4$ . It comprises bands of alternating velocity, the most striking example being the mean flow measured at  $Ro_i = 8.86 \times 10^{-2}$ .

To further quantify the properties of the mean flow as  $Ro_i$  is varied, we show in figure 3.27 its rms value and central vorticity. Despite the low number of points, the evolution of both quantities with  $Ro_i$  is no match with the  $f = 4$  case: the mean flow does not exhibit any instability type of behaviour. The rms velocity of the base flow always has significant values whose order of magnitude is similar to what has been observed at  $f = 4$  when the secondary transition has fully developed. Despite these quite large rms amplitudes, the dimensionless central vorticity never reaches the critical value  $-2$ . Unfortunately, lower forcing amplitudes were not explored and it is not possible to conclude whether a secondary transition is observed at lower  $Ro_i$ .

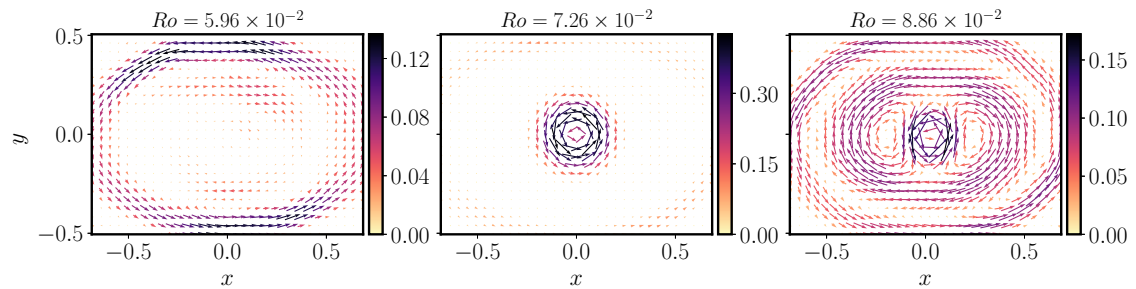


**Figure 3.26:** Vector field of the mean flow at  $f = 2.5$  and an Ekman number  $E = 5.0 \times 10^{-6}$ , for an increasing input Rossby number  $Ro_i$ . The colour scale of the arrows gives the norm of the velocity scaled by  $Ro_i a \Omega_0$ .

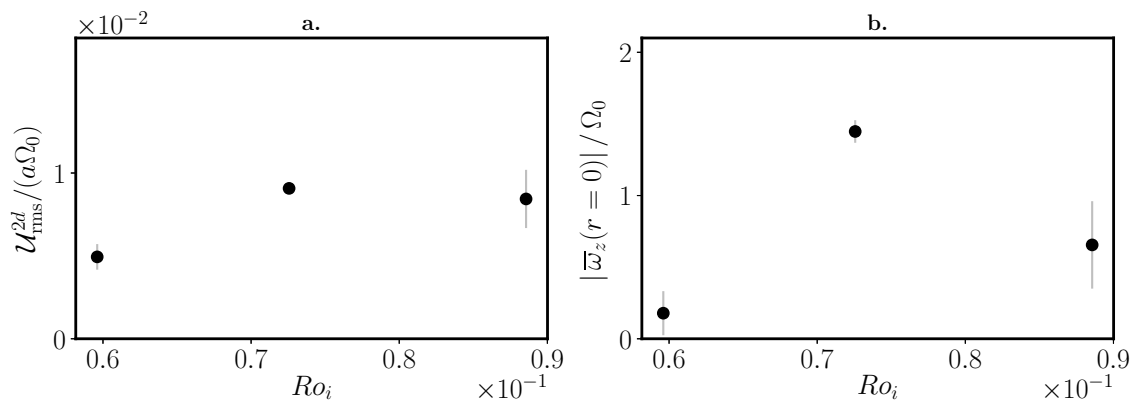


**Figure 3.27:** **a:** experimental measurement of the root mean square value of the mean flow, based on the measurement of the total kinetic energy of the mean flow. It is compared to the typical rotation velocity  $a\Omega_0$ , as in figure 3.18. **b:** experimental measurements of the central vorticity of the mean flow, normalised by the rotation rate  $\Omega_0$ . As in the case  $f = 4$ , the central vortex is always anticyclonic so that  $\bar{\omega}_z(r=0)$  and  $\Omega_0$  are of opposite signs.

Even if the mean flow does not emerge from an instability, its origin is also difficult to conciliate with direct forcing mechanisms (Tilgner, 2007b; Morize et al., 20100; Sauret et al., 20140). If the geostrophic mean flow was only driven by non-linear self-interaction of a particular mode, its shape would not change with the Rossby number, and the central vorticity should follow a quadratic trend with  $Ro_i$ . None of these features are observed in figures 3.26 and 3.27. One possibility is that each mode drives a geostrophic flow through non-linear interactions in the boundary layer, and the total mean flow results from the superposition of the ones driven by each mode, provided it does not alter too much the local rotation rate. As a result, when  $Ro_i$  is increased to  $8.86 \times 10^{-2}$ , the many different modes force a resulting mean flow with a more complex structure. Nevertheless, further experiments or numerical simulations are needed to clarify the origin of the mean flow.

### 7.3 The saturation scenario at $f = 2.5$

This forcing frequency is rather complicated to link with the study at  $f = 4$ . On one hand, the observation of triadic resonant interactions associated to narrow peaks in the temporal spectra of the flow suggests that the non-linear saturation of the instability is below the secondary transition observed in the  $f = 4$  case. On the other hand, the geostrophic flow has a significant amplitude and vorticity which is similar to those observed above the secondary transition in the  $f = 4$  case. We may thus formulate three hypotheses for the saturation scenario in the case  $f = 2.5$ . The first one, supported by the rather large amplitude of the geostrophic flow, is that the secondary transition occurs below the forcing amplitudes here considered. It is then difficult to conciliate our experimental result with the idea that shear instability drives the secondary transition since, conversely to the case  $f = 4$ , all the extracted modes are large scale. As a consequence, the secondary transition should be located at higher forcing amplitude compared to the  $f = 4$  threshold  $Ro_i \sim 6 \times 10^{-2}$ . The second hypothesis is that the transition occurs above the  $Ro_i$  range featured in the present section, which is supported by the increased number of daughter wave generation by triadic resonance as  $Ro_i$  is increased. The driving mechanism for the mean flow could be direct forcing by the waves via interaction in the viscous boundary layer (Tilgner, 2007b; Morize et al., 20100; Sauret et al., 20140). It is, however, difficult to confirm this hypothesis: the structure of the mean flow varies with the forcing amplitude and there is no simple scaling between  $Ro_i$  and the rms of the mean flow. The last hypothesis that should also be considered is that there is no secondary transition in the case  $f = 2.5$ . The universality of the secondary transition and its origin will be questioned in the next chapters. In any case, more experiments are needed to confirm which of these three hypotheses is adequate.

## 8. Conclusion

Throughout this chapter, we have explored the non-linear fate of the libration-driven elliptical instability in low dissipation and low forcing regimes. Despite it being mostly focused at one particular forcing frequency,  $f = 4$ , we believe it brings some clarifications regarding the dichotomy between wave-dominated and vortex-dominated types of saturation and their conditions of existence. The main result of our work is to prove the existence of a regime dominated by inertial waves in triadic resonance interactions at low forcing am-

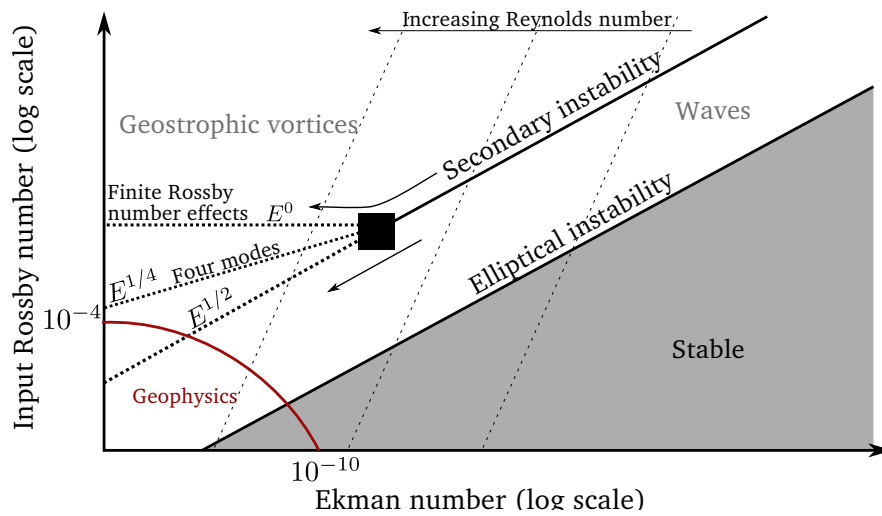


**Figure 3.28:** Schematic regime diagram of the saturation of the elliptical instability proposed after the present experimental study, depending on the Ekman number  $E$  and the input Rossby number  $Ro_i$ , building on figure 3.19. In particular, we place the geophysically relevant regime at low  $E$  and  $Ro_i$ . The elliptical instability threshold shown here is associated to a viscous damping rate dominated by wall boundary layer friction corresponding to a  $Ro \propto E^{-1/2}$  line. We report the possible behaviour of the limit between the geostrophic-dominated and the wave-dominated regimes at low  $E$  and  $Ro_i$  with the dotted lines: the case where the secondary transition would be a finite Rossby number effect ( $E^0$  line), the case where the four mode interaction causes the transition ( $E^{-1/4}$  line) and lastly the continuation of what is observed here ( $E^{-1/2}$  line). We also draw thin dashed lines for which the Reynolds number  $Re = Ro_i/E$  is constant, and the direction in which it increases.

plitude, *i.e.* a—discrete—inertial wave turbulence regime. Such a regime vanishes with increasing forcing amplitudes due to a secondary transition causing the emergence of a strong geostrophic anticyclone altering the inertial modes' structure. This transition sets the limits of the wave-dominated regime: it allows drawing a regime diagram of its existence depending on the dissipation and the forcing amplitude. We hence find that the wave-dominated regime, which is a precursor of inertial wave turbulence, is the relevant one for geo- and astrophysical applications, as planets subject to the elliptical instability are usually close to the primary instability threshold (Cébron et al., 2012a). It is the first time that a wave-dominated and a geostrophic-dominated regimes are observed within a single experimental set-up by changing one control parameter only. Note that transition from two-dimensional to three-dimensional rotating turbulence has been observed at high forcing amplitude, close to the point where non-linear effects and the Coriolis force are of similar importance (Barker and Lithwick, 2013; Alexakis, 2015; Yokoyama and Takaoka, 2017). We cannot propose a complete description of secondary transition with the presently available data. Investigation of secondary instability of inertial modes is carried out in chapter 4.

We propose a general non-linear saturation regime diagram in figure 3.28 based on our experimental study, and in particular on the results of figure 3.19. In the case where the geostrophic instability is caused by finite Rossby number effects, there should exist a critical input Rossby number below which only the wave-dominated regime is observed. If due to four-modes interaction (Kerswell, 1999; Smith and Waleffe, 1999), in the asymptotic regime of low dissipation, the secondary transition should follow a  $Ro_{i,c} \propto E^{1/4}$ . We also report in this diagram that drawing closer to the geophysical regimes is also associated with an increase of the input Reynolds number  $Ro_i/E$ . The saturation of the elliptical instability in planetary

cores and in stellar interiors should therefore be more turbulent than what is observed here. In particular, instead of the few secondary modes generated by triadic resonance that we report in this chapter, it is expected that a very large number of them should be excited in the form of inertial wave turbulence. This will be further explored with numerical modelling in chapter 6.

# Chapter 4

## Finite wave amplitude instabilities

### 1. Introduction: the geostrophic problem

In the preceding experimental study, we found a secondary instability of a geostrophic anticyclone which grows during the turbulent saturation of the elliptical instability. As explained in the introduction, according to the theorem of Greenspan (1969), geostrophic modes cannot be involved in resonant triads and should not undergo instability growing on time scale of order Rossby. Nevertheless, geostrophic modes are often observed to take over flows in which energy is supplied through waves (Kerswell, 1999), and our experiments are further evidence supporting this observation. To resolve this paradox, Kerswell (1999) and Smith and Waleffe (1999) have proposed four-modes interaction mechanisms to explain geostrophic instabilities. Noting  $Ro$  the dimensionless amplitude of waves ( $Ro$  is the Rossby number associated to the waves), the inviscid growth rate of the quartet instability is proportional to  $Ro^2$ . Instead of four-modes interaction, Smith and Lee (2005) have proposed that near-resonant triadic interactions are responsible for significant energy transfers towards geostrophic modes.

In this chapter, we propose to re-evaluate the wave-vortex interaction in the light of our experiments. We have indeed revealed in chapter 3 a secondary transition associated to the emergence of a strong geostrophic anticyclonic vortex, possibly due to an instability. According to the regime diagram displayed in figure 3.19, the input Rossby number threshold  $Ro_{i,c}$  of this instability follows a power law  $Ro_{i,c} \propto E^{1/2}$ . Assuming that the viscous damping of the resonant modes follows a  $\sqrt{E}$  law, this result indicates that the inviscid growth rate of the instability is proportional to the Rossby number of the saturation flow  $\sim Ro_i$ . In the present chapter, we explore with an idealised model the existence of instabilities driven by inertial waves and involving a geostrophic mode growing with a rate proportional to the wave amplitude. If such instabilities exist, they should however vanish when the amplitude of the waves is decreased to 0, and must therefore occur only at finite wave amplitude.

## 2. Investigating a single wave instability

### 2.1 Hypotheses and equations

The aim of this study is to investigate the stability of a single plane inertial wave  $U_w$  with eigen frequency  $\omega_0$  which writes:

$$U_w = \mathbf{h}_k e^{i(\mathbf{k} \cdot \mathbf{x} - \omega_0 t)} \quad (4.1)$$

where  $\mathbf{h}_k$  is a helical mode with  $s = 1$  (see chapter 2 section 2.1). We remind that  $U_w$  satisfies the linearised Euler equation including the Coriolis force:

$$\partial_t U_w + 2\boldsymbol{\Omega} \times U_w = -\nabla p_w, \quad (4.2)$$

and is even a non-linear solution since  $U_w \cdot \nabla U_w = i(\mathbf{k} \cdot U_w)U_w = 0$  and  $\mathbf{k} \cdot \mathbf{h}_k = 0$  for an incompressible plane wave.  $\omega$  and  $\mathbf{k}$  are related by the dispersion relation of inertial waves:

$$\omega_0 = 2\Omega \frac{k_z}{k}. \quad (4.3)$$

We investigate the stability of this inertial wave via solving the time evolution of perturbations  $\mathbf{u}$  to the wave  $U_w$ . The total flow writes  $U_w + \mathbf{u}$ , and as  $U_w$  is solution of the Euler equation, the dimensionless equations driving the dynamics of the perturbations are:

$$\begin{cases} \partial_t \mathbf{u} + Ro (U_w \cdot \nabla \mathbf{u} + \mathbf{u} \cdot \nabla U_w) + \mathbf{u} \cdot \nabla \mathbf{u} + 2\mathbf{e}_z \times \mathbf{u} &= -\nabla p + E \nabla^2 \mathbf{u} \\ \nabla \cdot \mathbf{u} &= 0 \end{cases} \quad (4.4)$$

where time is scaled by  $\Omega^{-1}$  and length by a typical domain size  $L$ . We have introduced the Ekman number  $E$  which compares viscosity and Coriolis force, and an input Rossby number  $Ro$  which quantifies the dimensionless amplitude of the plane wave. To derive the equations (4.4), we have taken into account the fact that  $U_w$  is a solution of the Euler equation, and we have assumed that its dissipation is compensated by a suitable body force to facilitate the study of its stability.

We choose to work mostly with a wave with  $\mathbf{k} = 2\pi [4, 0, 8]$ . This particular wave has been introduced by Embid and Majda (1998) and used by Smith and Waleffe (1999) as an adequate mode to study waves non-linear interactions as it is involved in an exact triadic resonance with the modes  $2\pi [-6, 0, 3]$  and  $2\pi [10, 0, 5]$ . Note that in the present problem four modes interactions cannot be observed since only one wave is maintained (Smith and Waleffe, 1999).

### 2.2 The SNOOPY code

To solve this equation, we use the code SNOOPY developed by Lesur and Longaretti (2005). It is a pseudo-spectral code which solves to full Navier-Stokes equation including rotation in a box with periodic boundary conditions.

The velocity and pressure fields  $\{\mathbf{u}, p\}$  are decomposed into plane waves such that:

$$\{\mathbf{u}, p\} = \sum_q \{\hat{\mathbf{u}}_q, \hat{\Pi}_q\} e^{iq \cdot \mathbf{x}}. \quad (4.5)$$

Calling  $L_{x,y,z}$  the size of the box in the  $x, y, z$  directions, the vectors  $\mathbf{q}$  are such that:

$$\mathbf{q} = 2\pi \left( \frac{n_x}{L_x}, \frac{n_y}{L_y}, \frac{n_z}{L_z} \right) \quad (4.6)$$

where  $n_{x,y,z}$  are integers ranging from 0 to  $N_{x,y,z}$  the resolution of the simulation in each direction. The Navier-Stokes equation is then solved as a dynamical system comprising of  $N_x \times N_y \times N_z$  coupled modes. For all  $\mathbf{q}$ , the equations on the mode  $\{\hat{\mathbf{u}}_q, \hat{\Pi}_q\}$  write:

$$\frac{d\hat{\mathbf{u}}_q}{dt} = -2\mathbf{e}_z \times \hat{\mathbf{u}}_q - Ek^2 \hat{\mathbf{u}}_q - i\mathbf{q} \hat{\Pi}_q - \widehat{\text{NL}}_q \quad (4.7)$$

$$\mathbf{q} \cdot \hat{\mathbf{u}}_q = 0. \quad (4.8)$$

where  $\widehat{\text{NL}}_q$  stands for the non-linear terms computed in the real space and then Fourier transformed to extract its  $\mathbf{q}$  component. To solve the problem (4.4),  $\widehat{\text{NL}}_q$  includes  $\mathbf{u} \cdot \nabla \mathbf{u}$  and the interaction terms between  $\mathbf{u}$  and  $\mathbf{U}_w$ . Although the  $\mathbf{U}_w/\mathbf{u}$  interaction is linear, including it in the non-linear term turned out to be the most straightforward implementation building on the original SNOOPY code. Taking  $\mathbf{U}_w$  as an initial condition was also used for comparison to ensure that the coding of the augmented non-linear term has been properly done.

Lastly, the SNOOPY code solves in fact implicitly the viscosity term  $-Eq^2 \hat{\mathbf{u}}_q$ , that is, it solves the dynamics of modified modes

$$\hat{\mathbf{u}}_q \exp(-q^2 Et).$$

The time evolution of these modified modes is determined with a 4<sup>th</sup> order Runge-Kutta method.

For the present chapter, all simulations are carried out with a resolution of 96 modes in each direction with  $L_{x,y,z} = L = 1$ . Increasing the resolution proves unnecessary as the present work only focuses on the growth of the instability and not on its saturation; there is no cascade towards smaller scales.

## 2.3 Geostrophic modes and inertial waves in the spectral space

Prior to delving into the stability of inertial waves, we first introduce how the spectral space is useful to track the respective time evolution of inertial waves and geostrophic mode.

### Diagnostic kinetic energy

Geostrophic modes are easily identified in the spectral space because one of their defining properties is their  $z$  invariance: their wave vectors  $\mathbf{q}$  are in the  $(xOy)$  plane,  $q_z = 0$ . We thus introduce two diagnostic kinetic energies to track the existence of geostrophic instabilities, the kinetic energy of two-dimensional modes  $\mathcal{E}_g$ —which includes slow geostrophic modes—and the kinetic energy of three-dimensional modes  $\mathcal{E}_{3d}$  defined as follows:

$$\mathcal{E}_g = \frac{1}{2} \sum_{q/q_z=0} |\hat{\mathbf{u}}_q|^2 \quad \text{and} \quad \mathcal{E}_{3d} = \frac{1}{2} \sum_{q/q_z \neq 0} |\hat{\mathbf{u}}_q|^2. \quad (4.9)$$

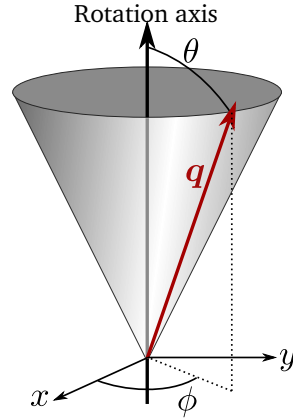


**Figure 4.1:** Schematic cartoon of a wave vector  $\mathbf{q}$  with its spherical angles  $\phi$  and  $\theta$ . The modes with the same frequency as  $\mathbf{q}$  have the same angle  $\theta$  with respect to the rotation axis and thus lie on a cone.

### Spatio-temporal energy spectrum projected onto the dispersion relation

The excitation of inertial waves may also be diagnosed with the use of spectral analysis: the energy spectrum of the flow is projected onto the space  $(\theta, \omega)$  where  $\theta$  is the angle between the rotation axis and the wave vector, and  $\omega$  is the temporal frequency. Such a projection is easily carried out from the spectral decomposition of the flow. A wave vector  $\mathbf{q}$  may be decomposed in spherical coordinates  $(q, \theta, \phi)$ , where  $\phi$  is the azimuthal angle of the wave vector and  $\theta$  is the angle with the rotation axis (see figure 4.1). We first integrate the real part of the modes complex amplitudes  $\hat{\mathbf{u}}_{\mathbf{q}}(t)$  over the azimuthal angles and wave numbers, *i.e.* we define the following quantity:

$$\hat{\mathbf{u}}(\theta, t) = \int_{q=0}^{q_m} \int_{\phi=0}^{2\pi} \hat{\mathbf{u}}_{\mathbf{q}}(t) q^2 \sin \theta dq d\phi \quad (4.10)$$

where  $q_m$  is the maximal wave number set by the resolution. The quantity  $\hat{\mathbf{u}}(\theta, t)$  is then applied a Fourier transform in time to compute  $\hat{\mathbf{u}}(\theta, \omega)$ , from which the energy map  $\mathcal{E}(\theta, \omega)$  is computed as

$$\mathcal{E}(\theta, \omega) = |\hat{\mathbf{u}}(\theta, \omega)|^2.$$

In this energy map, waves and geostrophic modes all align along the dispersion relation  $\omega = \pm 2 \cos \theta$  (see equation (4.3)).

Inertial waves are already known to be unstable via the triadic resonance mechanism described in chapter 2 section 2.3. Such an instability may be easily identified once the energy is projected in the  $(\theta, \omega)$  subspace, as the growing waves must be lying along the dispersion relation, and their frequencies  $\omega_1$  and  $\omega_2$  satisfy the resonance condition

$$\omega_1 + \omega_2 \pm \omega_0 = 0.$$

In addition, geostrophic modes are clearly identified at  $\theta = \pi/2$  and  $\omega \ll 1$  as geostrophic modes evolve slowly compared to the rotation time.

## 2.4 Outline

In the following, the stability of an inertial waves is explored via idealised numerical simulations. We first carry out simulations initiated with a low amplitude initial noise. In the

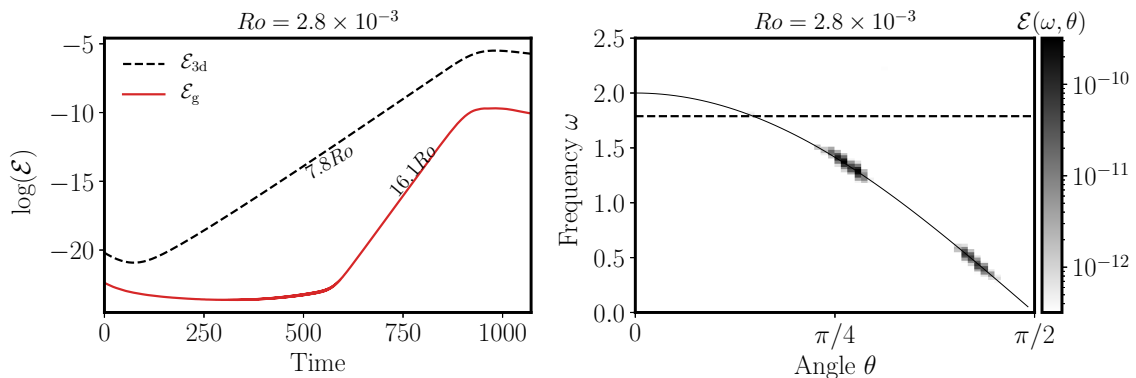


**Figure 4.2:** **Left:** time series of the kinetic energy contributions of the two- and three-dimensional modes  $\mathcal{E}_g$  and  $\mathcal{E}_{3d}$  (see definition (4.9)) at  $Ro = 2.8 \times 10^{-3}$ . The measured growth rates for the amplitude of the three- and two-dimensional modes are reported along the curves. **Right:** map of the spatio-temporal kinetic energy spectrum projected onto the dispersion relation sub-space  $\mathcal{E}(\theta, \omega)$  (see definition in section 2.3). The horizontal dashed line materialises the frequency of the forcing wave, and the plain line corresponds to the dispersion relation of inertial waves. Note that this map is symmetric with respect to the  $x$  axis since it is computed from the real part of the modes amplitudes only.

low wave amplitude regime, we retrieve the triadic resonant instability discussed in chapter 2 section 2.3. An exponential growth of two-dimensional modes is observed but appears to be slaved to the daughter waves. At higher wave amplitude, the simulations feature a more complex behaviour where three-dimensional modes and geostrophic flows grow together at the same rate. To understand the various mechanisms driving the growth of two-dimensional geostrophic modes, we proceed to idealised numerical simulations in well-controlled conditions. We first exhibit the mechanism driving the geostrophic growth at low wave amplitude: it is direct, non-linear forcing by the exponentially growing waves. Then, we proceed to numerical simulations of the inertial wave stability with an initial condition comprising only one geostrophic mode. We find that the latter is unstable provided the amplitude of the wave is larger than a threshold that is independent of viscosity. To conclude, we show that this finite amplitude instability is relevant to explain the experimental results, in particular the regime diagram in figure 3.19 in chapter 3.

## 3. Simulations of instabilities driven by an inertial wave

### 3.1 The low wave amplitude number limit: triadic resonances

To start with, we examine a simulation carried out at small wave amplitude  $Ro = 2.8 \times 10^{-3}$  with an Ekman number  $E = 10^{-6}$ . The initial condition is a random noise restrained to wave vectors  $\mathbf{q}$  such that  $|\mathbf{q}| < 20\pi$ . We track the energy of modes invariant along the rotation axis  $\mathcal{E}_g$  and the rest of the flow  $\mathcal{E}_{3d}$  to investigate the existence of instabilities characterised by exponential growth. We also map the energy spectrum projected onto the dispersion relation sub-space in order to characterise the nature of the growing modes. These diagnostic quantities are shown in figure 4.2.

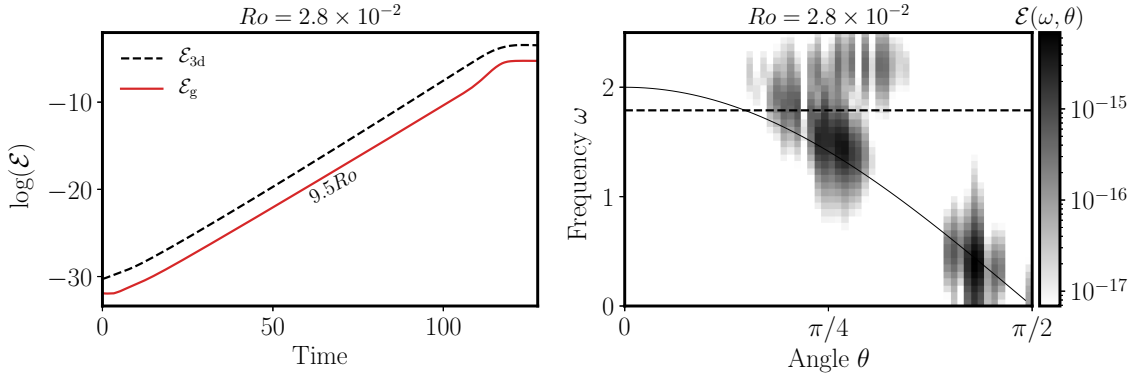


**Figure 4.3:** **Left:** time series of the kinetic energy contributions of the two- and three-dimensional modes  $\mathcal{E}_g$  and  $\mathcal{E}_{3d}$  (see definition (4.9)) at  $Ro = 2.8 \times 10^{-2}$ . The measured growth rates are reported along the curves. **Right:** map of the kinetic energy projected in the dispersion relation sub-space  $\mathcal{E}(\theta, \omega)$  (see definition in section 2.3). The horizontal dashed line materialises the frequency of the forcing wave, and the plain line corresponds to the dispersion relation of inertial waves.

After the initial noise has relaxed, we observe an exponential growth of three-dimensional modes with an  $\mathcal{O}(Ro)$  growth rate. The growth of the two-dimensional modes is delayed and is associated to a rate about twice larger than the three-dimensional modes. The energy map  $\mathcal{E}(\theta, \omega)$  reveals that the unstable structures are inertial waves since their energy is located along the dispersion relation. Moreover, the energy is focused on two spots whose frequencies are symmetrical with respect to  $\omega_0/2$ . It proves that the instability we observe is due to triadic resonant interaction: the frequencies of daughter waves  $\omega_1$  and  $\omega_2$  is related to the forcing wave frequency  $\omega_0$  by the relation  $\omega_1 + \omega_2 = \omega_0$ <sup>1</sup>. Although the kinetic energy time series indicate that two-dimensional modes grow exponentially, the delayed growth and the twice larger rate rather indicates that their amplitude is slaved to the growing waves. Among the unstable waves, the non-linear interaction of one or more pairs of them directly forces two-dimensional modes. This non-linear direct interaction deserves a section of its own and will be detailed later in section 4 of this chapter.

The growth ends with a saturation of the amplitude of the waves and the two-dimensional modes, which is due to the non-linearity.

### 3.2 The case of larger wave amplitude

We present in this section the results of a simulation of inertial wave stability at a larger wave amplitude  $Ro = 2.8 \times 10^{-2}$  while keeping the Ekman number to  $E = 10^{-6}$ . The initial conditions are the same as in the preceding section. The diagnostic kinetic energies time series and the diagnostic dispersion relation energy map are shown in 4.3.

We notice in the present simulation the exponential growth of geostrophic modes simultaneously with the growth of three-dimensional modes and at the same rate. This is different from the lower wave amplitude case where the growth of two-dimensional modes is delayed and has a rate twice as large as the three-dimensional perturbations. The computa-

<sup>1</sup>Note that the relation (2.34) derived in chapter 2 was rather  $\omega_1 + \omega_2 + \omega_0 = 0$  but since the field is real, both frequencies  $\pm\omega_{0,1,2}$  are present so that a relation of the type  $\omega_1 + \omega_2 = \omega_0$  is also characteristic of triadic interaction.

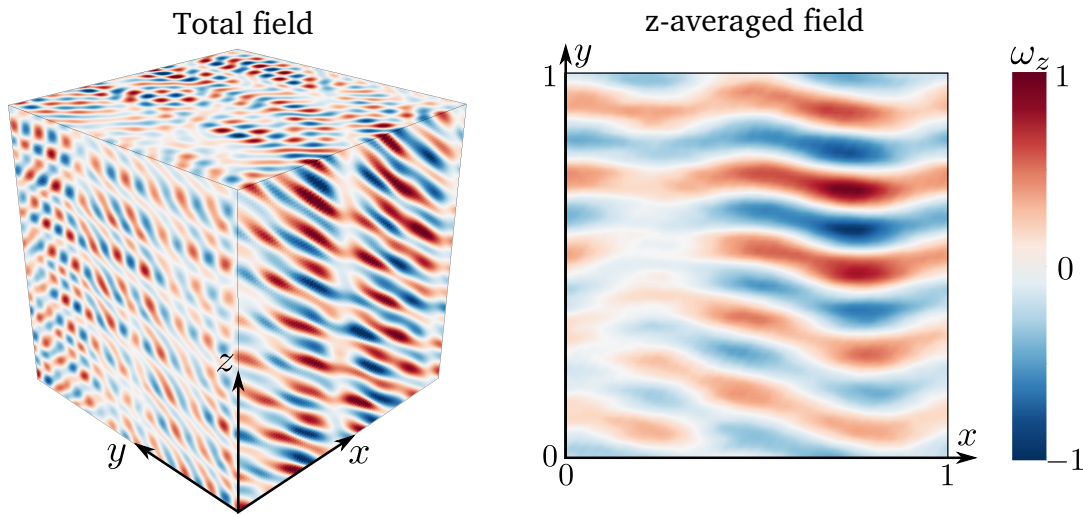


**Figure 4.4:** Snapshot of the  $z$ -component of the vorticity of the total perturbation velocity  $\omega_z = (\nabla \times \mathbf{u})_z$  (**left**) and its average along the rotation axis  $z$  (**right**). The snapshots are taken during the growth phase for  $Ro = 2.8 \times 10^{-2}$ . The principal observed geostrophic mode is  $\mathbf{k}_g = 2\pi [\pm 1, 5, 0]$ . The scale of the vorticity amplitude is arbitrary and different on both panels to highlight their structures.

tion of  $\mathcal{E}(\theta, \omega)$  confirms that the  $q_z = 0$  modes indeed have a slow evolution time scale since their frequency is concentrated towards  $\omega = 0$ . This geostrophic growth goes along with the emergence of a wealth of other three-dimensional structures that are close to the dispersion relation of inertial waves (see figures 4.3 and 4.4), and reminiscent of the triadic resonant interactions observed in figure 4.2. We show in figure 4.4 right a snapshot of the vorticity of the growing perturbation flow  $\mathbf{u}$ , and its vertical average showing the growing geostrophic mode at  $Ro = 2.8 \times 10^{-2}$ . We identify from the averaged snapshot the principal wave vector  $\mathbf{k}_g = 2\pi [\pm 1, 5, 0]$ .

The geostrophic exponential growth measured in figure 4.3 is a specific feature of the moderate inertial wave amplitude. Its vanishing at  $Ro = 2.8 \times 10^{-3}$  is not a consequence of viscous damping: the reduction of the growth rate due to bulk dissipation amounts to  $q^2 E \sim 4 \times 10^{-3}$  for  $q/(2\pi) \sim 10$ ; if the growth rate of the geostrophic mode is  $\sim 9.5Ro$  at  $Ro = 2.8 \times 10^{-2}$ , it should still be positive at  $Ro = 2.8 \times 10^{-3}$ . We therefore conclude that the inertial wave instability at higher amplitude is not solely driven by triadic interaction as in the low amplitude case. A more complex behaviour involving geostrophic modes is observed and remains to be characterised.

## 4. The low wave amplitude case: direct forcing of geostrophic modes

We have proposed that in the low amplitude case presented in figure 4.2, the growth of geostrophic modes is not due to an instability but to direct forcing where two growing modes interact non-linearly with each other to supply energy to a third mode. This mechanism is different from a resonance where two daughter inertial modes grow exponentially when a third one is maintained. In this section, we briefly introduce a mathematical description of

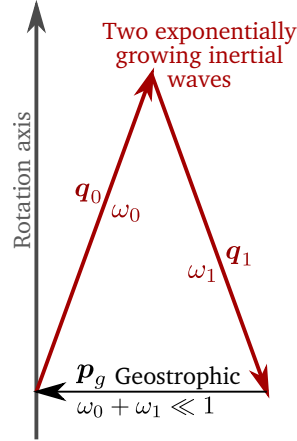


**Figure 4.5:** Schematic cartoon of the direct forcing of a two-dimensional mode  $\mathbf{p}_g$  which is excited at a very low frequency and is therefore geostrophic.

direct forcing in the context of the low wave amplitude simulation (section 3.1) and propose a proof-of-concept simulation.

## 4.1 A mathematical description of direct forcing

Consider two modes with wave vectors  $\mathbf{q}_0$  and  $\mathbf{q}_1$  that are excited at their eigen frequencies  $\omega_0$  and  $\omega_1$ . In what follows, we assume that the amplitudes  $b_{0,1}$  of the helical modes  $\mathbf{h}_{0,1}$  corresponding to these two waves has a prescribed temporal evolution. Following what is observed in the low wave amplitude simulation (see section 3.1), the modes  $\mathbf{q}_{0,1}$  could be, for instance, daughter modes of a triadic resonance with the imposed wave  $\mathbf{k}$ . Their amplitudes  $b_{0,1}$  are exponentially growing functions over a long timescale  $\mathcal{O}(Ro^{-1})$ . Among the collection of growing daughter waves, let us assume that  $\mathbf{q}_{0,1}$  are such that their non-linear interaction excite a two-dimensional mode  $\mathbf{p}_g$  such that  $\mathbf{q}_0 + \mathbf{q}_1 + \mathbf{p}_g = 0$  and  $p_{g,z} = 0$ , as depicted in figure 4.5. The temporal evolution of the amplitude  $b_g$  of the  $\mathbf{p}_g$  helical mode  $\mathbf{h}_g$  is related to the prescribed amplitudes  $b_{0,1}$  according to (see chapter 2 relation (2.26)):

$$\dot{b}_2(t) = \frac{1}{2} b_0(t)^* b_1(t)^* (s_1 q_1 - s_0 q_0) \mathbf{h}_g^* \cdot (\mathbf{h}_0^* \times \mathbf{h}_1^*) e^{i\Delta\omega t} \quad (4.11)$$

where the viscous damping has been dismissed for clarity, and where we have introduced  $s_0$  and  $s_1$  the sign of the helicity of waves  $\mathbf{q}_0$  and  $\mathbf{q}_1$ , and  $\Delta\omega = \omega_0 + \omega_1$ . Note that if  $b_{0,1}$  are slowly varying functions, the frequency of the two-dimensional mode is  $\Delta\omega$ ; in configurations such as the schematic cartoon of figure 4.5,  $\Delta\omega \ll 1$  so that the two-dimensional mode is low frequency, and thus geostrophic. Direct forcing is also a triadic interaction, but it differs from triadic resonance as two waves are maintained instead of one, and thus the amplitude of the third wave is slaved to the amplitudes of the two maintained waves.

Let us consider two waves  $\mathbf{q}_0$  and  $\mathbf{q}_1$  growing exponentially at the same rate  $\sigma$ , that is:

$$b_{0,1}(t) \propto e^{\sigma t} .$$

The equation on the amplitude  $b_2$  is recast into the following simplified form:

$$\dot{b}_2(t) = I e^{(2\sigma + i\Delta\omega)t} . \quad (4.12)$$

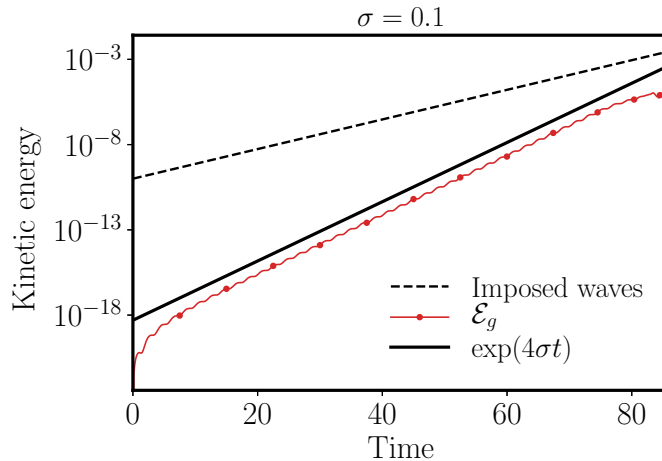


**Figure 4.6:** Time series of the kinetic energy of the imposed waves (not simulated but given for reference) and the two-dimensional modes ( $\mathcal{E}_g$ ). The imposed inertial waves' amplitudes grow at a rate  $\sigma = 0.1$ , and their energy grows at rate  $2\sigma$ . The expected growth rate of the two-dimensional modes' energy is  $4\sigma$  (see equation (4.14)), which clearly fits the data from the simulations.

Assuming that initially  $b_2 = 0$ , the preceding equation is simply solved by:

$$b_2(t) = \frac{I}{2\sigma + i\Delta\omega} (e^{(2\sigma + i\Delta\omega)t} - 1) \quad (4.13)$$

If  $b_2$  is a two-dimensional mode, *i.e.*  $k_{2z} = 0$ , the energy in the two-dimensional modes  $\mathcal{E}_{2d}$  writes:

$$\mathcal{E}_{2d} = \frac{1}{2} b_2^* b_2 = \frac{|I|^2}{2(4\sigma^2 + \Delta\omega^2)} [e^{4\sigma t} - e^{(2\sigma + i\Delta\omega)t} - e^{(2\sigma - i\Delta\omega)t} + 1]. \quad (4.14)$$

The fastest growing term in the two-dimensional modes energy is  $\exp(4\sigma t)$ . As a consequence, the energy of two-dimensional modes excited by direct forcing grows twice as fast as the growing modes  $\mathbf{k}_{0,1}$  (whose energy growth rate is  $2\sigma$ ) as observed in figure 4.2. Note that the frequency of the two-dimensional modes is  $\Delta\omega \neq 0$  according to (4.13): the two-dimensional modes are not necessarily slowly varying when they are directly forced.

## 4.2 Numerical simulation of direct forcing

We propose a proof-of-concept simulation of exponential growth of two-dimensional modes. Let us consider the two waves  $\mathbf{k}_0 = 2\pi[5, 5, 8]$  and  $\mathbf{k}_1 = 2\pi[5, 4, -8]$  with the same helicity signs  $s_0$  and  $s_1$ . Their eigen frequencies are  $\omega_0 \simeq 1.498$  and  $\omega_1 = -1.561$  so that  $|\Delta\omega| = |\omega_0 + \omega_1| \sim 6.3 \times 10^{-2}$ . As a consequence, the two-dimensional mode excited through direct interaction  $\mathbf{k}_2 = 2\pi[-10, -9, 0]$  is nearly geostrophic as its frequency  $\Delta\omega$  is small compared to the rotation rate.

We aim at showing with a simulation that the exponential growth of the two inertial waves  $\mathbf{k}_{0,1}$  drives the growth of the near-geostrophic mode  $\mathbf{k}_2$  with a rate twice as large via direct interaction. Exponentially growing amplitudes are imposed on the two inertial waves, that is:

$$b_{0,1} = 1 \times 10^{-5} e^{\sigma t}$$

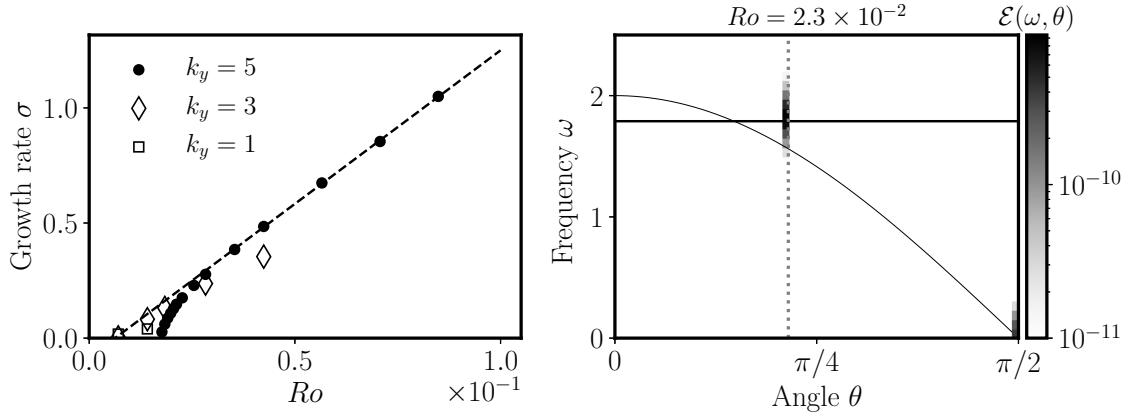


**Figure 4.7:** **Left:** Growth rate  $\sigma$  of the geostrophic modes as a function of the Rossby number  $Ro$  for a single two-dimensional mode initial condition  $\mathbf{k}_g = 2\pi[0, k_y, 0]$  with  $k_y \in \{5, 3, 1\}$ . For large values of  $Ro$  and  $k_y = 5$ , the growth rate  $\sigma$  is very well approximated by a law  $\sigma = 13.3(Ro - Ro_c)$  with  $Ro_c \simeq 6.2 \times 10^{-3}$ . Note that  $Ro_c$  is large compared to the critical Rossby number expected from viscous dissipation which is of order  $\sim 10^{-5}$ . **Right:** Energy map in the dispersion relation sub-space  $\mathcal{E}(\omega, \theta)$  for an idealised simulation of the growth of the instability with  $Ro = 2.3 \times 10^{-2}$  and  $k_y = 5$ . The spectrum is integrated over the growth phase. The vertical dashed line marks the value of  $\theta$  for the modes  $\mathbf{k} + \mathbf{k}_g$  and  $\mathbf{k} - \mathbf{k}_g$ , which in this case are symmetrical with respect to the  $(xOz)$  plane and thus have the same angle  $\theta$ .

with  $\sigma = 0.1$ . As in sections 2.1 and 2.2, we solve the perturbation  $\mathbf{u}$  to the imposed waves, and the interaction between  $\mathbf{u}$  and the waves is coded in the non-linear term.

We present in figure 4.6 the kinetic energy time series obtained from simulation the perturbation flow  $\mathbf{u}$ . The Ekman number is set to  $E = 10^{-8}$  to discard any effect of viscosity, and the initial condition is  $\mathbf{u} = 0$ . In addition, the spatial resolution is set to  $96^3$ . The kinetic energy time series of the imposed waves (which are not simulated, but given for reference) and the two-dimensional modes are shown in figure 4.6. We indeed observe an exponential growth of the near-geostrophic mode  $\mathbf{k}_2$  with the expected rate. This simulation supports that direct forcing by the growing inertial waves is responsible for the growth of two-dimensional modes in the low wave amplitude simulation first presented in this chapter (see figure 4.2).

## 5. The finite wave amplitude instability mechanism

### 5.1 Determining the properties of the geostrophic instability

The simulations of sections 3.1 and 3.2 suggest the existence at moderate Rossby number  $Ro$  of a finite wave amplitude instability involving geostrophic modes, *i.e.* an instability that vanishes below a finite value of  $Ro$  that is independent of the viscous dissipation. To precisely quantify the growth rate of a geostrophic mode alone in the moderate Rossby case, we proceed to simulations where the initial condition comprises only the mode  $\mathbf{k}_g = 2\pi[0, \pm k_y, 0]$  with  $k_y \in \{1, 2, 5\}$ . The Ekman number is set to  $10^{-8}$  in order to discard any effect of the viscosity

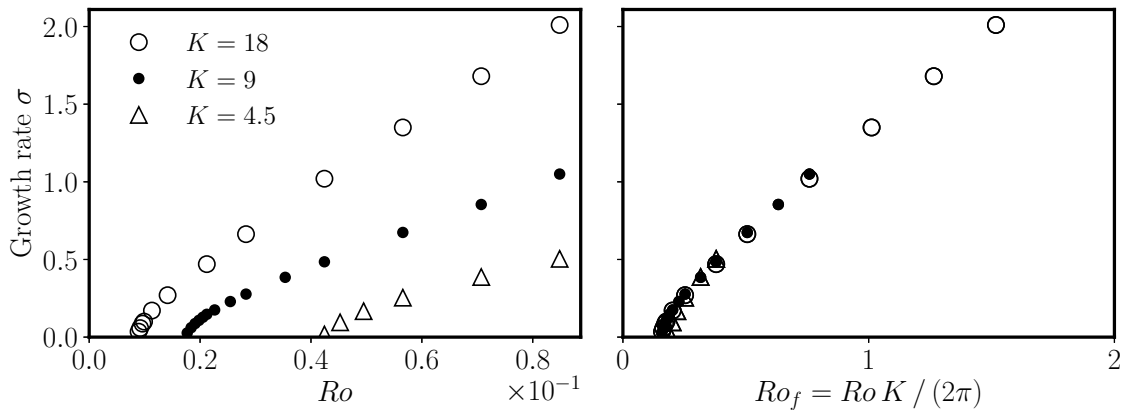


**Figure 4.8:** **Left:** growth rate of the geostrophic mode  $\mathbf{k}_g = 2\pi [0, \pm k_{gy}, 0]$  for different forcing wave numbers  $K = 0.5\mathbf{k}$ ,  $\mathbf{k}$  and  $2\mathbf{k}$ , with  $k_{gy} = 2, 5$  and  $10$ . **Right:** the same data is used but an effective Rossby number based on the forcing wave number  $Ro_f = Ro K / (2\pi)$  is used instead of a  $Ro$ .

in the instability.

These idealised simulations confirm the observations made in sections 3.1 and 3.2 with a noise as an initial condition. The growth rate of the geostrophic instability, shown in figure 4.7 is  $\mathcal{O}(Ro)$  at sufficiently large values of  $Ro$ , but decreases to 0 around  $Ro \simeq 10^{-2}$ . It is well above any viscous threshold since the typical viscous damping for a wave vector  $\mathbf{q}$  is  $|\mathbf{q}|^2 E \sim 3 \times 10^{-5}$  for  $q/(2\pi) \sim 10$ .

In order to gain further insight in the instability mechanism, the power spectrum projected in the dispersion relation sub-space  $\mathcal{E}(\theta, \omega)$  is displayed in figure 4.7 for  $Ro = 2.3 \times 10^{-2}$  and  $k_y = 5$ . For this Rossby number, the growth rate is small which enables to integrate the spectral content of the flow over long time periods. We again observe the focusing of energy in two particular locations. The first location is associated to geostrophic modes. The other location corresponds in terms of angle  $\theta$  to the modes closing the triads formed by  $\mathbf{k}$  and  $\mathbf{k}_g$ , that is  $\mathbf{k} \pm \mathbf{k}_g$ . These latter modes are excited outside their eigen frequencies since their energy location is off the dispersion relation. They are instead excited at the same frequency as the forcing mode  $\omega_0$ . We thus confirm that the instability mechanism does not correspond to exact resonant triads.

In order to understand what sets the critical Rossby number at which the instability vanishes, we vary the wave number of the forcing wave, *i.e.* we consider a forcing wave vector  $\mathbf{K} = 2\mathbf{k}$ ,  $\mathbf{k}$  and  $0.5\mathbf{k}$  as forcing waves while keeping  $\mathbf{k}_g = 2\pi [0, \pm k_{gy}, 0]$  as an initial condition with  $k_{gy} = 10, 5$  and  $3$  (in the order of  $|\mathbf{K}|$ ). We observe that larger wave numbers lead to an increase in the growth rate along with a decrease of the critical Rossby number (see figure 4.7). This result shows that the Rossby number based on the domain size is not adequate to describe the wave instability. The only relevant length in the problem is the maintained mode's wavelengths, which leads us to introduce an effective Rossby number  $Ro_f$  based on the wave length of the forcing wave, that is  $Ro_f = Ro K / (2\pi)$ . As it can be noticed in figure 4.8, using the  $Ro_f$  instead of  $Ro$  compels all the growth rates at different forcing wave numbers to fall on the same master curve, which proves it is the relevant parameter to describe the geostrophic instability. Moreover, the critical value of the Rossby number beyond which the instability ceases to exist is very well described by the effective critical Rossby number  $Ro_{f,c} \simeq 0.10 - 0.15$ .

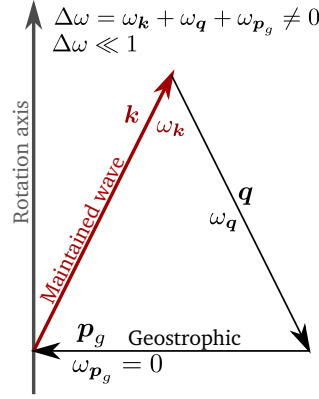


**Figure 4.9:** Schematic cartoon of a near resonance involving an imposed wave  $\mathbf{k}$  and a geostrophic mode  $\mathbf{p}_g$ . The three modes are such that the sum of the eigen frequencies  $\Delta\omega = \omega_{\mathbf{k}} + \omega_{\mathbf{q}} + \omega_{\mathbf{p}_g} = \omega_{\mathbf{k}} + \omega_{\mathbf{q}}$  does not satisfy the exact resonance condition, that is,  $\Delta\omega \neq 0$ . Note however that  $\Delta\omega \ll 1$  is *a priori* required to ensure significant energy transfer, according to chapter 2 relation (2.32).

## 5.2 An instability based on near-resonance?

In chapter 2 section 2.3 we have developed the triadic resonance and near-resonance mechanisms that transfer energy between three inertial waves. We have also shown in section 2.4 that exact resonance involving a geostrophic mode has exactly zero transfer coefficients. The existence and implications of near-resonance for the growth of geostrophic modes have not been yet examined, and we propose in this section a theoretical development to explore their relevance to the present finite Rossby number instability.

With the helical modes formalism, we aim at estimating the growth rate of quasi-resonances involving a two-dimensional mode. We consider three modes with wave vectors  $\mathbf{k}$ ,  $\mathbf{q}$  and  $\mathbf{p}_g$ , the last one being two-dimensional, *i.e.*  $p_{gz} = 0$ . Let us assume that this triad is near resonant, that is, there exists two wave vectors  $\mathbf{k}_0$  and  $\mathbf{q}_0$  that are close to  $\mathbf{k}$  and  $\mathbf{q}$  respectively and such that their wave vectors and eigen frequencies satisfy:

$$\begin{cases} \mathbf{k}_0 + \mathbf{q}_0 + \mathbf{p}_g = 0 \\ \omega_{\mathbf{k}_0} + \omega_{\mathbf{q}_0} + \omega_{\mathbf{p}_g} = \omega_{\mathbf{k}_0} + \omega_{\mathbf{q}_0} = 0. \end{cases} \quad (4.15)$$

We also define wave vector perturbations  $\delta\mathbf{k}$  and  $\delta\mathbf{q}$ :

$$\begin{cases} \mathbf{k} = \mathbf{k}_0 + \delta\mathbf{k} \\ \mathbf{q} = \mathbf{q}_0 + \delta\mathbf{q}. \end{cases} \quad (4.16)$$

We assume that the wave amplitude  $Ro$  is sufficiently small so that  $|\delta\mathbf{k}| \ll k$  and  $|\delta\mathbf{q}| \ll q$ ; we also assume that the sign of the helicity  $s$  of the perturbed wave vectors is the same as the modes involved in the exact resonance. As in chapter 2 section 2.4, the exact resonance conditions (4.15) give:

$$k_0 = q_0, \quad s_k = s_q \quad \text{and} \quad \frac{s_k k_{z0}}{k_0} + \frac{s_q q_{z0}}{q_0} = \omega_{\mathbf{k}_0} + \omega_{\mathbf{q}_0} = 0. \quad (4.17)$$

Besides, the necessary condition for interaction  $\mathbf{k} + \mathbf{q} + \mathbf{p}_g = \mathbf{0}$  imposes the following relation on the perturbations to the wave vectors:

$$\delta\mathbf{k} + \delta\mathbf{q} = \mathbf{0}. \quad (4.18)$$

According to relation (2.33), two quantities are important for the growth rate of near resonances: the frequency mismatch  $\Delta\omega = \omega_{\mathbf{k}} + \omega_{\mathbf{q}} + \omega_{\mathbf{p}_g}$  and the coupling coefficient  $C_0$ . The near resonance exists when  $\sqrt{C_0}Ro > \Delta\omega$  where  $Ro$  is the amplitude of the maintained wave. To derive a more explicit condition for the growth rate of near-resonance to exist and be positive, we first evaluate the frequency mismatch and relate it to the wave vector perturbations. Using Taylor expansion and relations (4.17, 4.18), we evaluate the frequency mismatch as a function of the wave vector perturbation:

$$\begin{aligned}
\frac{\Delta\omega}{2} &= s_{\mathbf{k}} \frac{k_z}{k} + s_{\mathbf{q}} \frac{q_z}{q} + s_{\mathbf{p}_g} \frac{p_{gz}}{p} \\
&= s_{\mathbf{k}} \frac{k_{z0} + \delta k_z}{|\mathbf{k}_0 + \delta \mathbf{k}|} + s_{\mathbf{q}} \frac{q_{z0} + \delta q_z}{|\mathbf{q}_0 + \delta \mathbf{q}|} \\
&= \omega_{\mathbf{k}_0} + \omega_{\mathbf{q}_0} + s_{\mathbf{k}} \frac{\delta k_z}{k_0} + s_{\mathbf{q}} \frac{\delta q_z}{q_0} - \frac{\omega_{\mathbf{k}_0}}{2} \frac{\delta \mathbf{k} \cdot \mathbf{k}_0}{k_0^2} - \frac{\omega_{\mathbf{q}_0}}{2} \frac{\delta \mathbf{q} \cdot \mathbf{q}_0}{q_0^2} \\
&= -\frac{\omega_{\mathbf{k}_0}}{2} \frac{\delta \mathbf{k} \cdot \mathbf{k}_0}{k_0^2} + \frac{\omega_{\mathbf{k}_0}}{2} \frac{-\delta \mathbf{k} \cdot \mathbf{q}_0}{k_0^2} \\
&= \frac{\omega_{\mathbf{k}_0}}{2} \frac{\delta \mathbf{k} \cdot \mathbf{p}_g}{k_0^2}. \tag{4.19}
\end{aligned}$$

Note that without the assumption that the  $s_{\mathbf{k},\mathbf{q}}$  are the same for the perturbed waves and the modes involved in the exact resonance, the frequency mismatch would have been of the same order as  $\omega_{\mathbf{k}_0, \mathbf{q}_0}$  instead of being a first order, and no near-resonance would be possible. Let us now compute the coupling coefficient  $C_0$  involved in the growth rate of the mode  $\mathbf{k}_g$  when a wave  $\mathbf{q}$  is imposed.  $\mathbf{k}_g$  and  $\mathbf{p}$  are the two daughter modes and the coefficient  $C_0$  writes:

$$\frac{C_0}{4} = (s_{\mathbf{p}_g} p_g - s_{\mathbf{k}} k)(s_{\mathbf{q}} q - s_{\mathbf{k}} k) \left| \mathbf{h}_{\mathbf{p}_g}^{s_{\mathbf{p}_g}} \cdot (\mathbf{h}_{\mathbf{k}}^{s_{\mathbf{k}}} \times \mathbf{h}_{\mathbf{q}}^{s_{\mathbf{q}}}) \right|^2. \tag{4.20}$$

In general:

$$(s_{\mathbf{p}_g} p_g - s_{\mathbf{k}_0} k_0) \left| \mathbf{h}_{\mathbf{p}_g}^{s_{\mathbf{p}_g}} \cdot (\mathbf{h}_{\mathbf{k}}^{s_{\mathbf{k}}} \times \mathbf{h}_{\mathbf{q}}^{s_{\mathbf{q}}}) \right|^2 \neq 0 \tag{4.21}$$

which can be proved by taking the particular case  $\mathbf{k}_0 = [k_x, 0, k_z]$ ,  $\mathbf{q}_0 = [k_x, 0, -k_z]$  and  $\mathbf{k}_g = [-2k_x, 0, 0]$  for which the term (4.21) does not cancel out. At exact resonance,  $s_{\mathbf{k}} k_0 - s_{\mathbf{q}} q_0 = 0$  implies that  $C_0$  is at least a first order with respect to the vector perturbation. A straightforward calculation gives:

$$s_{\mathbf{k}} k - s_{\mathbf{q}} q = \frac{s_{\mathbf{k}}}{k_0} \delta \mathbf{k} \cdot \mathbf{p}_g = s_{\mathbf{k}} k_0 \frac{\Delta\omega}{\omega_{\mathbf{k}_0}} \tag{4.22}$$

so that the coupling coefficient  $C_0$  writes:

$$C_0 = k_0 \frac{\Delta\omega}{4} c_0 \tag{4.23}$$

where we have introduced a coefficient  $c_0 = \mathcal{O}(1)$ . The near-resonance condition (2.32) on the wave amplitude  $Ro$  therefore translates as follows:

$$k_0 c_0 \Delta\omega Ro^2 - \Delta\omega^2 > 0 \quad i.e. \quad |\Delta\omega| < k_0 c_0 Ro^2. \tag{4.24}$$

According to the preceding relation, the frequency mismatch to observe a near resonance involving a geostrophic mode must be smaller than  $\mathcal{O}(Ro^2)$ . The growth rate is proportional

to  $\sqrt{k_0 c_0 \Delta \omega R o^2 - \Delta \omega^2}$  (see relation (2.32)). The maximum growth rate is given by the maximum of the function  $\Delta \omega \mapsto k_0 c_0 \Delta \omega R o^2 - \Delta \omega^2$  which is reached at

$$\Delta \omega_{\max} = \frac{k_0 c_0}{2} R o^2.$$

The growth rate reached for this maximum mismatch is

$$\sigma_{\max} = \frac{k_0 c_0}{4} R o^2. \quad (4.25)$$

The maximum growth rate of the near resonance is then also  $\mathcal{O}(R o^2)$ . To conclude, the above calculation suggests that a near-resonance involving a geostrophic mode cannot be responsible for the exponential growth cannot be responsible for the exponential growth of geostrophic modes over a time  $\mathcal{O}(R o)$ , and that other mechanisms must be investigated.

The fact that the adequate parameter to describe the instability is  $R o k$  (see figure 4.8) leads to consider that shear, and not amplitude alone, plays a role in the instability mechanism. It is possible that what we observe is in fact the instability of the plane wave structure itself.

To investigate the stability of the wave structure itself, it is necessary to return to a more general perturbative approach of stability instead of using the helical mode decomposition and the corresponding amplitude equations. Consider the problem (4.4) on the perturbation velocity  $\mathbf{u}$  in the following linearised, inviscid form:

$$\begin{cases} \partial_t \mathbf{u} + 2\mathbf{e}_z \times \mathbf{u} + \nabla p &= R o (\mathbf{u} \times (\nabla \times \mathbf{U}_w) + \mathbf{U}_w \times (\nabla \times \mathbf{u})) \\ \nabla \cdot \mathbf{u} &= 0. \end{cases} \quad (4.26)$$

It is a general linear stability analysis of the wave  $\mathbf{U}_w$  of the form  $\partial_t \mathbf{u} = \mathbb{L}_s(t) \mathbf{u}$  where  $\mathbb{L}_s$  is a linear operator with harmonic coefficients. This more general stability analysis may be carried out using Floquet analysis (Vanneste, 2005; Jouve and Ogilvie, 2014), and remains to be done. Although it should yield the triadic resonance at low Rossby number, it may also include at moderate Rossby number other instabilities.

## 6. Conclusions

### 6.1 Three-modes interactions and geostrophic flows

In the present chapter, we have explored with idealised numerical simulations the stability of a single inertial wave. At low wave amplitude, we have found that the primary inertial wave gives rise to daughter inertial waves via triadic resonant instability. This three-waves interaction is schematically described in figure 4.10-a, and has been further discussed in chapter 2. As the daughter waves grow, two-dimensional geostrophic modes grow with a twice larger rate, which is characteristic of non-linear direct forcing. This latter mechanism has been described in details in section 4, and the mode interaction at play is summarised in figure 4.10-b.

Most importantly, we have also identified and characterised an instability of geostrophic vortices driven by the maintained waves. The latter instability occurs when the wave amplitude is above a finite threshold that is independent of viscous dissipation. According to the calculation of section 5.2, near-resonant triadic interaction involving a geostrophic mode (see

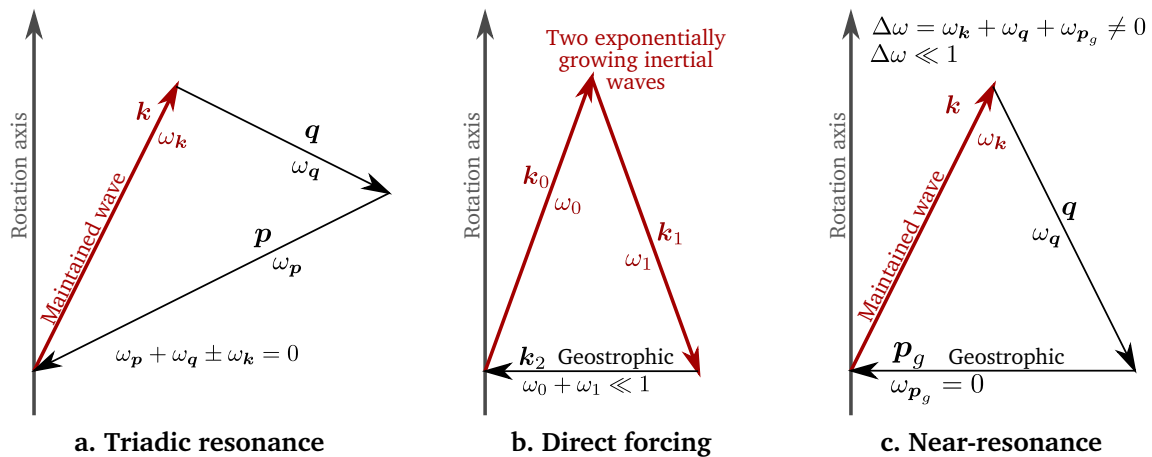


**Figure 4.10:** A schematic summarising the three different types of interaction between three modes that have been explored throughout the present chapter. The first one (a) is triadic resonant interaction which has been evidenced in the first simulation presented in figure 4.2. It is detailed at length in chapter 2 section 2.3. The second is direct resonant interaction (b) between exponentially growing inertial waves giving rise to a geostrophic mode. It has been found in the low amplitude simulation (see section 3.1) and formally explained in section 4. The last three mode interaction considered in this chapter is near-resonance involving a geostrophic mode (c). It has been proposed as a plausible mechanism to explain the finite wave amplitude instability but is possibly dismissed for not accounting for the law governing the growth rate of the instability.

figure 4.10-c) seems unable to explain the  $\mathcal{O}(Ro)$  growth rate— $Ro$  being the amplitude of the wave. Our results rather suggest that the finite wave amplitude instability is intrinsic to the wave spatial structure and may be driven by shear (see section 5.1). The most significant result pointing towards shear is the collapse on a master curve of the growth rate as a function of the local Rossby number  $Ro_f = Ro k/(2\pi)$ , as shown in figure (4.8).

## 6.2 A regime diagram for the elliptical instability

### Reproducing the experimental regime diagram

In this chapter, we have found that inertial waves drive geostrophic flows via direct forcing and finite amplitude instability. Both mechanisms are relevant to the turbulent saturation of the elliptical instability. The unstable waves drive geostrophic flows via direct forcing over the whole course of the elliptical instability, from the growth to the saturation. However, if the wave saturate to an amplitude  $\sim Ro_i$ , direct forcing should drive geostrophic flows with an amplitude  $\sim Ro_i^2$ . Such an evolution of the amplitude does not account for the sudden increase observed in figure 3.18 in chapter 3, and we therefore dismissed direct forcing to explain the experimental results. Nevertheless, the ability of this mechanism to drive a geostrophic-dominated saturation is discussed in chapter 5.

In the present section, we aim at showing that the finite wave amplitude instability discussed throughout the present chapter can explain the experimental regime diagram (displayed in figure 3.19) and the transition from inertial wave turbulence to geostrophic turbu-

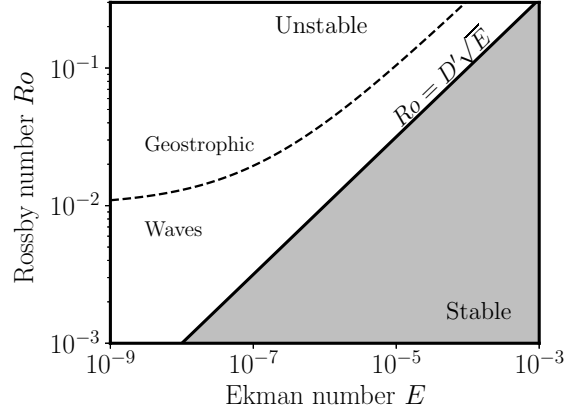


**Figure 4.11:** Schematic diagram of the different regimes expected for the saturation of the elliptical instability, built from the study presented throughout this chapter, based on the approximate laws (4.28) and (4.29) for  $D = 15$ ,  $D' = 10$ ,  $\alpha = 0.1$  and  $Ro_c = 0.3$  for illustration. We assume that the wavelength of the modes driven by the elliptical instability is  $\lambda = 2\pi/k = 1/5$ , the length being normalised by the ellipsoid largest axis  $a$ . Note that  $D'$  is chosen to match the threshold of the elliptical instability used in chapter 3. The thick black line is the threshold of the elliptical instability, and the dashed line is the threshold of the geostrophic secondary instability.

lence. The growth rate  $\sigma_g$  of this instability has the following approximate expression:

$$\sigma_g = \alpha \left( Ro \frac{k}{2\pi} - Ro_c \right) \quad (4.27)$$

where  $Ro$  is the amplitude of the inertial wave and  $k$  is its wave vector. The critical Rossby  $Ro_c$  is independent of viscous dissipation. These results may be transposed to the saturation of the elliptical instability. We already know, from an analysis presented in chapter 2 section 1, and from the results of numerical simulations (Grannan et al., 2017), that the velocity amplitude saturates like the typical amplitude of the tidal base flow, be it driven by differential rotation or libration. The input parameter  $Ro$  used in this idealised study is, therefore, a proxy for the amplitude of the base flow, and is equivalent to the input Rossby number used in the previous chapters. Let us assume the dissipation rate is mostly driven by friction at the boundaries, the inviscid growth rate is then reduced by a factor  $D\sqrt{E}$ . On one hand, the geostrophic instability growth rate writes  $\alpha(Ro(k/2\pi) - Ro_c) - D\sqrt{E}$  which is positive provided that:

$$Ro \geq \frac{2\pi}{k} \left( Ro_c + \frac{D}{\alpha} \sqrt{E} \right). \quad (4.28)$$

On the other hand, the elliptical instability grows when:

$$Ro \geq D' \sqrt{E} \quad (4.29)$$

where  $D'$  is a geometrical factor.

With the two approximate laws describing the threshold of the elliptical instability (4.29) and the geostrophic instability (4.28), we can draw schematic regime diagrams as the one displayed in figure 4.11. The geostrophic instability critical line delimits two areas in the parameter space, one which should be dominated by strong geostrophic vortices and another where energy should be transferred to waves only. Regime diagrams very similar to the one obtained in the experimental study (see figure 3.19 in chapter 3) can be drawn with the appropriate set of values for  $D$ ,  $D'$ ,  $\alpha$ ,  $k$  and  $Ro_c$ . This is the case in figure 4.11 were reasonable values for these parameters are used:

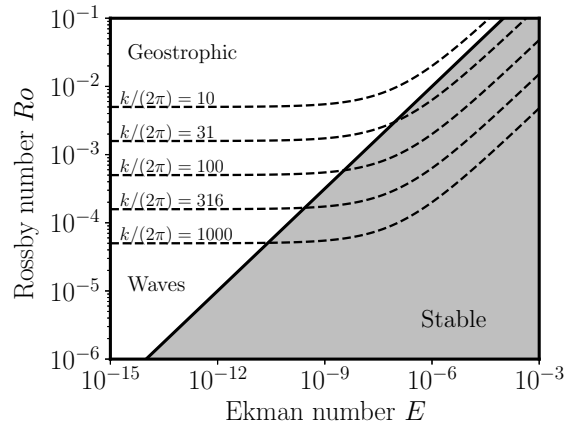


**Figure 4.12:** Schematic regime diagram of the elliptical instability with the same graphical code as in figure 4.11. The values of  $D$ ,  $D'$ ,  $\alpha$  and  $Ro_c$  are the same as in figure 4.11. The resonant wave number  $k$  is varied from  $2\pi \times 10$  to  $2\pi \times 1000$ . Note that geophysical regimes typically correspond to  $Ro < 10^{-4}$  and  $E < 10^{-10}$ .

- $D' = 10$  to match the threshold of the elliptical instability found in the experiment;
- $k = 2\pi/5$ , which means that the wavelength of the resonant inertial mode is five times smaller than the ellipsoid's largest axis  $a$ ;
- $D = 15$ , which is of the same order of magnitude as  $D$ ;
- $\alpha = 0.1$ , which is smaller than what has been found in the present chapter for the mode  $2\pi [4, 0, 8]$ , but could be consistent with a lower energy transfer from horizontal modes at  $\omega = \pm 2$ —excited in the experiment—and vertically invariant flows;
- $Ro_c = 0.05$ , which is only a factor 2 smaller than the value found in the previous study.

With this choice of parameters, we roughly reproduce the experimental regime diagram shown in figure 3.19. At intermediate Ekman numbers such as those considered in the experimental study ( $E \sim 10^{-6} - 10^{-5}$ ), the line separating the wave-dominated from the geostrophic-dominated regimes is parallel to the viscous threshold of the elliptical instability. Interestingly, the viscosity-independent threshold on the Rossby number for the geostrophic secondary instability translates into a minimal value of  $Ro = 2\pi Ro_c / k$  below which the saturation regime is dominated by inertial waves. If the finite wave amplitude instability is indeed responsible for the secondary transition observed in the experimental study, the determination of the minimal Rossby number remains, nevertheless, beyond the reach of our set-up.

### Influence of the wave number on the minimal input Rossby number

This minimal value of the wave amplitude or input Rossby number, however, depends on the wave vector of the resonant mode, and therefore on the mode selection by the elliptical instability. In the very low dissipation and forcing amplitude regimes, which is relevant for planetary cores, nothing prevents the resonant wavelength to be very small compared to the size of the core, thus pushing the minimal input Rossby number to very low values. In figure 4.12, we build a regime diagram with the same values as in figure 4.11 apart from the wave number  $k$  which is increased from  $2\pi \times 10$  to  $2\pi \times 1000$ . Even when the ratio between the size

of the core and the resonant wavelength reaches  $1/1000$ , the minimum input Rossby number is sufficiently high so that a wave dominated regime is still relevant to geophysical regimes.

### **Geostrophic instabilities below the minimal input Rossby number**

Lastly, when the forcing amplitude and the dissipation are such that elliptical instability saturation flow is stable to finite wave amplitude instability, other mechanism may drive exponential growth of geostrophic modes. The remaining processes transferring energy from inertial waves are four-waves interactions (Smith and Waleffe, 1999; Kerswell, 1999) and near-resonant three-waves interactions (Smith and Lee, 2005), that all lead to a  $\mathcal{O}(Ro^2)$  growth rate of geostrophic flow. These mechanisms remain difficult to probe with the idealised model used in the present chapter since they settle over very long time scales. Nevertheless, simple predictions may be drawn. The viscous threshold of these instabilities follows a  $Ro \propto E^{1/4}$  power law, which is shallower than the  $Ro \propto E^{1/2}$  threshold of the elliptical instability. Even with these mechanisms exciting geostrophic flows, there exists a regime at low dissipation and low forcing amplitude where waves dominate the saturation flow.

# Chapter 5

## Direct forcing of geostrophic modes in the saturation of the elliptical instability

To complete our determination of the boundary between the wave-dominated and the geostrophic-dominated regimes, we explore theoretically the role of direct forcing by inertial waves instead of instabilities. As it is reminded in the previous chapter, the theoretical result of Greenspan (1969) stating that non-linear interaction of waves does not transfer energy to geostrophic modes is only valid in the asymptotic limit of vanishing viscosity and wave amplitude. In the preceding chapter, we have given a first evidence that outside this asymptotic framework, three-dimensional structures are able to transfer energy to geostrophic flows via finite wave amplitude instability. This transfer is however cancelled when the wave amplitude is sufficiently small, below a threshold that is independent of viscosity. When the forcing amplitude is below this threshold, the saturation of the elliptical instability should be dominated by inertial waves in resonant interaction, unless other mechanisms significantly transfer energy to geostrophic flows. We have already mentioned among the possible mechanisms the four-mode interaction described by Kerswell (1999). In this chapter, we explore the role played by direct forcing of geostrophic flows by non-linear self-interaction of an inertial mode in viscous boundary layers, which is also out of the asymptotic framework of Greenspan (1969).

It has been proved in numerical and experimental works that self-interaction of the viscous inertial modes in the boundary layers leads to significant geostrophic axisymmetric flows, also called “zonal winds” (Tilgner, 2007b; Sauret et al., 2010; Morize et al., 2010; Sauret et al., 2014). This mechanism is a direct forcing from waves to geostrophic flows, similarly to the direct forcing considered in the preceding chapter, section 4. Unlike the direct forcing in a Cartesian box, however, the mechanism here examined entirely relies on viscosity and confinement. The aim of this chapter is to explore whether such direct forcing may lead to a geostrophic-dominated saturation, especially in regimes of low dissipation and low forcing

where finite amplitude instabilities, detailed in the previous chapter, vanish.

We first introduce a reduced model of the elliptical instability which builds on the work of Lagrange et al. (2011). It features two resonant modes and a zonal wind which is directly forced via non-linear self-interaction in the boundary layer, and includes the non-linear back-reaction of the zonal wind on the resonant modes. It leads to an upper bound on the forcing base flow amplitude below which the geostrophic component of the saturation flow should be sub-dominant. This upper bound is a non-trivial function of the dissipation or Ekman number and requires proper quantification. Based on the study of Tilgner (2007b) and Vidal and Schaeffer (2015), we implement a numerical method to determine this upper bound in the special case of the sphere. Our results suggest that at vanishing Ekman number, the upper bound tends to saturate and become independent of the Ekman number.

## 1. Deriving a low order model

In order to examine the ability of direct forcing via boundary layers to drive a geostrophic type saturation of the elliptical instability, we derive a low order model involving the resonant waves and an axisymmetric zonal wind. This simple model keeps the essential interactions between the inertial modes and the geostrophic flow in order to determine the hierarchy of amplitudes between these two components in the saturation of the elliptical instability. Despite its simplicity, the model is derived from an analysis of the rotating Navier-Stokes equations and the spatial structure of inertial modes. A similar development can be found in the related context of precession-driven instabilities in cylinders studied by Lagrange et al. (2011).

### 1.1 The amplitude equations

To derive a low order model on a reduced number of modes, we first transcribe the rotating Navier-Stokes equation into a set of mode amplitude equations, as derived in chapter 2 to determine the coupling between the modes and the tidal flow (see section 3.3), or in the case of plane helical modes interaction (see section 2). We consider a flow  $\mathbf{U}$  resulting from the superposition of the base flow  $\mathbf{U}_b$  due to either libration or tides, and a perturbation  $\mathbf{u}$ . The equation governing the perturbation  $\mathbf{u}$  are :

$$\partial_t \mathbf{u} + \mathbf{U}_b \cdot \nabla \mathbf{u} + \mathbf{u} \cdot \nabla \mathbf{U}_b + 2\mathbf{e}_z \times \mathbf{u} + \mathbf{u} \cdot \nabla \mathbf{u} = -\nabla p + E \nabla^2 \mathbf{u} \quad (5.1)$$

$$\nabla \cdot \mathbf{u} = 0 \quad (5.2)$$

where  $E$  is the Ekman number. As done in chapter 1 section 3.3, the interaction between  $\mathbf{u}$  and the base flow  $\mathbf{U}_b$  can be written as a linear operation  $Ro_i \mathcal{L}(t) \mathbf{u}$  where  $Ro_i$  is the amplitude of the base flow. We also introduce the following linear operator associated to the Coriolis force and dissipation such that:

$$\mathcal{L}_\Omega[\mathbf{u}, p] = -2\mathbf{e}_z \times \mathbf{u} - \nabla p + E \nabla^2 \mathbf{u} . \quad (5.3)$$

The non-linear term  $\mathbf{u} \cdot \nabla \mathbf{u}$  is shortened into a bi-linear symmetric operator  $\text{NL}(\cdot, \cdot)$  defined as follows:

$$\text{NL}(\mathbf{u}_1, \mathbf{u}_2) \equiv \frac{1}{2} [\mathbf{u}_1 \times (\nabla \times \mathbf{u}_2) + \mathbf{u}_2 \times (\nabla \times \mathbf{u}_1)] . \quad (5.4)$$

The equation of evolution of the velocity perturbation  $\mathbf{u}$  (5.1) is therefore written into the following compact form:

$$\partial_t \mathbf{u} = \mathcal{L}_\Omega[\mathbf{u}, p] + Ro_i \mathcal{L}(t)\mathbf{u} + \text{NL}(\mathbf{u}, \mathbf{u}). \quad (5.5)$$

The flow  $\mathbf{u}$  may be decomposed into a superposition of eigenmodes of the linear operator  $\mathcal{L}_\Omega$ , noted  $\Psi_i$ , that is:

$$[\mathbf{u}, p] = \sum_i a_i e^{i\omega_i t} [\Psi_i, P_i] \quad (5.6)$$

where the  $a_i$  are time dependent amplitudes and  $\omega_i$  is the eigen frequency of the eigenmodes  $[\Psi_i, P_i]$ . Note that we have discarded a non-linear contribution in the pressure field. It does not play a role in the dynamics apart from ensuring the non-linear interaction of modes is divergence-free. Discarding this term will not affect the following discussion since we are rather interested in the nature (complex or real) and sign of non-linear interactions. As in chapter 2 section 2, a rigorous derivation would start from the vorticity equation, but would here complicate the derivation of the local model.

In the eigenvalue problem  $\mathcal{L}_\Omega \mathbf{u}[\mathbf{u}, p] = \lambda[\mathbf{u}, p]$ , the eigenvalues  $\lambda_i$  include a negative real part  $D_i$  which is a dissipation coefficient depending on the Ekman number, and an imaginary part  $\omega_i$  accounting for the inertial oscillation of the eigenmode due to the Coriolis force. The steps to derive the amplitude equations are the same as in the theoretical derivation of the growth rate of the elliptical instability (see chapter 1 section 3.3), except that we keep the non-linear term. The obtained mode amplitude equations are then:

$$\begin{aligned} \dot{a}_i + D_i a_i = \\ Ro_i \sum_j a_j \langle \Psi_i | \mathcal{L}(t)\Psi_j \rangle e^{i(\omega_j - \omega_i)t} + \sum_{j,k,s_j,s_k} a_{j,s_j} a_{k,s_k} \langle \Psi_i | \text{NL}(\Psi_j^{s_j}, \Psi_k^{s_k}) \rangle e^{i(s_j\omega_j + s_k\omega_k - \omega_i)t} \end{aligned} \quad (5.7)$$

where the coefficients  $s_j$  and  $s_k$  take their value in  $\{-1, 1\}$  and where we have introduced the notations  $a_{j,1} = a_j$  and  $a_{j,-1} = a_j^*$  to shorten the sum.

## 1.2 Hypotheses on the structure of inertial modes

An equation similar to (5.7) has already been derived in the case of an unbounded rotating fluid for which eigenmodes were helical plane waves. In the following development, we rather dwell on confined geometries for which energy is also transferred from waves to vortices via boundary layers. Instead of considering the inertial modes of an ellipsoid, we consider that the modes of a sphere are sufficient to derive a low order model.

To give an explicit form to the inertial modes, we first consider the inviscid Poincaré equation on the pressure  $p$  (Poincaré, 1885):

$$\partial_{tt} \nabla^2 p + 4\partial_{zz} p = 0. \quad (5.8)$$

Because of the invariance of this equation by rotation around the  $z$  axis, the pressure eigenmodes  $P_j$  of this equation take the following form in cylindrical coordinates  $(\rho, \phi, z)$ :

$$P_j(\rho, \phi, z, t) = p_j(\rho, z) e^{i(m_j \phi + \omega_j t)}. \quad (5.9)$$

where we have introduced the azimuthal wave number  $m_j$ , and a function  $p_j$  describing the structure of the mode in  $(\rho, z)$  (see Kerswell (1993b) and Rieutord (2014) for further details). As in chapter 1 section 3.3, the structure of a mode  $\Psi_j$  may be expanded as the product of a structure function  $\Phi_j(\rho, z)$  and the azimuthal variation  $\exp(im_j\phi)$ . In the mode amplitude equation (5.7), the dot product  $\langle \cdot | \cdot \rangle$  acting on the three spherical coordinates can be reduced to a dot product acting the variables  $(\rho, z)$  and the structure  $\Phi$  only and which is noted  $(\cdot | \cdot)$ . The non-linear term in the amplitude equations (5.7) is then simplified as follows:

$$\begin{aligned} & \sum_{j,k,s_j,s_k} a_{j,s_j} a_{k,s_k} \left\langle \Psi_i \mid \text{NL}(\Psi_j^{s_j}, \Psi_k^{s_k}) \right\rangle e^{i(s_j\omega_j + s_k\omega_k - \omega_i)t} \\ &= \sum_{j,k,s_j,s_k} a_{j,s_j} a_{k,s_k} \left( \Phi_i \mid \text{NL}(\Phi_j^{s_j}, \Phi_k^{s_k}) \right) \delta(s_j m_j + s_k m_k - m_i) e^{i(s_j\omega_j + s_k\omega_k - \omega_i)t}. \end{aligned} \quad (5.10)$$

In the bulk of the sphere, we assume that the viscous mode matches the corresponding inviscid mode.<sup>1</sup> This allows writing an explicit expression of the spatial structure  $\Phi_j$  as a function of  $m_j$ ,  $\omega_j$  and  $p_j$ . The mathematical expression of the inviscid modes deduced from (5.9) and the linear, rotating Euler equation is then (Kerswell, 1993b):

$$\Phi_j = \begin{bmatrix} \frac{-i}{4 - \omega_j^2} \left( \frac{2m_j}{\rho} p_j + \omega_j \partial_\rho p_j \right) \\ \frac{1}{4 - \omega_j^2} \left( \frac{2\omega_j m_j}{\rho} p_j + 2\partial_\rho p_j \right) \\ \frac{i}{\omega_j} \partial_z p_j \end{bmatrix}. \quad (5.11)$$

This expression will prove particularly useful to compute non-linear feedback of zonal flows on the resonant modes.

### 1.3 Direct forcing of geostrophic zonal flows

As it is known from the theoretical result of Greenspan (1969), the inviscid eigenmodes cannot transfer energy to geostrophic flows via non-linear interaction. It is not the case, however, for the viscous modes, whose non-linear self-interaction has been shown experimentally (Sauret et al., 2010; Morize et al., 2010; Sauret et al., 2014) and numerically (Tilgner, 2007b) to generate significant zonal winds, *i.e.* axisymmetric mean flows.

It appears clearly from the non-linear term (5.10) that a geostrophic mode  $i$  with  $\omega = 0$  and  $m_i = 0$  can receive energy from a single mode  $j = k$  provided that  $s_j = -s_k$ . The non-linear transfer is then shortened into:

$$a_j a_j^* \left( \Phi_i \mid \text{NL}(\Phi_j^{s_j}, \Phi_j^{-s_j}) \right) \equiv a_j a_j^* F(E). \quad (5.12)$$

Again, the dot product acting on the spatial structure of the modes in the preceding expression would strictly cancel out for inviscid eigenmodes, and the relevant contributions come here from viscous corrections. The interaction term  $F$  is, therefore, a function of the Ekman number  $E$ , but also of the inertial mode.

<sup>1</sup>Note that this assumption is not true in the case of spherical shells for which modes are confined on thin attractors whose thickness depends on the viscosity.

## 1.4 Back-reaction of the zonal flow on the resonant waves.

Consider an inertial wave mode  $\Phi_w = [\Phi_\rho, \Phi_\phi, \Phi_z]$  with wave number  $m$ . As inferred from the amplitude equations (5.7) and (5.10), this mode may interact with a zonal flow, that is, a  $z$ -invariant, axisymmetric flow  $\Phi_g$  with  $m_g = 0$ . According to 5.11,  $\Phi_g$  inferred from its pressure function  $p_g(\rho)$  writes:

$$\Phi_g = \frac{1}{2} \frac{\partial p_g}{\partial \rho} e_\phi. \quad (5.13)$$

The dot product quantifying the non-linear interaction (see equation (5.10)) has the following explicit expression:

$$(\Phi_w | \text{NL}(\Phi_w, \Phi_g)) = -\frac{1}{2} \int_{r,z} [\Phi_w^* \cdot (\Phi_g \times \nabla \times \Phi_w) + \Phi_w^* \cdot (\Phi_w \times \nabla \times \Phi_g)] dr dz. \quad (5.14)$$

With the equations (5.11) and (5.13), taking into account that the pressure function  $p_g$  is real, the integrands are simplified as:

$$\Phi_w^* \cdot (\Phi_g \times \nabla \times \Phi_w) = \frac{m^2}{2\rho} \partial_\rho p_g (\Phi_r^* \Phi_z - \Phi_r \Phi_z^*) \quad (5.15)$$

$$\Phi_w^* \cdot (\Phi_w \times \nabla \times \Phi_g) = \frac{1}{2\rho} \partial_\rho (\rho \partial_\rho p_g) (\Phi_\rho^* \Phi_\phi - \Phi_\phi^* \Phi_\rho) \quad (5.16)$$

which are both imaginary scalars. To conclude, the back-reaction term of the geostrophic modes (with amplitude  $a_g$ ) on the waves (with amplitude  $a_w$ ) simply writes:

$$(\Phi_w | \text{NL}(\Phi_g, \Phi_w)) a_g a_w = i\mu a_w a_g \quad (5.17)$$

where  $\mu$  is a real coefficient. This back-reaction occurs in the bulk of the fluid: it corresponds to the advection and deformation of a bulk-filling inertial mode by a bulk-filling zonal wind, contrary to the wave interaction giving rise to the geostrophic zonal flow which is concentrated in the viscous boundary layer.

## 1.5 The reduced model

Building on the preceding sections, we can now propose a simple reduced model involving a geostrophic zonal flow and the inertial waves undergoing parametric resonance. Consider  $a_1$ ,  $a_2$  and  $a_g$  the amplitudes of the resonant modes and the geostrophic mode respectively, the most simple model one can write is:

$$\begin{cases} \dot{a}_1 = Ro_i I_1 a_2 + i\mu_1 a_1 a_g - D_1 a_1 \\ \dot{a}_2 = Ro_i I_2 a_1 + i\mu_2 a_2 a_g - D_2 a_2 \\ \dot{a}_g = F(E)(|a_1|^2 + |a_2|^2) - D_g a_g \end{cases} \quad (5.18)$$

where all the coefficients  $I_{1,2}$ ,  $\mu_{1,2}$ ,  $D_{1,2,g}$ ,  $F(E)$  are real, and that the interaction term  $F$  is the same for both modes. The first terms in the two resonant waves amplitude equations simply correspond to the calculation of section 3.3 in chapter 1, which has thus not been repeated.

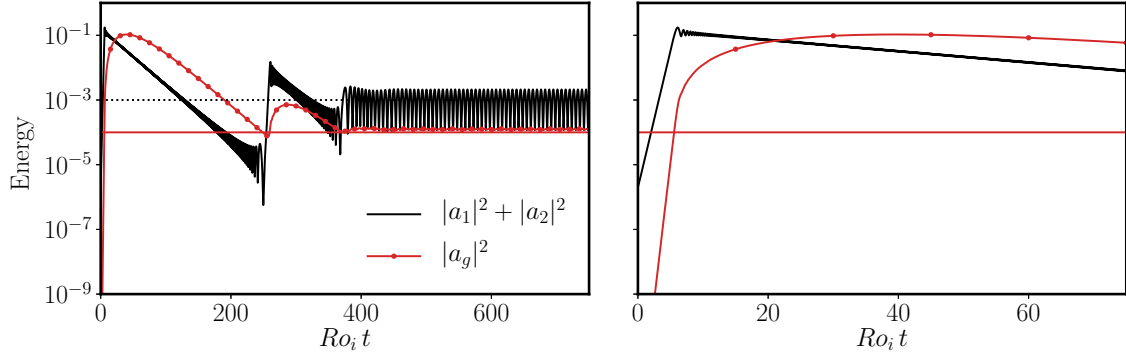


**Figure 5.1:** Typical time evolution of the energy of the wave modes  $a_1$  and  $a_2$  and the geostrophic mode  $a_g$  according to the reduced model (5.18) of the non-linear behaviour of the elliptical instability. The control parameters are  $Ro_i = 5 \times 10^{-2}$ ,  $I_{1,2} = 1$ ,  $\mu_1 = -\mu_2 = 5$ ,  $D_{1,2,g} = 1 \times 10^{-3}$  and  $F = 5 \times 10^{-3}$ . Time is normalised by a non-linear time scale  $Ro_i^{-1}$ . The horizontal red line materialises the energy associated to the fixed point value of  $a_g$  given by (5.25), or equivalently the critical amplitude  $a_g$  above which the growth rate of inertial modes is zero according to (5.23). The horizontal dashed line materialises the energy associated to the fixed point values of  $a_1$  and  $a_2$  given by relation (5.27). It may be noticed that the resonant modes energy decays when the amplitude of the geostrophic modes crosses the fixed point value materialised by the red line, as expected from the discussion in section 1.5.

### Saturation by detuning

We can carry out a simple analysis of the amplitude equations by assuming that  $a_g$  is constant and analysing the behaviour of the system. To facilitate the discussion, we can also assume the dissipation to be negligible compared to the interaction with the base flow. The reduced model then writes:

$$\begin{cases} \dot{a}_1 = Ro_i I_1 a_2 + i\mu_1 a_1 a_g \\ \dot{a}_2 = Ro_i I_2 a_1 + i\mu_2 a_2 a_g . \end{cases} \quad (5.19)$$

Let us first ignore the elliptical instability by assuming that  $Ro_i = 0$ . The linear system (5.19) is then solved by

$$a_1 \propto \exp(i\mu_1 a_g t) \quad \text{and} \quad a_2 \propto \exp(i\mu_2 a_g t) . \quad (5.20)$$

In presence of a geostrophic mode, the inertial modes eigen frequencies  $\omega_{1,2}$  are modified according to:

$$\omega'_1 = \omega_1 + \mu_1 a_g \quad \text{and} \quad \omega'_2 = \omega_2 + \mu_2 a_g . \quad (5.21)$$

As explained in chapter 1 section 3.2 the two resonant modes frequencies must satisfy the resonance condition, that is,  $|\omega_1 - \omega_2|$  must be equal to the forcing frequency ( $2\gamma$  for tides and  $f$  for librations). In presence of a geostrophic zonal flow, and if  $\mu_1 \neq \mu_2$ , the resonance condition cannot be fulfilled anymore. As a consequence, the elliptical instability is disrupted by frequency detuning induced by the zonal wind.

This qualitative understanding may be formally validated by a mathematical analysis of the system of ordinary differential equations (5.19). This system has two eigenvalues that are complex conjugate. When the geostrophic amplitude is sufficiently small, more precisely when

$$\left( \frac{\mu_1 - \mu_2}{2} \right)^2 a_g^2 < Ro_i^2 I_1 I_2 , \quad (5.22)$$

the eigenvalue  $\lambda_p$  yielding a positive growth rate of the inertial waves is:

$$\lambda_p = \sqrt{Ro_i^2 I_1 I_2 - \left(\frac{\mu_1 - \mu_2}{2}\right)^2 a_g^2} + i \frac{\mu_1 + \mu_2}{2} a_g. \quad (5.23)$$

At larger geostrophic amplitudes, both eigenvalues—noted  $\lambda_{\pm}$ —are imaginary quantities when  $\mu_1 \neq \mu_2$ :

$$\lambda_{\pm} = i \sqrt{\left(\frac{\mu_1 - \mu_2}{2}\right)^2 a_g^2 - Ro_i^2 I_1 I_2} \pm i \frac{\mu_1 + \mu_2}{2} a_g. \quad (5.24)$$

We retrieve the result of the qualitative analysis: the growth rate of the elliptical instability decreases to 0 as the amplitude of the zonal wind increases, provided that  $\mu_1 \neq \mu_2$ . In short, the rate of energy transfer from the base flow to the waves is decreased by non-linear detuning induced by the zonal wind.

A typical time evolution of the reduced model (5.18) is given in figure 5.1. The process at early times is the following: as the resonant waves grow in amplitude, they directly force the geostrophic mode, whose amplitude increases with a rate twice larger than the resonant waves. The latter induces a frequency detuning of the resonant waves and disrupt the interaction with the forcing flow when the geostrophic amplitude becomes too large, typically when the resonance condition (5.22), materialised by a red line in figure 5.1, is no more satisfied. The waves and the geostrophic mode then undergo viscous dissipation, until the detuning is small enough to let the resonant waves resonate again. Although this model is very simple, it does capture, at least at early times, the dynamics reported for instance by Barker and Lithwick (2013) of cyclic resonance and collapse of the elliptical instability and which will be detailed in the next chapter. Later on, with the present model, the geostrophic amplitude reaches a steady state. The growth rate of the resonant modes is null, which means that

$$\left(\frac{\mu_1 - \mu_2}{2}\right)^2 a_g^2 \gtrsim Ro_i^2 I_1 I_2.$$

As a consequence, at this stage, the resonant modes amplitudes oscillate at a slow rate given by the eigenvalues  $\lambda_{\pm}$  (see relation (5.24)).

## 1.6 Saturation amplitudes of the modes

The reduced model (5.18) has a non-trivial fixed point. It is found by stating that the two-first equations which are linear respective to  $a_1$  and  $a_2$  must have a non-zero solution. It compels the following relation on the amplitude  $a_g$ :

$$a_g^2 = -\frac{Ro_i^2 I_1 I_2}{\mu_1 \mu_2 + i(\mu_1 D_1 + \mu_2 D_2)}. \quad (5.25)$$

This relation is simplified in the small dissipation limit, *i.e.* assuming that  $D_{1,2} \ll 1$ . We also assume that  $\mu_1 = -\mu_2$  and  $D_1 = D_2$  so that  $a_g$  is real, although it does not change the absolute value of this amplitude. With these hypotheses, we find for the geostrophic mode amplitude:

$$a_g^2 = Ro_i^2 \frac{I_1 I_2}{\mu_1^2}. \quad (5.26)$$

The saturation amplitudes of the resonant modes are deduced from the last equation of the reduced model (5.18):

$$|a_1|^2 = |a_2|^2 = \frac{D_g}{2F(E)} a_g = Ro_i \frac{D_g}{2F(E)} \frac{\sqrt{I_1 I_2}}{\mu_1}. \quad (5.27)$$

We will assume for what follows that the amplitude of this fixed point gives a proxy for the respective saturation amplitudes of the resonant waves and the geostrophic modes. Note that in the numerical resolution of the system (5.18), the long time values of the energy contained in the waves and geostrophic modes is consistent with the fixed points derived in equations (5.25) and (5.27), as indicated in figure 5.1. In addition, the amplitude of the geostrophic flow is slightly higher than the fixed point value, which is coherent with the fact the resonant modes have a null growth rate.

## 1.7 Conditions for additional triadic resonances

Let us assume that the resonant waves and geostrophic modes have amplitudes given by what has been derived in the preceding paragraph. We now explore the conditions under which a triadic resonance involving a resonant mode and two daughter waves may be excited. We assume for simplicity that the resonant wave 1 is maintained to the fixed point amplitude  $a_1$ , and that the daughter modes undergo detuning with the same coefficients  $\pm\mu_1$  as the resonant waves. We also simplify the derivation by assuming that the triadic resonance is inviscid. The growth rate  $\sigma_t$  of the daughter waves then writes:

$$\sigma_t = \sqrt{C^2 |a_1|^2 - \mu_1^2 a_g^2} \quad (5.28)$$

where  $C$  is a coupling coefficient. This growth rate is real and positive provided that:

$$C^2 |a_1|^2 > \mu_1^2 a_g^2. \quad (5.29)$$

Using the results of the preceding subsection, the condition on the input Rossby number for triadic resonances to grow is therefore:

$$Ro_i < \frac{C^2}{2\sqrt{I_1 I_2}} \frac{D_g(E)}{2F(E)}. \quad (5.30)$$

We therefore have found an upper bound on the forcing amplitude below which the saturation of the elliptical instability should be dominated by non-linear transfers towards waves. Although the mechanism explored in the present chapter is different, this result is consistent with the experimental results and the finite Rossby number instability analysis carried out in the previous chapter. This upper bound is *a priori* a non-trivial function of the Ekman number, and the variety of boundary layers that may be encountered in rotating flows (Roberts and Stewartson, 1963; Tilgner, 2007a; Sauret and Le Dizès, 2013).

## 1.8 Universality of the upper bound

According to the derivation of the preceding paragraph, the resonant inertial modes reach a saturation amplitude proportional to  $Ro_i^{1/2}$  (see relation (5.27)), which is in contradiction

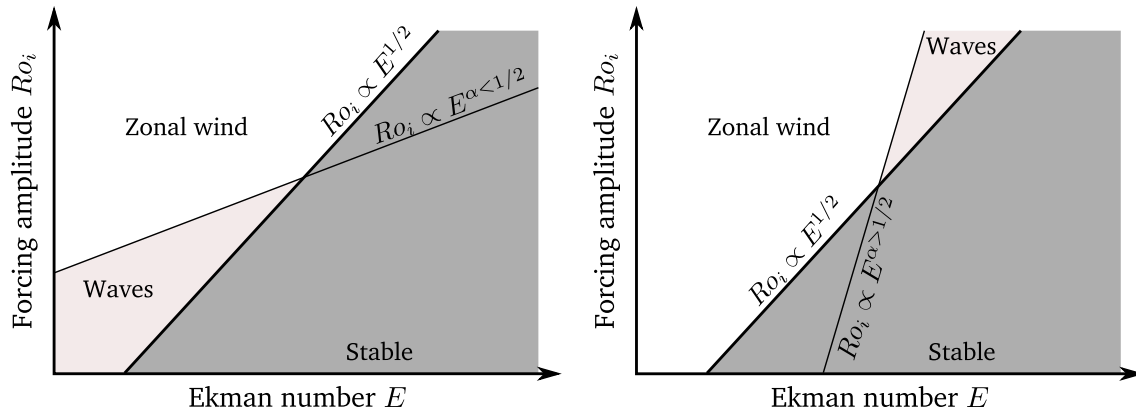


**Figure 5.2:** Schematic cartoon of the expected regime diagrams in terms of Ekman number and forcing amplitude depending on the value of the exponent of the power law of the Ekman number of the function  $D_g(E)/F(E)$ . The geophysical limit is located at low  $E$  and low  $Ro_i$ . The thick line materialises the threshold of the elliptical instability  $Ro_i \propto E^{1/2}$ . We show that a wave-dominated regime is expected in planetary cores only if the exponent of the upper bound is below  $1/2$ .

with the qualitative scaling in  $Ro_i$  of section 1 in chapter 2, and also with the numerical results presented in Grannan et al. (2017), which also indicate a  $\propto Ro_i$  amplitude saturation. The  $Ro_i^{1/2}$  scaling has been found by assuming that the saturation is entirely due to the dissipation of the geostrophic modes whereas it could rather come from a non-linear cascade of energy towards other modes that was not included in the model.

Nevertheless, the relation (5.30) may be more general than a consequence of a simple low order model. To prove that, let us consider that the saturation of the resonant modes is entirely driven by non-linear processes, so that their amplitudes reach a saturation value  $a_{1,2} \sim Ro_i$ . The direct forcing results in a zonal wind with amplitude  $u_g$  that we consider, as earlier, to be determined by a balance between forcing and dissipation. The last equation of the system (5.18) thus yields:

$$u_g \propto Ro_i^2 \frac{F(E)}{D_g(E)}. \quad (5.31)$$

We infer that the amplitude ratio between the three-dimensional wave modes and the zonal wind is:

$$\frac{u_{3d}}{u_g} \propto \frac{1}{Ro_i} \frac{D_g(E)}{F(E)}. \quad (5.32)$$

We retrieve that three-dimensional wave modes dominate provided that the forcing amplitude  $Ro_i$  is smaller than the upper bound function, that is:

$$Ro_i \lesssim \frac{D_g(E)}{F(E)}. \quad (5.33)$$

## 1.9 Conclusion: the condition for a wave-dominated regime in geophysics

To conclude, the upper bound on the wave-dominated regime  $Ro_i \propto D_g(E)/F(E)$  must be compared to the threshold of the instability  $Ro_i \propto E^{1/2}$ . Let us assume that  $D_g(E)/F(E)$

eventually follows a —positive— power law of the Ekman number as  $E \rightarrow 0$ . Two very different situations may be considered, they are shown in figure 5.2. A wave-dominated regime in the geophysical limit  $Ro_i$ ,  $E \rightarrow 0$  is possible only if the exponent of the upper bound power law is lower than  $1/2$ . To predict the saturation of the elliptical instability in planetary cores or stellar interiors, it is therefore important to quantify the upper bound function in the asymptotic limit of small forcing and dissipation.

## 2. The upper bound on the wave-dominated regime

The present section focuses on quantifying the upper bound function  $D_g(E)/F(E)$  and its dependence with the Ekman number. We first recall that this upper bound has in fact been determined in previous numerical and experimental studies, but for certain inertial waves only (Tilgner, 2007b; Sauret et al., 2010; Morize et al., 2010; Sauret et al., 2014). We then introduce a numerical procedure to systematically determine the upper bound function.

### 2.1 Predictions based on previous works

To determine the upper bound ratio, one simple experiment is to maintain a wave to a constant amplitude  $a_0$ , the amplitude of the forced zonal wind  $a_g$  in steady state is then:

$$a_g = \frac{F(E)}{D_g(E)} |a_1|^2. \quad (5.34)$$

The quantification of this non-linear transfer by the method of imposing a mode has been done numerically by Tilgner (2007b) but also experimentally by Morize et al. (2010) and Sauret et al. (2014). All these studies show that the upper bound function  $D_g(E)/F(E)$  tends to be a positive power law of the Ekman number, that is, the amplitude of the zonal wind increases as  $E$  is lowered. Nevertheless, the exponent of the power law depends on the excited mode. Morize et al. (2010) measured  $D_g(E)/F(E) \propto E^{0.3}$  for a mode with eigen frequency  $\omega = 0.38$ . In addition, Sauret et al. (2014) measured  $D_g(E)/F(E) \propto E^{0.64}$  at  $\omega = 0.384$  and  $D_g(E)/F(E) \propto E^{2.1}$  at  $\omega = 0.178$ . Our aim is therefore to carry out a systematic study to find scalings of the zonal wind forcing with the Ekman number. We then propose regime diagrams of the elliptical instability and clarify its dependence with the forcing frequency.

### 2.2 The process to determine zonal wind forcing

In order to determine the upper bound function  $D_g(E)/F(E)$  for the inertial eigenmodes of the sphere, we use the method of Tilgner (2007b) which has been implemented to study zonal winds forced in spherical shells by attractor modes. It proceeds in two steps, and the first one is to determine the viscous inertial eigenmodes of a sphere including the no-slip boundary layers, the latter being crucial to the zonal wind forcing. We therefore solve the eigenvalue problem corresponding to the linearised, rotating Navier-Stokes equation:

$$\lambda \mathbf{u} + 2\mathbf{e}_z \times \mathbf{u} + \nabla p - E \nabla^2 \mathbf{u} = 0 \quad (5.35)$$

or equivalently the vorticity equation:

$$\lambda \nabla \times \mathbf{u} + 2\mathbf{e}_z \cdot \nabla \mathbf{u} - E \nabla^2 \nabla \times \mathbf{u} = 0, \quad (5.36)$$

with all three components of the velocity vanishing at the boundaries.

The second step is to compute the zonal wind  $\mathbf{u}_g$  forced by the non-linear self-interaction of an eigenmode  $\Psi$ , *i.e.* to solve the following linear equation:

$$2\mathbf{e}_z \times \mathbf{u}_g + \nabla p_g - E \nabla^2 \mathbf{u}_g = \int_{\phi=0}^{2\pi} \Psi \times (\nabla \times \Psi) = \Phi \times (\nabla \times \Phi) = \mathcal{F} \quad (5.37)$$

or the corresponding vorticity equation. The azimuthal average ensures the geostrophic mode is  $\phi$  invariant, and the absence of time dependence in this equation should ensure that it is geostrophic. The solution to equation (5.37) should thus be mostly invariant along the rotation axis. The upper bound function  $F(E)/D_g(E)$  is simply determined by:

$$\frac{F(E)}{D_g(E)} = \sqrt{(\mathbf{u}_g | \mathbf{u}_g)}. \quad (5.38)$$

where  $\mathbf{u}_g$  is the solution to equation (5.37). The method to determine the upper bound thus requires solving two linear problems.

## 2.3 Numerical method

We briefly describe hereafter the numerical method implemented to proceed to the two steps mentioned in the preceding section. It is based on the work of Tilgner (2007b) and Vidal and Schaeffer (2015).

### Solving the eigenvalue problem

To solve the eigenvalue problem (5.35) in a sphere or a spherical shell, we use the open-source code SINGE which has been implemented by Vidal and Schaeffer (2015). It builds on an efficient PYTHON library performing fast spherical harmonics decomposition (Schaeffer, 2013). The flow  $\mathbf{u}$  is decomposed onto the basis of vector spherical harmonics (Rieutord, 1987; Rieutord and Valdetaro, 1997) in spherical coordinates  $(r, \theta, \phi)$ :

$$\mathbf{u}(r, \theta, \phi) = \sum_{lm} [u_{lm}(r)\mathbf{R}_{lm}(\theta, \phi) + v_{lm}(r)\mathbf{S}_{lm}(\theta, \phi) + w_{lm}(r)\mathbf{T}_{lm}(\theta, \phi)] \quad (5.39)$$

where the vector fields  $\mathbf{R}_{lm}$ ,  $\mathbf{S}_{lm}$  and  $\mathbf{T}_{lm}$  are defined using the spherical harmonics  $Y_{lm}$  as:

$$\mathbf{R}_{lm} = Y_{lm}\mathbf{e}_r, \quad \mathbf{S}_{lm} = \nabla Y_{lm} \quad \text{and} \quad \mathbf{T}_{lm} = \nabla \times \mathbf{R}_{lm}. \quad (5.40)$$

The indices  $l$  and  $m$  are the number of zeros of the function  $Y_{lm}$  when  $\theta$  is varied in  $[0, \pi]$  and  $\phi$  is varied in  $[0, 2\pi]$  respectively. Because the field  $\mathbf{u}$  is divergence-free, the coefficients  $u_{lm}(r)$  and  $v_{lm}(r)$  are both related to a single set of coefficients  $V_{lm}$  such that:

$$u_{lm}(r) = \frac{l(l+1)}{r} V_{lm}(r) \quad \text{and} \quad v_{lm}(r) = \frac{1}{r} \frac{\partial r V_{lm}}{\partial r}. \quad (5.41)$$

The coefficients  $V_{lm}$  and  $w_{lm}$  are in fact the decomposition in spherical harmonics of the poloidal and toroidal scalars which can also be used to describe the field  $\mathbf{u}$  (Vidal and Schaeffer, 2015; Rieutord and Valdettaro, 1997):

$$\mathbf{u} = \sum_{lm} [\nabla \times (\nabla \times (\mathbf{r} V_{lm} Y_{lm})) + \nabla \times (\mathbf{r} w_{lm} Y_{lm})], \quad (5.42)$$

$\mathbf{r}$  being the position vector.

Substituting the decomposition (5.39) into the vorticity equation (5.36) gives for each  $(l, m)$  a pair of second order differential equations with the radius  $r$  as a variable. They both couple the  $u_{lm}$  and  $w_{lm}$  coefficients together and with the coefficients  $u_{l', m'}$  and  $w_{l', m'}$  of other  $(l', m')$  pairs. From equation (5.36), The SINGE code computes the eigenmodes of a sphere at a given azimuthal wave number  $m$ . The radius  $r$  is discretised over  $N_r$  grid points and the derivatives are computed with second order accurate finite differences. The grid can be chosen to be irregular to account for sharper variations close to the boundaries. The spherical harmonics decomposition is truncated to  $N_l$  modes ranging from  $l = m$  to  $l = m + N_l$ . The coupled ordinary differential equations on the coefficients  $V_{lm}$  and  $w_{lm}$  transcribing the vorticity equation (5.36) therefore reduce to a set of  $\sim 2 \times (N_l/2) \times N_r$  linear equations.<sup>2</sup> Calling  $\mathbf{X}$  a vector containing all the discretised coefficients  $u_{lm}[r_i]$  and  $w_{lm}[r_i]$ , the system of linear equations takes the form of a generalised eigenvalue problem:

$$\mathbb{L}_i \mathbf{X} = \lambda \mathbb{L}_e \mathbf{X} \quad (5.43)$$

where  $\mathbb{L}_i$  and  $\mathbb{L}_e$  are two sparse matrices (see Vidal and Schaeffer (2015) for further details). These matrices also include the boundary conditions, *i.e.* here the cancellation of all coefficients at solid boundaries.

The generalised eigenvalue problem (5.43) is solved with the parallelised routines of the PETSc and SLEPc libraries to find the eigenvalues  $\lambda$  and the corresponding eigenvectors. To find a mode oscillating at frequency  $\omega$ , we look for specific eigenvalue  $\lambda$  whose imaginary part is in a close neighbourhood of  $\omega$ ; the code then returns the modes with the smallest real part, *i.e.* the modes with the lowest dissipation rate. The spatial structure of the eigenmodes and the corresponding eigenvalues are saved into a file that can be used for further computations.

### Computing the structure of the zonal flow

From the the spatial structure of an eigenmode  $\mathbf{u}_e$  associated with a wave number frequency  $\omega_e$ , we can compute  $\nabla \times \mathbf{u}$  with spectral accuracy using the spherical harmonic decomposition of the mode. By azimuthal averaging, it is then straightforward to compute the non-linear forcing term  $\mathcal{F}$  (see equation (5.37)). With the spatial discretisation described in the previous paragraph, solving the curl of the equation (5.37) is then tantamount to inverting the linear system:

$$\mathbb{L}_i \mathbf{Y} = \mathbf{F} \quad (5.44)$$

where  $\mathbf{Y}$  is the vector describing the spatial structure of the geostrophic mode to be computed. The operator  $\mathbb{L}_i$  is the same as in the generalised eigenvalue problem (5.43), and  $\mathbf{F}$  is a vector transcribing the spatial structure of  $\nabla \times \mathcal{F}$  decomposed into spherical harmonics and discretised along the radius. As earlier, this sparse matrix inversion is carried out using the PETSc and SLEPc libraries.

<sup>2</sup>For symmetry reasons, half the coefficients of both  $V_{lm}$  and  $w_{lm}$  are null when  $l$  is varied.

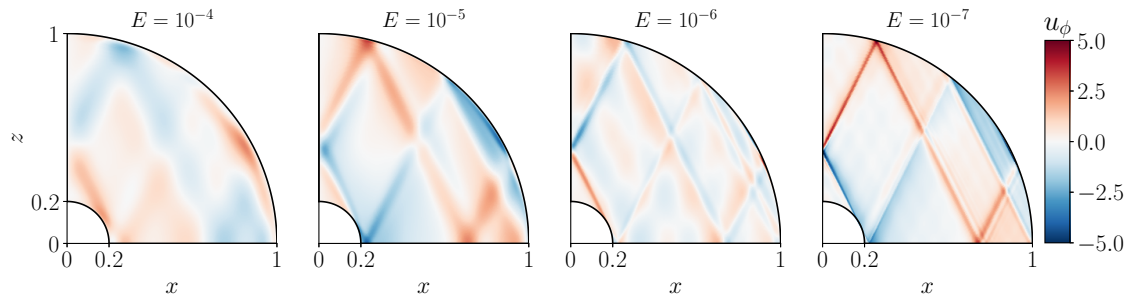


**Figure 5.3:** Eigenmodes in a spherical shell in the reference case  $\omega_e = 0.88$  of Tilgner (2007b),  $m = 2$  and  $r_i = 0.2$  at decreasing Ekman numbers. We show a meridional cut of the azimuthal velocity. Note that the field is symmetric respective to the horizontal axis, and that this structure is modulated by a  $\sin(2\phi)$  around the  $z$  axis.

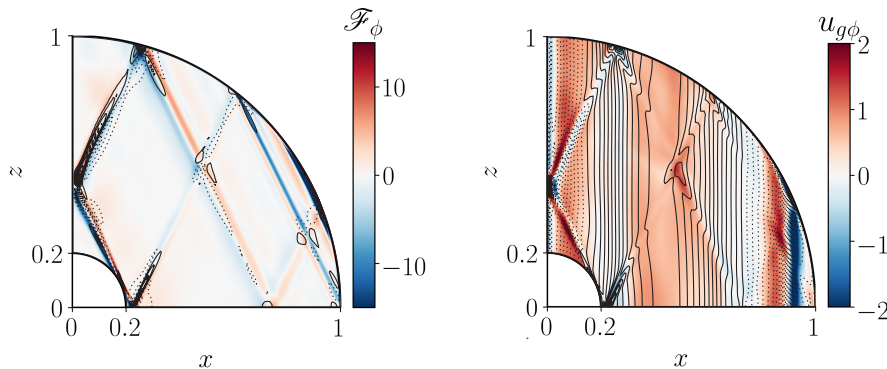


**Figure 5.4:** Superposition of the azimuthal component of the non-linear forcing field (left) and the geostrophic flow (right), obtained with the present method (colour map) and by Tilgner (2007b) (contours, dashed is negative and plain is positive).

## 2.4 Testing the numerical process

The process described above follows the work of Tilgner (2007b). The latter uses stress-free boundary conditions, which could not be implemented in the present code. Nevertheless, we use this previous study as a reference in the implementation of the mean flow computation.

We compare the methods in the case of a spherical shell of outer radius  $r_o = 1$  and inner radius  $r_i = 0.2$ . The frequency of the eigenmode on which the comparison is based is  $\omega_e = 0.88$  and it has an azimuthal wave number  $m = 2$ . Meridional cuts of the computed eigenmodes determined with the SINGE code are displayed in figure 5.3. At this frequency and for this geometry, the inertial mode of the spherical shell is an attractor, the energy of the flow being focused along lines at vanishing Ekman number. The typical thickness of the attractor increases with the Ekman number (see the theoretical development of Ogilvie (2005); Jouve and Ogilvie (2014)).

We also show in figure 5.4 the forcing field  $\mathcal{F}_\phi$  and the resulting geostrophic zonal flow  $u_{g\phi}$ ; we superpose both our calculations and the results presented in Tilgner (2007b) to enhance the comparison. We first notice that, as expected, the steady zonal wind is mostly invariant with the height  $z$ . The location of the largest forcing and the sign changes in this quantity are overall in agreement between the two realisations of the method described in sections 2.2 and 2.3. Some discrepancies are noticeable between the two processes, especially

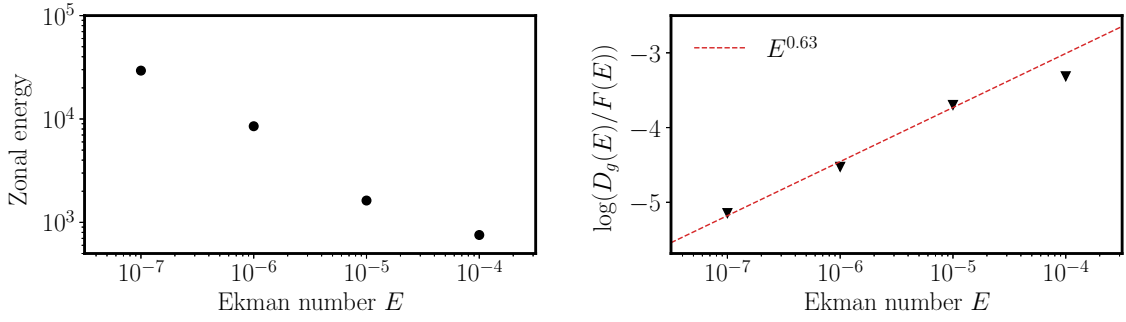


**Figure 5.5:** Determination of the zonal flow energy ( $\mathbf{u}_g | \mathbf{u}_g$ ) (left) and the corresponding upper bound function  $D_g(E)/F(E)$  in the test case of a spherical shell with an eigenmode at  $\omega_e = 0.88$  and  $m = 2$  (right).

in the zonal flow, possibly owing to the different boundary conditions; such inconsistency caused by boundary conditions is indeed a known feature that has been reported for instance by Livermore et al. (2016) and is thus not surprising.

Lastly, we show in figure 5.5 the evolution of the energy of the zonal flow ( $\mathbf{u}_g | \mathbf{u}_g$ ) determined with our method, and the upper bound function dependence with the Ekman number, the latter following a  $\sim -0.6$  power law. The increase of the zonal energy as the Ekman number is decreased is steeper in the calculation of Tilgner (2007b), although the present values are within a factor two compared to the preceding study at  $E < 10^{-5}$ . This is, again, likely to be a consequence of the boundary condition used here which induces an additional forcing in the boundary layer, especially at large Ekman numbers. Despite these discrepancies, the comparison between the results of Tilgner (2007b) and ours is rather convincing.

## 2.5 Application to the full sphere

### Determination of the upper bound

Now that the method of Tilgner (2007b) is implemented and tested, we use it in the case of the full sphere to determine the upper bound function  $D_g(E)/F(E)$ , as explained in 2.2. We thus explore the amplitude of geostrophic zonal winds driven in the full sphere by inertial modes whose frequency  $\omega$  ranges from 0.221 to 1.98. The result of computing the eigenmodes, the forcing field and the subsequent zonal wind is shown in figure 5.6 for the case  $\omega = 0.880$  and  $m = 2$ , which is the same as in the test apart from the presence of an inner core. In the present case, the modes are no longer attractors, which were specific to the case of the spherical shell. We manage to follow the same global mode structure as the Ekman number is decreased, even though smaller scale variations appear. The typical scale of the forcing field is observed to decrease, and the largest forcing values are focused close to the critical latitude, *i.e.* the points of the solid boundary at latitude  $\theta$  such that  $2 \cos \theta = \omega$ . It corresponds to the point where an inertial wave beam is reflected on itself, and where the boundary layer is thicker than the usual  $E^{1/2}$  scaling and reaches a typical  $E^{1/5}$  thickness over a  $E^{2/5}$  width (Roberts and Stewartson, 1963; Noir et al., 2001; Tilgner, 2007a).

The upper bound on the wave domain as a function of the Ekman number  $E$  is shown in figure 5.7 where it is compared to a typical threshold law of the elliptical instability, *i.e.*  $Ro_i =$

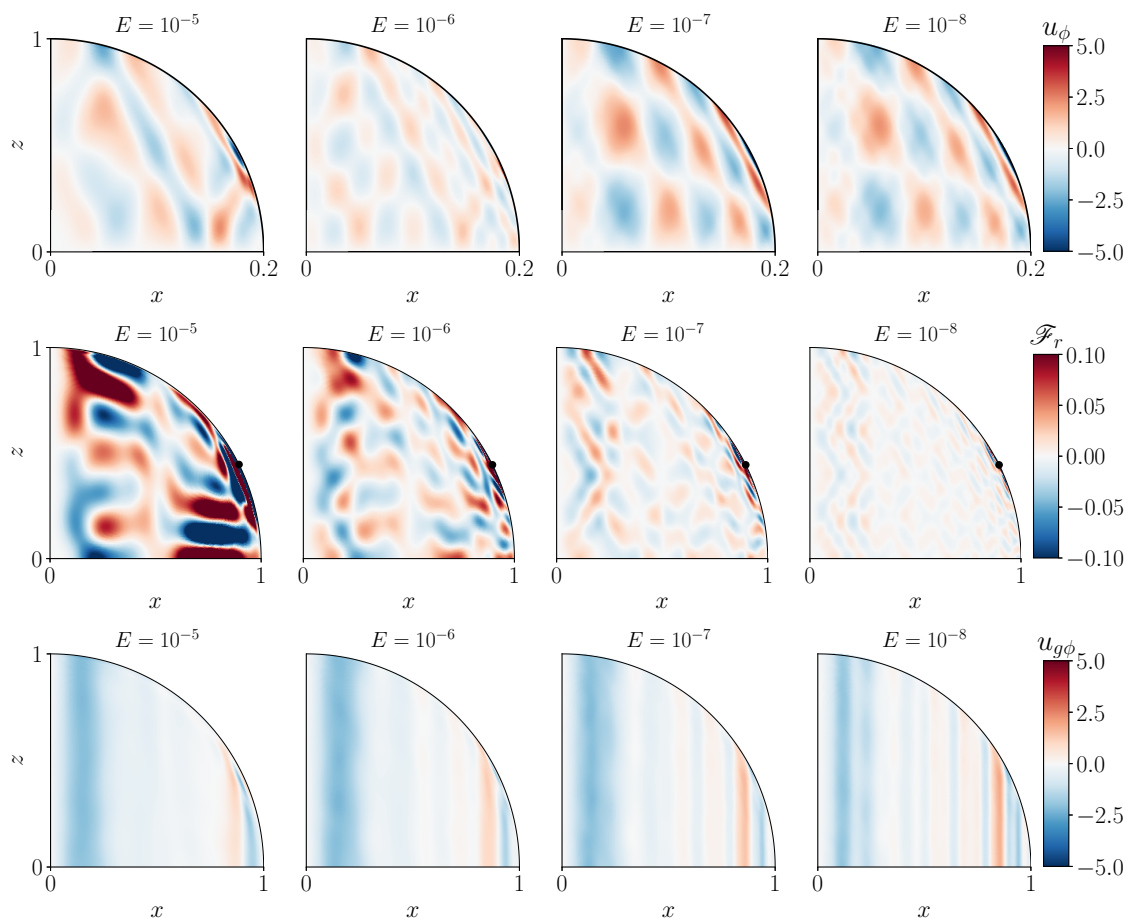


**Figure 5.6:** **Top:** vertical cut of the azimuthal component of the eigenmodes at  $\omega = 0.880$  for  $m = 2$  for decreasing Ekman numbers. **Centre:** vertical cut of the radial component of the forcing field. It is normalised by the spatial rms value of  $\mathcal{F}$ . The black dot highlights the critical latitude  $\theta$  such that  $2 \cos \theta = \omega = 0.88$ . **Bottom:** vertical cut of the zonal wind, normalised by its spatial rms value.

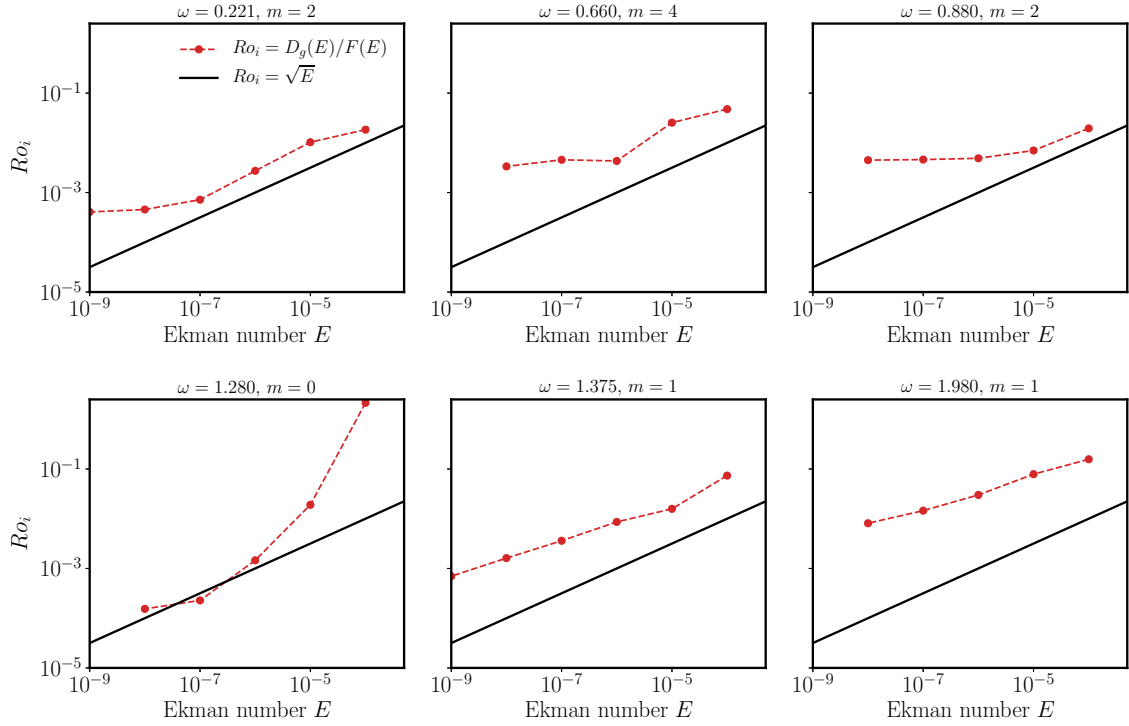


**Figure 5.7:** Representation of the upper bound on the forcing amplitude  $Ro_i$  for the existence of a wave dominated regime ( $Ro_i = D_g(E)/F(E)$ , see equation (5.30)), compared to the typical threshold of the elliptical instability  $Ro_i = \sqrt{E}$ . For each plot, the frequency of the eigenmodes and its chosen wave number  $m$  are given in the title.

$\sqrt{E}$ . The Ekman number has been made as low as possible; however, because the number of eigenmodes increases when  $E$  is decreased, it is sometimes difficult to track a mode down to the low dissipation regimes without switching to another one with a close frequency and a quite different spatial structure.

Despite the variety of behaviours of the wave regime upper bound function  $D_g(E)/F(E)$  at high Ekman number  $E$ , we observe a tendency to a saturation towards a constant at low  $E$  for many different frequencies. In other words, the amplitude of the zonal wind forced by the self-interaction of an inertial mode saturates at low Ekman number, so that direct forcing via viscous boundary layers is unable to drive a geostrophic-dominated flow below a certain forcing amplitude. This observation has already been made by Tilgner (2007b), but with stress-free boundary conditions and only at one frequency. Sauret et al. (2014) also found a saturation of the amplitude of the zonal wind at low Ekman number but it was rather due to centrifugal and shear instabilities undergone by the large amplitude zonal wind driving bulk turbulence. In the few cases where the saturation is not observed, possibly because sufficiently low values of the Ekman number could not be reached, the upper bound is shallower than the threshold of the elliptical instability so that a wave-dominated regime is preferred anyway. To conclude, our results suggest that in weak forcing amplitude and dissipation regimes, direct forcing via viscous boundary layers is unable to drive strong geostrophic modes in planetary interiors, at least when there is no solid inner core.

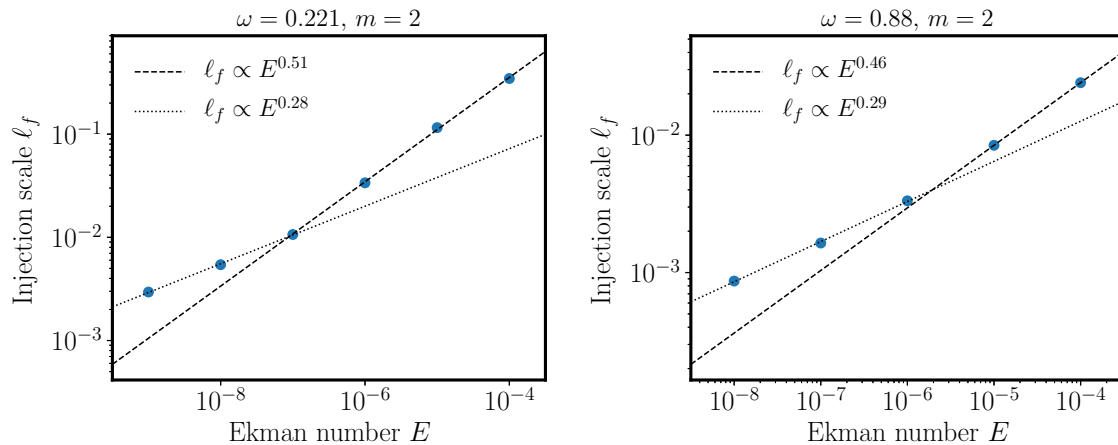


**Figure 5.8:** Computation of the injection scale  $\ell_f$  for two frequencies where the saturation of the upper bound  $D_g(E)/F(E)$  is the most visible. It is fitted with power laws of the Ekman number.

### Understanding the upper bound saturation?

To understand the origin of the saturation of the upper bound function reported in figure 5.7, we follow again the ideas of Tilgner (2007b) to compute a typical forcing scale  $\ell_f$  based on a mode self-interaction. It is computed from the spatial average of the forcing term as follows:

$$\ell_f = \left[ \int_{\rho, \theta} |\Phi \times \nabla \times \Phi|^2 \right]^{-1/2} \quad (5.45)$$

where the integration is performed over the cylindrical coordinates  $(\rho, \theta)$  to compute a volume average of an axisymmetric quantity. In addition,  $\Phi$  is an inertial mode structure normalised such that  $(\Phi|\Phi) = 1$ . The injection scale  $\ell_f$  is shown in figure 5.8 as a function of the Ekman number  $E$  number for two cases where the saturation of the upper bound function is striking (see figure 5.7). It reveals that  $\ell_f(E)$  follows power laws with a striking change of exponents where the upper bound function saturates. At high Ekman number, the power law is close to  $\ell_f \propto E^{-1/2}$  which suggests that the wave forcing is controlled by the Ekman boundary layer. At low Ekman number, the exponent switches to about 0.3.

As observed in figure 5.6, this power law change may be due to a forcing concentrated at the critical latitudes. However, according to Roberts and Stewartson (1963), the thickness of the boundary layer scales like  $E^{1/5}$  and it extends on the surface of the sphere over a band of typical width  $E^{2/5}$ . Neither of these power laws matches the scaling observed in figure 5.8. We have presently no simple explanation for the saturation of the upper bound function relying on typical boundary layer thickness.

## 3. Conclusion on the direct forcing of geostrophic modes by waves

In this chapter, we have investigated direct forcing of geostrophic flows by non-linear self-interaction of inertial modes via boundary layer in order to examine its ability to drive

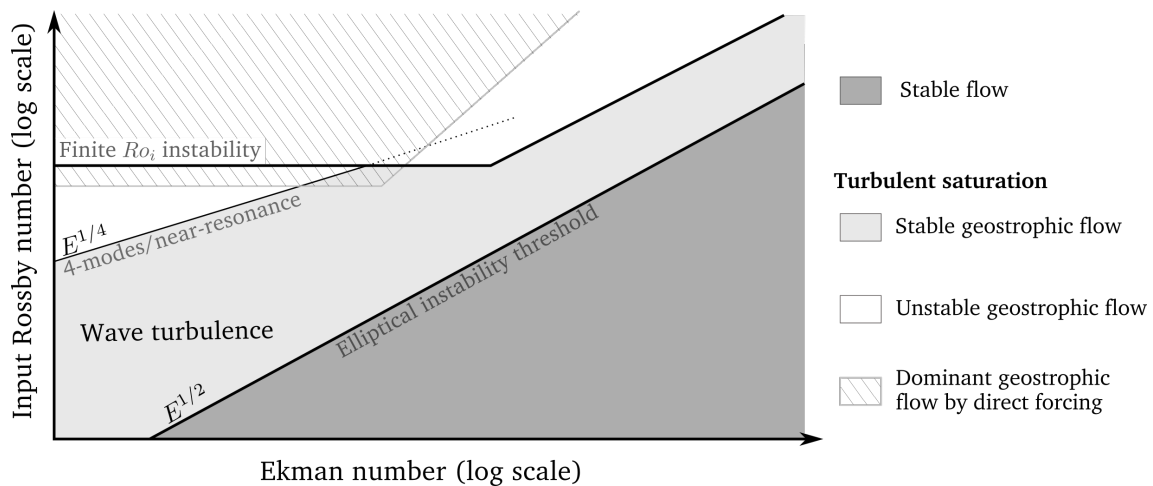


**Figure 5.9:** A schematic regime diagram of the saturation of the elliptical instability based on the results of chapters 4 and 5. This diagram features the different mechanisms transferring energy from waves to geostrophic flows that have been discussed so far. We include the finite wave amplitude—or  $Ro_i$ —instability discussed in chapter 4 and the threshold of four-modes and near-resonant instabilities. We also indicate where direct forcing via boundary layers is expected to drive strong zonal winds. The white and hatched areas materialise control parameters for which a geostrophic type of saturation is expected. Above the elliptical instability threshold, the light grey area materialises the values of the control parameters for which we expect a wave turbulence regime, as found in the experimental study presented in chapter 3. We notice that this regime is expected in the low forcing amplitude and dissipation regimes.

a geostrophic-dominated regime in planetary cores. We have first introduced a reduced dynamical system describing the interaction of two inertial waves in resonant interaction with a tidal or libration base flow. In this reduced model, mode self-interaction—via boundary layers—forces geostrophic, axisymmetric zonal winds. The latter back-reacts on the modes by detuning their frequency, which is formally proved by analytical computation of the wave-vortex interaction. From the analysis of this model, we have derived an upper bound on the forcing amplitude  $Ro_i$  below which we expect a wave-dominated regime of saturation for the elliptical instability. This upper bound is a function of the Ekman number, and it has been investigated with a numerical model based on Tilgner (2007b).

We have noted that because of its simplicity, the reduced model may not capture the non-linear fate of the elliptical instability as the saturation amplitude of the modes is related to the viscous damping of geostrophic flows. Nevertheless, we have shown that if the resonant mode amplitude is directly imposed by non-linear processes and is proportional to  $Ro_i$ , as anticipated in chapter 2 section 1, the same upper bound function applies.

Despite the important simplifications, this chapter brings useful information and results. We recall with a mathematical analysis that the wave-vortex interaction translates into a detuning of the wave frequency which is proportional to the amplitude of the vortex. We have also found that a simple model based on vortex direct forcing and detuning back-reaction partly reproduces cycles of growth and collapse of the elliptical instability, as discussed in 3.1 in chapter 2.

Lastly, we have shown numerically that the upper bound on the wave-dominated regime tends to saturate as the Ekman number is decreased (see figure 5.7). This result has important consequences: there should exist for all frequencies a minimum forcing amplitude below which

direct forcing is unable to drive a geostrophic-dominated saturation of the elliptical instability.

So far, we have proved in the preceding chapter that inertial waves drive geostrophic flows via a finite amplitude instability, but we have also proved that it is unable to drive a geostrophic-dominated saturation below a certain forcing amplitude that is independent of viscous dissipation. In the present chapter, we have shown that direct forcing via viscous boundary layer drives strong geostrophic flows, but is also unable to produce a saturation of the elliptical instability dominated by geostrophic flows below a finite forcing amplitude. In the asymptotic regimes of weak forcing amplitude and dissipation that are relevant for planetary cores, the only remaining mechanisms that could be responsible for a geostrophic saturation are four-mode interaction or near-resonance, discussed in the conclusion of the previous chapter. As shown in figure 5.9, the transition from the wave-dominated to the geostrophic-dominated regimes due to these two mechanisms is shallower than the threshold of the elliptical instability. As a consequence, taking into account all the mechanisms transferring energy from waves to geostrophic flows, we conclude that there should exist a domain at low forcing amplitude and dissipation where the elliptical instability saturates into an inertial wave turbulence, as found in the experimental study (see figure 5.9). Therefore, we conclude that the inertial wave turbulence regime is relevant to the saturation of the elliptical instability in geo- and astrophysical contexts.



# Chapter 6

## A local model to investigate the saturation of the elliptical instability

The experimental study has revealed the existence of two regimes in the saturation of the elliptical instability, one dominated by strong geostrophic vortices and the other dominated by inertial modes in non-linear resonant interaction. Nevertheless, the set-up presented in chapter 3 has not allowed exploring a wide range of parameters, in particular to determine how the wave-dominated regime evolves as both the forcing amplitude and dissipation are decreased and the Reynolds number increases.

In the following, we present an idealised numerical model that simulates the tidally driven instability in a cubic box with periodic boundary conditions. It has been first proposed by Barker and Lithwick (2013) to quantify bulk dissipation driven by mechanical forcing in planets and stars. Instead of simulating the flow in an ellipsoid, the local model solves the dynamics in a cube with periodic boundary conditions and a background tidal base flow using the shearing box model (Rogallo, 1981). Because there is no boundary layer to resolve, this numerical method is able to reach low forcing and low dissipation regimes. It uses in addition efficient pseudo-spectral methods, which are particularly well-suited to investigate the presence of waves in the saturation of the elliptical instability. Although the experiment has already shown strong evidence of a saturation dominated by waves, we aim at further supporting this finding with such a numerical tool, and at exploring this regime in the low dissipation and low forcing limit.

The work presented hereafter also builds on the idealised simulations of wave stability carried out in chapter 4. We have indeed proved that below a minimum Rossby number, or forcing amplitude, geostrophic modes are stable and should remain sub-dominant independently of the Ekman number. At moderate forcing amplitude (the input Rossby number ranging typically from 0.05 to 0.1), Barker and Lithwick (2013) observed only turbulent saturation with strong geostrophic vortices. With the exploration of low forcing regimes, we hope to clarify the role of finite Rossby instabilities in the saturation of the parametric wave resonance.

# 1. The idealised local model

## 1.1 Tidal base flow

In this chapter, we switch to the study of tidally driven elliptical instability, conversely to the experiment which focused on the libration-driven instability. Although the base flows are different, they drive the same kind of parametric subharmonic instability of inertial waves detailed in chapter 1. We consider a planet rotating at rate  $\Omega \mathbf{e}_z$  undergoing tidal deformation due to a moon orbiting at rate  $n \mathbf{e}_z$  as pictured in figure 1.1 in chapter 1. As earlier, we suppose the tidal deformation to be elliptical and uniform in the whole fluid planetary interior. We recall that in the frame of reference following the rotation of the planet, the base flow  $\mathbf{U}_b^\Omega$  has the following analytical expression:

$$\mathbf{U}_b = -\gamma\beta \begin{bmatrix} \sin(2\gamma t) & \cos(2\gamma t) & 0 \\ \cos(2\gamma t) & -\sin(2\gamma t) & 0 \\ 0 & 0 & 0 \end{bmatrix} \begin{bmatrix} x \\ y \\ z \end{bmatrix} = \gamma\beta A(t)\mathbf{X} \quad (6.1)$$

with  $\beta$  the ellipticity and  $\gamma = \Omega - n$  the differential rotation rate between the body and its tidal bulge. This base flow is a solution of the full incompressible Navier-Stokes equations, apart from the boundary layers. As mentioned in the introduction, another natural frame of reference is the “orbital” frame locked to the moon’s orbit and for which the base flow is stationary. Carrying out simulations in the planetary frame is however more suited to characterise structures related to rotation including inertial waves and geostrophic modes.

## 1.2 The local approach to the dynamics

We aim at studying the incompressible perturbations to the basic flow  $\mathbf{U}_b$  defined in (6.1). Instead of modelling the whole planetary fluid layer, we develop a local model to study this perturbation flow in the neighbourhood of a Lagrangian point  $M$  at position  $\mathbf{x}_0(t)$  following the elliptical streamlines such that  $\dot{\mathbf{x}}_0 = \mathbf{U}_b(\mathbf{x}_0(t), t)$ . Although it has been developed by Barker and Lithwick (2013) we propose here a detailed derivation of the local model equations, in first place for the reader to fully understand how it is built, but also to provide a reliable base to include buoyancy effects in the last chapter.

Let us call  $\mathbf{U}^i$  the total velocity field in the planetary frame and  $\mathbf{U}^c$  the total velocity field in the frame bound to  $\mathbf{x}_0$ .  $\mathbf{U}^i$  satisfies the following Navier-Stokes equation:

$$\partial_\tau \mathbf{U}^i + \mathbf{U}^i \cdot \nabla_{\mathbf{x}} \mathbf{U}^i + 2\Omega \mathbf{e}_z \times \mathbf{U}^i = -\frac{1}{\rho} \nabla P^i + \nu \nabla_{\mathbf{x}}^2 \mathbf{U}^i \quad (6.2)$$

where  $\tau$  stands for time,  $\nabla_{\mathbf{x}}$  for the gradient in the  $\mathbf{x} = (x, y, z)$  coordinates,  $P^i$  is the pressure and  $\rho$  is the density of the fluid.  $\mathbf{U}^i$  is the total velocity and includes the base flow  $\mathbf{U}_b(\mathbf{x})$  and velocity perturbations  $\mathbf{u}^i$  so that  $\mathbf{U}^i = \mathbf{U}_b(\mathbf{x}) + \mathbf{u}^i$ . To transform this equation into the frame in translation bound to  $\mathbf{x}_0$ , we proceed to the following coordinate change:

$$\begin{cases} \tilde{\mathbf{x}} &= \mathbf{x} - \mathbf{x}_0(t) \\ t &= \tau . \end{cases} \quad (6.3)$$

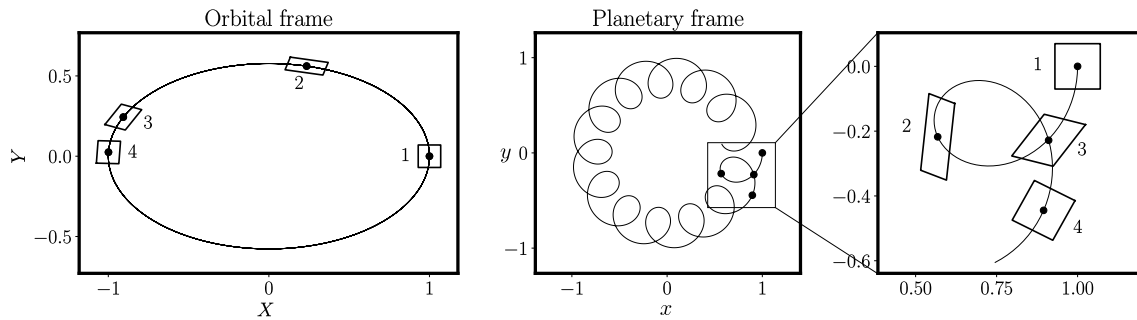


**Figure 6.1:** Trajectory of an initially square patch of fluid for an ellipticity  $\beta = 0.5$  represented in the orbital frame (left) in which the bulge has a stationary shape, and in the planetary frame (right). The four configurations correspond to the same instants. The solid black line materialises the trajectory of the center of the patch. This picture highlights the periodic stretching and shearing undergone by the lagrangian parcel.

The corresponding change in derivatives is  $\nabla_{\mathbf{x}} = \nabla_{\tilde{\mathbf{x}}} = \nabla$  and  $\partial_{\tau} = \partial_t - \mathbf{U}_b \cdot \nabla_{\tilde{\mathbf{x}}}$ . The velocity measured in the frame bound to  $\mathbf{x}_0$  is  $\mathbf{U}^c = \mathbf{U}^i - \mathbf{U}_b(\mathbf{x}_0, t)$ . Transforming the equation (6.2) into this frame yields:

$$\partial_t \mathbf{U}^c + \partial_t \mathbf{U}_b(\mathbf{x}_0) + \mathbf{U}^c \cdot \nabla \mathbf{U}^c + 2\Omega \mathbf{e}_z \times \mathbf{U}^c + 2\Omega \mathbf{e}_z \times \mathbf{U}_b(\mathbf{x}_0) = -\frac{1}{\rho} \nabla P^i(\mathbf{x}_0 + \tilde{\mathbf{x}}) + \nu \nabla^2 \mathbf{U}^c. \quad (6.4)$$

The homogeneous acceleration terms  $\partial_t \mathbf{U}_b(\mathbf{x}_0)$  and  $2\Omega \mathbf{e}_z \times \mathbf{U}_b(\mathbf{x}_0)$  are regarded as homogeneous volume forces. In the frame bound to  $\mathbf{x}_0$  the Navier-Stokes equation reads:

$$\partial_t \mathbf{U}^c + \mathbf{U}^c \cdot \nabla \mathbf{U}^c + 2\Omega \mathbf{e}_z \times \mathbf{U}^c = -\frac{1}{\rho} \nabla P^c - \partial_t \mathbf{U}_b(\mathbf{x}_0) - 2\Omega \mathbf{e}_z \times \mathbf{U}_b(\mathbf{x}_0) + \nu \nabla^2 \mathbf{U}^c \quad (6.5)$$

where we have introduced  $P^c(\tilde{\mathbf{x}}) = P^i(\mathbf{x}_0 + \tilde{\mathbf{x}})$ . As  $\mathbf{U}^c = \mathbf{U}^i - \mathbf{U}_b(\mathbf{x}_0)$ , it is straightforward that  $\mathbf{U}^c = A(t)\tilde{\mathbf{x}} + \mathbf{u}^c$  with  $\mathbf{u}^c = \mathbf{u}^i = \mathbf{u}$ . In the neighbourhood of  $\mathbf{x}_0$ , the perturbed flow  $\mathbf{u}$  satisfies the following equation:

$$\partial_t \mathbf{u} + A(t)\tilde{\mathbf{x}} \cdot \nabla \mathbf{u} + A(t)\mathbf{u} + \mathbf{u} \cdot \nabla \mathbf{u} + 2\Omega \mathbf{e}_z \times \mathbf{u} = -\frac{1}{\rho} \nabla \Pi + \nu \nabla^2 \mathbf{u} \quad (6.6)$$

along with the incompressibility condition  $\nabla \cdot \mathbf{u} = 0$ . The modified pressure includes the homogeneous volume force terms, that is  $\Pi \equiv P^c + \rho(\partial_t \mathbf{U}_b(\mathbf{x}_0) + 2\Omega \mathbf{e}_z \times \mathbf{U}_b(\mathbf{x}_0)) \cdot \tilde{\mathbf{x}}$ .

### 1.3 Lagrangian effects of the base flow

This paragraph aims at exhibiting the Lagrangian trajectory of the point  $M$  at  $\mathbf{x}_0$  to provide a better understanding of the model derived in the preceding paragraphs. The Lagrangian equation  $\dot{\mathbf{x}}_0 = \mathbf{U}_b(\mathbf{x}_0)$  can be solved analytically and the position of  $M$  at any time can be related to the initial position  $(x_{0i}, y_{0i}, z_{0i})$  following:

$$\mathbf{x}_0 = \text{Rot}(-\gamma t) \begin{bmatrix} \cos(\tilde{\omega} t) & -\Lambda \sin(\tilde{\omega} t) & 0 \\ \frac{1}{\Lambda} \sin(\tilde{\omega} t) & \cos(\tilde{\omega} t) & 0 \\ 0 & 0 & 1 \end{bmatrix} \begin{bmatrix} x_{0i} \\ y_{0i} \\ z_{0i} \end{bmatrix} \quad (6.7)$$

where  $\text{Rot}(-\gamma t)$  is a rotation matrix of angle  $-\gamma t$  around the  $z$  axis.  $\tilde{\omega}$  and  $\Lambda$  are defined as follows:

$$\tilde{\omega} = \gamma \sqrt{1 - \beta^2} \quad \text{and} \quad \Lambda = \sqrt{\frac{1 + \beta}{1 - \beta}}. \quad (6.8)$$

The corresponding trajectories are plotted in figure 6.1 for  $\beta = 0.5$ ,  $\gamma = 1$  and an initial condition  $(1, 0, 0)$ . The equivalent trajectory in the orbital frame (consistently aligned with the moon) is also indicated for comparison. In the small  $\beta$  limit, it can be shown that, in the planetary frame, the Lagrangian particle rotates around the  $z$  axis at rate  $-\gamma\beta^2/2$ . Around this slow mean rotation, the particle also accomplished epicycles at a much higher rate  $\gamma/2$  with a displacement of order  $\beta\ell$  and velocity  $\beta\gamma\ell$ , where  $\ell$  is the average distance from the centre of the planetary body. Lastly, the slow mean rotation corresponds to a Stokes drift with velocity  $\sim \gamma\beta^2\ell$ .

To materialise the local effects of the base flow, we also plot in figure 6.1 the trajectories of four points forming an initially square pattern around the tracked point. It can be noticed that this pattern is stretched and sheared during an epicycle and rotates as the particle moves around the  $z$  axis. Note that the slow mean rotation around the  $z$  axis is exaggerated in figure 6.1 because of the very high ellipticity.

## 1.4 Direct numerical simulations in a shearing box

The dynamics of the perturbations  $\mathbf{u}$  to the equilibrium state can be simulated via a decomposition of  $\{\mathbf{u}, \Pi\}$  into plane waves such that:

$$\{\mathbf{u}, \Pi\} = \sum_{\mathbf{k}} \{\hat{\mathbf{u}}_{\mathbf{k}}(t), \hat{\Pi}_{\mathbf{k}}(t)\} e^{i\mathbf{k}(t) \cdot \mathbf{x}}. \quad (6.9)$$

Evolving the wave vectors  $\mathbf{k}$  through time accounts for the periodic shearing induced by the base flow  $\mathbf{U}_b$ . To proceed to numerical simulation of the perturbation flow  $\mathbf{u}$ , the Kelvin wave expansion is discretised and truncated so that the simulated domain is a cube of size  $L$  with periodic boundary conditions. The initial wave vectors  $\mathbf{k}_0$  take the following form:

$$\mathbf{k}_0 = \frac{2\pi}{L} (n_x, n_y, n_z) \quad (6.10)$$

where  $n_{x,y,z}$  are integers ranging from  $-N$  to  $N$ ,  $2/N$  giving an order of magnitude of the ratio between the smallest resolved scale and the size of the cube.

The numerical simulation is equivalent to solving a set of ordinary differential equations. For all  $\mathbf{k}$ , plugging the decomposition (6.9) in the equation (6.6) yields the following ordinary differential equations:

$$\begin{cases} \frac{d\mathbf{k}}{dt} = -\gamma\beta\mathbf{A}^T(t)\mathbf{k} = -\gamma\beta\mathbf{A}(t)\mathbf{k} \\ \frac{d\hat{\mathbf{u}}_{\mathbf{k}}}{dt} = -\gamma\beta\mathbf{A}(t)\hat{\mathbf{u}}_{\mathbf{k}} - 2\mathbf{e}_z \times \hat{\mathbf{u}}_{\mathbf{k}} - i\mathbf{k}\hat{\Pi}_{\mathbf{k}} - k^2 E \hat{\mathbf{u}}_{\mathbf{k}} - \widehat{(\mathbf{u} \cdot \nabla \mathbf{u})}_{\mathbf{k}} \end{cases} \quad (6.11)$$

which is closed by the incompressibility condition  $\mathbf{k} \cdot \hat{\mathbf{u}}_{\mathbf{k}} = 0$ . Time is normalised by the rotation rate  $\Omega$  and lengths by the size of the domain  $L$ . In the preceding equations, the differential rotation rate  $\gamma$  is in rotation rate units, and we have introduced the Ekman number  $E = \nu/(L^2\Omega)$ . The contribution of the non-linear term to each differential equation is computed

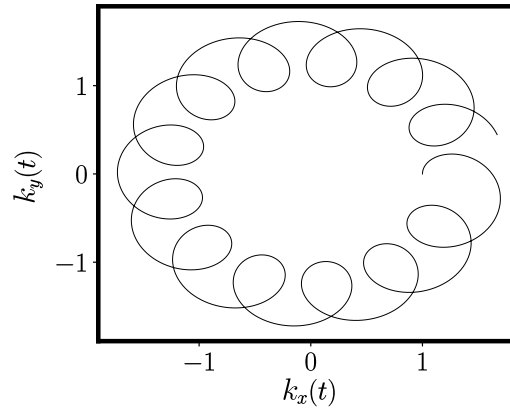


**Figure 6.2:** Plot of the typical time evolution of the horizontal component of the wave-vector  $\mathbf{k}(t)$ . The ellipticity has been set to  $\beta = 0.5$ . As in the case of the Lagrangian trajectory, the trajectory of  $\mathbf{k}$  is a combination of a slow, counter-clockwise rotation and fast epicycles.

in two steps: the set of coefficients  $\hat{\mathbf{u}}_{\mathbf{k}}$  is Fourier transformed from the spectral space into the real space to compute  $\mathbf{u} \cdot \nabla \mathbf{u}$ , this real field is Fourier transformed back to the spectral space. The numerical method implemented here is thus called “pseudo-spectral”.

Compared to standard pseudo-spectral models, the important feature of the present method is the inclusion of the periodic tidal shear via the time evolution of the wave vector  $\mathbf{k}(t)$ . This “shearing box” development allows to simulate the perturbations to the base flow while keeping the efficient pseudo-spectral methods, as originally devised by Rogallo (1981). The shearing box method has been implemented in the SNOOPY code by Lesur and Longaretti (2005) and adapted to the case of tidal forcing by Barker and Lithwick (2013).

In the code, the time evolution of the vector  $\mathbf{k}$  is determined analytically:

$$\mathbf{k}(t) = \text{Rot}(-\gamma t) \begin{bmatrix} \cos(\tilde{\omega} t) & -\frac{1}{\Lambda} \sin(\tilde{\omega} t) & 0 \\ \Lambda \sin(\tilde{\omega} t) & \cos(\tilde{\omega} t) & 0 \\ 0 & 0 & 1 \end{bmatrix} \begin{bmatrix} k_{x0} \\ k_{y0} \\ k_{z0} \end{bmatrix} = \text{Rot}(-\gamma t) \hat{\mathbf{R}}(t) \mathbf{k}_0 \quad (6.12)$$

where we have used the same expression as in the previous sections. This time evolution is very similar to the trajectory of the Lagrangian particle presented earlier, and is shown in figure 6.2. Lastly, the code solves the velocity Fourier coefficient ODEs (6.11) with a fourth order Runge-Kutta method and applying a 2/3-rule for dealiasing the non-linear terms.

## 1.5 Control parameters and resolution

For all the following simulations, we chose to work with a fixed forcing frequency  $\gamma = 1.5$ . We could not choose  $\gamma = 2$ , which is analogous to the  $f = 4$  case in the libration experiment, because of the degeneracy of the selected modes: all the modes with  $k_x = k_y = 0$  are resonant, and large-scale waves emerge out of the elliptical instability. At  $\gamma = 1.5$ , there is no exactly resonant mode due to the discretisation of wave vectors. As in the case of triadic resonance (see chapter 2 section 2.3), near-resonances are authorised for the elliptical instability within a  $\mathcal{O}(Ro_i)$  tolerance on the difference between  $\gamma$  and the resonant mode’s frequency. The use of  $\gamma = 1.5$  thus allows selecting quasi-resonant modes—whose exact frequency will be specified

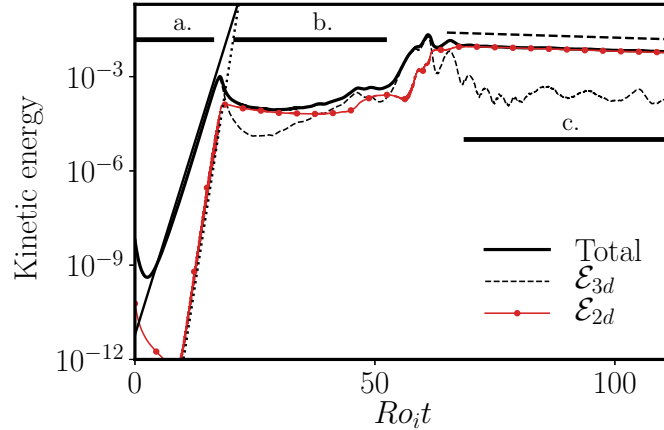


**Figure 6.3:** Times series of the kinetic energy of the perturbation flow  $\mathbf{u}$  and of its two- and three-dimensional components (see definitions (6.13)), for  $Ro_i = 7.5 \times 10^{-2}$  and  $E = 10^{-5}$ . Time is normalised by a non-linear time scale  $Ro_i^{-1}$ . The plain line materialises the theoretical growth rate (1.58) including a viscous correction  $-k_{\text{res}}^2 E$ , and the dotted line indicates twice this theoretical growth rate. The time periods **a**, **b** and **c** correspond to three different phases of the instability, the first one being the initial growth of unstable inertial waves, and the two others being part of the saturation. Typical snapshots of the vertical vorticity for each are shown in figure 6.4. Lastly, the dashed line materialises the viscous decay of a geostrophic mode with wave number  $2\pi [1, 1, 0]$  as observed in the snapshot of phase **c**.

hereafter—with fast growth along with a reasonable scale separation between the resonant wavelength and the size of the box.

We therefore control two dimensionless parameters, the Ekman number  $E$  and the input Rossby number  $Ro_i = \beta\gamma$  which accounts for the typical amplitude of the tidal flow relative to solid body rotation, but also for the typical saturation velocity (see section 1 in chapter 2). Throughout this chapter,  $Ro_i$  typically ranges from  $7.5 \times 10^{-3}$  to  $7.5 \times 10^{-2}$  and the Ekman number from  $10^{-7}$  to  $10^{-5}$ . The total number of simulated Fourier modes is either  $256^3$  or  $512^3$  depending on the spatial resolution needed. Control parameters and resolutions are recalled in tables throughout this chapter.

## 2. The geostrophic-dominated regime

### 2.1 A typical simulation

In this paragraph, we present the results of numerical simulations carried out at  $\beta = 5 \times 10^{-2}$ ,  $E = 10^{-5}$  and with a differential rotation rate of the planet and the bulge of  $\gamma = 1.5$ . The input Rossby number is therefore  $Ro_i = 7.5 \times 10^{-2}$ . This simulation of the elliptical instability is initiated by an infinitesimal amplitude white noise restricted to wave numbers up to  $k/(2\pi) = 20$ .

To determine the type of saturation (wave-dominated or geostrophic-dominated), in addition to the total kinetic energy  $\mathcal{E}$  of the perturbation flow, we compute the energy  $\mathcal{E}_{2d}$  contained in two-dimensional modes with  $k_z = 0$  and the energy  $\mathcal{E}_{3d}$  contained in three-dimensional modes for which  $k_z \neq 0$ . The kinetic energy of the different parts of the flow is

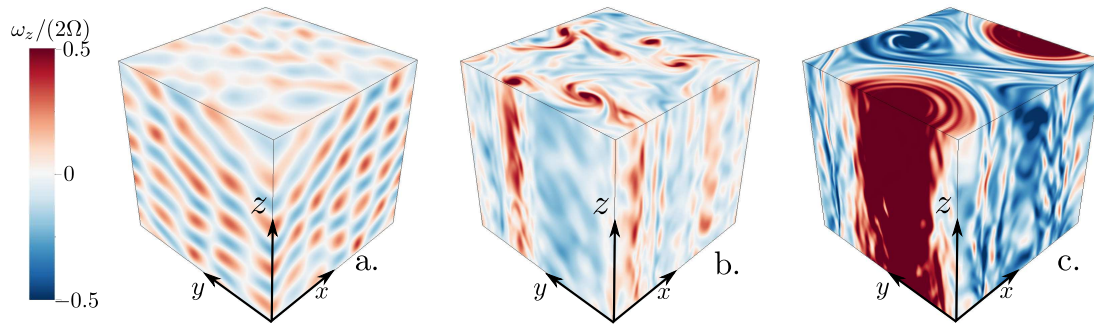


**Figure 6.4:** Typical snapshots of the vertical vorticity  $\omega_z$  in the three different phases of the instability highlighted in figure 6.3 for  $Ro_i = 7.5 \times 10^{-2}$  and  $E = 10^{-5}$ . The rotation axis is along the  $z$  axis, and the local vorticity of the perturbation flow is normalised by the planetary vorticity  $2\Omega = 2$ .

computed directly in the spectral space according to the following formulae:

$$\mathcal{E} = \frac{1}{2} \sum_{\mathbf{k}} |\hat{\mathbf{u}}_{\mathbf{k}}|^2, \quad \mathcal{E}_{2d} = \frac{1}{2} \sum_{\mathbf{k}/k_z=0} |\hat{\mathbf{u}}_{\mathbf{k}}|^2 \quad \text{and} \quad \mathcal{E}_{3d} = \frac{1}{2} \sum_{\mathbf{k}/k_z \neq 0} |\hat{\mathbf{u}}_{\mathbf{k}}|^2. \quad (6.13)$$

The evolution of these three quantities is displayed in figure 6.3.

Three different phases can be identified from the kinetic energy time series, for which typical snapshots of the vertical vorticity of the perturbation flow  $\omega_z = (\nabla \times \mathbf{u}) \cdot \mathbf{e}_z$  are displayed in figure 6.4. The first one is the growth of the elliptical instability, that is, the exponential amplification of a pair of inertial modes that can be identified in figure 6.4.a. These inertial waves has a wave vector  $\mathbf{k}_{\text{res}} = \pm 2\pi [3, 2, 6]$ <sup>1</sup> whose eigen frequency is  $\omega_{\text{res}} = 1.48$  such that  $|\gamma - \omega_{\text{res}}| = 2 \times 10^{-2} = \mathcal{O}(Ro_i)$ . It can be noticed in figure 6.3 that two-dimensional modes grow with the unstable inertial waves, with a growth rate that is exactly twice the growth rate of the growing waves. This is indicative of direct forcing of the two-dimensional modes by non-linear and non-resonant interaction between the growing waves which has been formally discussed in chapter 4 section 4.

The growth is followed by a first saturation phase (b) where both two- and three-dimensional components of the flow take a similar share of the saturation kinetic energy. In the snapshot b in figure 6.4, several geostrophic vortices are clearly identifiable by their columnar structure parallel to the rotation axis. Then, they undergo an inverse cascade process which leads to the progressive condensation of the several vortices down to two vortices with opposite rotation directions in the phase c. The end of the condensation process coincides with the transition from phase b to c. The non-linear process of the inverse cascade acting on the geostrophic modes is a rather standard observation that has been reported first in two-dimensional turbulence (Boffetta and Ecke, 2012) and in several set-ups of rotating turbulence forced for instance by random structures (Campagne et al., 2014; Herbert et al., 2016), or by small-scale convection (Favier et al., 2014; Stellmach et al., 2014). As the condensate forms, a sudden rise of the two dimensional kinetic energy  $\mathcal{E}_{2d}$  is followed by the decrease of the three-dimensional component of the flow: the two strong vortices observed in figure 6.4 completely dominate the flow. Interestingly, a slight decay of the geostrophic kinetic energy is noticeable in figure 6.3 where it is shown to match the viscous decay of a large-scale mode similar to what is observed in the snapshot of figure 6.4. In the last phase displayed in figure 6.3, there is no transfer of energy to geostrophic modes with the resonant wave as an intermediate. As observed by

<sup>1</sup>The  $\pm$  sign is dropped hereafter since opposite wave vectors must always be paired to ensure the flow  $\mathbf{u}$  is real.

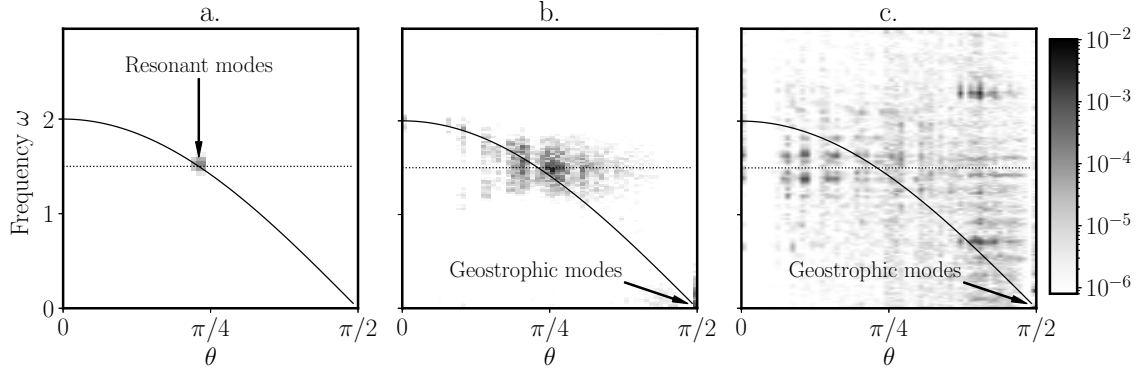


**Figure 6.5:** Maps of the kinetic energy spectrum projected in the sub-space of the dispersion relation  $\mathcal{E}(\theta, \omega)$  (see chapter 4 section 2.3) for the different phases of the tidally driven elliptical instability at  $Ro_i = 7.5 \times 10^{-2}$  and  $E = 10^{-5}$ . The labels **a**, **b** and **c** correspond to the phases labelled in figures 6.3 and 6.4. The temporal Fourier transforms are performed over time periods indicated by the solid, thick black lines of figure 6.3. The solid black line materialises the dispersion relation of inertial waves  $\omega = 2 \cos \theta$ , and the dashed line highlights the expected resonant frequency of 1.5.

Barker and Lithwick (2013), the geostrophic vortices are dissipated until the instability may grow again (see figure 2.4 in chapter 2). It should also be noted that the condensation of the vortices ends when the condensate reaches the size of the simulated domain, which has no physical meaning since we have assumed the homogeneity of the planetary interior to introduce the local model. Increasing the horizontal size of the box yields a larger condensate, whereas Barker and Lithwick (2013) has proved that coherent vortices are unstable in taller boxes. The saturation flow observed in phase **c** is thus probably artificial.

We therefore observe saturation which is completely dominated by strong geostrophic vortices. Although the presence of a strong geostrophic flow is similar to what has been observed in the experiments, many differences can be noted. First, although it takes a significant share of the energy, the geostrophic anticyclone characterised in the experiment has never been observed to take over the flow to the point it carries the energy of the entire flow as it is the case in figure 6.4.c. In addition, there is no evidence of an inverse cascade and condensation of several vortices down to the anticyclone in the experiment; the anticyclone may rather be the product of small-scale turbulence organising directly into a coherent vortex, probably due to confinement by the geometry and wall topography. Lastly, in the present simulations, there is no preferential emergence of a cyclone or an anticyclone as both can be noticed in figure 6.4.

## 2.2 Inertial waves in the geostrophic regime

Although the geostrophic saturation observed in the local model should be interpreted with care in regard of the experiments, the local model remains nevertheless a very useful tool to explore the interaction between waves and vortices in the saturation phase. As in the experimental study of Yarom and Sharon (2014), we propose to explore the presence of inertial waves and their interaction with geostrophic vortices by projecting the energy of the flow in the sub-space of the dispersion relation. Computing such a quantity is made rather straightforward by the use of pseudo-spectral methods in our numerical model. As explained in chapter 4, section 2.3, from the amplitude of the velocity sorted by wave-vectors in the spectral

space  $\hat{\mathbf{u}}_k$ , we extract by summation and temporal Fourier transform the kinetic energy of the flow as a function of  $\theta = \arccos(k_z/k)$  the angle between the wave-vector and the rotation axis, and  $\omega$  the temporal frequency, a quantity denoted as  $\mathcal{E}(\theta, \omega)$ . The result of computing the energy map  $\mathcal{E}(\theta, \omega)$  is shown in figure 6.5 for the different phases of the instability—**a**, **b** and **c**. The location of the kinetic energy is to be compared to the line materialising the dispersion relation of inertial waves  $\omega = 2 \cos \theta$ .

In the energy maps  $\mathcal{E}(\theta, \omega)$ , it appears clearly that the resonant structures in the growth of the instability are along the dispersion relation and at the resonant frequency, which confirms the standard elliptical instability mechanism. In the first phase of the saturation (**b**), we notice an accumulation of energy at  $(\omega, \theta) \rightarrow (0, \pi/2)$ , which corresponds to slowly evolving geostrophic modes—invariant along the  $z$  axis. In the meantime, the energy of three-dimensional modes does not follow the dispersion relation of inertial waves. Instead, it remains somewhat localised around the resonant frequency. To explain this result, we propose that energy is still supplied to the perturbation flow via the elliptical instability. The resonant structures are not plane waves anymore but a combination of modes to account for the presence of geostrophic vortices that locally change the local rotation rate of the fluid. The total vertical vorticity of the fluid writes  $2 + \omega_z^g$  where  $\omega_z^g$  is the vertical vorticity of geostrophic flows. We may qualitatively estimate the angles  $\theta$  of the superposition of plane waves that resonate with the base flow. In the core of a vortex with vorticity  $\omega_z^g$  that is assumed to vary slowly in space, plane waves have a modified eigen frequency  $(2 + \omega_z^g) \cos \theta$ . Resonant waves inside the vortex are such that the angle  $\theta$  satisfies the following relation:

$$\cos \theta = \frac{\gamma}{2 + \omega_z^g}. \quad (6.14)$$

For positive vorticity in the vortex, the angle  $\theta$  of the resonant wave vectors is such that  $\cos \theta$  is decreased, which means that  $\theta$  is increased. In the real flow, the local vorticity varies continuously, hence the signature of the resonant structures in the  $(\omega, \theta)$  plane: they resonate around the frequency  $\gamma$ , and display a continuous spectrum towards increasing  $\theta$ .

The final stage of the saturation (**c**) of the instability is rather complicated as energy is neither located around the dispersion relation nor around the resonance frequency  $\gamma$ . Some symmetric structures around the  $\omega = \gamma$  line may be noticed, and may be interpreted as resonant structures distorted by the strong geostrophic vortices and verifying the resonance condition (1.45)  $\omega_1 + \omega_2 = \omega_{\text{res}}$ .<sup>2</sup>

## 2.3 Temporal and spatial spectra of the geostrophic saturation

In this section, we present the temporal and spatial spectra of the saturation flow. The former is used for comparison with the experimental results of chapter 3. The spatial spectrum is computed for comparison with classical results of rotating turbulence (Godefert and Moisy, 2015).

The spectral density of kinetic energy  $T(k)$  is computed directly in the spectral space according to the following formula:

$$T(k) = \sum_{|k| \in [k, k+\Delta k]} \frac{1}{2} |\hat{\mathbf{u}}_k|^2 \quad (6.15)$$

<sup>2</sup>Note that the relation (2.34) derived in chapter 2 was rather  $\omega_1 + \omega_2 + \omega_{\text{res}} = 0$  but since the field is real, all frequencies  $\pm\omega_{0,1,\text{res}}$  are present so that a relation of the type  $\omega_1 + \omega_2 = \omega_{\text{res}}$  is also significant of triadic interaction.

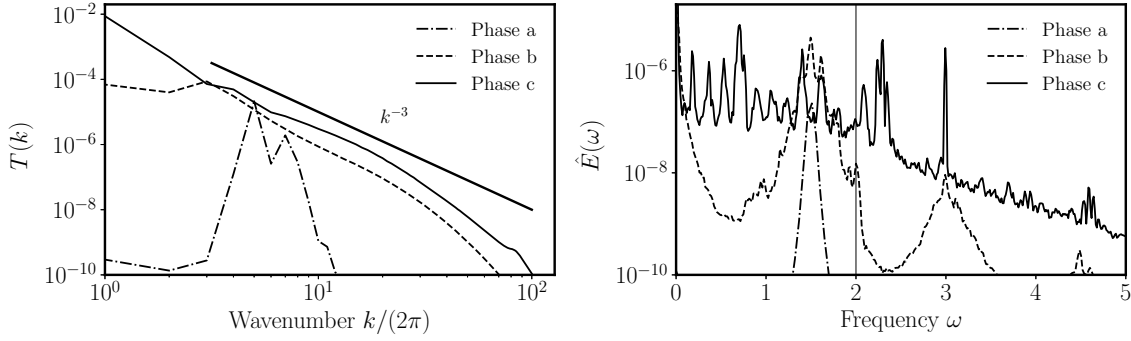


**Figure 6.6:** Spatial (left) and temporal (right) spectra of the flow resulting from the elliptical instability computed during the three different phases of the instability highlighted in figure 6.3. The spatial spectra in the saturation phases are compared to a  $k^{-3}$  power law. In the temporal spectra, the vertical black line marks the upper limit of the inertial waves domain  $\omega = 2$ . In the growth phase (a), the resonant waves appear in a narrow band of wavenumbers, at a frequency of 1.5 which is half the forcing frequency  $2\gamma = 3$ .

where  $\Delta k$  is set by the discretisation of the spectral grid, and in the present study  $\Delta k = 2\pi$ . The quantity  $T(k)$  is displayed in figure 6.6-left for the three phases of the instability. In the growth phase, the reduced number of growing modes translates into a narrow band of wavenumbers bearing a significant amount of energy. During the saturation of the instability, the spectral density of kinetic energy is very close to a  $k^{-3}$  power law, which is a usual feature of geostrophic rotating turbulence (see for instance the work of Sen et al. (2012)). Three-dimensional spatial spectra are significant outcome of the local model to complement the experiment for which this quantity is difficult to determine since it requires a large resolution, a low signal to noise ratio and a three-dimensional velocity field. In addition, the experiment is intrinsically inhomogeneous and scale analysis based on spatial Fourier transform may be irrelevant.

The temporal power spectra are computed from data in the physical space. Similarly to what has been done in the experimental study (see Chapter 3), the temporal spectra are determined from local recordings of the three components of the velocity. The result of the process, which involves Fourier transform of the time series and ensemble average, is shown in figure 6.6-right. In the growth phase (phase a), the unstable inertial wave clearly appears at half the frequency, that is at  $\omega = \gamma$ . In the first saturation phase, the energy concentrates around the resonant frequency with a significant spreading. This spreading could be interpreted as a consequence of the detuning of the resonant structures by advection-induced Doppler shift. Consider the resonant waves with wave vector  $\mathbf{k}_{\text{res}} = 2\pi [3, 2, 6]$ , for which  $k_{\text{res}} \simeq 2\pi \times 6.2$ , and a geostrophic flow with typical rms amplitude  $u_g \sim 10^{-2}$ . The resulting Doppler shift of the frequency is of order  $(k_{\text{res}}/(2\pi)) \times u_g \simeq 6 \times 10^{-2}$ . The full width at half maximum of the  $\omega_{\text{res}} = 1.5$  peak is  $6 \times 10^{-2}$  which is in good agreement with the qualitative evaluation of the detuning by Doppler-shifting.

Later, in the final saturation phase (phase c), many rather sharp peaks appear, some being located outside the inertial wave domain. The presence of the large-scale vortices makes the interpretation of these peaks difficult. They could very well be associated with inertial modes that exist in the core of the vortex, and that would be eigenmodes of the rotating vortex. As explained in the preceding section, the clear symmetry around  $\omega_{\text{res}}$  could be explained by resonances of pairs of inertial waves verifying the resonance condition (1.45).

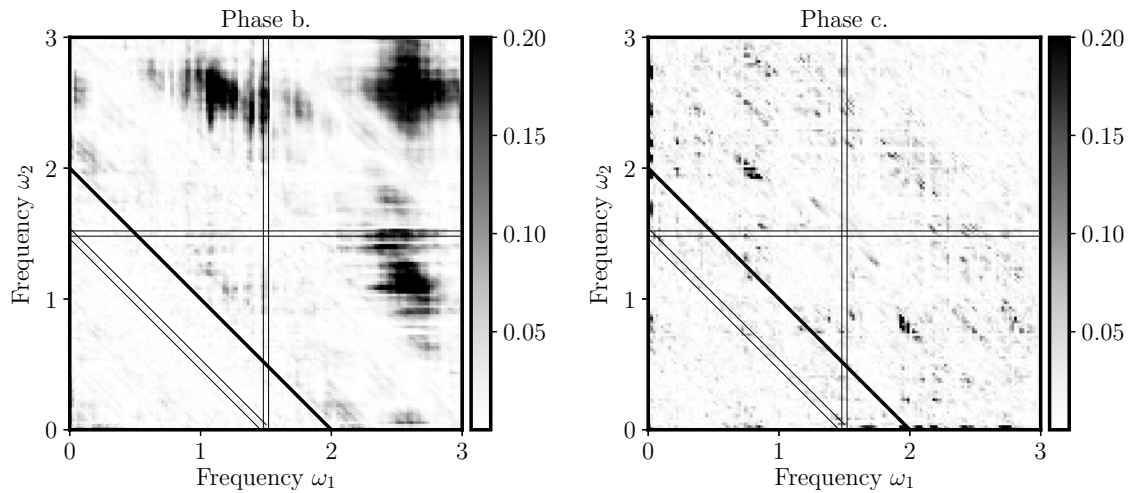


**Figure 6.7:** Bicoherence spectra computed in the phases **b** and **c** of the geostrophic saturation. The thick black line materialises the limit of the inertial wave domain and the thin lines frame the location of the triadic interaction involving the resonant mode at  $\omega = \gamma = 1.5$  and  $Ro_i = 7.5 \times 10^{-2}$ .

## 2.4 Non-linear triadic interactions in the geostrophic saturation

In the experimental study presented in chapter 3, we have shown in figure 3.22 that even though the saturation is dominated by a strong geostrophic anticyclone, the bicoherence spectrum showed that triadic resonant interactions are still occurring between modified modes that must account for the altered background rotation. In the present section, we aim at investigating the presence of non-linear processes such as triadic resonances in the saturation of the tidally driven instability dominated by geostrophic vortices. We use the bicoherence spectra diagnostic, as in chapter 3, and we recall for clarity how it is computed. It is determined from the temporal Fourier transform of the velocity local measurements  $\hat{u}_i$ , the index  $i$  referring to the index of the velocity measurement (for  $N$  probes,  $3N$  measurements are carried out since the three component of the velocity are recorded). The bicoherence may be defined by the following formula:

$$\mathcal{B}(\omega_1, \omega_2) = \frac{|\langle \hat{u}_i(\omega_1) \hat{u}_i(\omega_2) \hat{u}_i^*(\omega_1 + \omega_2) \rangle|^2}{\langle |\hat{u}_i(\omega_1) \hat{u}_i(\omega_2)|^2 \rangle \langle |\hat{u}_i^*(\omega_1 + \omega_2)|^2 \rangle} \quad (6.16)$$

where the operation  $\langle \cdot \rangle$  here denotes an ensemble average over all the  $\hat{u}_i$ . This diagnostic quantity is such that it peaks when two structures at frequencies  $\omega_1, \omega_2$  significantly interact with a structure at  $\omega_1 + \omega_2$ .

The bicoherence spectra in the two phases of the saturation (**b** and **c**) are shown in figure 6.7. Significant three-mode interactions exist, and most of them are outside the inertial wave domain. This is possibly due to the strong distortion of waves in the core of geostrophic vortices in both phases of the saturation which locally strongly alters their frequency. Note that this frequency shift is different from the detuning by Doppler shift mentioned earlier in section 2.3 which rather affect waves outside the core of the vortices. The triadic interactions remain nevertheless difficult to interpret since the inertial modes are no longer plane waves and the geostrophic modes are unsteady.

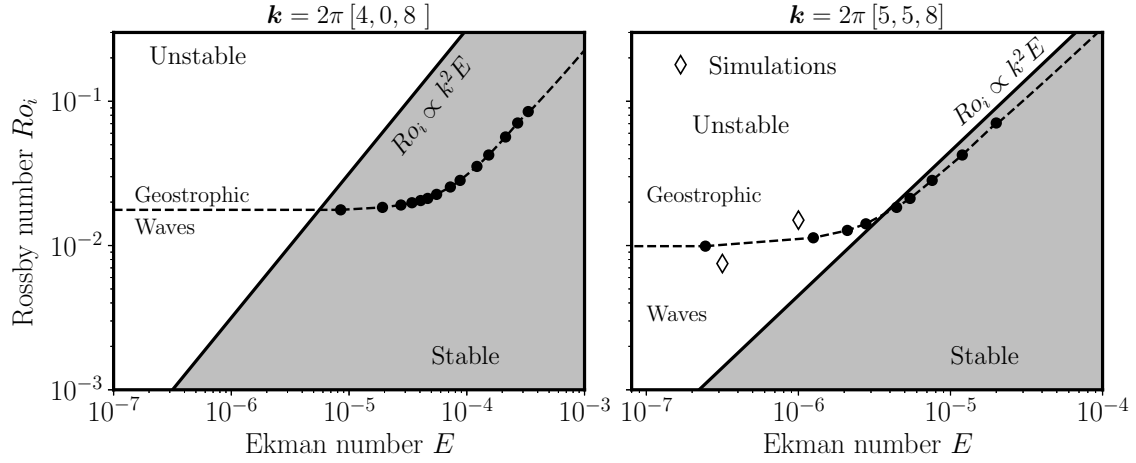


**Figure 6.8:** Diagram of the different regimes expected for the saturation of the elliptical instability for wave vectors  $\mathbf{k} = 2\pi [4, 0, 8]$  (the wave studied in the previous chapter) and  $\mathbf{k} = 2\pi [5, 5, 8]$  (the resonant mode at  $Ro_i = 7.5 \times 10^{-2}$  and  $E = 10^{-6.5}$ ). The control parameters are the Ekman number and the Rossby number  $Ro_i$ . The plain line materialises the threshold of the elliptical instability and the dashed line the threshold of the secondary instability. On the latter, the black dots materialise the  $Ro_i$  values at which the inviscid growth rate has been determined numerically. The dashed line separates the parameters space in a wave-dominated and a geostrophic-dominated area. The diamonds materialise the locations of the two simulations introduced in section 3.2 and summarised in table 6.1.

### 3. Attempts to observe a wave-dominated regime with the local model

The preceding section was targeted at the geostrophic-dominated regime in the numerical local model that bears some similarities with the regime observed in the experiments. Similarly to what has been detailed in the first chapter, we should be able to observe a wave-dominated regime. The present section builds on the study of finite Rossby instabilities to look for a wave-dominated regime.

#### 3.1 Predicting the saturation regime with finite Rossby instabilities

We carry out a short study to build a predictive regime diagram of the saturation of the elliptical instability based on the idealised study presented in chapter 4. As explained in the introduction, the saturation amplitude of the resonant wave should scale like  $Ro_i$ . Let us assume that  $Ro_i$  is a sufficient proxy for the saturation amplitude, and that studying the stability of the resonant wave respective to secondary geostrophic instability exactly corresponds to the analysis of the previous chapter. The goal of this short investigation is to find the minimal Rossby number below which the saturation should always be dominated by waves in interaction.

We focus on the case where the frequency of the resonant modes  $\omega_{\text{res}} = \gamma = 1.5$ . As recalled in the introduction, the growth rate of the instability is an increasing function of the differential rotation rate  $\gamma$ ; choosing  $\gamma = 1.5$  produces rapid turbulent saturation and ensures sufficient scale separation between the size of the simulated domain and the resonant wavelength. Different resonant modes can be excited as the input Rossby number  $Ro_i$

is lowered. At  $Ro_i = \beta\gamma = 7.5 \times 10^{-2}$ , the resonant mode is  $2\pi[3, 2, 4]$  (see figure 6.4) of frequency  $\omega_{\text{res}} \simeq 1.485$ , that is,  $|\omega_{\text{res}} - \gamma| \sim Ro_i/5$ . When  $Ro_i$  is decreased by an order of magnitude to  $7.5 \times 10^{-3}$ , the resonant mode switches to  $2\pi[5, 5, 8]$  for which  $\omega_{\text{res}} = 1.4985$  and  $|\omega_{\text{res}} - \gamma| \sim Ro_i/5$ . Although it is closer to the exact resonance condition, this mode is not the most unstable one at  $Ro_i = 7.5 \times 10^{-2}$ . This is due to viscous damping which is about four times larger—at the same Ekman number—for the mode  $2\pi[5, 5, 8]$  compared to  $2\pi[3, 2, 4]$  so that the latter has a larger viscous growth rate. At  $Ro_i = 7.5 \times 10^{-3}$ ,  $2\pi[3, 2, 4]$  is out of the near-resonance tolerance, and  $2\pi[5, 5, 8]$  becomes the most unstable mode. Note that selecting a specific forcing frequency  $\gamma$  to match the frequency of a mode does not solve the shift in mode selection at moderate input Rossby number. For instance, even if we choose  $\gamma = 1.4985$ , which is the eigen frequency of the mode  $2\pi[5, 5, 8]$ , at  $Ro_i = 7.5 \times 10^{-2}$ , the near-resonant mode  $2\pi[3, 2, 5]$  remains the most unstable.

Building on the idealised study, we wish to predict what is the input Rossby number  $Ro_i = \beta\gamma$  below which finite Rossby number instabilities should vanish. For  $k/2\pi \sim 10$ , this yields a critical input Rossby number of  $Ro_{i,c} = 1 \times 10^{-2}$ . To obtain a precise regime diagram of the secondary instability, we therefore investigate the stability of the wave  $\mathbf{k}_{\text{res}} = 2\pi[5, 5, 8]$  respective to finite Rossby instabilities with the method presented in chapter 4.

For a very low Ekman number, we find the inviscid growth rate  $\sigma_{2,i}$  of this secondary instability as a function of the Rossby number  $Ro_i$ . In the triply periodic cubic box, the damping rate of waves is set only by bulk dissipation, the viscous growth rate  $\sigma_2(Ro_i)$  is therefore deduced from  $\sigma_{2,i}(Ro_i)$  by:

$$\sigma_2(Ro_i) = \sigma_{2,i}(Ro_i) - k_{\text{res}}^2 E. \quad (6.17)$$

To determine the critical line separating the wave-dominated from the geostrophic dominated regimes in the  $(E, Ro_i)$  space, we compute the corresponding critical Ekman number  $E_{\text{crit}}$  according to:

$$E_{\text{crit}} = \frac{\sigma_{2,i}(Ro_i)}{k_{\text{res}}^2}. \quad (6.18)$$

This secondary instability line is to be compared with the elliptical instability critical line given by the equation:

$$\frac{Ro_i}{16} (2 + \gamma)^2 - k_{\text{res}}^2 E = 0. \quad (6.19)$$

based on the instability growth rate presented in the chapter 1 equation (1.58).

The result of such a process is shown in figure 6.8 for two different wave numbers,  $2\pi[4, 0, 8]$  which is the one used for the study of chapter 4, and  $\mathbf{k}_{\text{res}}$ . As found previously, the fact that this instability occurs only at finite Rossby translates into a horizontal line below which geostrophic modes should never grow out of the saturation of the instability. Nevertheless, the respective growth rates of the primary and secondary instabilities in the present idealised and homogeneous set-up is such that the secondary instability always develops above the horizontal line  $Ro_i = Ro_{i,c}$ . This feature is different from what is observed in the experiments where there exists for intermediate Ekman numbers a band between the primary and secondary critical lines above  $Ro_{i,c}$ , as found in figures 3.19 and 4.11.

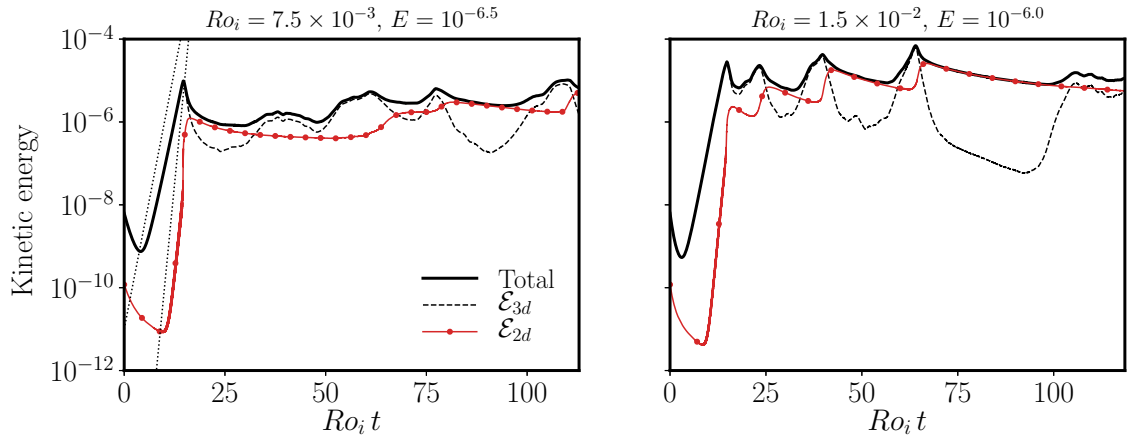


**Figure 6.9:** Temporal series of the kinetic energy of the flow driven by the elliptical instability for the two experiments located in figure 6.8. As in figure 6.3, the total kinetic energy is decomposed into two- and three-dimensional contributions ( $\mathcal{E}_{2d}$  and  $\mathcal{E}_{3d}$ ). The two dotted lines in the left panel give the viscous growth rate of the tidally driven elliptical instability and twice its value. Note that time is normalised by a non-linear time  $Ro_i^{-1}$ .

Resolution	$E$	$Ro_i$	$u_{\text{rms}}$
$256^3$	$10^{-6.5}$	$7.5 \times 10^{-3}$	$2.5 \times 10^{-3}$
$256^3$	$10^{-6.0}$	$1.5 \times 10^{-2}$	$5.1 \times 10^{-3}$

**Table 6.1:** Table of the input control parameters for the simulations presented here, and the output measurements comprising the root mean square (rms) value of the velocity.

### 3.2 The systematic emergence of geostrophic vortices

According to the regime diagram presented in figure 6.8, and assuming that  $Ro_i = \beta\gamma$  is an adequate proxy for the saturation amplitude of the resonant wave, choosing parameters

$$Ro_i = 1.5 \times 10^{-2} \quad \text{and} \quad Ro_i = 7.5 \times 10^{-3}$$

should lead to two different saturation regimes. For the lowest value of  $Ro_i$ , the saturation amplitude of the mode is expected to be below the critical amplitude giving rise to finite Rossby number instability of the geostrophic mode. We therefore expect the saturation at lower  $Ro_i$  to be dominated by inertial waves.

Simulations of the tidally driven elliptical instability have been carried out for the two sets of control parameters shown in figure 6.8 and presented in table 6.1. The kinetic energy of the flow in both cases is shown in figure 6.9; it is decomposed into its two- and three-dimensional components as in the previous section. For both simulations, the kinetic energy of the geostrophic flow is of similar amplitude as the rest of flow, whereas it was expected that for  $Ro_i = 7.5 \times 10^{-3}$ , it should remain sub-dominant. This is all the more surprising that the rms velocity, determined from the kinetic energy temporal average  $\bar{\mathcal{E}}$  by  $u_{\text{rms}} = (2\bar{\mathcal{E}})^{1/2}$ , is lower than the minimal Rossby number below which the finite amplitude instability does not develop, which is  $\sim 1 \times 10^{-2}$  (see figure 6.8) by more than a factor 2 (see table 6.1).

### 3.3 Understanding the emergence of geostrophic modes with direct forcing

#### Evidence for direct forcing

We presently aim at understanding the origin of the systematic geostrophic saturation that does not match the predictions based on finite Rossby instabilities. As it may be noticed from figure 6.9, geostrophic vortices take a significant share of the flow as soon as the primary instability saturates. In both the simulations of figure 6.9 and in the previous section, two-dimensional modes with non-zero horizontal velocities emerge during the growth of the unstable waves. It is found that they also grow exponentially with a growth rate twice as large as the waves' in the early stages of the instability. It is clear that in this phase of the instability, the emergence of geostrophic modes is not driven by an instability, otherwise their growth would have been super-exponential.

The latter observation rather points towards a direct forcing of two-dimensional modes by the resonant waves. It has been noted for instance from the spatial spectrum in the growth phase of the instability in figure 6.6 (phase a) that more than one wave resonate with the tidal forcing. It is, therefore, a patch of modes that resonates with the tidal base flow; it interacts with itself and excites many structures as it grows. Note also that because of the axial symmetry of the tidal flows, if a mode at a particular wave vector is excited, the symmetric wave vector respective to the rotation axis is also resonant. As all these waves grow, they directly feed a cascade of structures through non-linear, non-resonant interaction.

Direct forcing has been formally described in chapter 4 section 4. We have proved for instance that two exponentially-growing inertial waves, whose wave vectors are nearly symmetrical waves with respect to the  $k_z = 0$  plane,  $2\pi [5, 5, 8]$  and  $2\pi [5, 4, -8]$ , drive the growth mode  $2\pi [-10, -9, 0]$ .

#### Direct forcing in the saturation

At the end of the exponential growth, a superposition of structures with very different scales is excited and collapses into turbulence via direct non-linear forcing and triadic resonances. It corresponds to the non-linear overshoot of the instability which is systematically observed (see figures 6.3 and 6.9). Slowly evolving geostrophic modes are part of the flow excited at this particular moment and then undergo viscous decay until another secondary growth of the elliptical instability directly excites geostrophic structures. This scenario is supported by figure 6.9 where it appears clearly that geostrophic modes are mainly excited during short-lived non-linear overshoots of the three-dimensional energy, whereas they decay viscously between the overshoots.

## 4. A wave-dominated regime in the local model

The preceding section suggests that it is difficult to observe a wave-dominated regime, even below the threshold of finite amplitude instability, possibly because of the non-linear direct forcing of geostrophic flows by resonant forcing. At very small  $Ro_i$ , this direct forcing

should remain sub-dominant, but this regime remains hardly accessible. Nevertheless, we would like to extend our understanding of the wave-dominated regime with the local model, in order to complement the experimental study, without performing simulations at extremely low input Rossby numbers and Ekman numbers. This is done in the following by adding a friction specific to the geostrophic modes which turns out to be sufficient to switch to a wave-dominated regime.

## 4.1 A specific friction applied to geostrophic modes

To retrieve the wave-dominated type of saturation that has been observed in experiments, we propose to apply an artificial specific friction to the geostrophic modes only. Let us consider the following decomposition of the perturbation flow  $\mathbf{u}$  in the triply periodic box.

$$\mathbf{u} = \mathbf{u}_{2d} + \mathbf{u}_{3d} \quad \text{where} \quad \mathbf{u}_{2d} = \sum_{k/k_z=0} \hat{\mathbf{u}}_k e^{-ik \cdot \mathbf{x}} \quad \text{and} \quad \mathbf{u}_{3d} = \sum_{k/k_z \neq 0} \hat{\mathbf{u}}_k e^{-ik \cdot \mathbf{x}} \quad (6.20)$$

or equivalently:

$$\mathbf{u}_{2d} = \frac{1}{L} \int_0^L \mathbf{u} dz \quad \text{and} \quad \mathbf{u}_{3d} = \mathbf{u} - \mathbf{u}_{2d} . \quad (6.21)$$

The evolution equation of the two-dimensional modes  $\mathbf{u}_{2d}$  is therefore inferred from Navier-Stokes equation by vertical averaging, that is:

$$\partial_t \mathbf{u}_{2d} + 2\boldsymbol{\Omega} \times \mathbf{u}_{2d} + \nabla p_{2d} + \mathcal{L}_\Gamma \mathbf{u}_{2d} - E \nabla^2 \mathbf{u}_{2d} = \frac{1}{L} \int_{z=0}^L (\mathbf{u}_{3d} \cdot \nabla \mathbf{u}_{3d}) dz + \mathbf{u}_{2d} \cdot \nabla \mathbf{u}_{2d} - f_r \mathbf{u}_{2d} \quad (6.22)$$

where  $\mathcal{L}_\Gamma$  is the linear operator of the —non-resonant— interaction with the tidal base flow. The last term of equation (6.22) is an additional friction specific to two-dimensional modes. The parameter  $f_r$  controls the typical damping time of these modes and affects in the same way small and large scales. Similar terms that affect large scales, in particular, have been used for instance in two-dimensional turbulence or quasi-geostrophic models (see for instance the review article by Boffetta and Ecke (2012)) to prevent the anomalous accumulation of energy at scales as large as the size of the simulated domain under the action of an inverse cascade. In the present set-up, the specific geostrophic friction could model wall friction and Ekman pumping undergone by the geostrophic modes: since the latter are  $z$ -invariant, they must indeed reconnect to the solid boundaries of the container in which the local cartesian model is enclosed. The implementation of this specific friction is made particularly easy here by the use of pseudo-spectral methods as it is added in the evolution equations of modes with  $k_z = 0$ .

## 4.2 Saturation with friction: a wave-dominated regime

### A three-dimensional saturation flow

In this section, we focus on simulations carried out at the same input Rossby number  $Ro_i$  as in section 2, and we include the specific friction on geostrophic modes with amplitude  $f_r = 10^{-2}$  and  $f_r = 1$ . The Ekman number is here decreased down to  $10^{-6}$ ; such a low dissipation could not be achieved in the geostrophic type of saturation, even with a  $512^3$  resolution. In the preceding simulations at  $Ro_i = 7.5 \times 10^{-2}$  the intense shear driven between

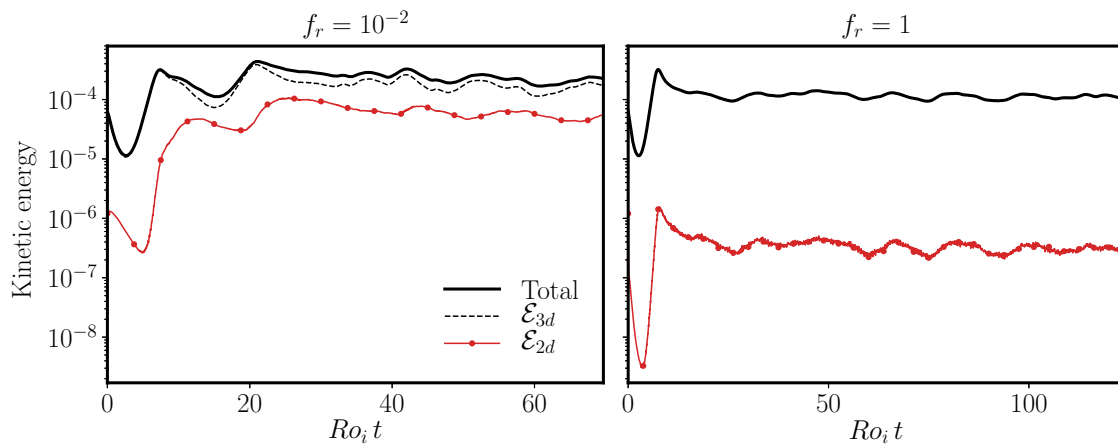


**Figure 6.10:** Kinetic energy time series for two simulations of the elliptical instability at  $Ro_i = 7.5 \times 10^{-2}$  and  $E = 10^{-5.5}$ , that is, at the same control parameters as in figure 6.3, but with the additional specific friction added on the two-dimensional modes —see equation (6.22).

Resolution	$E$	$Ro_i$	$f_r$
$256^3$	$10^{-5.0}$	$7.5 \times 10^{-2}$	1.0
$256^3$	$10^{-5.0}$	$7.5 \times 10^{-2}$	1.0
$512^3$	$10^{-5.5}$	$7.5 \times 10^{-2}$	$1.0 \times 10^{-2}$
$512^3$	$10^{-5.5}$	$7.5 \times 10^{-2}$	1.0
$512^3$	$10^{-6.0}$	$7.5 \times 10^{-2}$	1.0

**Table 6.2:** Table of the input control parameters for the simulations presented in section 4.2, including the friction amplitude  $f_r$  —see equation (6.22) .

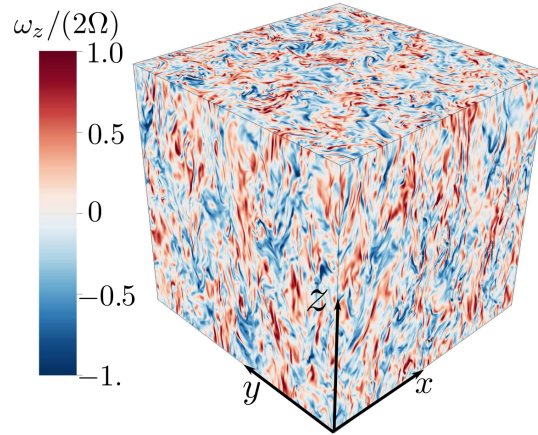


**Figure 6.11:** A typical snapshot of the saturation flow's vertical vorticity, at  $Ro_i = 7.5 \times 10^{-2}$  and  $E = 10^{-6}$  with a friction  $f_r = 1$ . The vorticity is normalised by the planetary vorticity  $2\Omega = 2$ .

the geostrophic vortices lead to small scales that could not be resolved with the currently available computing power. Such large shear zones do not exist in the present case where the strong geostrophic modes are over-damped by the specific friction. The simulations presented throughout this section and the associated control parameters are summarised in table 6.2.

As it can be noticed in figure 6.10, the friction does not only force the two-dimensional modes to be sub-dominant, it also drastically changes the nature of the saturation. Instead of observing several phases in the evolution of the saturation flow, the latter reaches a statistically steady state with dominant three-dimensional modes. A typical snapshot of the saturation flow's vorticity is given in figure 6.11 where three-dimensional as well as small-scale structures can be noticed.

### The energy of the flow in the dispersion relation subspace

To determine the type of structures excited in this new regime of the saturation of the elliptical instability, and in particular to quantify the presence of waves, we project the energy of the flow onto the dispersion relation subspace  $(\omega, \theta)$ . We use the process detailed in paragraph 2.2 to compute the energy  $\mathcal{E}(\theta, \omega)$ . The result of this process is shown in figure 6.12 which clearly reveals that the energy focuses along the dispersion relation of inertial waves as the friction increases while keeping any other parameter constant. Such a result is consistent with the outcomes of the experimental investigation presented in chapter 3: provided the geostrophic flow is sub-dominant (regardless of the cause), the non-linear break-down of the resonant inertial waves gives rise to daughter inertial waves at different frequencies. Note also that other structures can be spotted in the energy maps of figure 6.12 which have a symmetric signature to inertial waves respective to the line  $\omega = \gamma$ . They are excited by non-linear and non-resonant interaction between the waves at frequencies  $\pm 2 \cos \theta$  and the base flow at frequency  $2\gamma$  giving rise to structures such that  $\omega = 2\gamma - 2 \cos \theta$ .

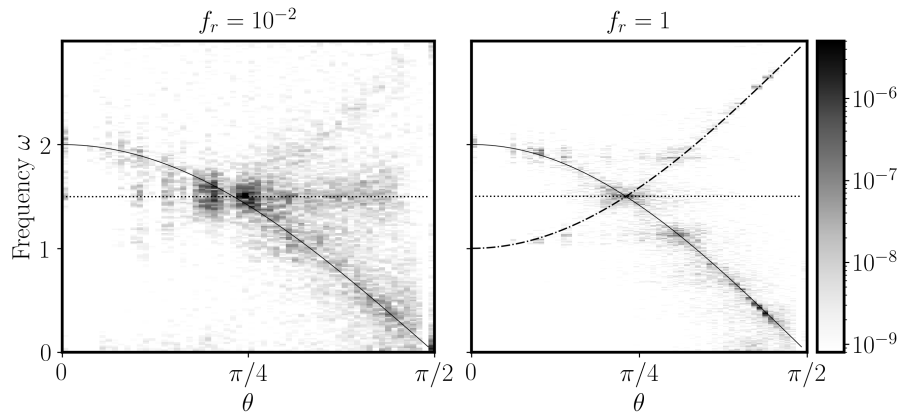


**Figure 6.12:** Spatiotemporal spectra  $\mathcal{E}(\theta, \omega)$  of the saturation flow onto the relation dispersion. The simulations are carried out at an input Rossby number  $Ro_i = 7.5 \times 10^{-2}$  and an Ekman number  $E = 10^{-5.5}$  for two values of the friction parameter,  $f_r = 10^{-2}$  (**left**) and  $f_r = 1$  (**right**). The solid black line materialises the dispersion relation  $\omega = 2 \cos \theta$ . The dashed line highlights the resonance frequency  $\omega_{\text{res}} = \gamma = 1.5$ . The dashed-dotted line corresponds to the non-linear, non-resonant interaction between the inertial waves and the tidal base flow at frequency  $2\gamma - 2 \cos \theta$ .

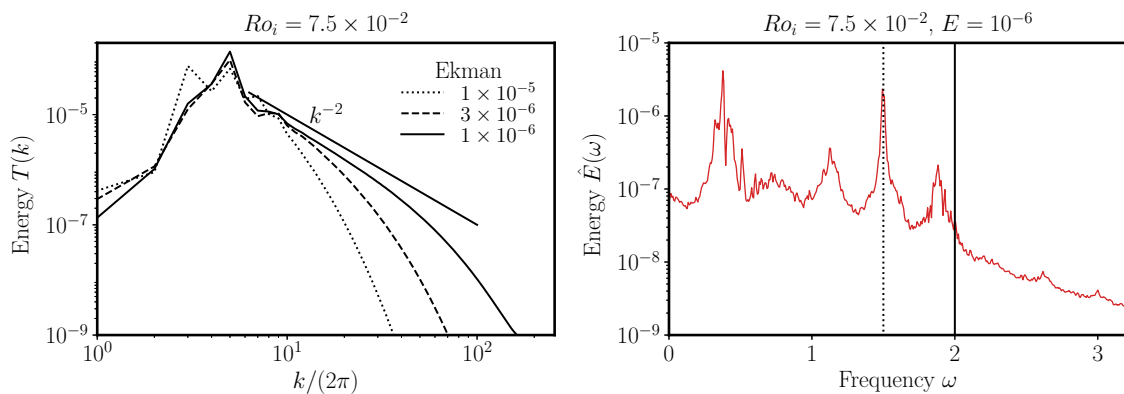


**Figure 6.13:** **Left:** spectral density of kinetic energy as a function of the wavenumber  $k$  at  $Ro_i = 7.5 \times 10^{-2}$  with a friction  $f_r = 1$ . A  $k^{-2}$  power law is given for reference. **Right:** temporal power spectra of the saturation flow at  $Ro_i = 7.5 \times 10^{-2}$ ,  $E = 10^{-6}$  and  $f_r = 1$ . The vertical lines materialise the resonant frequency  $\omega = \gamma$  (dotted) and the upper limit of the inertial waves domain at  $\omega = 2$  (plain).

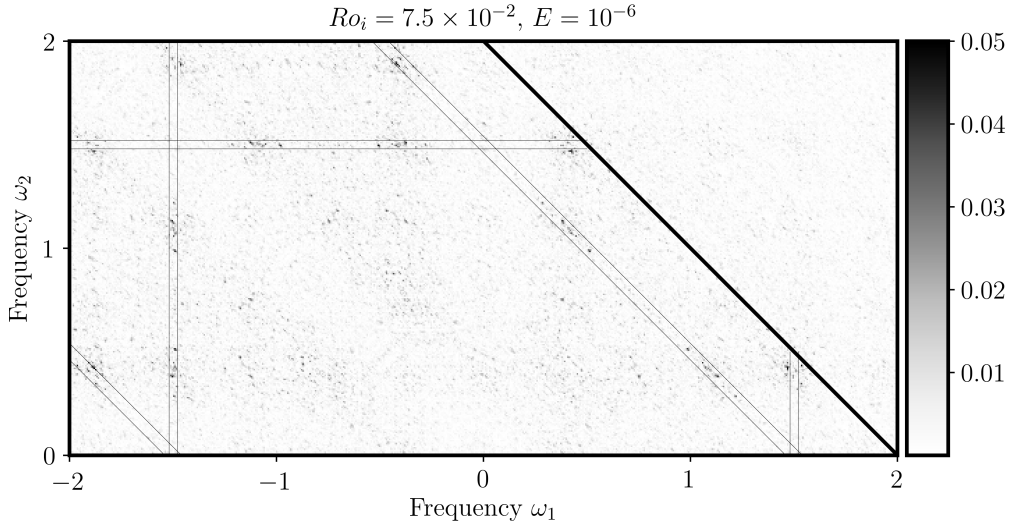


**Figure 6.14:** Bicoherence  $\mathcal{B}(\omega_1, \omega_2)$  of the saturation flow at  $Ro_i = 7.5 \times 10^{-7}$ ,  $E = 10^{-6}$  and  $f_r = 1$ . The thick black line materialises the limit of the inertial wave domain  $\omega_1 + \omega_2 = 2$ . The thin dashed lines frame all the triadic resonances involving the resonant wave, *i.e.* for which either  $\omega_1$ ,  $\omega_2$  or  $\omega_1 + \omega_2 = \gamma = 1.5$ . All the other significant interactions involve daughter waves only. The domain  $\omega_1 < 0$  is shown in this figure to include the interaction between waves with opposite sign frequencies, in particular around  $\omega_1 = -0.36$  and  $\omega_2 = 1.87$ .

### Triadic resonances

As in the experiment, the presence of triadic resonances is further assessed by the analysis of the temporal spectral content of the saturation flow shown in figure 6.13 right. It is determined as in paragraph 2.3 with local measurements of the three components of the velocity. The spectra displays several peaks with principal frequencies verifying the following triadic resonance conditions,<sup>3</sup> for instance:

$$\begin{aligned} 1.87 - 0.36 &= 1.51 \\ 1.14 + 0.36 &= 1.50 \\ 0.78 + 0.36 &= 1.14 . \end{aligned}$$

To provide a more quantitative account of the presence of triadic resonant interaction, we propose to compute bicoherence spectra  $\mathcal{B}(\omega_1, \omega_2)$  as done previously. An example of bicoherence is given in figure 6.14 where we confirm the triadic resonant interactions guessed from the temporal spectra. We can notice in this bicoherence spectrum triadic resonances involving the unstable waves (along the thin lines), but also the existence of second generation of daughter waves. Note however that the peaks remain narrow: as in the experimental study, the turbulent saturation is in this regime a discrete inertial wave turbulence.

<sup>3</sup>Note that the relation (2.34) derived in chapter 2 was rather  $\omega_1 + \omega_2 + \omega_0 = 0$  but since the field is real, all frequencies  $\pm\omega_{0,1,2}$  are present so that a relation of the type  $\omega_1 + \omega_2 = \omega_0$  is an equivalent formulation of triadic interaction.

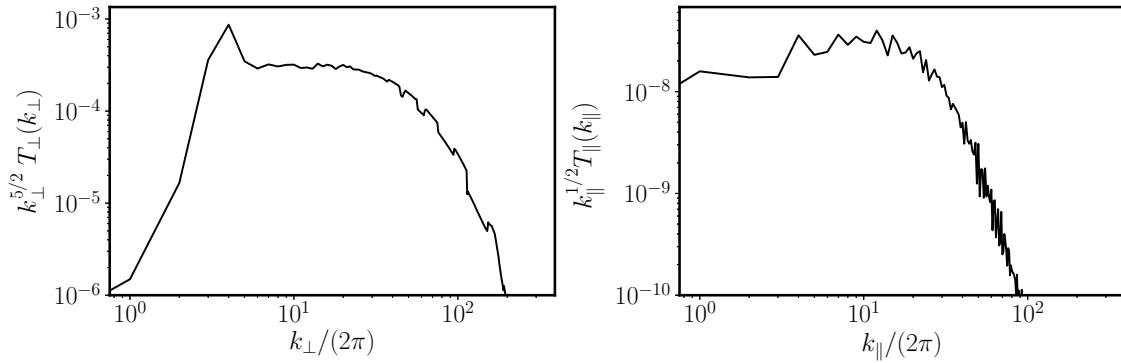


**Figure 6.15:** Plots of the anisotropic spatial spectra  $T_{\perp}(k_{\perp})$  and  $T_{\parallel}(k_{\parallel})$ . They are compensated by the expected theoretical power laws (6.27) and (6.29) to facilitate the comparison between theory and simulations.

### Isotropic spatial spectra

The excitation of many inertial waves in the saturation of the instability is also associated with the excitation of a continuum of scales, as shown in the spatial spectra presented in figure 6.13. Our simulations show that in the asymptotic regime of small dissipation or small Ekman number, the spectral density of kinetic energy follows a  $k^{-2}$  power law with the wave vector  $k$ , which contrasts with the geostrophic type of saturation where a  $k^{-3}$  power is measured (see figure 6.6). This observation is consistent with the phenomenology of rotating turbulence introduced by Zeman (1994) and Zhou (1995) who both predict such a power law with a phenomenology relying on a time scale balance between turnover and fast inertial oscillations, which is consistent with the inertial wave saturation we observe here. However, their theories do not take into account the spatial anisotropy due to rotation.

### Anisotropic spatial spectra

To extend our analysis of spatial spectra, we propose to compare our simulations to theoretical predictions derived by Galtier (2003) from the kinetic equations of inertial wave turbulence, the latter being the kinetic energy equivalent of the amplitude equations derived in chapter 2 section 2. Instead of dealing with the isotropic spectrum discussed in the preceding section, the prediction made by Galtier (2003) on the kinetic energy repartition through scale is a function of the two components of the wavenumber  $k_{\perp}$  and  $k_{\parallel}$  defined such that:

$$\begin{cases} k_{\parallel} &= \mathbf{k} \cdot \mathbf{e}_z = k \cos \theta \\ k_{\perp} &= k \sin \theta \end{cases} \quad (6.23)$$

where  $\theta$  is the angle between the wave vector and the rotation axis. Galtier (2003) predicts that  $T(k_{\parallel}, k_{\perp})$ , the kinetic energy sum over the modes whose wave vectors have vertical and horizontal components close to  $k_{\parallel}$  and  $k_{\perp}$  respectively, follows the following two-component power law:

$$T(k_{\parallel}, k_{\perp}) \propto k_{\parallel}^{-1/2} k_{\perp}^{-5/2} \quad (6.24)$$

but only in the limit  $k_{\perp} \gg k_{\parallel}$ .

To test this theoretical prediction, we compute from the present simulations the quantity  $T(k_{\parallel}, k_{\perp})$ . Such a process bears some similarities with the computation of the kinetic energy

map in the dispersion relation sub-space. In the spectral space, we compute the kinetic energy  $T(k, \theta)$  as a function of the wave vector  $k$  and the angle  $\theta$  by azimuthal summation of the kinetic energy of the modes:

$$T(k, \theta) = \int_{\phi} \frac{1}{2} |\mathbf{u}_k|^2 k^2 \sin \theta d\phi \quad (6.25)$$

where  $\phi$  is the azimuthal angle of  $\mathbf{k}$  around the rotation axis. It is then straightforward to transform  $T(k, \theta)$  into  $T(k_{\perp}, k_{\parallel})$  using relations (6.23).

To provide a quantitative test of the theory of Galtier (2003), we propose to examine two one-dimensional quantities extracted from  $T(k_{\parallel}, k_{\perp})$  in the limit  $k_{\perp} \gg k_{\parallel}$ . We first define  $T_{\perp}$  as:

$$T_{\perp}(k_{\perp}) \equiv \int_{k_{\parallel}=0}^{5 \times 2\pi} T(k_{\parallel}, k_{\perp}) dk_{\parallel} \quad (6.26)$$

which is a summation of  $T(k_{\parallel}, k_{\perp})$  over small  $k_{\parallel}$  to ensure the condition of validity  $k_{\perp} \gg k_{\parallel}$  for the theory of Galtier (2003) is fulfilled. According to Galtier (2003), we expect:

$$T_{\perp}(k_{\perp}) \propto k_{\perp}^{-5/2}. \quad (6.27)$$

Similarly, we also define a function  $T_{\parallel}$  as a summation of  $T(k_{\parallel}, k_{\perp})$  over large values of  $k_{\perp}$  that are yet in the inertial range of the turbulence (see figure 6.13) in order to fulfill the condition of validity  $k_{\perp} \gg k_{\parallel}$  for the theory of Galtier (2003) :

$$T_{\parallel}(k_{\parallel}) \equiv \int_{k_{\perp}=50 \times 2\pi}^{60 \times 2\pi} T(k_{\parallel}, k_{\perp}) dk_{\perp}. \quad (6.28)$$

It should follow a power law:

$$T_{\parallel}(k_{\parallel}) \propto k_{\parallel}^{-1/2} \quad (6.29)$$

at small  $k_{\parallel}$ .

The anisotropic spatial spectra  $T_{\parallel}$  and  $T_{\perp}$  are shown in figure 6.15; they are compensated by the expected power laws (6.27) and (6.29) to facilitate the comparison between theory and simulations. Figure 6.15 indicates that  $T_{\perp}$  follows the theoretical prediction. The power law followed by  $T_{\parallel}$  is close to  $k_{\parallel}^{-1/2}$  but on quite a small range of scales. Although promising, a larger inertial range may be required to fully confirm that we observe the theoretical anisotropic spectra of inertial wave turbulence.

### 4.3 Towards extreme regimes: the low dissipation and low forcing limit

#### Inertial wave turbulence

In the preceding sections, the local cartesian model has led to the confirmation that a state reminiscent of inertial wave turbulence is obtained in the saturation of the elliptical instability when the geostrophic component is sub-dominant. This numerical model is also useful to explore regimes that are beyond the reach of any experiment and global numerical simulations,

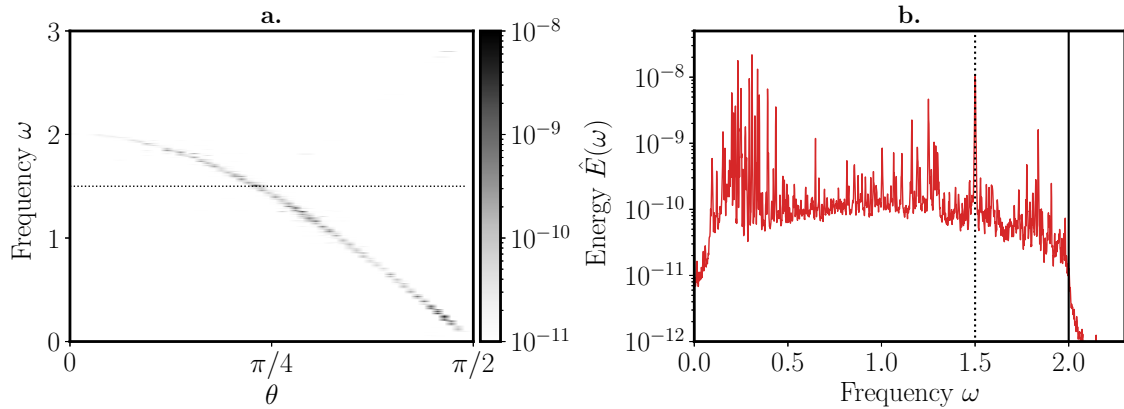


**Figure 6.16:** Energy map in the dispersion relation subspace  $(\omega, \theta)$  (a) and ensemble average of temporal spectra (b) for control parameters  $Ro_i = 7.5 \times 10^{-3}$  and  $E = 10^{-7}$  with a geostrophic friction of  $f_r = 1$ .

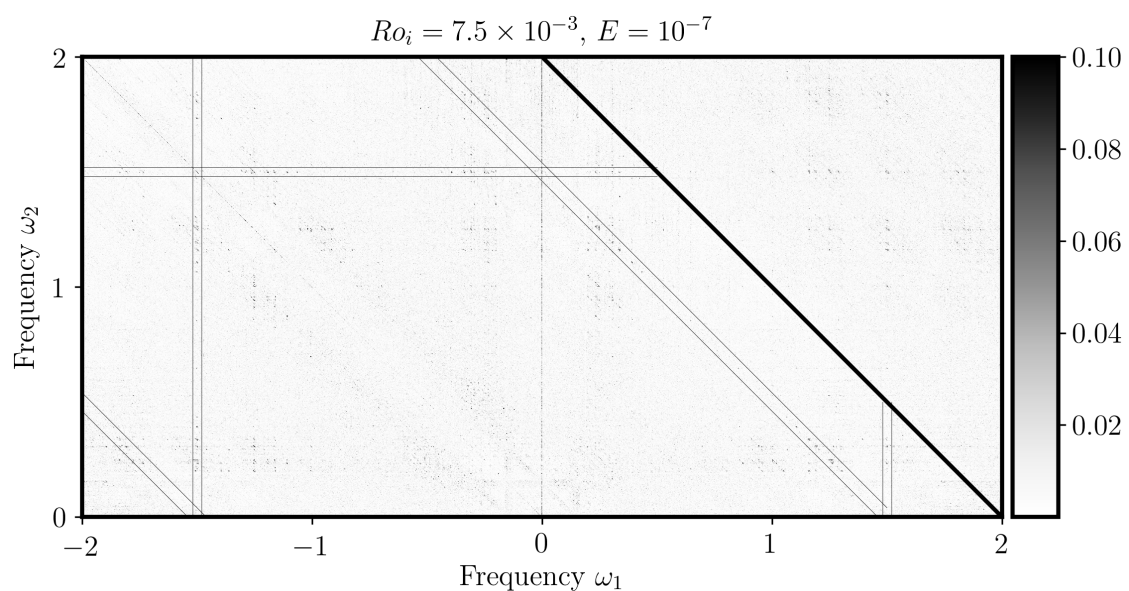


**Figure 6.17:** Bicoherence spectrum  $\mathcal{B}(\omega_1, \omega_2)$  of the saturation flow at  $Ro_i = 7.5 \times 10^{-3}$ ,  $E = 10^{-7}$  and  $f_r = 1$ . The thick black line materialises the limit of the inertial wave domain  $\omega_1 + \omega_2 = 2$ . The thin dashed lines frame all the triadic resonances involving the resonant wave, *i.e.* for which either  $\omega_1$ ,  $\omega_2$  or  $\omega_1 + \omega_2 = \gamma = 1.5$ . All the other significant interactions involve daughter waves only.

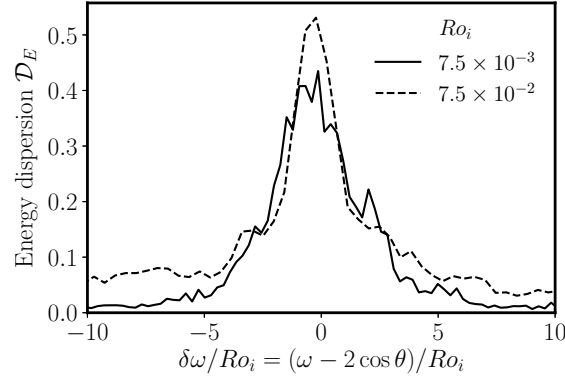


**Figure 6.18:** Computation of the energy dispersion  $\mathcal{D}_E$  along the dispersion relation, for the two set of parameters ( $Ro_i = 7.5 \times 10^{-2}, E = 10^{-6}$ ) and ( $Ro_i = 7.5 \times 10^{-3}, E = 10^{-7}$ ); the friction coefficient is set to  $f_r = 1$  for both cases. The computation is carried out according to the formula (6.30) and the frequency discrepancy  $\delta\omega$  is normalised by  $Ro_i$  to emphasize that the focus of the energy is  $\mathcal{O}(Ro_i)$ .

and allows to draw closer to geophysical regimes where both the forcing amplitude and the dissipation are small. In the following, we keep the friction parameter to  $f_r = 1$  and we explore the saturation state obtained at  $Ro_i = 7.5 \times 10^{-3}$  and  $E = 10^{-7}$ . We show in figure 6.16 the map of the saturation flow energy in the dispersion relation sub-space  $\mathcal{E}(\theta, \omega)$  and the ensemble average of local measurements of the velocity. We observe that the energy of the saturation flow is sharply focused along the dispersion relation of inertial waves. In addition, the temporal spectrum  $\hat{E}(\omega)$  comprises a very large number of sharp peaks in the inertial waves range and a significant energy cut-off beyond the maximum frequency of inertial waves  $\omega = 2$  and towards geostrophic modes at  $\omega = 0$ .

The bicoherence spectrum for this simulation is displayed in figure 6.17 where, as earlier at higher  $Ro_i$ , we observe triadic interaction of daughters inertial waves with the resonant modes, but also further generation of daughter waves. The number of peaks in the bicoherence spectrum is increased, and their typical width is thinner. One would therefore expect that in the asymptotic limit of small forcing amplitude and small dissipation, an increased number of daughter waves are excited, and possibly turn into a continuum.

### Increase of the spreading of the wave frequency with $Ro_i$

It appears clearly from the energy maps at  $Ro_i = 7.5 \times 10^{-2}$  (figure 6.12) and  $Ro_i = 7.5 \times 10^{-3}$  (figure 6.17) that the spreading of the energy of the saturation flow along the dispersion relation increases with  $Ro_i$ . As shown in chapter 2 section 2.3, near-resonance are allowed within a tolerance  $\mathcal{O}(Ro_i)$  on the frequency mismatch  $\Delta\omega$  between the eigen frequencies of the three modes involved. To confirm that the typical spreading is roughly proportional to  $Ro_i$ , we compute a mean energy dispersion around the dispersion relation in order to confirm quantitatively that the energy is focused with a tolerance  $\mathcal{O}(Ro_i)$  along the line  $\omega = 2 \cos \theta$ . This energy dispersion  $\mathcal{D}_E$  is computed as a function of the distance to the dispersion relation  $\delta\omega = \omega - 2 \cos \theta$  with the following formula:

$$\mathcal{D}_E(\delta\omega) = \int_{\theta=0}^{\pi/2} \frac{\mathcal{E}(\theta, 2 \cos \theta + \delta\omega)}{\max_{\delta\omega}(\mathcal{E}(\theta, 2 \cos \theta + \delta\omega))} d\theta. \quad (6.30)$$

In other words, it is a summation of the energy spectrum carried out over all angles as a function of a shifted frequency so that at every angle the frequency reference is the given by the dispersion relation. Note that the  $\max_{\delta\omega}(\mathcal{E}(\theta, 2 \cos \theta + \delta\omega))$  is reached close to  $\delta\omega = 0$ , *i.e.* close to the dispersion relation. The result of this process is displayed in figure 6.18, where we clearly confirm that the spreading of the energy along the dispersion relation is proportional to  $Ro_i$ . This confirms the result of the simple calculation carried out in chapter 2 section 2.3.

## Conclusion: the asymptotic regime of the saturation of the elliptical instability

The use of the local model has allowed us throughout this paragraph to explore the wave-dominated regime that has been exhibited in our experiment at low dissipation and low forcing amplitude. We show that the non-linear saturation flow comprises an increasing number of daughter inertial wave generations that are all excited by triadic resonances. In addition, our result clearly indicates that in this asymptotic regime, all the structures excited have spatial and temporal variations that exactly match the dispersion relation. This particular state also tends to excite a continuum of scales, and the energy density varies with the wave number  $k$  according to power law  $k^{-2}$ . The anisotropic repartition of kinetic energy in the spectral space tends to follow inertial waves turbulence theoretical predictions made by Galtier (2003).

We believe that the cartesian model simulations allow to state that in the asymptotic regime of low dissipation and low forcing amplitude ( $Ro_i, E \rightarrow 0$ ), which is relevant for planetary and stellar interiors, the elliptical instability tends to excite an inertial wave turbulence provided that the geostrophic flow remains subdominant. Yet, the observation in the local cartesian model at moderate input Rossby number of a wave-dominated regime was made possible with the use of a specific friction applied to the geostrophic modes.

# 5. Exploring the stability of wave turbulence

## 5.1 The case against friction

The preceding study, despite its interest for our understanding of the wave-dominated regime that has been observed in our experiments, may be criticised in particular for the introduction of an artificial and selective damping of the geostrophic modes. One may argue that this friction is a consequence of the invariance of the geostrophic vortices along the  $z$  axis: they must reconnect to the solid boundaries of the container in which the local cartesian model is enclosed and undergo wall friction. Nevertheless, the local model is built on the assumption that the planetary core is homogeneous, that is, the cartesian box could be placed anywhere in the liquid interior. As a consequence, the Ekman pumping is not specific to the geostrophic vortices: if geostrophic modes are connected to boundaries and undergo friction, then all the modes should, although the amplitude of the friction would depend on the direction of propagation of the modes. A derivation of the wall friction for plane waves in the case of a rotating channel has been carried out by Scott (2014) who finds that the mode damping rate by wall friction follows a law  $F_r(k_z/k)\sqrt{E}$  where  $F_r$  is a continuous function, reaching a maximum at 0. Although the damping rate is larger for  $k_z = 0$ , the friction undergone by most of the

modes is of the same order of magnitude. The physical argument based on wall boundary layer to support the use of a friction specific to geostrophic modes is therefore questionable. The geostrophic-specific friction is nevertheless a useful tool to retrieve a regime dominated by three-dimensional flows as it has been observed in our experiments. Such a specific damping could also take place naturally in presence of an imposed background magnetic field. Barker and Lithwick (2014) indeed showed with the same local cartesian model that we use here that a weak background magnetic field prevents the emergence of the  $z$ -invariant geostrophic vortices, and the saturation is then fully three-dimensional.

One would thus wonder whether the turbulent state we observe is representative of inertial wave turbulence. It is indeed well known in rotating turbulence that triadic transfers tend to focus the energy towards smaller  $k_z$  modes and therefore towards the geostrophic subset (Waleffe, 1993; Smith and Waleffe, 1999). We observe this particular feature in the study of the saturation with friction, for instance in the temporal spectra displayed in figures 6.13 and 6.16 where it is clear that low frequency modes are of larger amplitudes. In the preceding study, the use of friction prevents efficient transfers towards  $k_z = 0$  modes, but not to modes for which  $k_z/k \ll 1$ . Although it is clear that we observe waves in non-linear resonant interactions, the state we create with the specific friction could very well be a blocked intermediate step towards bi-dimensionalisation of the turbulent flow. It would then be particularly interesting for the study of the elliptical instability to find a way to create a mostly three-dimensional, friction-free saturation flow, and to compare it with the previous results.

## 5.2 Sub-criticality in the emergence of geostrophic modes

The present section aims at exploring the stability of inertial wave turbulence against the growth of geostrophic flows. We use different initial conditions to show that wave turbulence persists over long time periods provided the forcing amplitude is sufficiently low. As geostrophic-dominated states were reported earlier for the same range of parameters (see section 3.2) we conclude that there exists a sub-critical instability of geostrophic modes.

### The use of friction at the early stages of the saturation

Motivated by the investigation of inertial wave turbulence stability, we first create such a state via the use of the specific friction on the geostrophic modes which is removed once the instability has reached saturation. To carry out this study, we use the same input parameters ( $Ro_i, E$ ) as in the two simulations of section 3 which were used to look for inertial wave turbulence relying on the secondary instability detailed in chapter 2, and which are reminded in table 6.1, and for which the kinetic energy time series are displayed in figure 6.9. The kinetic energy time series for these new simulations with friction at early stages is presented in figure 6.19. They reveal that at larger forcing ( $Ro_i = 1.5 \times 10^{-2}$ ), the inertial wave turbulence is unstable: geostrophic modes grow exponentially once the friction is released and eventually dominate the flow. The situation is completely changed when the forcing amplitude is decreased to  $Ro_i = 7.5 \times 10^{-3}$ : although a slow exponential growth of geostrophic modes is observed once the friction is released, their energy saturates and they remain sub-dominant. As shown in figure 6.20, the saturation of the instability in the case where the inertial wave turbulence remains stable bears very similar properties to what has been found throughout section 4.2, including larger wave amplitudes at lower  $\omega$ .

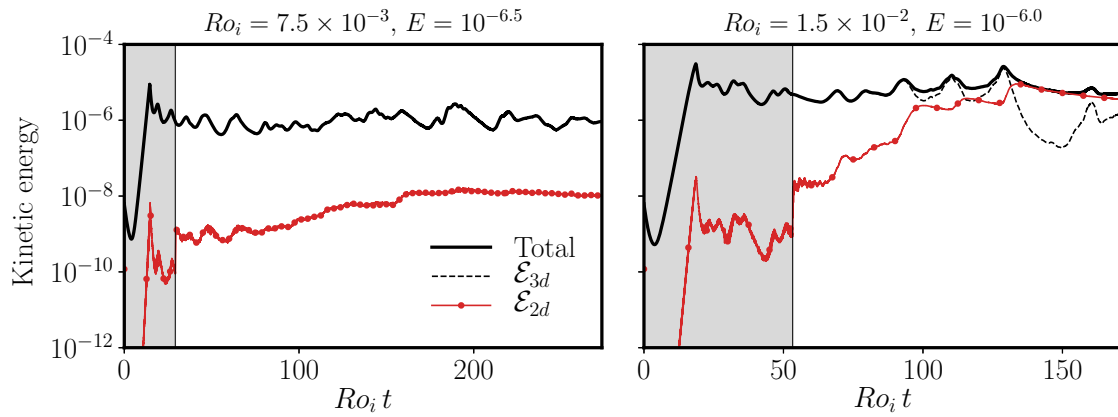


**Figure 6.19:** Temporal series of the kinetic energy of the flow driven by the elliptical instability, with a specific friction  $f_r = 1$  applied on the geostrophic modes at the early times of the simulations, materialised by the shaded area. When the friction is relaxed, the evolution of two-dimensional modes is relaxed. We observe slow exponential growth over time periods of order  $Ro_i^2$ . This figure must be compared to the corresponding frictionless simulations of figure 6.9. Exponential growth are noticeable after the friction released; the associated rates are studied in section 5.3 and reported in figure 6.22.

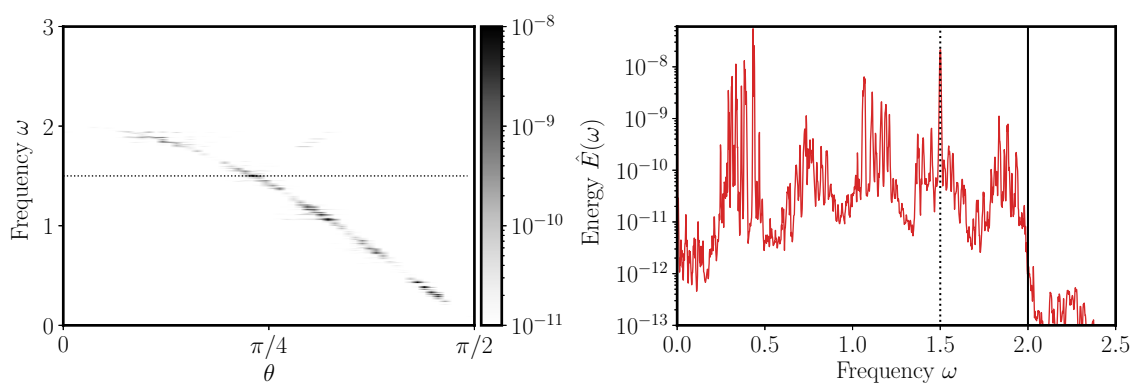


**Figure 6.20:** Energy spectrum  $\mathcal{E}(\theta, \omega)$  projected onto the dispersion relation sub-space (left) and temporal spectrum of the saturation flow in the case of stable inertial wave turbulence at  $Ro_i = 7.5 \times 10^{-3}$  and  $E = 10^{-6.5}$ . On both panels the dotted line materialises the excitation frequency. The plain vertical line is the upper limit of the inertial wave domain.

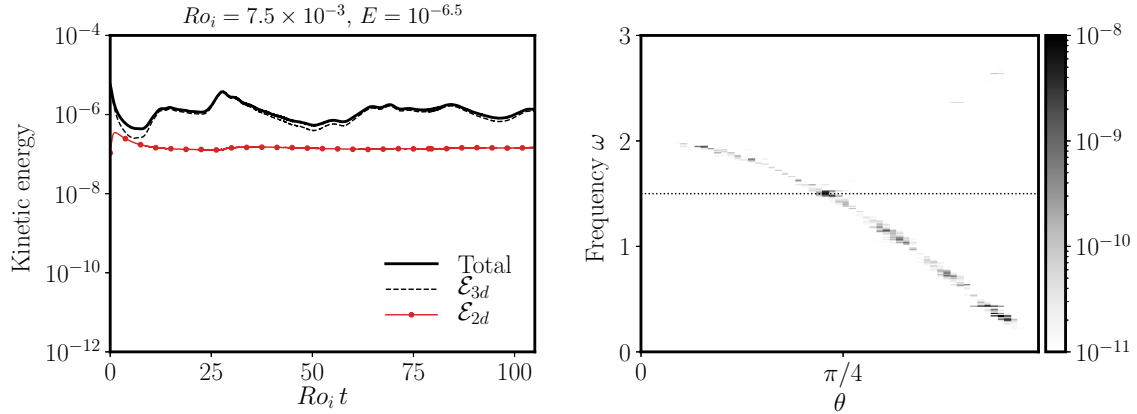


**Figure 6.21:** Kinetic energy time series of a simulations carried out at  $Ro_i = 7.5 \times 10^{-3}$  and  $E = 10^{-6.5}$  using a strong large-scale noise ( $k/(2\pi) \in [2, 20]$ ) with a rms amplitude set to  $3 \times 10^{-3}$  instead of  $10^{-4}$ —used in other simulations.

The latter result is particularly interesting: using either a random noise or a geostrophic-free inertial wave turbulence as an initial condition leads to two completely different final states, one being dominated by three-dimensional inertial waves and the other by two-dimensional geostrophic vortices. This happens, however, provided that the forcing amplitude  $Ro_i$  is small enough.

### Large amplitude noise initiation

To further investigate the bifurcation towards a wave-dominated regime, we propose here to examine simulations initiated with a broad-band noise (as done earlier  $k/(2\pi) \in [2, 20]$ ) with a strong rms amplitude, larger than the expected saturation velocity rms. The initial noise is purely three-dimensional and does not contain any geostrophic structure to avoid starting the simulations with strong vortices. We run a simulation with this special initial condition in the case where we have reported previously stable inertial wave turbulence, that is  $Ro_i = 7.5 \times 10^{-2}$  and  $E = 10^{-6.5}$ . The initial velocity rms is set to  $3 \times 10^{-3}$ .

The kinetic energy time series for this simulation are displayed in figure 6.21. Although a rapid growth of geostrophic modes is observed, probably through direct forcing, their amplitude remains below three-dimensional structures over the whole course of the simulation. In addition, it is clear from the energy map projected in the sub-space of the dispersion relation, also shown in figure 6.21, that the three-dimensional state is also an inertial wave turbulence.

### Conclusion: multi-stability in the saturation of the elliptical instability

With the previous numerical results, we conclude that the saturation of the elliptical instability simulated with the local model features multi-stability. At the lowest forcing amplitude reached with the present model, depending on the initial state, the saturation of the elliptical instability is either a stable inertial wave turbulence, or a geostrophic turbulence. The transition from stable to unstable inertial wave turbulence is related to the finite Rossby number instability developed throughout chapter 4. It remains to be seen whether the wave turbulence saturation remains stable even at very low forcing amplitude and dissipation. It

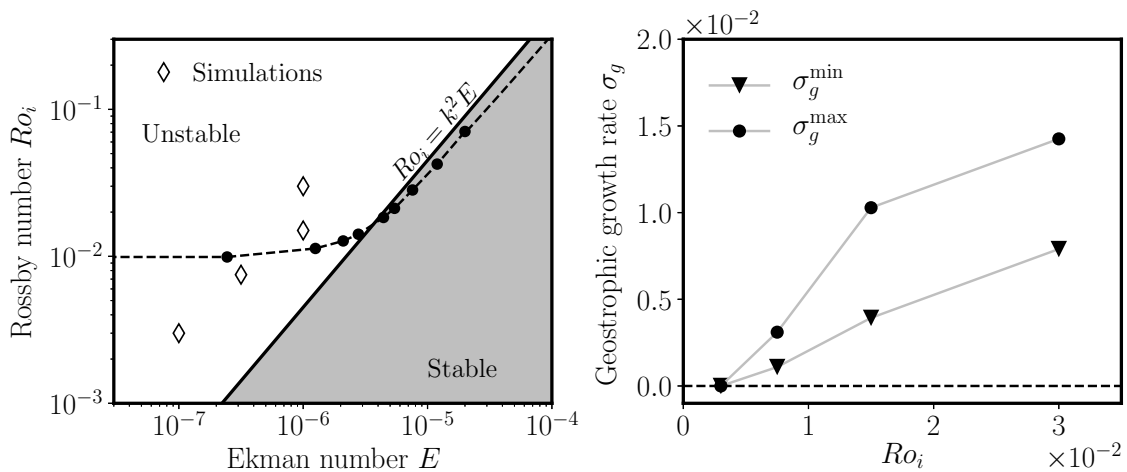


**Figure 6.22:** **Left:** reproduction of the stability diagram of figure 6.8 of the wave  $2\pi [5, 5, 8]$  under the elliptical instability (solid line) and the finite wave amplitude instability (dashed line). We locate the simulations used to measure the geostrophic growth rate. Note that two of these locations were already included in figure 6.8. **Right:** geostrophic growth rate measured once the friction is released in the set of simulations whose control parameters are indicated in the left panel. The growth rate is compensated by a viscous correction  $+k^2E$  with  $E$  the Ekman number and  $k$  the wave number. Two extremal wave numbers are taken for this compensation  $2\pi \times 9$  ( $\sigma_g^{\min}$ ) and  $2\pi \times 15$  ( $\sigma_g^{\max}$ ).

would require extreme simulations over very long time, which could not be achieved over the course of this work.

### 5.3 The growth of geostrophic modes out of wave turbulence

In the preceding section, we have used the geostrophic-specific friction to force the non-linear saturation into an inertial wave turbulence. Releasing the friction has allowed finding that at sufficiently small input Rossby number  $Ro_i$ , the saturation amplitude of free geostrophic modes remains sub-dominant. In figure 6.19-right, we have observed that when the inertial wave turbulence is unstable, the energy of geostrophic modes grows exponentially. Yet, in the smaller forcing amplitude case  $Ro_i = 7.5 \times 10^{-3}$  where waves are dominant, a slow exponential growth occurs until the geostrophic energy reaches a low saturation value. This indicates that despite the low value of  $Ro_i$ , geostrophic modes are still unstable.

To further quantify the stability of geostrophic modes, we propose to repeat the simulations presented in figure 6.19, but at higher and smaller values of  $Ro_i$  and to measure the growth rate of geostrophic modes. The input Rossby numbers and the Ekman numbers for the set of simulations that we analyse here are displayed in figure 6.22-left. The spatial resolution is kept to  $256^3$  for the two new simulations.

The input Rossby number has been decreased down to  $Ro_i = 3 \times 10^{-3}$  and the Ekman number to  $E = 10^{-7}$ . At such a weak forcing amplitude, no growth of the geostrophic energy is reported once the friction is released. For the three other cases—including the two shown in figure 6.19—the growth rate is measured via a linear fit on the logarithm of the geostrophic energy at the early stages following the friction release. To estimate an inviscid growth rate, the viscous growth rate is corrected by an approximate viscous correction  $+k^2E$  with  $E$  the Ekman number and  $k$  the wave number. Yet, several geostrophic modes are ob-

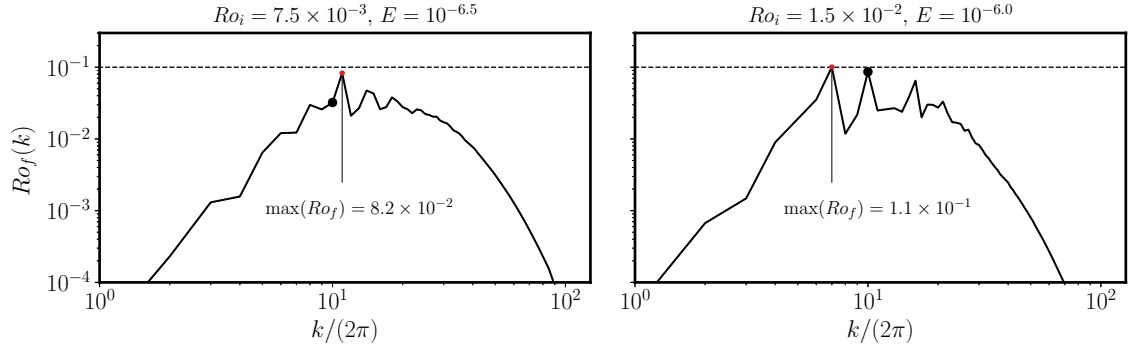


**Figure 6.23:** Plot of the wavelength-based Rossby number  $Ro_f(k) = k(kT(k))^{1/2}/(2\pi)$  as a function of the wave number  $k$ . It is compared to the threshold of finite Rossby number instability of geostrophic modes found in chapter 2, which was  $Ro_f \simeq 0.1$ . The two considered cases are associated with the kinetic energy time series shown in figure 6.19. The kinetic energy spectra  $T(k)$  are averaged around the time where the friction is removed over a few non-linear time scales. The black dot materialises the resonant wave number, it does not necessarily coincides with the largest  $Ro_f(k)$ .

served to grow at the same time, and they sometimes differ from one value of  $Ro_i$  to another. Analysis of the snapshots suggests that the wave number of the growing geostrophic modes typically ranges from  $2\pi \times 9$  to  $2\pi \times 15$ . Since the growing wave numbers are unclear and sometimes change from one simulation to another, we give the extremal values  $\sigma_g^{\min}$  and  $\sigma_g^{\max}$  of the inviscid growth rates estimated with the extremal wave numbers. The extremal values of the geostrophic growth rate  $\sigma_g^{\min}$  and  $\sigma_g^{\max}$  are shown in figure 6.22-right.

Since the unstable geostrophic modes comprise several wave vectors that change from one set of control parameters to another, it remains difficult to definitely state upon the nature of the geostrophic instability. However, we provide below a few hints pointing towards the finite wave amplitude instability detailed in chapter 4. First, we notice that the estimate of the inviscid growth rate is of the same order of magnitude as the input Rossby number, thus suggesting that the four-modes interaction or near-resonances are irrelevant to the observed instability since their growth rate is rather  $\mathcal{O}(Ro_i^2)$ . In addition, we recall that we found in chapter 4 that finite Rossby instabilities grow when the Rossby number based on the wave amplitude  $u_w$  and scale  $\lambda$ ,  $Ro_f \equiv u_w/\lambda$  is larger than  $\sim 0.1$ . Such a scale-dependent Rossby number can be evaluated from the spectral density of kinetic energy  $T(k)$ . The typical velocity at scale  $\lambda = 2\pi/k$  is  $(kT(k))^{1/2}$  so that:

$$Ro_f(k) = \frac{k}{2\pi} (kT(k))^{1/2}. \quad (6.31)$$

The quantity  $Ro_f(k)$  is shown in figure 6.23 for the two simulations whose kinetic energy time series are displayed in figure 6.19. It is compared to the typical finite Rossby number instability threshold.  $Ro_f(k)$  is averaged over a few non-linear time scales before and after the instant when the friction is released in order to determine whether the initial three-dimensional flow is able to drive finite wave amplitude instability. We find that  $Ro_f(k)$  peaks for both simulations close to the critical value 0.1 found in chapter 4. This result is consistent with the existence of a geostrophic growth for the two simulations shown in figure 6.10. In addition, a shift towards higher wave numbers of the maximum value of  $Ro_f(k)$  is noticeable when the forcing amplitude is decreased.

These results highlight the difficulty of predicting exactly the stability of the inertial wave turbulence based on the resonant wave only, for two main reasons:

1. the inertial wave turbulence excites a range of wave numbers around the resonant one, some of them are above the threshold of the finite wave amplitude instability, as observed for instance in figure 6.23; these new wave numbers are not taken into account in the simple analysis of section 3;
2. even if a geostrophic stability criterion can be deduced from finite wave amplitude instability, the saturation amplitude of geostrophic modes cannot be predicted from this criterion.

The first reason may explain why a slow growth is still observed at  $Ro_i = 7.5 \times 10^{-3}$  (see figure 6.19). The stability analysis is based on the resonant mode only, and the highest  $Ro_f(k)$  is reached at a slightly larger wave number (see figure 6.23-left). However, despite their growth, geostrophic modes reach a low saturation amplitude in the case  $Ro_i = 7.5 \times 10^{-3}$  so that the inertial wave turbulence remains stable.

More systematic simulations in better controlled conditions are still needed to fully characterise the stability of inertial wave turbulence and its relation to the finite wave amplitude instability. Nevertheless, finding stable wave turbulence in the low forcing amplitude regime is a promising result pointing towards the relevance of this regime for geo- and astrophysical applications. Yet, simulations reaching a wave-dominated saturation from any initial condition, if possible, remains to be carried out.

## 6. Conclusion: the contributions of the local model

The use of a local model of the elliptical instability has allowed us exploring the details of the non-linear turbulent saturation of the inertial wave resonance. The two saturation regimes revealed in the experiments are both reproduced in the simulations presented throughout this chapter. Using a local model proves particularly useful to investigate the properties of the wave saturation in extreme regimes of low forcing amplitude and dissipation. We confirm that the wave-dominated regime is an inertial wave turbulence, which is strikingly illustrated by the kinetic energy focusing along the dispersion relation of inertial waves.

Nevertheless, additional physics were necessary to produce in the numerical set-up a turbulent saturation that is not dominated by strong geostrophic vortices. This systematic observation of geostrophic saturation, even at low forcing amplitude, is related to direct forcing in the non-linear overshoot, a phenomenon which does not seem to play an important role in the experimental realisation of the elliptical instability. A wave-dominated regime has therefore been produced first by applying a specific friction to geostrophic modes to force them to be sub-dominant. Releasing this friction has allowed investigating the stability of the wave turbulence created via the use of a specific friction restrained to the growth phase and the early stages the elliptical instability saturation. We have thus shown that the inertial wave turbulence is stable provided the forcing amplitude  $Ro_i$  is sufficiently small, and that the threshold of the wave turbulence instability may be related to the finite Rossby instabilities explored in chapter 4. The existence of multi-stability in the non-linear saturation of the elliptical instability found at  $Ro_i = 7.5 \times 10^{-3}$  and  $E = 10^{-6.5}$  suggests that the instability of geostrophic modes is sub-critical. More extreme simulations at even lower forcing amplitudes are required

to determine if wave turbulence can be found in the saturation of the instability without the use of friction at all and with any random, small amplitude initial condition. Although the secondary transition from two regimes of saturation is not as straightforward as in the experiments, this numerical investigation draws a correspondence between the experimental study and the theoretical investigation of inertial wave stability.

# Chapter 7

## Tidally driven parametric instability in stratified flows

### 1. The relevance of stratification to tides in planetary cores

#### 1.1 Stable stratification and internal oscillations

Stable stratification refers to a physical situation in a fluid with a density gradient aligned with gravity, and for which a fluid particle moved adiabatically upward is denser than the ambient fluid (see figure 7.1). Any local, vertical displacement of fluid results in a restoring buoyancy force leading it back towards its initial, static configuration. When dissipation is sufficiently small, inertia causes oscillations, which can be qualitatively found with a simple Lagrangian model. Consider a fluid particle with static stable height  $z_0$ , and an adiabatic vertical displacement  $\zeta$  so that the total height reads  $z = z_0 + \zeta$ . We assume a linear stratification profile ( $\partial\rho/\partial z = \overline{cst} < 0$ ) such that for any  $\zeta$ :

$$\rho(\zeta) = \rho_0 + \frac{\partial\rho}{\partial z}\zeta. \quad (7.1)$$

An adiabatic vertical displacement of the particle with neutral density  $\rho_0$  results in a density contrast  $\Delta\rho$  between the particle and the ambient writing:

$$\Delta\rho = -\frac{\partial\rho}{\partial z}\zeta. \quad (7.2)$$

To compute the buoyancy force resulting from the density contrast, we assume that the volume variation associated with the adiabatic displacement is negligible, which is a valid

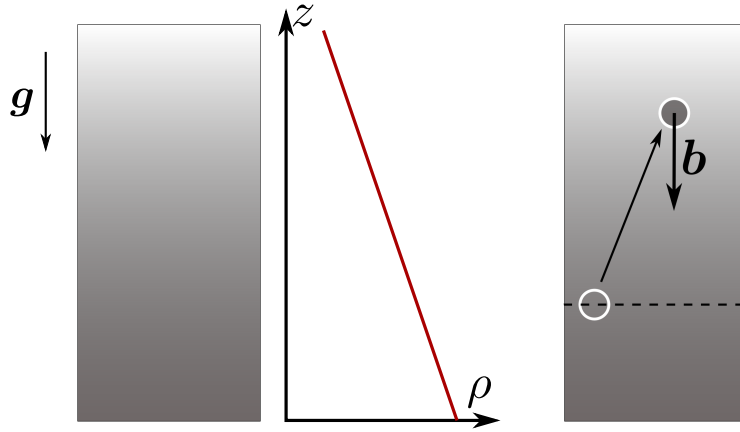


**Figure 7.1:** Schematic cartoon of a stable density stratification in a fluid, where we have indicated the gravity vector  $\mathbf{g}$ . The stable density may result, for instance, from a gradient in solute concentration or temperature. The right stratified fluid column illustrates a fluid particle moved upward and undergoing a restoring buoyancy force  $\mathbf{b}$  pointing downward.

approximation in the Earth’s ocean for instance. This approximation does not hold, however, in the Earth’s atmosphere or in stellar interiors where the compressibility of the fluid is large, or in the Earth’s core where the size of the fluid medium is so large that compressibility effects must be taken into account. Including compressibility effects would not affect the present reasoning but leads to some complications that might obscure the discussion and which are therefore discarded. We call  $dV$  the —constant— volume of the fluid particle; calling  $\mathbf{g} = -g\mathbf{e}_z$  the gravitational acceleration, the buoyancy force  $\mathbf{b}$  induced by the density contrast is:

$$\mathbf{b} = \Delta\rho dV\mathbf{g} = g \frac{\partial\rho}{\partial z} \zeta dV \mathbf{e}_z . \quad (7.3)$$

According to Newton’s second law, the differential equation governing the position of the fluid particle is the following:

$$\frac{d^2\zeta}{dt^2} - \frac{g}{\rho_0} \frac{\partial\rho}{\partial z} \zeta = 0 . \quad (7.4)$$

Because  $\partial\rho/\partial z < 0$ , the equation (7.4) shows that the particle displacement results in internal oscillations at a typical frequency  $N$  such that:

$$N^2 = -\frac{g}{\rho_0} \frac{\partial\rho}{\partial z} > 0 \quad (7.5)$$

$N$  is called the Brunt-Väisälä frequency,  $N^{-1}$  is a typical oscillation time in stratified fluids.

Two dissipative mechanisms may prevent internal oscillations to occur in stratified fluids. The first one is viscous friction which damps the inertial dynamics. The second is molecular diffusion of the stratifying agent, be it solute or temperature. When the fluid particle undergoes vertical motion, molecular diffusion tends to homogenise its density with the ambient thus suppressing the density contrast and reducing the buoyancy force.

## 1.2 Internal waves

The discussion in this section aims at showing that waves caused by the interplay between stable stratification and inertia, called “internal waves”, exist in stratified fluids. Instead of

using a qualitative Lagrangian method, we use the linearised Euler and advection equation.

We consider here an unbounded stably stratified medium. We assume for instance that density variations are imposed by a temperature gradient, and we call  $\alpha$  the thermal expansion of the fluid. The thermal gradient is in  $z$  and is aligned with gravity. The temperature field writes  $T = T_0 + Sz$ ,  $T_0$  being a reference temperature, so that the density of the fluid  $\rho$  is expanded as follows:

$$\rho = \rho_0(1 - \alpha(T - T_0)) = \rho_0(1 - \alpha Sz) \quad (7.6)$$

where  $\rho_0$  is the density of the fluid at the reference temperature.

We aim at deriving the equations governing the spatial and temporal variations of a velocity and temperature perturbation ( $\mathbf{U}, \Theta$ ) to this stable base state. Under the Boussinesq approximation, the Euler equation along with the incompressibility condition writes:

$$\partial_t \mathbf{U} + \mathbf{U} \cdot \nabla \mathbf{U} = -\nabla p + \alpha g \Theta \mathbf{e}_z + \nabla^2 \mathbf{U} \quad (7.7)$$

$$\nabla \cdot \mathbf{U} = 0, \quad (7.8)$$

where  $U_z$  is the vertical component of the velocity. The diffusionless advection of the temperature field is modelled by the following equation:

$$\partial_t \Theta + \mathbf{U} \cdot \nabla \Theta = -S U_z. \quad (7.9)$$

A wave equation very similar to the Poincaré equation (see chapter 1 section 3.1) can be derived from (7.7–7.9) in the linear limit. The process yielding the wave equation is similar to what is done in chapter 1 and the advection equation (7.9) is used for substitution to finally obtain an equation on the velocity field only:

$$\partial_{tt} \nabla^2 \mathbf{U} = -N^2 (-\partial_{zz} U_z \mathbf{e}_z + \nabla^2 \mathbf{U}) \quad \text{with} \quad N^2 = \alpha g S = -\frac{g}{\rho_0} \frac{d\rho}{dz}. \quad (7.10)$$

The vertical velocity  $U_z$  satisfies the following equation:

$$\partial_{tt} \nabla^2 U_z + N^2 (\partial_{xx} + \partial_{yy}) U_z = 0 \quad (7.11)$$

and the temperature fluctuation  $\Theta$  follows the same equation.

To find oscillating solutions to the equation (7.11), we look for plane waves with wave vector  $\mathbf{k}$  and frequency  $\omega$  yielding the following dispersion relation:

$$\omega^2 = N^2 \frac{k_x^2 + k_y^2}{|\mathbf{k}|^2} = N^2 \sin^2 \xi \quad (7.12)$$

with  $\xi$  the angle between the density gradient (or gravity) and the wave vector. As in the case of inertial waves, the frequency of these “internal waves” is always below  $N$ , the Brunt-Väisälä frequency which is related to gravity and the strength of the density gradient, as indicated in equation (7.10).

### 1.3 Stratification of fluid planetary interiors

Many planetary cores are thought to be at least partly stably-stratified, including the Earth. There is indeed seismic evidence for the existence of a stratified layer at the bottom

and the top of the Earth core (Hirose et al., 2013), and evidence provided by the analysis of periodic fluctuations of the magnetic field supporting the existence of a top stratified layer (Buffett, 2014). Besides, the experimental and numerical evidence for high values of liquid iron thermal conductivity also points towards the existence of a stratified layer at the top of the core (see Labrosse (2015) and references therein). In addition to the Earth, other terrestrial bodies are thought to be at least stably-stratified according to interior models, although they are known for maintaining a large-scale magnetic field (see Stanley and Mohammadi (2008) for a review).

Stable stratification of terrestrial bodies' liquid core may also be a consequence of their formation process. The later stage of planetary accretion is dominated by large impacts between partially differentiated proto-planets, *i.e.* terrestrial bodies with a growing iron core at its centre. Proto-planets' iron cores bear light elements such as carbon, sulfur, oxygen, etc. whose proportions vary from one body to another. Landeau et al. (2016) have shown that after an impact, iron migration through a partially molten silicate mantle and a molten iron core results in very little chemical mixing of light elements. At the end of the migration process, the iron reaches a neutral height in the core which depends on light element composition. The resulting iron core should therefore be stratified in density via solute (*i.e.* light elements) concentration.

To conclude, several reasons exist for a stable stratification in a planetary core, and it seems not to prevent the emergence of a magnetic field (Stanley and Mohammadi, 2008). As in the case of rotation, internal oscillations sustained by the stable stratification could very well be excited by mechanical forcing. The aim of this chapter is to investigate this hypothesis.

Note also that terrestrial planets' iron cores are not the only internal fluid layers that are stratified. It could also be the case of icy satellites' sub-surface oceans, such as in Enceladus, Dione and Europa, which are large, salted oceans lying underneath their ice crusts. Investigating how mechanical forcing may drive significant compositional mixing in such internal oceans is also one of the goals of the present chapter.

## 1.4 A parametric instability of internal waves driven by tides?

Similarly to the tidally driven elliptical instability, the large scale tidal flow could also couple with internal gravity waves in the case where these planetary interiors are stratified. Several routes exist for the excitation of three-dimensional turbulent motion within a stably-stratified layer by tides or other mechanisms. It is a common issue in physical oceanography where the interaction of the large-scale tidal flow with ground topography is known for exciting (St. Laurent and Garrett, 2002), focusing (Maas and Lam, 1995; Bajars et al., 2013) and scattering (Bühler and Holmes-Cerfon, 2011) internal waves which break down into small-scale turbulence via triadic resonant interactions (MacKinnon and Winters, 2005; Bourget et al., 2013; Scolan et al., 2013; Brouzet et al., 2016; Brouzet et al., 2017). In addition, several studies have striven to examine the resonant excitation of global internal modes by a homogeneous tidal flow without relying on any small-scale topography. This has been done for instance by Miyazaki and Fukumoto (1992); Kerswell (1993a); Miyazaki (1993); McWilliams and Yavneh (1998); Aspden and Vanneste (2009); Guimbard et al. (2010) with either radial or vertical stratification compared to deformation, but always in the situation where the Coriolis force is of greater or similar influence compared to buoyancy effects. Whether these resonant instabilities can drive three-dimensional turbulence in the bulk of a stratified core or subsurface

ocean when stratification dominates over rotation (*i.e.* when  $N \gg \Omega$ ) remains to be seen.

In this chapter, we derive a local model of fluid planetary interiors, be it a liquid core or a subsurface ocean, which allows to study the idealised limit where stratification completely dominates over rotation, with the stratification axis pointing in any direction relative to that of the tidal deformation. We show in particular that tides excite a parametric subharmonic resonance of internal waves. Moreover, such an idealised local model allows to thoroughly analyse the turbulent saturation of this tidally driven resonance, and we show that tidal forcing drives bulk internal wave turbulence.

Note that parametric resonances of internal waves driven by large-scale homogeneous forcing have already been investigated in particular experimental setups. McEwan and Robinson (1975) designed a setup to examine how large-scale internal waves spontaneously generate smaller scale oscillations in a stratified tank designed to mimic the advection by large scales. In close analogy, Benielli and Sommeria (1996); Benielli and Sommeria (1998) showed that vertically shaking a stratified fluid leads to a parametric resonance of internal waves (similarly to the classical Faraday instability) whose growth saturates into turbulence. The originality of our study resides in the investigation of the stability of a more realistic homogeneous tidal flow. We also provide a detailed spatio-temporal analysis of the non-linear break-down into turbulence from the primary resonance.

This chapter is organised as follows. The first part is devoted to introducing the tidal base flow and developing a local approach to study its stability following the work of Barker and Lithwick (2013). We carefully introduce buoyancy effects under the Boussinesq approximation. With this model, we then investigate the resonance of internal waves via direct numerical simulations and Wentzel-Kramers-Brillouin (WKB) analysis of the local model (Lifschitz and Hameiri, 1991). We then thoroughly explore the turbulence resulting from the non-linear saturation of the instability. We show that it is best described as a wave turbulence and study the subsequent mixing and dissipation rates.

## 2. Local study of the equilibrium tidal base flow

### 2.1 Tidal base flow

We consider a non-rotating planet undergoing tidal deformation due to a moon orbiting at rate  $n\mathbf{e}_z$  as pictured in figure 7.2. We suppose the tidal deformation to be ellipsoidal and uniform in the whole fluid planetary interior; this assumption corresponds to planetary cores or oceans in between two boundaries whose response to tidal force is the same as that of the fluid's. The other limit, which won't be considered here, is an ocean on top of a non-deformable solid core or inside a non-deformable solid shell for which the ellipticity of the deformation can no longer be considered uniform. Any planetary fluid layer stands between these two limits.

In the reference frame following the tidal deformation, we recall that the base flow  $U_b^{\text{bulge}}$

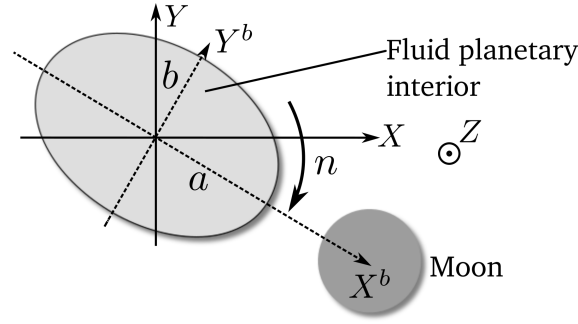


**Figure 7.2:** Schematic representation of a companion orbiting a planet at rate  $n$ . Tidal interactions induce an ellipsoidal deformation of the whole planet, which is supposed uniform: this corresponds to the behaviour of a fully deformable planet.

can be approximated to the following analytical solution (see chapter 1 section 1.3):

$$U_b^{\text{bulge}} = \gamma \begin{bmatrix} 0 & -1 - \beta & 0 \\ 1 - \beta & 0 & 0 \\ 0 & 0 & 0 \end{bmatrix} \begin{bmatrix} X \\ Y \\ Z \end{bmatrix} = \mathbf{B}\mathbf{X}_b, \quad (7.13)$$

where we have introduced  $\gamma = -n$ , the rotation rate of the fluid in the orbital frame, by analogy with previous chapters, and  $\beta$  the ellipticity of the tidal deformation defined as  $\beta = (a^2 - b^2)/(a^2 + b^2)$  (where  $a$  and  $b$  are the semi-major and semi-minor axes respectively, see figure 7.2).  $\mathbf{X}^b$  is the position vector whose coordinates are written in the orbital frame rotating with the tidal bulge. In the planetary frame of reference, after coordinate change and velocity transformation, the base flow  $U_b$  translates into (see chapter 1 section 1.3):

$$U_b = -\gamma\beta \begin{bmatrix} \sin(2\gamma t) & \cos(2\gamma t) & 0 \\ \cos(2\gamma t) & -\sin(2\gamma t) & 0 \\ 0 & 0 & 0 \end{bmatrix} \begin{bmatrix} x \\ y \\ z \end{bmatrix} = \mathbf{A}(t)\mathbf{X}. \quad (7.14)$$

Note that this base flow is also a solution of the Navier-Stokes equations in the presence of stable stratification in the Boussinesq approximation. Assuming an equilibrium state for which isopycnals are also the surfaces with constant gravitational potential  $\phi$ , including centrifugal force and tides, the density can be written as a continuous and monotonic function  $f$  of  $\phi$  so that  $\rho\mathbf{g} = -f(\phi)\nabla\phi = -\nabla F(\phi)$  with  $dF/d\phi = f$ . The equilibrium buoyancy term can then be absorbed in the pressure gradient so that this basic situation is purely barotropic. Such a barotropic assumption is valid when the isopycnals can move sufficiently fast to keep track of the orbital motion of the moon and the rotating tidal potential; it is valid for high Brunt-Väisälä frequency compared to the differential rotation frequency  $\gamma$  (see Ogilvie (2014) for further discussion). In the opposite regime where the stratification is weaker, the slow motion of the isopycnals should lead to baroclinicity and excite large scale flow consistently trying to restore the alignment between isopycnal and isopotential. This chapter is rather focused on small scale instabilities in the regime where the Brunt-Väisälä frequency is larger than  $\gamma$ . We therefore discard any baroclinic situation to keep only the global tidal distortion as a source of instability. Tidally-driven baroclinicity should deserve a study of its own.

In the following, we introduce buoyancy effects under the Boussinesq approximation. We study the tidal instability problem developing a local approach inspired by Barker and Lithwick (2013) and which is developed in chapter 7. We use the planetary frame of reference,

which is considered to be non-rotating. Introducing rotation of this frame at rate  $\Omega \mathbf{e}_z$  in the model developed hereafter would only require the addition of a Coriolis force in the planetary frame. The base flow would not be modified apart from the fluid rotation rate in the orbital reference frame  $\gamma$  which would then write  $\gamma = \Omega - n$  (Barker and Lithwick, 2013).

## 2.2 The local approach to the dynamics

We aim at studying the incompressible perturbations to the base flow  $\mathbf{U}_b$  defined in (7.14). Instead of modelling the whole planetary fluid layer, we develop a local model to study this perturbation flow in the neighbourhood of a Lagrangian point  $M$  at position  $\mathbf{X}_0(t)$  following the elliptical streamlines such that  $\dot{\mathbf{X}}_0 = \mathbf{U}_b$ . This local model will prove particularly convenient to include buoyancy effects as the stratification can be assumed to be locally uniform and linear around the tracked point. We reproduce here its derivation to carefully introduce buoyancy effects.

Let us call  $\mathbf{U}^i$  the total velocity field in the frame bound to the planet and  $\mathbf{U}^c$  the total velocity field in the frame bound to  $\mathbf{X}_0$ .  $\mathbf{U}^i$  satisfies the following Navier-Stokes equation:

$$\partial_\tau \mathbf{U}^i + \mathbf{U}^i \cdot \nabla_{\mathbf{X}} \mathbf{U}^i = -\frac{1}{\rho} \nabla P^i + \nu \nabla_{\mathbf{X}}^2 \mathbf{U}^i \quad (7.15)$$

where  $\tau$  stands for time,  $\nabla_{\mathbf{X}}$  for the gradient in the  $\mathbf{X} = (x, y, z)$  coordinates,  $P^i$  is the pressure and  $\rho$  is the density of the fluid.  $\mathbf{U}^i$  is the total velocity and includes the base flow  $\mathbf{U}_b(\mathbf{X})$  and velocity perturbations  $\mathbf{u}^i$  so that  $\mathbf{U}^i = \mathbf{U}_b(\mathbf{X}) + \mathbf{u}^i$ . To transform this equation into the frame in translation bound to  $\mathbf{X}_0$ , we process the following coordinate change:

$$\begin{cases} \mathbf{x} &= \mathbf{X} - \mathbf{X}_0(t) \\ t &= \tau \end{cases} . \quad (7.16)$$

The corresponding change in derivatives is  $\nabla_{\mathbf{X}} = \nabla_{\mathbf{x}} = \nabla$  and  $\partial_\tau = \partial_t - \mathbf{U}_b \cdot \nabla_{\mathbf{x}}$ . The velocity measured in the frame bound to  $\mathbf{X}_0$  is  $\mathbf{U}^c = \mathbf{U}^i - \mathbf{U}_b(\mathbf{X}_0, t)$ . Transforming the equation (7.15) into this frame yields:

$$\partial_t \mathbf{U}^c + \partial_t \mathbf{U}_b(\mathbf{X}_0) + \mathbf{U}^c \cdot \nabla \mathbf{U}^c = -\frac{1}{\rho} \nabla P^i(\mathbf{X}_0 + \mathbf{x}) + \nu \nabla^2 \mathbf{U}^c . \quad (7.17)$$

The acceleration term  $\partial_t \mathbf{U}_b(\mathbf{X}_0)$  is regarded as a volume force. In the frame bound to  $\mathbf{X}_0$  the Navier-Stokes equation reads:

$$\partial_t \mathbf{U}^c + \mathbf{U}^c \cdot \nabla \mathbf{U}^c = -\frac{1}{\rho} \nabla P^c - \partial_t \mathbf{U}_b(\mathbf{X}_0) + \nu \nabla^2 \mathbf{U}^c \quad (7.18)$$

where we have introduced  $P^c(\mathbf{x}) = P^i(\mathbf{X}_0 + \mathbf{x})$ . As  $\mathbf{U}^c = \mathbf{U}^i - \mathbf{U}_b(\mathbf{X}_0)$ , it is straightforward that  $\mathbf{U}^c = \mathbf{A}\mathbf{x} + \mathbf{u}^c$  with  $\mathbf{u}^c = \mathbf{u}^i = \mathbf{u}$ . In the neighbourhood of  $\mathbf{X}_0$ , the perturbed flow satisfies the following equation:

$$\partial_t \mathbf{u} + \mathbf{A}(t)\mathbf{x} \cdot \nabla \mathbf{u} + \mathbf{A}(t)\mathbf{u} + \mathbf{u} \cdot \nabla \mathbf{u} = -\frac{1}{\rho} \nabla P^c - \partial_t \mathbf{U}_b(\mathbf{X}_0) + \nu \nabla^2 \mathbf{u} \quad (7.19)$$

along with the incompressibility condition  $\nabla \cdot \mathbf{u} = 0$ .

## 2.3 Introducing buoyancy in the local Navier-Stokes equation

The local model introduced above is particularly useful when introducing buoyancy effects, be it due to temperature or solute concentration. In a sufficiently small patch, the background stratification can be assumed to be uniform, while being mostly radial in global planetary layers. Let us call  $\mathbf{S}(t)$  the background active scalar gradient such that the total scalar field  $T$  can be written as:

$$T = T_0 + \mathbf{S}(t) \cdot \mathbf{x} + \vartheta \quad (7.20)$$

where  $\vartheta$  is the scalar fluctuation around the background stratification. As it will be pointed out later, it is required to include a temporal dependence in the stratification to account for periodic stretching induced by the background base flow defined in (7.14) and illustrated in figure 6.1.

The buoyancy effects are first introduced in equation (7.19), in the Boussinesq approximation, via the volume effective gravitational force  $\rho_0(\mathbf{g} - \partial_t \mathbf{U}_b(\mathbf{X}_0))(1 - \alpha(T - T_0))$  where  $\alpha$  is an isobaric thermal expansion coefficient. As we assume the base state to be barotropic, the term  $\rho_0(\mathbf{g} - \partial_t \mathbf{U}_b(\mathbf{X}_0))(1 - \alpha \mathbf{S} \cdot \mathbf{x})$  can be absorbed in a modified pressure  $\Pi$ . Including buoyancy effects, the equations (7.19) now reads:

$$\partial_t \mathbf{u} + \mathbf{A}(t)\mathbf{x} \cdot \nabla \mathbf{u} + \mathbf{A}(t)\mathbf{u} + \mathbf{u} \cdot \nabla \mathbf{u} = -\nabla \Pi - \alpha [ \mathbf{g} - \partial_t \mathbf{U}_b(\mathbf{X}_0) ] \vartheta + \nu \nabla^2 \mathbf{u} . \quad (7.21)$$

Note that the field  $\mathbf{u}$  also satisfies the incompressibility condition  $\nabla \cdot \mathbf{u} = 0$ .

Two possible instability sources are worth considering. In the RHS of (7.21), the Lagrangian advection of the studied patch translates into an effective gravity with varying intensity. Such a forcing has already been shown to parametrically excite internal waves with a growth rate proportional to the oscillating acceleration amplitude (McEwan and Robinson, 1975; Benielli and Sommeria, 1998). The base flow is also coupled in the left hand side to the velocity perturbation; in the analogue context of rotating flows, the induced tidal stretching and shearing is well known for triggering parametric excitation of a pair of inertial waves. This instability mechanism has also been studied in the context of strained vortices with a stratification aligned with the background vorticity (Miyazaki and Fukumoto, 1992; Miyazaki, 1993; Kerswell, 1993a; McWilliams and Yavneh, 1998; Aspden and Vanneste, 2009; Guimbard et al., 2010). Whether a similar stirring mechanism occurs in purely stratified fluids, *i.e.* with no background vorticity, has never been investigated to the best of our knowledge. In the present study, we propose to drop the gravity-driven parametric excitation to focus on tidal stretching and shearing effects.

To support this approximation, we suggest to compare the order of magnitude of the expected growth rate of both instabilities. In the case of excitation by gravity variations, the amplitude of the forcing is proportional to the acceleration of a Lagrangian particle during an epicycle:  $\beta \ell \gamma^2$ . Following Benielli and Sommeria (1998), the corresponding growth rate  $\sigma_g$  should scale like  $\sigma_g \sim \gamma(\beta \ell \gamma^2)/g$  where  $g$  is the mean intensity of gravity. On the other hand, if the coupling between the base flow and the velocity perturbation acts as in the elliptical instability in rotating fluids, the growth rate  $\sigma_e$  should then scale like  $\sigma_e \sim \beta \gamma$  (see eq. (4) in Barker and Lithwick (2013)). As a consequence,  $\sigma_e/\sigma_g \sim g/(\ell \gamma^2)$ . As  $\gamma$  is at most comparable to the spin rate of the considered planetary body, this ratio equivalently compares the self-gravity of the body to the centrifugal acceleration. It should then always be large to ensure self-cohesion. For instance, for the Moon-Earth system,  $\gamma = 2\pi/(1\text{day})$ ; at the Core-Mantle boundary  $\ell \sim 3 \times 10^3$  km and  $g \sim 10$  m.s<sup>-2</sup>. The ratio  $\sigma_e/\sigma_g$  is about  $3 \times 10^2$  at the Core-Mantle boundary and  $1.5 \times 10^2$  at the surface of the Earth, which justifies dropping the varying

gravity forcing term. Note however that in the case of a confined layer above a non-deformable core, the elliptical base flow, which is then no longer described by (7.14), would create large-amplitude lateral flows whose contribution to the effective gravity would not necessarily be negligible. Although of interest for instance for the Earth's oceans, we do not consider the latter case here to focus on a fully deformable object.

## 2.4 The buoyancy equation and time dependence of stratification

The Navier-Stokes equation (7.21) is coupled to the advection-diffusion equation for the scalar  $T$ :

$$\partial_t T + (\mathbf{A}(t)\mathbf{x} + \mathbf{u}) \cdot \nabla T = \kappa \nabla^2 T \quad (7.22)$$

where  $\kappa$  is a diffusivity coefficient assumed to be constant. Plugging the assumption (7.20) in (7.22) leads to the following modified advection-diffusion equation:

$$\frac{d\mathbf{S}}{dt} \cdot \mathbf{x} + \frac{\partial \vartheta}{\partial t} + \mathbf{A}(t)\mathbf{x} \cdot \mathbf{S} + \mathbf{A}(t)\mathbf{x} \cdot \nabla \vartheta + \mathbf{S} \cdot \mathbf{u} + \mathbf{u} \cdot \nabla \vartheta = \kappa \nabla^2 \vartheta. \quad (7.23)$$

Assuming that in the equilibrium state there is no perturbation, *i.e.*  $(\mathbf{u}, \vartheta) = (\mathbf{0}, 0)$ , compels the time evolution of the stratification vector  $\mathbf{S}(t)$  to follow:

$$\frac{d\mathbf{S}}{dt} = -\mathbf{A}^T(t)\mathbf{S} \quad (7.24)$$

where  $\mathbf{A}^T$  stands for the transpose of  $\mathbf{A}$  given in equation (7.14). The periodic stretching and shearing induced by the base flow, as represented in figure 6.1, impacts the local background density profile. It has the same temporal variation as the wave vectors described by equation 6.12.

A typical time evolution of  $\mathbf{S}(t)$  is pictured in figure 7.3. The initial stratification can arbitrarily be set in the  $(xMz)$  plane. It is then fully parameterised by the angle  $s$  such that  $\mathbf{S}_0 = S_0(\sin s, 0, \cos s) = S_0 \tilde{\mathbf{s}}_0$ ; it represents the mean latitude at which the tracked patch is located.

Note that to avoid the spontaneous appearance of baroclinic instability, the gravity has to change its direction to stay aligned with the buoyancy gradient. This is consistent with the fact that the point  $\mathbf{X}_0$  is following an elliptical streamline included in an equipotential surface of the total gravitational field including tidal force and self-gravitation of the unperturbed state; the gravitational field must remain perpendicular to streamlines. We arbitrarily choose to keep the gravitational field amplitude constant throughout time. Calling  $g$  the gravity intensity, the final set of local equations is, in addition to (7.24):

$$\frac{\partial \mathbf{u}}{\partial t} + \mathbf{A}(t)\mathbf{x} \cdot \nabla \mathbf{u} + \mathbf{A}(t)\mathbf{u} + \mathbf{u} \cdot \nabla \mathbf{u} = -\nabla \Pi + \alpha g \frac{\mathbf{S}}{\|\mathbf{S}\|} \vartheta + \nu \nabla^2 \mathbf{u} \quad (7.25)$$

$$\frac{\partial \vartheta}{\partial t} + \mathbf{A}(t)\mathbf{x} \cdot \nabla \vartheta + \mathbf{u} \cdot \nabla \vartheta = -\mathbf{S}(t) \cdot \mathbf{u} + \kappa \nabla^2 \vartheta. \quad (7.26)$$

## 2.5 Conclusion on the equations and the local model

We will consider hereafter a patch of typical size  $L$ . Typical time and velocity scales are then given by  $1/\gamma$  and  $L\gamma$ . The initial stratification amplitude  $S_0$  can be used to build a

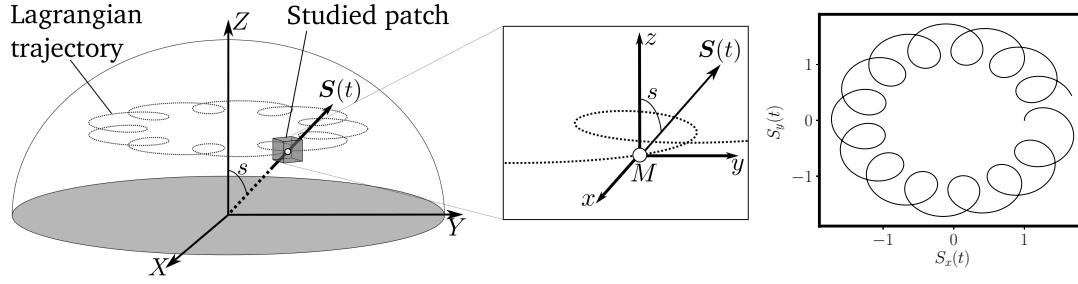


**Figure 7.3:** **Left:** schematic picture linking stratification seen from a global and a local view. The angle  $s$  between stratification and  $(OZ)$  is then a proxy for the latitude at which the patch is located. Note that the local axes  $(Mxyz)$  are in translation around the  $Z$  axis. **Right:** time evolution of the  $x$  and  $y$  components of the stratification. Note that the slow rotation of  $\mathbf{S}$  is due to the translating motion of the Lagrangian particle around  $Z$ .

buoyancy scale  $LS_0$ . With those definitions, the dimensionless velocity-temperature dynamics satisfies:

$$\frac{\partial \mathbf{u}}{\partial t} + A(t)\mathbf{x} \cdot \nabla \mathbf{u} + A(t)\mathbf{u} + \mathbf{u} \cdot \nabla \mathbf{u} = -\nabla \Pi + N^2 \vartheta \mathbf{e}_s + \frac{1}{Re} \nabla^2 \mathbf{u} \quad (7.27)$$

$$\frac{\partial \vartheta}{\partial t} + A(t)\mathbf{x} \cdot \nabla \vartheta + \mathbf{u} \cdot \nabla \vartheta = -\tilde{\mathbf{S}}(t) \cdot \mathbf{u} + \frac{1}{Pr Re} \nabla^2 \vartheta \quad (7.28)$$

$$\nabla \cdot \mathbf{u} = 0 \quad (7.29)$$

where we have introduced the dimensionless Brunt-Väisälä frequency  $N$  such that  $N^2 = \alpha g S_0 / \gamma^2$ .  $Re$  is the Reynolds number  $L^2 \gamma / \nu$  and  $Pr$  is the Prandtl number  $\nu / \kappa$ .  $\tilde{\mathbf{S}}(t)$  and  $\mathbf{e}_s$  are defined as follows:

$$\tilde{\mathbf{S}}(t) = \text{Rot}(-\gamma t) \hat{\mathbf{R}}(t) \mathbf{S}_0 / S_0 = \text{Rot}(-\gamma t) \hat{\mathbf{R}}(t) \tilde{\mathbf{s}}_0 \quad \text{and} \quad \mathbf{e}_s = \tilde{\mathbf{S}}(t) / \|\tilde{\mathbf{S}}(t)\| \quad (7.30)$$

where we have used the same notations as in chapter 6 equation (6.12).

This set of equations is particularly convenient as it reduces a global problem with a non-trivial ellipsoidal geometry to a local one in Cartesian coordinates with uniform stratification. It retains all the key ingredients to understand the homogeneous dynamics of tidally-forced flows in stratified layers while avoiding to account for boundary layers.

## 2.6 The local model in the orbital frame

The same analysis can be performed in the orbital frame tracking the elliptical deformation rotation at rate  $n\mathbf{e}_z$ . The set of equations obtained is very similar to (7.27) except that  $A(t)$  must be replaced by the matrix  $B$  defined in (7.13) and a Coriolis acceleration  $2n\mathbf{e}_z \times \mathbf{u}$  must be added to the left hand side of the momentum conservation. In addition, the time evolution of the stratification vector reads  $\tilde{\mathbf{S}}(t) = \hat{\mathbf{R}}(t) \tilde{\mathbf{s}}_0$  where  $\hat{\mathbf{R}}$  has been introduced in (6.12). The two frames of reference are equivalent; nevertheless we prefer the planetary frame as it allows to introduce planetary rotation with the mere intuitive addition of a Coriolis acceleration. In the non stratified case, this frame allows to clearly identify the inertial waves frequencies (see chapter 6). We have therefore considered the model in this frame to facilitate future works concerned with the interplay between rotation and stratification.

## 2.7 Direct numerical simulations in a shearing box

The dynamics of the perturbations  $\mathbf{u}$  to the equilibrium state can be simulated via a decomposition of  $\{\mathbf{u}, \Pi, \vartheta\}$  into Kelvin modes such that:

$$\{\mathbf{u}, \Pi, \vartheta\} = \sum_{\mathbf{k}} \{\hat{\mathbf{u}}_{\mathbf{k}}(t), \hat{\Pi}_{\mathbf{k}}(t), \hat{\vartheta}_{\mathbf{k}}(t)\} e^{i\mathbf{k}(t) \cdot \mathbf{x}} . \quad (7.31)$$

In close analogy to the model developed in section 2.4 where stratification is found to be time dependent, evolving the wave vectors  $\mathbf{k}$  accounts for the periodic shearing induced by the base flow  $U_b$ . For all  $\mathbf{k}$ , the equations (7.27) are equivalent to:

$$\left\{ \begin{array}{l} \frac{d\mathbf{k}}{dt} = -A^T(t) \mathbf{k} = -A(t) \mathbf{k} \\ \frac{d\hat{\mathbf{u}}_{\mathbf{k}}}{dt} = -A(t) \hat{\mathbf{u}}_{\mathbf{k}} - i\mathbf{k} \hat{\Pi}_{\mathbf{k}} + N^2 \hat{\vartheta}_{\mathbf{k}} \mathbf{e}_s - \frac{k^2}{Re} \hat{\mathbf{u}}_{\mathbf{k}} - \widehat{(\mathbf{u} \cdot \nabla \mathbf{u})}_{\mathbf{k}} \\ \frac{d\hat{\vartheta}_{\mathbf{k}}}{dt} = -\tilde{S}(t) \cdot \hat{\mathbf{u}}_{\mathbf{k}} - \frac{k^2}{Re Pr} \hat{\mathbf{u}}_{\mathbf{k}} - \widehat{(\mathbf{u} \cdot \nabla \vartheta)}_{\mathbf{k}} \end{array} \right. . \quad (7.32)$$

A similar derivation was first carried out by Barker and Lithwick (2013) and presented in chapter 6 to study the tidally-driven elliptical instability in rotating non-stratified fluids. Note that the time evolution of  $\mathbf{k}(t)$  is the same as in (6.12). These equations are solved with the SNOOPY code with exactly the same method as detailed in section 2.7 in chapter 6.

## 3. Stability analysis

### 3.1 Direct Numerical Simulations

We first investigate the stability of the elliptical base flow by performing direct numerical simulations of the full problem, including viscosity and non-linearities. This is done with the SNOOPY code mentioned in section 2.7 which solves the equations (7.32). The Reynolds number  $Re$  is usually set between  $10^6$  and  $10^7$  while the Prandtl number  $Pr$  is kept constant at 1. The resolution used is up to 96 modes in each direction in a square box of size  $L$  which is used as a length scale. The simulations are initiated by a broad-band noise with  $k/(2\pi)$  ranging from 4 to 20. The time evolution of the volume-averaged kinetic energy of the fluctuations is tracked until an exponential phase is reached from which a growth rate is derived.

### 3.2 WKB and Floquet analysis

Along with solving the full problem, we examine the linear inviscid limit of equations (7.27) via a Wentzel-Kramers-Brillouin analysis (Lifschitz and Hameiri, 1991). It is easier to perform the stability analysis in the orbital frame, following the rotation of the elliptical deformation, where the base flow matrix  $B$  does not depend on time (see paragraph 2.6 for the corresponding change in equations (7.27)).

We then assume that the velocity, pressure and buoyancy fluctuations around the equilibrium state may be written as follows:

$$\{\mathbf{u}, \Pi, \vartheta\} = \{\mathbf{a}, p, \Theta\} e^{i \frac{\phi(\mathbf{x}, t)}{\eta}} \quad (7.33)$$

where  $\eta$  is a small parameter accounting for the quick wave-like spatial variations of the phase  $\phi$  compared to the secular evolution of amplitudes  $\mathbf{a}$ ,  $p$  and  $\Theta$ .

Plugging the assumption (7.33) into (7.27) in the linear inviscid limit and performing a series expansion in  $\eta$  lead to the following set of equations (Lifschitz and Hameiri, 1991):

$$\begin{cases} \mathcal{K} &= \nabla \phi \\ \frac{d\mathcal{K}}{dt} &= -\mathbf{B}^T \mathcal{K} \\ \frac{d\mathbf{a}}{dt} &= \left( 2 \frac{\mathcal{K} \mathcal{K}^T}{\mathcal{K}^2} - \mathbf{I} \right) \mathbf{B} \mathbf{a} - 2 \left( \frac{\mathcal{K} \mathcal{K}^T}{\mathcal{K}^2} - \mathbf{I} \right) (\mathbf{e}_z \times \mathbf{a}) - N^2 \left( \frac{\mathcal{K} \mathcal{K}^T}{\mathcal{K}^2} - \mathbf{I} \right) \Theta \mathbf{e}_s \\ \frac{d\Theta}{dt} &= -\tilde{\mathbf{S}}(t) \cdot \mathbf{a} \end{cases} \quad (7.34)$$

The equation on  $\mathcal{K}$  can be solved analytically: it follows the same time evolution as  $\tilde{\mathbf{S}}(t)$ ,  $\mathcal{K} = \hat{\mathbf{R}}(t) \mathcal{K}_0$  where  $\hat{\mathbf{R}}(t)$  has been defined in the time evolution of stratification (6.12) and  $\mathcal{K}_0$  is an initial condition vector.

At the lowest order ( $\beta = 0$ ), the linear operators  $\mathbf{B}$  and  $\mathbf{e}_z \times \cdot$  are equal. Since the shearing and stretching effects are entirely due to the ellipticity of streamlines, the stratification  $\tilde{\mathbf{S}}$  and wave-vector  $\mathcal{K}$  have a purely rotating motion at rate  $\gamma$ . Taking the time derivative of the last equation in (7.34) gives a second order differential equation:

$$\frac{d^2\Theta}{dt^2} - N^2 \left( \frac{(\tilde{\mathbf{s}}_0 \cdot \mathcal{K}_0)^2}{\mathcal{K}_0^2} - 1 \right) \Theta = 0 \quad (7.35)$$

where  $\tilde{\mathbf{s}}_0$  is the unit vector defining the initial stratification direction, as defined in (7.30). It is then convenient to introduce  $\xi$ , the angle between the initial stratification and wave-vector as represented in figure 7.4.  $\Theta$ , and consequently the velocity component sensitive to the stratification  $\mathbf{a} \cdot \tilde{\mathbf{S}}$ , oscillate at a frequency  $\lambda = \pm N \sin \xi$ . At the lowest order, the internal wave dispersion relation is retrieved.

To further analyse the linear growth of the instability and to obtain quantitative growth rates, we perform the Floquet analysis of the system (7.34) (Bender and Orszag, 1978). This can be done since the vectors  $\mathcal{K}$ ,  $\tilde{\mathbf{S}}$  and  $\mathbf{e}_s$  all oscillate at the same frequency  $\varpi$ , defined in (6.8). The linear operator RHS of (7.34) therefore oscillates with a period  $2\pi/\varpi$ . Knowing the time evolution of  $\mathcal{K}$ , we solve the differential equations over the vector  $(\mathbf{a}, \theta)$  from  $t = 0$  to  $t = T = 2\pi/\varpi$ . The initial condition is the identity matrix  $\mathbf{I}$ . The final value  $(\mathbf{a}(T), \theta(T))$  for each initial condition corresponds to a monodromy matrix  $\tilde{\mathbf{M}}$  and the growth rate  $\sigma$  of the instability is then related to its eigenvalues  $\mu_i$  such that (Bender and Orszag, 1978; Cébron et al., 2014):

$$\sigma = \frac{\varpi}{2\pi} \max \{ \ln \mu_i \} \quad \text{or} \quad \tilde{\sigma} = \varpi \max \{ \ln \mu_i \} \quad (7.36)$$

where  $\tilde{\sigma}$  refers to a growth computed per tidal cycles. As the resonant wave-vector is *a priori* unknown, the Floquet analysis is performed for different  $\mathcal{K}_0$ . This initial wave vector is parameterised by its norm  $\mathcal{K}_0$  (which does not play any role in the inviscid limit), the angles  $s$ ,

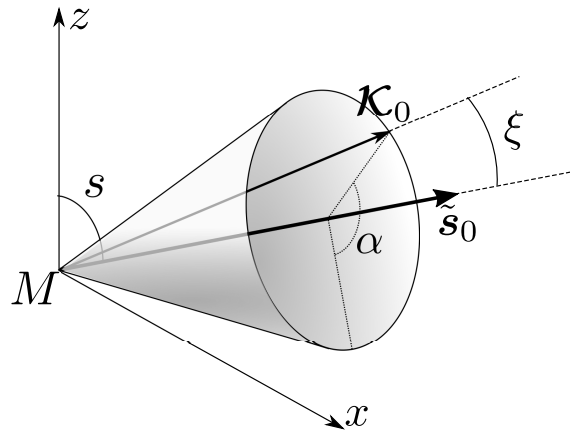


**Figure 7.4:** Schematic diagram defining the relevant angles to describe the relative position between initial stratification  $\tilde{s}_0$  and wave-vector  $\mathcal{K}_0$ . The angle between  $\tilde{s}_0$  and the axis  $z$  is  $s$  defined in figure 7.3.

$\xi$  and  $\alpha$  represented in figure 7.4, such that:

$$\mathcal{K}_0 = \mathcal{K}_0 \begin{bmatrix} \sin \xi \cos \alpha \cos s + \sin s \cos \xi \\ \sin \xi \sin \alpha \\ -\sin \xi \cos \alpha \sin s + \cos s \cos \xi \end{bmatrix}. \quad (7.37)$$

Such a parameterisation merely comes from the expression of  $\mathcal{K}_0$  in the spherical coordinates  $(\alpha, \xi)$  with a polar axis  $(M, \tilde{s}_0)$  (see figure 7.4). With  $s$  used as a control parameter, resonance is found exploring the values of  $\tilde{\sigma}$  in the  $(\xi, \alpha)$  space.

The range of angles  $\xi$  to explore is non-trivial. We show in figure 7.5 the maximum (respectively to  $\alpha$ ) growth rate computed with the Floquet theory as a function of  $\xi$  and  $\beta$ . The non-zero growth rate area delimits Floquet tongues which stretch towards  $N \sin \xi = \gamma = 1$  as  $\beta$  goes to 0. The resonant waves are therefore parametrically excited close to half the frequency of the forcing flow. Note however that the Floquet tongues are not symmetric around  $N \sin \xi = 1$ : the areas with maximum growth rates are always slightly above this line. As a consequence, to compute the theoretical maximum growth rate, we explore a range of angle  $\xi$  around  $\arcsin(1/N)$  with a tolerance of order  $\beta$ .

Note that the theoretical growth rate could also have been analytically computed via a multi-scale analysis where  $\beta t$  is the slow time. This would have given the asymptotic resonant values of  $\alpha$  for  $\beta \rightarrow 0$ . However, the complexity of the first order operator respective to  $\beta$  is such that the problem might be intractable. This might be due to the low degree of symmetry as the angle between the orbital plane and the stratification axis is arbitrary.

### 3.3 Comparison between DNS and linear stability analysis

We perform direct numerical simulations setting  $\beta = 0.05$ ,  $N = 1.5$ ,  $s = 90^\circ$  with a Reynolds number  $Re = 10^{6.5}$ . A first try was initiated from a broadband white noise with  $k/(2\pi) \in [4, 20]$ . The kinetic energy displays an exponential growth but snapshots reveal several entangled growing modes. To better quantify the growth rate and modes selection, we then restrict the broad-band noise to three intervals **1**: $[5, 10]$ , **2**: $[10, 14]$  and **3**: $[14, 20]$  which allows to isolate growing modes with approximately the same wavelength. The kinetic

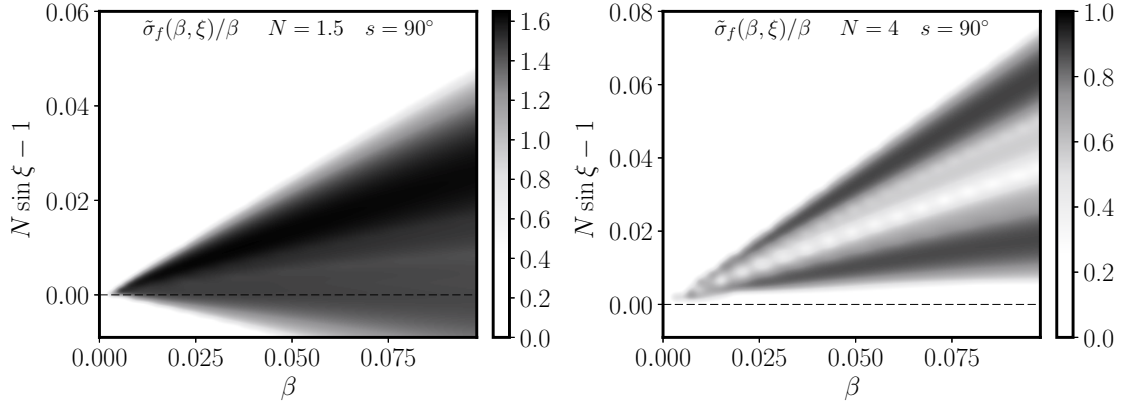


**Figure 7.5:** Map of the growth rate computed via the Floquet theory  $\tilde{\sigma}_f$  as a function of the ellipticity  $\beta$  and the angle  $\xi$  defined in figure 7.4 and equation (7.37) for **left:**  $N = 1.5$  and  $s = 90^\circ$  and **right:**  $N = 4$  and  $s = 90^\circ$ . As it will be shown hereafter, the growth rate is linearly growing with the ellipticity. We therefore normalise the growth rate by  $\beta$  which allows to identify the limits of the Floquet resonance tongue. The latter converges towards  $N \sin \xi = \gamma = 1$  for  $\beta \rightarrow 0$  showing that the resonance is subharmonic. Note that the higher growth rate area is always above the dashed line  $N \sin \xi = 1$ .

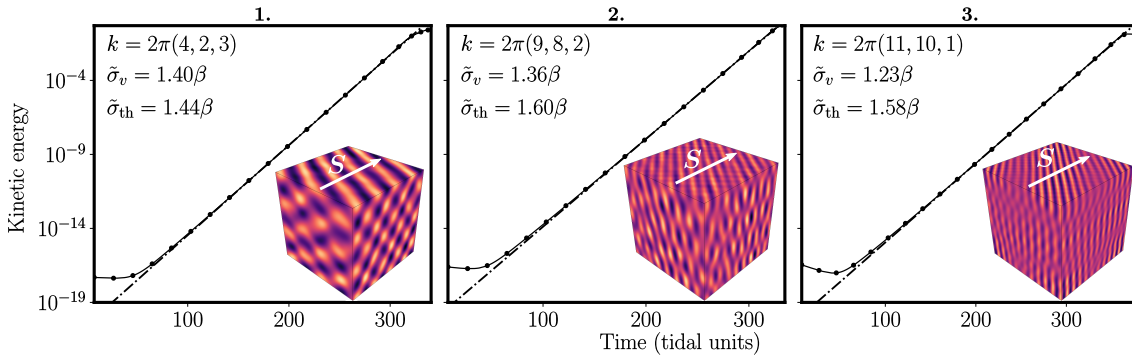


**Figure 7.6:** Growth of the instability for  $\beta = 5 \times 10^{-2}$ ,  $N = 1.5$  and  $s = 90^\circ$  initiated from broadband white noise with  $k/(2\pi)$  in three different intervals **1:**[5, 10], **2:**[10, 14] and **3:**[14, 20]. The viscous growth rate is obtained by a linear fitting in log-lin coordinates (shown as dashed-dotted lines). The corresponding snapshot of the buoyancy perturbation field is given for each experiment with an indication of the stratification direction. It is used to determine the growing mode.

energy corresponding to these three initial conditions is shown in figure 7.6 with snapshots of the buoyancy perturbation field  $\vartheta$  during the exponential growth phase. In each case, the kinetic energy is exponentially growing and the buoyancy field bears a plane wave structure, confirming that the instability mechanism is based on wave resonance. These DNS results allow to calculate the viscous growth rate  $\tilde{\sigma}_v$  in tidal units. The inviscid growth rate  $\tilde{\sigma}_{th}$  (expressed in tidal cycles) is then obtained by subtracting the viscous damping of the growing mode, *i.e.*  $\tilde{\sigma}_{th} = \tilde{\sigma}_v + 2\pi k^2 Re^{-1}$  with  $k$  the wave number of the mode (as  $\tilde{\sigma}_{th}$  is in tidal units, a  $2\pi$  factor must be added to the damping rate).

These results are then compared to the theoretical inviscid growth rate  $\tilde{\sigma}_f$  given by the Floquet analysis of equations (7.34). The map of  $\sigma_f(\alpha, \xi)$  is displayed in figure 7.7 where the location of the growing mode for each DNS is highlighted by a black dot associated to the corresponding  $\tilde{\sigma}_f$ . We first note that, both in DNS and theory, the angle  $\xi$  satisfies the condition  $N \sin \xi = 1$  with a tolerance smaller than  $\beta$ , as it was expected from qualitative

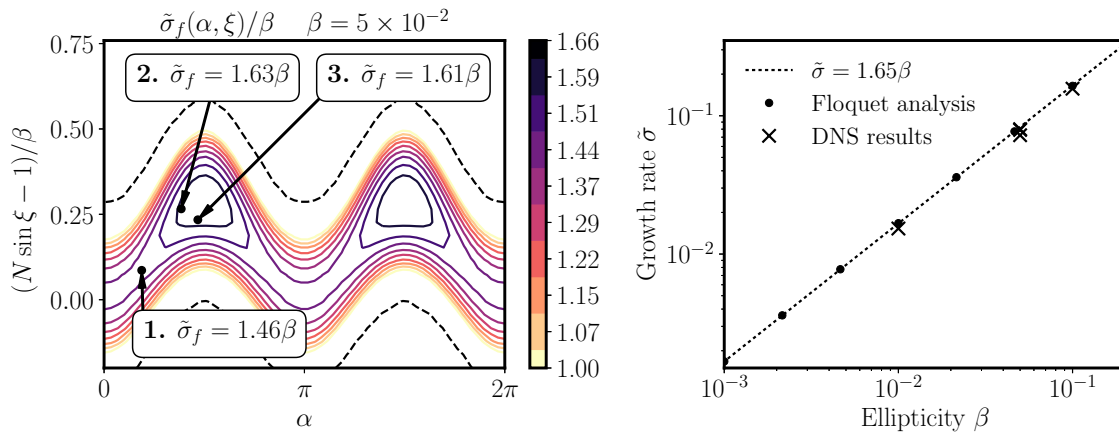


**Figure 7.7:** **Left:** map of the growth rate  $\tilde{\sigma}_f$  computed with the Floquet analysis as a function of the angles  $\xi$  and  $\alpha$ . The black dots correspond to the location of the growing modes observed in figure 7.6 for which the theoretical  $\tilde{\sigma}_f$  growth rate is given. The dashed black lines highlight the marginal stability. **Right:** comparison between systematic calculation of the maximum growth rate from the Floquet analysis and DNS results. The growth rates  $\tilde{\sigma}_f$  computed with Floquet theory are all aligned on  $\tilde{\sigma}_f = 1.65\beta$ .

arguments developed in the preceding paragraph. In addition, the theoretical growth rate  $\tilde{\sigma}_f$  is close to the growth rate  $\tilde{\sigma}_{th}$  measured in DNS with a relative difference less than 2%. With this very good agreement between DNS and the linear theory, we can now analyse the dependence of the growth rate on the control parameters using rapid linear theory only.

### 3.4 Linearity with the ellipticity $\beta$

The amplitude of the periodic stretching and shearing responsible for the parametric excitation of internal waves is proportional to the ellipticity  $\beta$ . Another way to validate the DNS and the linear stability analysis is to examine the consequent expected linearity in  $\beta$  of the growth rate as in the case of tidally-driven elliptical instability (Le Dizès, 2000; Kerswell, 2002; Grannan et al., 2017). As shown in figure 7.7 (right panel), the theoretical maximal growth rate  $\tilde{\sigma}_f$  inferred from Floquet theory is very well described by a linear function over several orders of magnitude, in the case with  $N = 1.5$  and  $s = 90^\circ$ . The growth rate computed from DNS is in addition very close to this theoretical line.

### 3.5 Dependence on the stratification angle $s$

To illustrate the dependence on the latitude or equivalently the stratification angle  $s$  (see figures 7.3 and 7.4), we show in figure 7.8 the maximum theoretical growth rate of the instability for fixed  $N = 1.5$ . The main conclusion is that this instability can be triggered at any latitude in a planetary fluid layer. For this Brunt-Väisälä frequency, the growth is optimal between roughly  $50^\circ$  and  $60^\circ$ . The mode selection of the parametric instability changes with latitude. Unlike the mode selected in the case  $N = 1.5$  and  $s = 90^\circ$  where  $\alpha \simeq \pi/2$  (see figure 7.7), the mode selected at  $s = 60^\circ$  lies in the plane  $(xMz)$ , *i.e.*  $\alpha \simeq \pi$  (see figure 7.4).

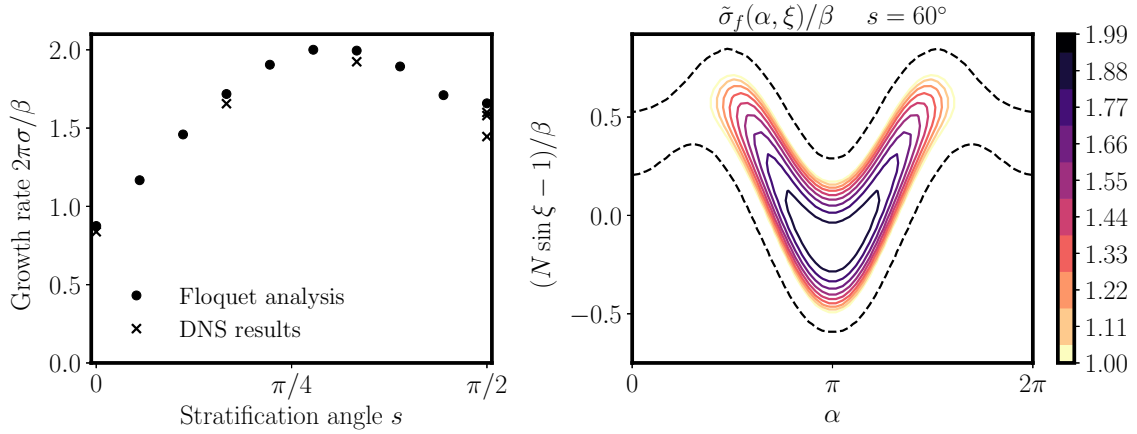


**Figure 7.8:** Left: theoretical and numerical growth rates with  $\beta = 5 \times 10^{-2}$  and  $N = 1.5$  varying the stratification angle  $s$ . Right: corresponding map of the growth rate  $\tilde{\sigma}_f$  computed with Floquet theory for the case  $s = 60^\circ$ . The black dashed lines highlight the marginal stability.

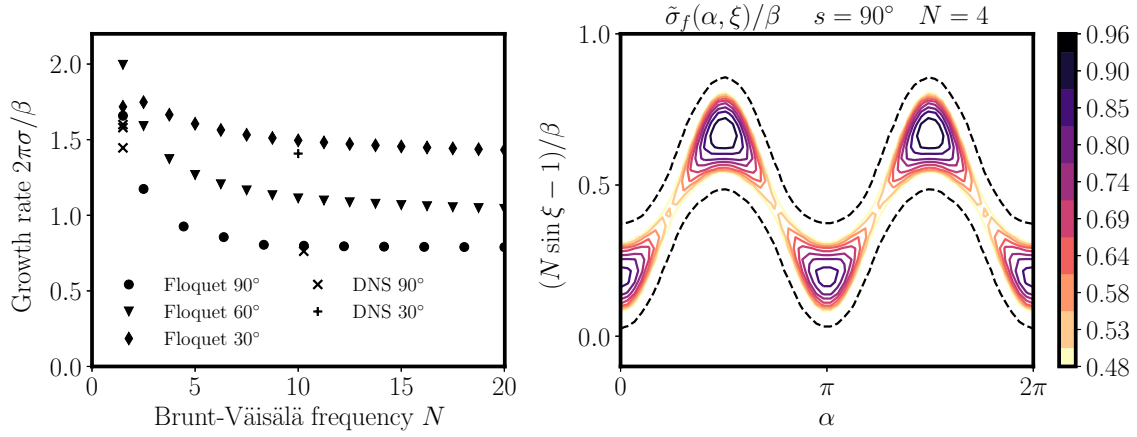


**Figure 7.9:** Left: evolution of the maximum growth rate for  $\beta = 5 \times 10^{-2}$  at three different stratification angles; a few simulations have been carried out to confirm the agreement between theory and numerics. Right: map of the growth rate computed from the Floquet analysis in the case  $N = 4$  with  $s = 90^\circ$ . The black dashed lines highlight the marginal stability

### 3.6 Dependence on the Brunt-Väisälä frequency $N$

The growth rate of the instability is also a function of the Brunt-Väisälä frequency. As shown in figure 7.9, it tends to a limit value when  $N \gg 1$ . The consequence is that the instability can be triggered at any Brunt-Väisälä frequency provided that it is larger than 1 in tidal units. Note that for large  $N$ , the selected modes' wave vectors draw closer to the stratification direction as  $\sin \xi \sim 1/N$ .

### 3.7 Conclusion

The linear stability analysis examined theoretically via WKB analysis and Floquet theory is quantitatively consistent with the results of direct numerical simulations. This first study has two consequences. It allows to assert that provided the dissipation is low enough, a parametric

excitation of internal waves can be excited in a planetary fluid layer undergoing homogeneous tidal deformations. This instability can be triggered at any latitude. However, the mode selection seems difficult to predict as it depends on latitude. At least it is confirmed that the growing waves are selected because their frequencies are close to half the forcing frequency  $2\gamma$ . In addition, this first linear study validates the use of local direct numerical simulations under a shearing box approximation with time-varying wave-vectors, as this method is in excellent agreement with the linear WKB-Floquet theory.

## 4. Non-linear saturation of the instability

To further analyse this tidally-driven instability of internal waves, we now focus on its non-linear saturation. This regime is the most relevant to the understanding of natural systems, in particular to comprehend the dissipation rate of the input tidal energy and the turbulent mixing in the oceans, or to study the possible existence of dynamo action in stably stratified planetary cores. Although we cannot address here all those issues, we strive to exhibit the key features of the non-linear saturation of this tidally-driven instability as a basis for future works.

We performed many simulations, all with an ellipticity  $\beta = 5 \times 10^{-2}$ , to explore the influence of the Reynolds number  $Re$ , the Brunt-Väisälä frequency  $N$ , and the latitude or stratification angle  $s$  in the low forcing intensity and low dissipation regime relevant to geophysics. The Prandtl (or Schmidt) number  $Pr$  is kept constant at  $Pr = 1$ . These simulations are all summed up in table 7.1 where the input parameters are referenced along with the main output statistical quantities.

### 4.1 Sustained instability and turbulence

As in the linear stability analysis, the non-linear fate of the instability is mainly tracked via the time evolution of the total kinetic energy in the Lagrangian box. Figure 7.10 shows that once the instability has reached saturation, the kinetic energy is maintained throughout time for the considered parameters. As indicated by figure 7.10, changing the Reynolds number from  $10^6$  to  $10^7$  does not influence the time-averaged value of the kinetic energy provided that  $N$  and  $s$  are kept constant. We note though that the variations around the mean energy level are larger for the lowest values of the Reynolds number. This is reminiscent of cyclic resonance and turbulence breakdown often occurring in systems close to the instability threshold. It has been observed for instance for the elliptical instability in rotating fluids (Grannan et al., 2014; Favier et al., 2015) or in the case of parametrically excited internal waves in a Faraday instability setup (Benielli and Sommeria, 1998).

To examine whether the saturation flow is influenced by stratification, we compute the Froude number based on the resonant wavelength and the rms velocity. The resonant wavelength  $\lambda_{\text{res}} = 2\pi/k_{\text{res}}$  is an output parameter resulting from the mode selection during the growth phase (see table 7.1), and the rms value of the velocity in the saturated phase is computed from the saturation time-average of the kinetic energy  $\overline{E_k}$  such that  $u_{\text{rms}} = \sqrt{2\overline{E_k}}$ . The

Input variables				Output variables					
Resolution	$N$	$\log(Re)$	$s$	$k_{\text{res}}/(2\pi)$	$u_{\text{rms}} (\times 10^{-3})$	$Fr$	$\varepsilon_k (\times 10^{-8})$	$Re_o$	$\mathcal{R}$
$256^3$	1.5	6.0	$45^\circ$	12.0	$4 \pm 1$	0.032	$5 \pm 3$	332	0.35
$256^3$	1.5	6.5	$45^\circ$	12.0	$4.8 \pm 0.4$	0.039	$3 \pm 1$	1279	2.0
$256^3$	1.5	6.75	$45^\circ$	12.0	$4.4 \pm 0.4$	0.035	$2.1 \pm 0.7$	2049	2.6
$512^3$	1.5	7.0	$45^\circ$	12.0	$4.4 \pm 0.3$	0.035	$1.8 \pm 0.1$	3673	4.7
$256^3$	1.5	6.5	$0^\circ$	5.4	$3.7 \pm 0.7$	0.030	$1.3 \pm 0.6$	980	0.9
$256^3$	1.5	6.5	$90^\circ$	11.2	$5.9 \pm 0.6$	0.047	$4 \pm 1$	1550	3.6
$256^3$	2.0	6.5	$90^\circ$	5.8	$5.4 \pm 0.5$	0.016	$3 \pm 1$	2950	0.74
$256^3$	4.0	6.5	$90^\circ$	14.6	$2.3 \pm 0.9$	0.008	1	500	0.03
$256^3$	4.0	7.0	$90^\circ$	14.6	$3.3 \pm 0.5$	0.012	$1.5 \pm 0.2$	720	0.10

**Table 7.1:** Input parameters and measured statistical properties of the flow for each simulation.  $k_{\text{res}}$  is the principal wave number of the resonant modes emerging during the growth phase.  $u_{\text{rms}}$  is the rms velocity computed from the mean of the kinetic energy. The Froude number  $Fr$  is computed as  $u_{\text{rms}}/(N\lambda_{\text{res}})$ .  $\varepsilon_k$  is the saturation dissipation rate defined as  $-Re^{-1}\langle\partial_i u_j \partial_i u_j\rangle$  summed over the whole box. The output Reynolds  $Re_o$  number and the buoyancy Reynolds number  $\mathcal{R}$  are respectively defined in equations (7.40) and (7.41). When errorbars are given, they correspond to the variance of the quantity over the total duration of the saturation phase. Note that  $N = 4$  and  $Re = 10^{6.5}$  is intermittently turbulent and the Reynolds number had to be pushed up to  $10^7$  to observe a sustained turbulence.

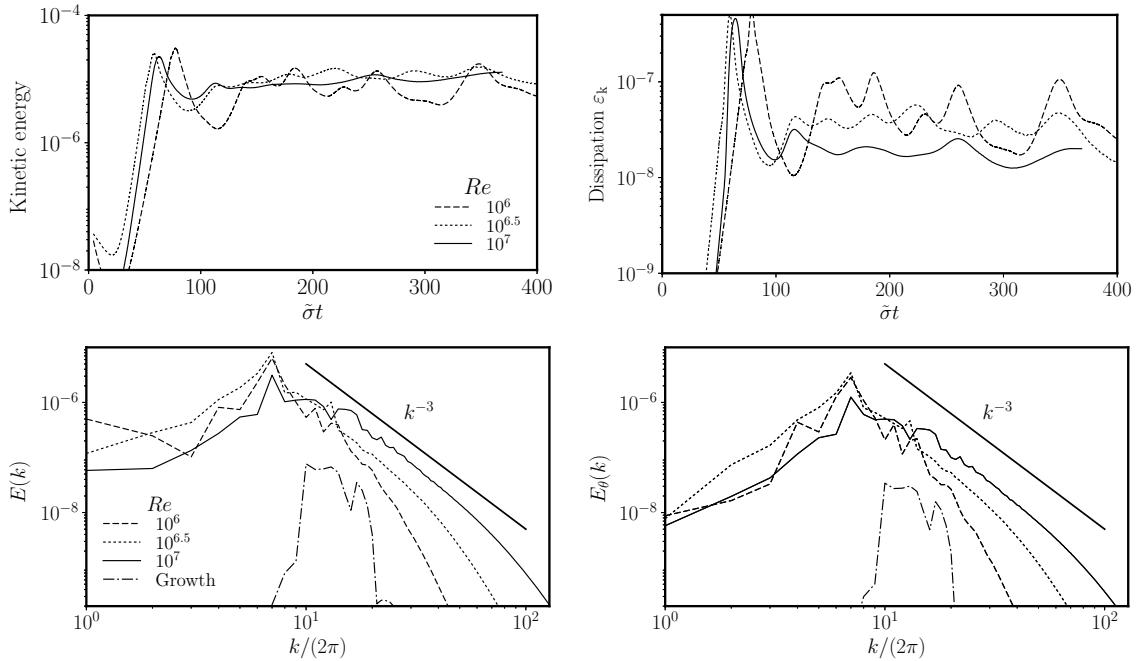


**Figure 7.10:** **Top:** Time evolution of the kinetic energy and the dissipation  $\varepsilon_k$  when  $Re$  is varied while keeping constant  $s = 45^\circ$  and  $N = 1.5$ . The time is normalised by the theoretical growth rate  $\sigma = \tilde{\sigma}_f$ . **Bottom:** corresponding power spectra of the velocity  $E(k)$  and of the buoyancy  $E_\theta(k)$ ; they are averaged for  $\tilde{\sigma}t \in [150, 400]$ . The black solid line materialises a  $k^{-3}$  power law. The dashed-dotted spectra is computed during the growth phase to show that the energy is primarily injected in a narrow band of wave numbers through the instability mechanism.

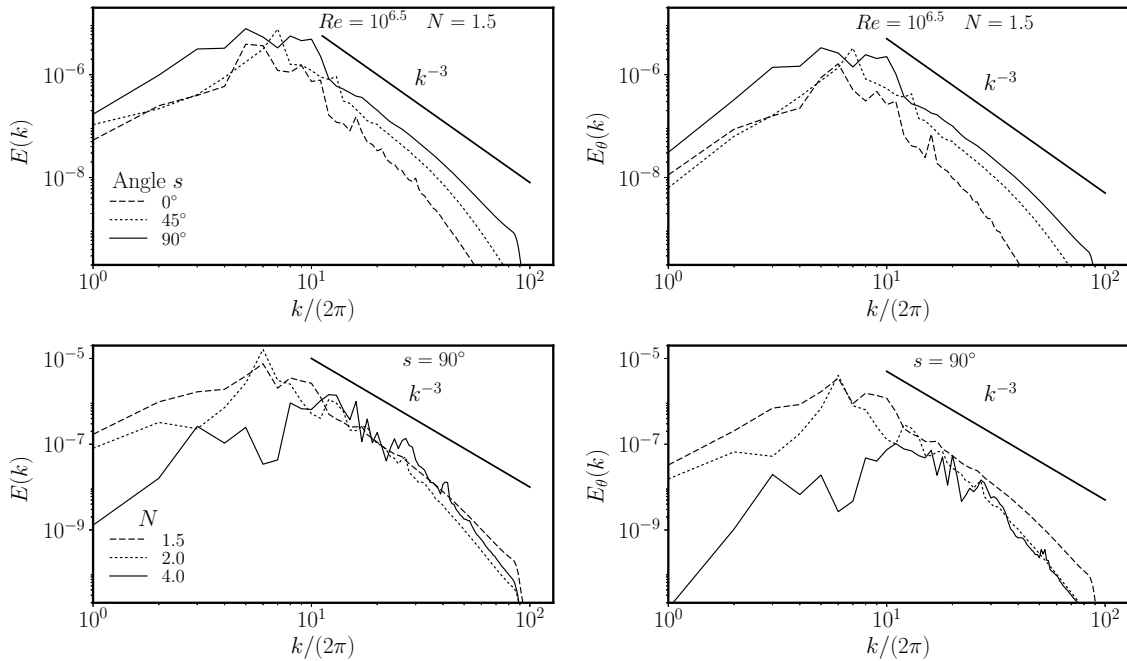


**Figure 7.11:** **Top:** power spectra of the velocity  $E(k)$  and of the buoyancy  $E_\theta(k)$  for  $s \in \{0^\circ, 45^\circ, 90^\circ\}$  at  $Re = 10^{6.5}$  and  $N = 1.5$ . **Bottom:** the same quantities for  $s = 90^\circ$  with  $N \in \{1.5, 2, 4\}$ . The Reynolds number is  $10^{6.5}$  except for  $N = 4$  where it had to be increased to  $10^7$  to observe sustained turbulence.

Froude number  $Fr$  is therefore defined as

$$Fr = \frac{u_{\text{rms}}}{\lambda_{\text{res}} N}. \quad (7.38)$$

The values of  $u_{\text{rms}}$  and  $Fr$  are all referenced in table 7.1. As  $Fr = \mathcal{O}(10^{-2})$  for all the simulated configurations, we conclude that the background stable stratification strongly affects the saturated flow.

In addition, the saturation of the instability is associated with the spontaneous creation of small scales. The isotropic power spectrum of both velocity ( $E(k)$ ) and buoyancy ( $E_\theta(k)$ ) are shown in figures 7.10 and 7.11. They are computed as:

$$E(k) = \sum_{k \leq |\mathbf{k}| < k+1} |\hat{\mathbf{u}}_{\mathbf{k}}|^2 \quad \text{and} \quad E_\theta(k) = \sum_{k \leq |\mathbf{k}| < k+1} |\hat{\vartheta}_{\mathbf{k}}|^2. \quad (7.39)$$

In the high Reynolds number limit, they converge towards a  $k^{-3}$  power spectrum, independently of  $N$  and  $s$ . A similar velocity power spectrum has been observed by Brouzet (2016) in the close context of turbulence driven by a forced internal wave attractor. It has also been measured at low Froude number by Rorai et al. (2015) in a stratified turbulence randomly forced at large scale. From the excitation of a few unstable internal waves, this instability mechanism manages to create sustained stratified turbulence and smaller scales. In addition, the apparent equipartition between velocity and buoyancy power spectra points towards a dynamics dominated by internal waves.

To better characterise the turbulent flow resulting from the saturation of the instability, we introduce two dimensionless parameters. We compute an output Reynolds number  $Re_o$  based on the rms velocity and the resonant wavelength such that:

$$Re_o = Re u_{\text{rms}} \lambda_{\text{res}}. \quad (7.40)$$

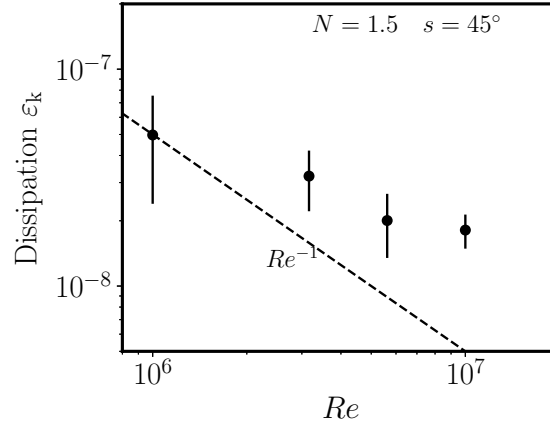


**Figure 7.12:** Mean value of the dissipation rate  $\varepsilon_k$  as a function of the Reynolds number for  $N = 1.5$  and  $s = 45^\circ$ . The errorbars account for the standard deviation of  $\varepsilon_k$  during the saturation phase.

With this output Reynolds number, we can also compute the buoyancy Reynolds number  $\mathcal{R}$  defined as (Brethouwer et al., 2007):

$$\mathcal{R} = Re_o Fr^2. \quad (7.41)$$

It compares a scale  $\ell_b$  beyond which buoyancy effects are negligible and a scale  $\ell_v$  beyond which viscosity affects the flow (Godoy-Diana et al., 2004; Brethouwer et al., 2007). For instance, in the context of classical stratified turbulence, it compares the so-called Ozmidov and the Kolmogorov length scales (Brethouwer et al., 2007). The output Reynolds number is a  $\mathcal{O}(100 - 1000)$  but because the Froude number is small, the buoyancy Reynolds number is at most  $\mathcal{O}(1)$  (see table 7.1). This means that although the flow is turbulent, there is no significant range of scales where inertia dominates over buoyancy: all the non-dissipative scales are affected by the background stratification. This is drastically different from recent studies on forced stratified turbulence, which are mostly focused on the  $\mathcal{R} \gg 1$  regime (see for instance Brethouwer et al. (2007); Bartello and Tobias (2013); Maffioli et al. (2016); Maffioli and Davidson (2016)). Lastly, the instantaneous dissipation rate associated with this type of turbulence is shown in figure 7.10 and its mean saturation value is given in table 7.1. They are computed in our dimensionless units as  $\varepsilon_k = -Re^{-1} \langle \partial_i u_j \partial_i u_j \rangle > 0$  where  $\langle \cdot \rangle$  is a volume averaging operator. Figure 7.12 sums up the evolution of this dissipation with the Reynolds number at constant  $N$  and  $s$ . The dissipation rate  $\varepsilon_k$  is a decreasing function of the Reynolds number in the considered range of parameters and this decay is shallower than a  $Re^{-1}$  decrease. This is an additional signature of the development of turbulence as it indicates that the velocity gradients become steeper as the input Reynolds number is decreased. However, in the present range of parameters accessible with reasonable computing time, no saturation of  $\varepsilon_k$  at high  $Re$  is reached.

As a conclusion, at large Reynolds number, the flow resulting from the saturation of this tidally-driven instability is developing over a wide range of spatial scales from an initial resonance dominated by a most unstable wavelength. At a given Brunt-Väisälä frequency, this turbulence develops at any latitude. Typical snapshots of this turbulent state can be found in figure 7.13.

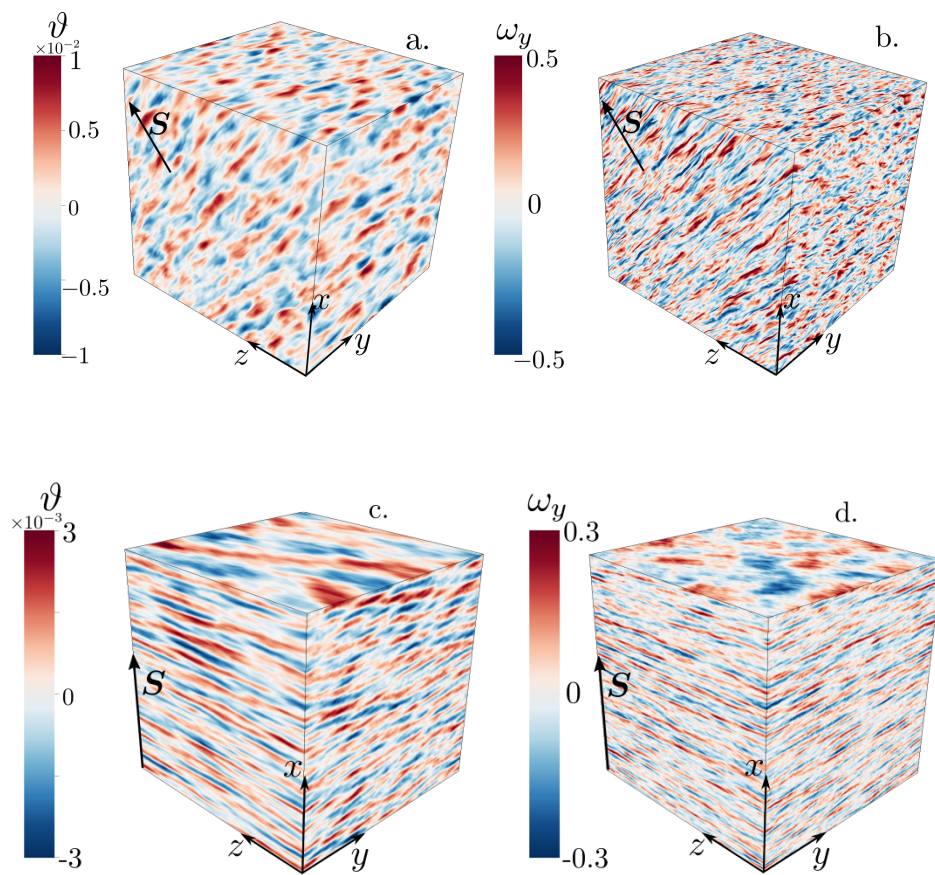


**Figure 7.13:** Typical snapshots of the buoyancy field (a. and c.) and the  $y$  component of the vorticity (b. and d.) in the saturated phase for a., b.:  $N = 1.5$ ,  $s = 45^\circ$  and  $Re = 10^7$ ; c., d.:  $N = 4$ ,  $s = 90^\circ$  and  $Re = 10^7$ .

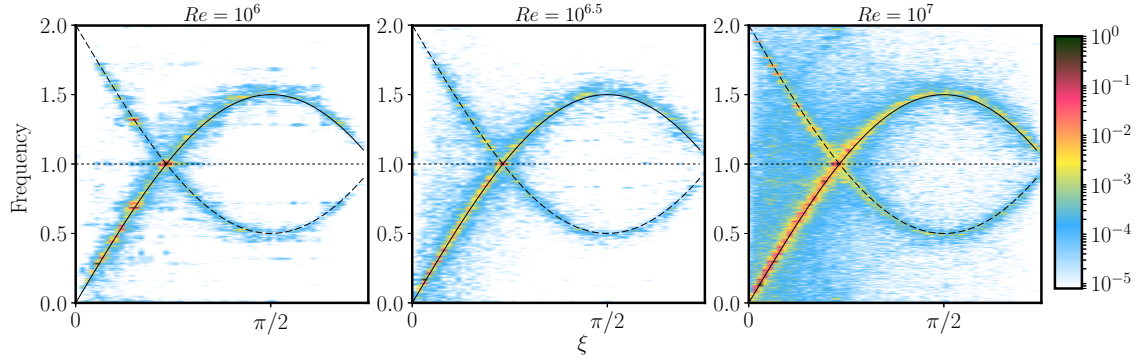


**Figure 7.14:** Map of the kinetic energy as a function of the frequency of the modes and the angle  $\xi$  between the stratification and the wave vector of a mode for  $Re = 10^6$ ,  $10^{6.5}$  and  $10^7$  at  $N = 1.5$  and  $s = 45^\circ$  kept constant. The Fourier transforms are performed for  $\tilde{\sigma}t \in [200, 400]$  and the energy is normalised by its maximum value. The range of wave number  $k$  over which the transform is processed goes from  $k = 3$  to  $k = 100$ ; changing these boundaries does not affect the map provided the most energetic scales ( $k \lesssim 20$ ) are included. The horizontal line represents the frequency of the first excited modes, the plain line gives the dispersion relation of the internal waves  $\omega = N \sin \xi$  and the dashed line locates the modes due to non-resonant non-linear interactions between the tidal base flow and the internal waves resulting in frequencies  $2 - N \sin \xi$ . The SNOOPY code computes the time evolution of half the spectral space as the fields are real, the angle  $\xi$  is therefore between  $0$  and  $\pi - \pi/4 = 3\pi/4$ .

## 4.2 Internal wave turbulence

In this paragraph, we aim at thoroughly characterising the structures generated by the non-linear saturation of the initially unstable waves. In simulations and experiments of stratified turbulence, the emergence of layerwise structures in which the flow is quasi-two-dimensional is frequently observed. These so-called ‘‘pancakes modes’’ correspond to the quasi-static limit of the internal waves dynamics (*i.e.*  $\xi \rightarrow 0$  and  $\omega \rightarrow 0$ ); three-dimensional motion comes through shear instability between those layers (see *e.g.* Billant and Chomaz (2001); Brethouwer et al. (2007)). Conversely, the turbulence excited by internal wave attractors leads to a different situation where the turbulence is a cascade of triadic resonances between the excited waves and a swarm of daughter waves. It results in an internal wave turbulence (Brouzet et al., 2016).

To determine which scenario is relevant here, we propose to map the energy in the same representation as in chapter 6 section 2.2, *i.e.* to project the energy in the spectral space along the temporal frequency  $\omega$  and the angle  $\xi$  between the stratification direction  $\vec{S}$  and the wave vector of a mode. This allows to determine where the energy is located around the dispersion relation of internal waves. This energy map is in the present case straightforward to draw thanks to the spectral nature of our simulations. The flow is indeed known through the velocity in spectral space  $\hat{\mathbf{u}}_k(t)$ . They can be sorted by their angles  $\xi$  to obtain the quantity  $\hat{\mathbf{u}}(\xi, t)$  defined as:

$$\hat{\mathbf{u}}(\xi_0, t) = \sum_{k, \alpha, \tilde{\xi} \in [\xi_0, \xi_0 + \Delta\xi]} \hat{\mathbf{u}}_k(t) \quad \text{with} \quad \mathbf{k} = k \begin{bmatrix} \sin \xi \cos \alpha \cos \xi + \sin \xi \cos \xi \\ \sin \xi \sin \alpha \\ -\sin \xi \cos \alpha \sin \xi + \cos \xi \cos \xi \end{bmatrix}, \quad (7.42)$$

where  $\alpha$  is an azimuthal angle,  $\xi$  is a polar angle respective to the stratification axis as defined in figure 7.4 and  $k$  is the norm of the wave vector  $\mathbf{k}$ .  $\Delta\xi$  is a given tolerance to assume the angle  $\xi$  of a mode is equal to  $\xi_0$ . A time Fourier transform is applied to  $\hat{\mathbf{u}}(\xi, t)$  to finally get

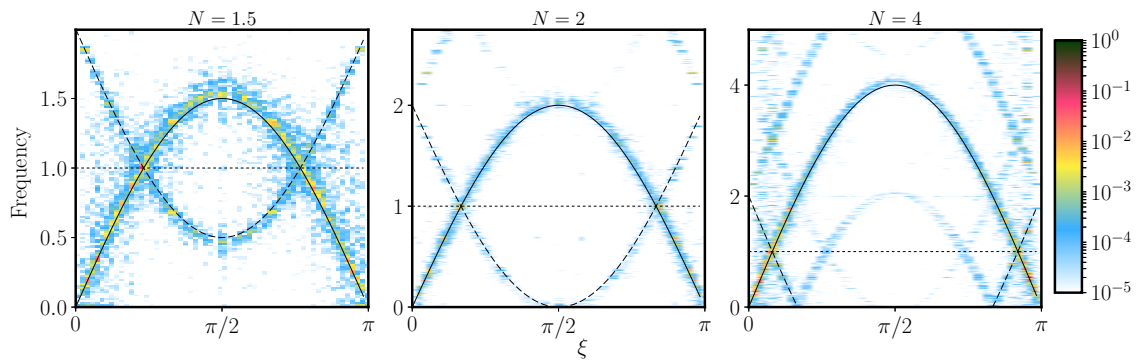


**Figure 7.15:** Map of the kinetic energy as a function of the frequency of the modes and the angle  $\xi$  for  $N = 1.5, 2$  and  $4$  with  $s = 90^\circ$ . The Reynolds number is  $10^6$  except for  $N = 4$  for which it was increased to  $Re = 10^7$  to observe sustained turbulence. The Fourier transforms are performed for  $\tilde{\sigma}t \in [150, 400]$  and the energy is normalised by the maximum value. Again, secondary and mirroring locations of the energy corresponding to non-resonant and nonlinear interaction of the waves and the base flow can be noticed.

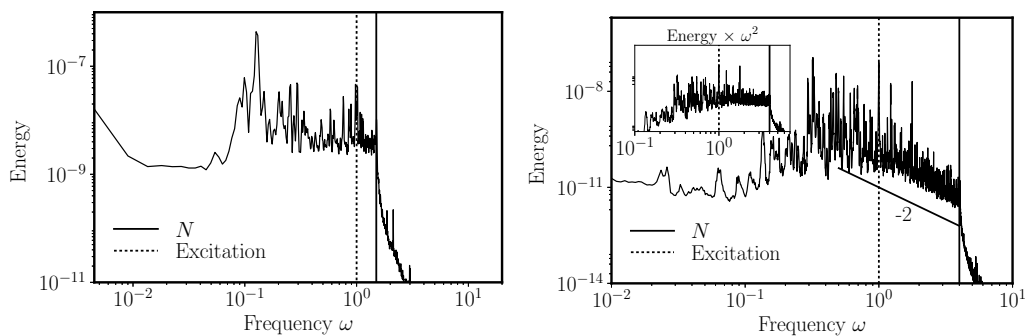


**Figure 7.16:** Temporal spectrum resulting from the acquisition of 1024 local velocity signals of all three components. The plain line marks the upper boundary of internal waves and the dashed line highlights the excitation frequency. **Left:** temporal spectrum for  $N = 1.5$ ,  $s = 45^\circ$  and  $Re = 10^7$ . **Right:** temporal spectrum for  $N = 4$ ,  $s = 90^\circ$  and  $Re = 10^7$ . The insert shows the same amplitude compensated by  $\omega^2$  with  $\omega$  the frequency to highlight a  $\omega^{-2}$  power law consistent with the high-frequency branch of the Garrett and Munk spectrum (Garrett and Munk, 1979).

$\hat{u}(\xi, \omega)$ . With these definitions, we remind at this point that the dispersion relation of internal waves at a given  $\mathbf{k}(k, \xi, \alpha)$  is  $\omega^2 = N^2 \sin^2 \xi$ .

The result of such a process is shown in figures 7.14 and 7.15. The most striking feature is the coincidence between the main energy locations and the dispersion relation of internal waves, similarly to the rotating fluid case (chapter 6), but also to Brouzet et al. (2016) in stratified fluids. It confirms that, in the saturation phase, the non-linear interactions between the growing modes give rise to a cascade of daughter internal waves. In figure 7.14, it can be noticed at low Reynolds number that only a few modes emerge in the non-linear saturation. Increasing the Reynolds number leads to filling continuously the dispersion relation. Note that as energy is injected into the resonant modes only and as the Froude number is always small, the only way to create new waves is via a cascade of triadic resonances.

Secondary locations of the energy mirroring the dispersion relation of internal waves can be noticed in figures 7.14 and 7.15. Their frequencies match the relation  $\omega = 2 - N \sin \xi$  and are therefore associated to non-linear and non-resonant interactions between the waves of frequency  $\pm N \sin \xi$  and the base flow of frequency  $\pm 2$ .

The filling of the dispersion relation depends though on the Brunt-Väisälä frequency (figure 7.15). When  $N$  is increased, modes with frequency around or below  $\gamma$  seem to be more excited via nonlinear interactions than modes with frequency between  $\gamma$  and  $N$ , at least for the Reynolds numbers considered here (see  $N = 4$  in figure 7.15).

In order to quantify more precisely how frequencies are excited, we propose to focus on temporal spectra obtained via the local acquisition of the three components of the velocity at several points. As shown in figure 7.16, and as expected theoretically for an internal wave turbulence, there are no significant fluctuations beyond the Brunt-Väisälä frequency  $N$ . Below this frequency the excited modes are homogeneously distributed down to frequencies which are an order of magnitude smaller than both  $N$  and  $\gamma$  (see figure 7.16 left). These frequencies correspond to the lower branch (*i.e.* small  $\xi$ ) of the dispersion relation observed in figures 7.14 and 7.15. When  $N$  is increased, *i.e.* when a scale separation appears between the forcing frequency  $\gamma$  and  $N$ , the energy contained in the higher frequencies ( $N \sin \xi > 1$ ) follows a  $\omega^{-2}$  power law. Such a trend is reminiscent of oceanographic measurements of the velocity which display a similar  $\omega^{-2}$  power law in the range of frequencies above the tidal forcing and which is interpreted as a signature of internal wave turbulence (Garrett and Munk, 1972; Garrett and Munk, 1975; Garrett and Munk, 1979; Levine, 2002). To provide a definitive comparison, it would be necessary to increase  $N$  while keeping a turbulent saturation, which requires large computational time as the Reynolds number must also be increased.

As a conclusion, the tidally-driven parametric instability of internal waves saturates in a state reminiscent of “internal wave turbulence”. The sustained, broadband frequency and small-scale saturation flow is composed of non-linearly interacting internal waves, although the non-linearity is weak compared to the effects of the background stratification.

### 4.3 Anisotropy and decoupling

Stratified turbulence has often been studied in the perspective of the emergence of layerwise, low-frequency structures, leading to a strong anisotropy and decoupling between horizontal and vertical variations. This paragraph aims at comparing the internal wave turbulence previously identified to the classical theories of stratified turbulence in the high buoy-

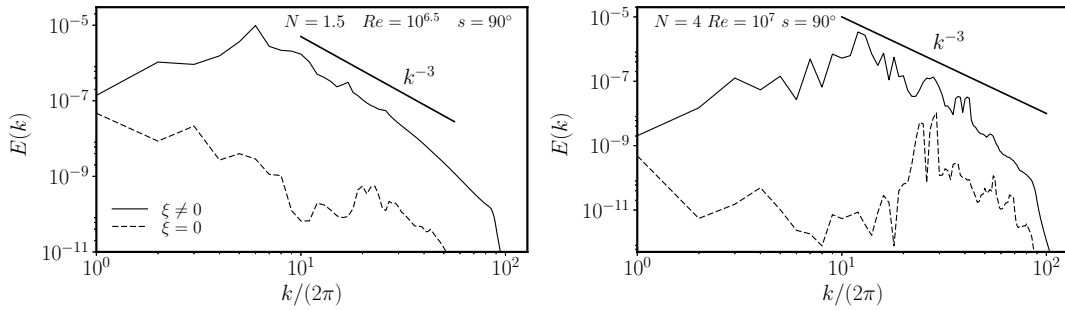


**Figure 7.17:** Kinetic energy spectrum of the layerwise slow modes defined by  $\xi = 0$  and the rest of the flow for **left:**  $N = 1.5$ ,  $Re = 10^{6.5}$  and **right:**  $N = 4$ ,  $Re = 10^7$  at  $s = 90^\circ$ .

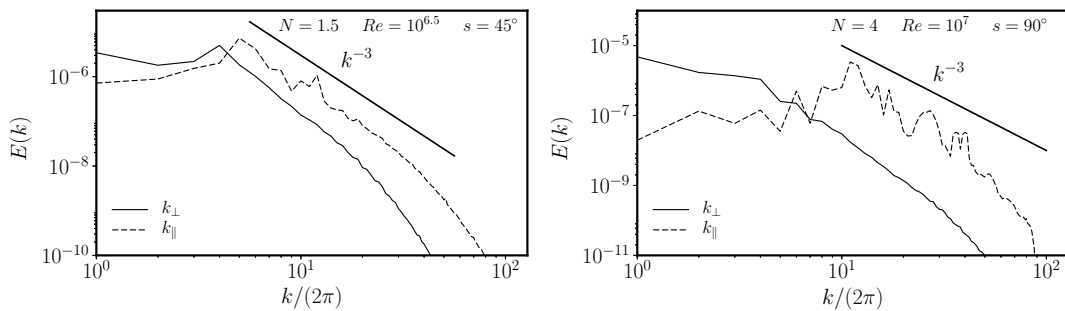


**Figure 7.18:** Anisotropic velocity power spectra as functions of  $k_\perp$  and  $k_\parallel$  for **left:**  $N = 1.5$ ,  $Re = 10^{6.5}$  and  $s = 45^\circ$  and **right:**  $N = 4$ ,  $Re = 10^7$  and  $s = 90^\circ$ . On each plot, the black solid line materialises a  $k^{-3}$  power law for comparison.

any Reynolds number regime developed in particular by Billant and Chomaz (2001), Lindborg (2006) and Brethouwer et al. (2007).

First, figures 7.14 and 7.15 do not indicate any energy accumulation in the layerwise structures around  $\xi = 0$  and  $\omega = 0$ . To support this assertion, we show in figure 7.17 the kinetic energy spectrum for the layerwise modes at  $\xi = 0$  and for the rest of the flow. As in the two cases the stratification is along the  $x$  axis, the layerwise modes are easily identified in the spectral space as their wave number  $\mathbf{k}$  is such that  $k_x, k_y = 0$ . As it can be noticed, at all scales, the slow modes are subdominant. This could be confusing as layers perpendicular to the stratification can be noticed in figure 7.13, they however do not correspond to slow modes since they are not exactly invariant along the axes perpendicular to the stratification.

Although layerwise structures are ubiquitous in stratified turbulence excited by a random forcing or by large scale vortices, forcing waves leads to a completely different state with low energy transfers towards those particular modes. The present picture is reversed in the close context of rotating turbulence excited by inertial waves: geostrophic vortices happen to grow up to taking over the whole dynamics in absence of specific dissipative process and to strongly back-react on wave propagation (see chapter 6. This could be linked to the fundamental mathematical difference between layerwise modes in stratified turbulence and geostrophic vortices in rotating turbulence (Cambon, 2001), which leads in particular to the absence of inverse cascade in the purely stratified case (Marino et al., 2013; Herbert et al., 2016).

This result regarding slow modes has strong implications in the anisotropy of the turbulent flow. In the classical theory of stratified turbulence, the velocity power spectrum is

an anisotropic function of  $k_{\perp} = k \sin \xi$  and  $k_{\parallel} = k \cos \xi$ . The velocity power spectrum integrated over  $k_{\parallel}$ , *i.e.* along the stratification axis,  $E(k_{\perp})$ , follows a Kolmogorov-like power law  $k_{\perp}^{-5/3}$ , while conversely  $E(k_{\parallel}) \propto k_{\parallel}^{-3}$  (Lindborg, 2006; Brethouwer et al., 2007). However, in the case of the internal wave turbulence presented above, both spectra  $E(k_{\perp})$  and  $E(k_{\parallel})$  follow the same power law close to  $k_{\parallel,\perp}^{-3}$ , as it can be seen in figure 7.18. The situation is even reversed as  $E(k_{\perp})$  is slightly below  $E(k_{\parallel})$  at large  $k$  while it is expected to be dominant in classical stratified turbulence. This result shows that there is no decoupling between the horizontal and vertical variations, as observed in the frequently studied high buoyancy Reynolds number regime, which is coherent with the fact that the turbulent state considered here is a superposition of many internal waves propagating in multiple directions in a quasi-isotropic manner.

The spectra displayed in figure 7.18 suggest that the gradients in the direction perpendicular to the stratification are less steep than they should be if the turbulence was due to shear instability between layerwise modes. To investigate whether shear instabilities are possible in the saturated flow, we compute the local Richardson number defined as:

$$Ri(\mathbf{x}, t) = \frac{N^2 \left( 1 + \frac{d\theta}{dz_s}(\mathbf{x}) \right)^2}{\left( \frac{dU_{\perp}}{dz_s}(\mathbf{x}) \right)^2}. \quad (7.43)$$

where  $z_s$  is a linear coordinate along the stratification axis and  $U_{\perp}$  is the velocity component perpendicular to the stratification direction. It compares the local Brunt-Väisälä frequency, including buoyancy fluctuations, with the shearing rate along the stratification direction. Linear stability analysis indicates that a sheared stratified flow is unstable when  $Ri < Ri_c = 1/4$ . Following Brethouwer et al. (2007), we compute for several Reynolds numbers, at  $N = 1.5$  and  $s = 45^\circ$ , the PDFs of the local Richardson number. As shown in figure 7.19, for the two lower input Reynolds numbers, there is no event likely to create shear instabilities. The buoyancy Reynolds number  $\mathcal{R}$  being smaller than one, this is coherent with the remark of Brethouwer et al. (2007) that in the low buoyancy Reynolds number regime, there should be no disturbances of Kelvin-Helmholtz type in the flow. The picture seems to change at the highest Reynolds number ( $10^7$ ), which corresponds to our most extreme simulation where rare events with  $Ri < 1/4$  are observed. The appearance of rare unstable events could be reminiscent of a transition towards a high buoyancy Reynolds number regime, which is further discussed in the concluding section of the present chapter. Still we conclude that in the regime we explore here, the internal wave turbulence is mostly stable to shear instabilities and is unable to drive strong overturning events.

## 4.4 Mixing

At this stage, we know that tides are able to amplify buoyancy perturbations over a background stratification, and that this amplification saturates into an internal wave turbulence. We would like to quantify then how this turbulent state mixes the buoyancy perturbations, *i.e.* how it irreversibly converts potential energy perturbations into background potential energy (Peltier and Caulfield, 2003). Following the work of Lindborg and Brethouwer (2008), Salehipour and Peltier (2015) and Maffioli et al. (2016), we propose to quantify the mixing via a

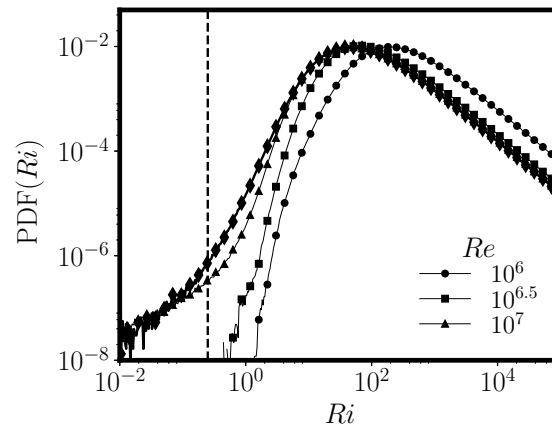


**Figure 7.19:** Probability density function of the Richardson number for  $s = 45^\circ$  and  $N = 1.5$  with  $Re \in \{10^6, 10^{6.5}, 10^7\}$ . PDFs are computed from snapshots of the buoyancy and velocity fields, the result presented here is the ensemble average of all the PDFs computed in the saturation phase. The number of samples is usually between 10 and 20.

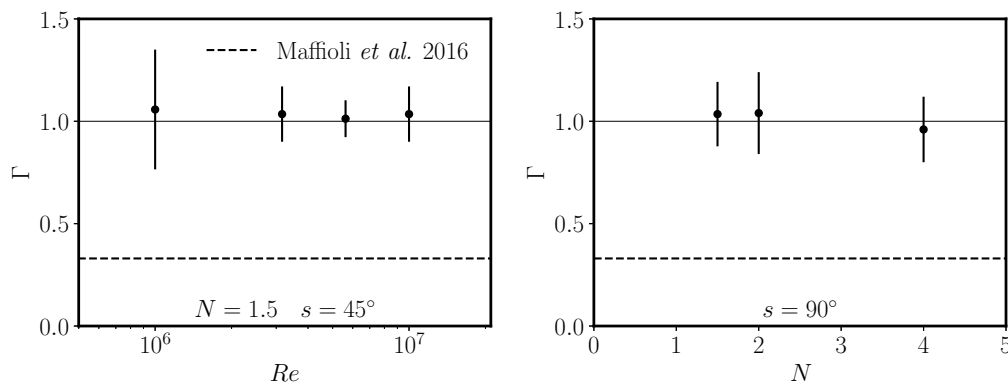


**Figure 7.20:** **Left:** mixing coefficient  $\Gamma$  as defined by (Maffioli et al., 2016) as a function of the input Reynolds number. The limit value in the small Froude regime obtained by Maffioli et al. (2016) is given as a reference. **Right:** evolution of the mixing coefficient with  $N$  for  $s = 90^\circ$  and  $Re = 10^{6.5}$  except at  $N = 4$  where  $Re = 10^7$ .

coefficient  $\Gamma$  defined as:

$$\Gamma = \frac{\varepsilon_p}{\varepsilon_k} \quad (7.44)$$

where  $\varepsilon_p = -N^2(Re Pr)^{-1} \langle (\nabla \vartheta)^2 \rangle$  quantifies the diffusion of the buoyancy perturbations and  $\varepsilon_k$  is the kinetic energy dissipation defined earlier. This coefficient  $\Gamma$  was originally introduced to evaluate how turbulence induces an effective diapycnal diffusivity  $K = \Gamma \varepsilon_k / N^2$  (Osborn, 1980; Salehipour et al., 2016). The expression given for  $\varepsilon_p$  can be retrieved by considering that it is a potential energy dissipation (Lindborg and Brethouwer, 2008). In the derivation of the energy equations from (7.27), the buoyancy equation must be multiplied by  $N^2 \vartheta$  to obtain the same energy transfer from velocity to buoyancy, which finally yields to the definition given earlier to  $\varepsilon_p$ .

In their study, Maffioli et al. (2016) found that, forcing a turbulence in a stratified fluid with vortices aligned with stratification, at low Froude and high buoyancy Reynolds numbers the mixing coefficient  $\Gamma$  converges towards 0.33. In figure 7.20 (left), we display the mixing coefficient  $\Gamma$  at  $N = 1.5$  as a function of the input Reynolds number  $Re$  with the limit value found by Maffioli et al. (2016) given as a reference. Despite  $Re$  is increased from  $10^6$  up to  $10^7$  we do not observe any variation of the mixing coefficient. Instead,  $\Gamma$  remains constant around 1, well above the limit reference value. The evolution of the mixing coefficient  $\Gamma$  with the Brunt-Väisälä frequency  $N$  is also computed for  $s = 90^\circ$ . As it can be noticed in figure 7.20 (right), again,  $\Gamma$  remains constant and around 1.

This result can be inferred from a very simple model assuming the flow is only a superposition of low amplitude internal waves with weak non-linear interactions. A single wave of frequency  $\omega$  and wave vector  $\mathbf{k}$ ,  $\{\mathbf{u}, \vartheta, \Pi\} = \{\mathbf{u}_{k0}, \vartheta_{k0}, \Pi_{k0}\} e^{i(\mathbf{k} \cdot \mathbf{x} - \omega t)}$  with  $\omega^2 = N^2 \sin^2 \xi$ , must obey the following linear inviscid set of equations:

$$\begin{cases} \partial_t \mathbf{u} = -\nabla \Pi + N^2 \vartheta \mathbf{e}_s \\ \partial_t \vartheta = -\mathbf{e}_s \cdot \mathbf{u} \end{cases} \Rightarrow \begin{cases} -i\omega \mathbf{u}_{k0} = -\mathbf{k} \Pi_{k0} + N^2 \vartheta_{k0} \mathbf{e}_s \\ -i\omega \vartheta_{k0} = -\mathbf{e}_s \cdot \mathbf{u}_{k0} \end{cases} \quad (7.45)$$

where  $\mathbf{e}_s$  is the stratification direction unit vector. We wish then to compute the volume averaged dissipation associated with the wave field, which is merely the sum of each single wave dissipation. For one wave only,  $\langle \mathbf{u}^* \cdot \nabla^2 \mathbf{u} \rangle = -k^2 |\mathbf{u}_{k0}|^2$  and  $\langle \vartheta^* \nabla^2 \vartheta \rangle = -k^2 |\vartheta_{k0}|^2$ . To compute  $\Gamma$ , we need to relate  $|\mathbf{u}_{k0}|^2$  to  $|\vartheta_{k0}|^2$  which can be done for instance applying  $\mathbf{k} \times (\mathbf{k} \times \cdot)$  to the velocity equation in (7.45). We then obtain the exact balance  $|\mathbf{u}_{k0}|^2 = N^2 |\vartheta_{k0}|^2$  (which does not apply at  $\omega = 0$ ). Thus we find with the following simple scaling for the mixing coefficient:

$$\Gamma = \frac{1}{Pr} \quad (7.46)$$

where  $Pr$  is the Prandtl or Schmidt number. We retrieve for our simulations at  $Pr = 1$  that  $\Gamma = 1$ . The numerical result  $\Gamma = 1$  should therefore be regarded as an additional signature of internal wave turbulence.

To conclude, internal wave turbulence offers a picture completely different from the classical stratified turbulence at high buoyancy Reynolds number. The flow being a superposition of low to moderate amplitude waves, the mixing coefficient is different compared to a situation where the most energetic structures are the non-propagative layerwise modes. Note that although the mixing coefficient is increased, the consequent turbulent diapycnal diffusivity should still be lower than what is measured in high buoyancy Reynolds number regime, essentially because the forcing introduced here and the associated dissipation rates are small.

## 5. Conclusion

Throughout this chapter, we have shown with an idealised local Lagrangian model that tidal flows are able to drive bulk turbulence in stratified planetary fluid layers. This turbulence is driven by the parametric subharmonic resonance of unstable internal waves. The latter continuously feeds a cascade of daughter waves to create a flow which bears signatures of internal wave turbulence, in particular the focusing of the energy along the dispersion relation of internal waves. Such a turbulent flow has already been characterised in an experimental setup designed to mimic the effects of tides on a particular topography (Brouzet et al., 2016). We claim from our results that internal wave turbulence can take place homogeneously in a whole fluid layer undergoing tidal distortion, provided that the latter's amplitude is large enough to overcome dissipation and that the Brunt-Väisälä frequency  $N$  is larger than the tidal frequency  $\gamma$ .

In addition, our local approach provides an efficient way to numerically investigate the detailed and possibly universal properties of weakly forced internal wave turbulence in low dissipation regimes. Despite recent experimental (Brouzet et al., 2016) and theoretical (Gamba et al., 2017) advances, this particular state of stratified turbulence remains challenging and difficult to be compared to the classical theory of wave turbulence (Zakharov et al., 2012; Nazarenko, 2011). As in rotating turbulence, this is essentially due to the anisotropy of the dispersion relation (see for instance the discussion in Brouzet (2016)), the role played by near-resonant interactions and the non-linear interaction with non-propagative modes (Cambon, 2001; Galtier, 2003; Smith and Lee, 2005; Bellet et al., 2006; Scott, 2014; Gelash et al., 2017; Gamba et al., 2017). Although our model is introduced in a targeted geophysical context, it could be used to test universal internal wave turbulence models or closure.

Future work will strive to introduce rotation, which is also a key ingredient to planetary fluid dynamics. In particular, in the limit where buoyancy effects still dominate over the Coriolis force, it should be interesting to study the consequence of its introduction on the filling of the dispersion relation and the subsequent low-frequency cut-off. As it can be noticed in figure 7.16, for  $N = 4$ , there is an energy accumulation at frequencies  $\omega \in [0.1, 1]$ . If the rotation rate were to be in this range, would the energy accumulate in the lowest frequency modes, *i.e.* the layerwise structures which were never observed to develop in our simulations? If so, tidal flows would convey energy into modes which could then undergo shear instabilities and therefore drive more intense turbulence with enhanced dissipation rate and mixing. Whether this turbulence is sustained or lead to the temporary inhibition of the instability which feeds it remains to be seen.

Moreover, it would be interesting to investigate the persistence of the results found here in the regime of high or low Prandtl (or Schmidt) number, which are both relevant to geophysical fluid dynamics. Note though that it is already known from the experiments of Brouzet et al. (2016) that internal wave turbulence can be excited in salted water, *i.e.* at high Schmidt number. As linear internal waves are characterised by energy equipartition (see paragraph 4.4), we should expect that the resonant energy transfer towards small scale is inhibited as soon as either viscosity or diffusion balances non-linear advective transfer. What happens to the non-dissipated quantity and how it interacts with the larger scale waves beyond this cut-off remains an open question. The Prandtl (or Schmidt) number should not play any significant role in the large scale behaviour of the flow.

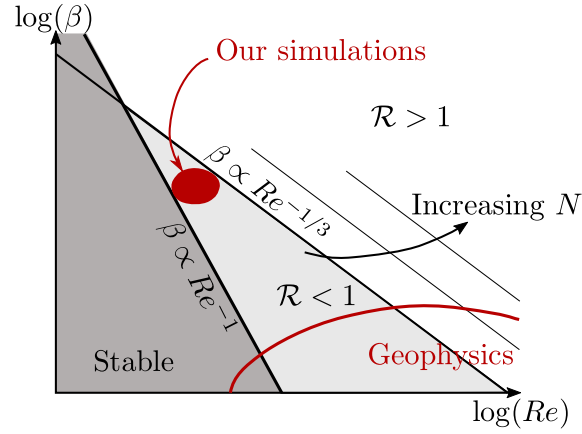


**Figure 7.21:** Schematic relative distribution of the low and high buoyancy Reynolds number  $\mathcal{R}$  regimes as a function of the input Reynolds number  $Re$  and the ellipticity of the deformation  $\beta$ . The area covered by geophysical regimes and our simulations is indicated in particular to highlight the fact that the low  $\mathcal{R}$  regime is also relevant to planetary layers in the case of bulk wave turbulence excited by tides.

Lastly, the type of turbulence resulting from the saturation of the tidally-driven instability occurs in a regime of high Reynolds, low Froude and low buoyancy Reynolds ( $\mathcal{R}$ ) numbers, which leads to a completely different picture compared to the high  $\mathcal{R}$  regime frequently studied and branded as the regime relevant to geophysical flows. In particular, the mixing coefficient is increased in the regime we describe, and is coherent with the scaling  $\Gamma = 1/Pr$  that we have derived theoretically assuming the flow is a superposition of linear internal waves only. This result is an additional signature of wave turbulence. However, this enhanced mixing coefficient may not result in an increase in the turbulent diapycnal diffusivity as the forcing and the dissipation are small.

A regime of high buoyancy Reynolds number turbulence excited by the parametric instability introduced here is possible in the very high Reynolds number limit, but could not be investigated because it is highly demanding in resolution and computational time, or it requires an increase of the ellipticity  $\beta$  to unrealistic values. As seen earlier, events with Richardson number under  $1/4$  are measured in the most extreme simulation where the dissipation is so small that the buoyancy Reynolds number reaches  $\sim 5$ . It would be interesting to see whether at high  $\mathcal{R}$  wave turbulence can drive strong over-turning events or not, and how it would impact the mixing coefficient and the turbulent diapycnal viscosity. Still we claim that both regimes should be considered as relevant to geophysical applications due to the specificity of our forcing mechanism favouring weak wave interactions. Indeed, the buoyancy Reynolds number  $\mathcal{R}$  can be expanded as

$$\mathcal{R} = \frac{u_{\text{rms}}^3 Re}{\lambda_{\text{res}} N^2}. \quad (7.47)$$

Assuming that the saturation results from the balance between the forcing term  $A(t)\mathbf{u} \sim \beta u_{\text{rms}}$  and the non-linear term  $\mathbf{u} \cdot \nabla \mathbf{u} \sim u_{\text{rms}}^2 / \lambda_{\text{res}}$  leads to  $u_{\text{rms}} \sim \beta \lambda_{\text{res}}$ . As a result, the buoyancy Reynolds number goes like:

$$\mathcal{R} \sim \beta^3 Re \left( \frac{\lambda_{\text{res}}}{N} \right)^2. \quad (7.48)$$

The area with high  $\mathcal{R}$  lies above a line  $\beta \propto Re^{-1/3} (N/\lambda_{\text{res}})^{2/3}$ . In addition, the instability grows when the forcing overcomes the volume viscous dissipation, *i.e.* for  $\beta \gtrsim (\lambda_{\text{res}}^2 Re)^{-1}$ . As a result, in the  $(\beta, Re)$  plane, both regimes are worth considering in the geophysical limit

where usually  $\beta$  is smaller than  $10^{-3}$  and  $Re$  is large, as indicated in figure 7.21. Note that this discussion is unchanged if we consider the dissipation to be due to solid wall friction, for which the unstable zone lies above the line  $\beta \propto Re^{-1/2}$ . Moreover, as indicated in figure 7.21, the area of small  $\mathcal{R}$  is extended as  $N$  is increased. In future work, it would be interesting to delimit more precisely those two regimes. Note that a possible transition could be approached in our most extreme simulation for which  $\mathcal{R} \sim 5$ . Exploring the internal wave turbulence driven at high buoyancy Reynolds number would therefore require increasing the ellipticity and thus the forcing intensity. This, we believe, deserves a study of its own.

Lastly, we believe the results presented here should not change as the ellipticity is lowered provided that  $\mathcal{R} < 1$  and the flow is unstable. In addition, when three waves of frequencies  $(\omega_1, \omega_2, \omega_3)$  exchange energy via triadic resonance, the resonance condition on frequency must be satisfied with a tolerance  $\mathcal{O}(Fr)$  i.e  $\omega_1 \pm \omega_2 \pm \omega_3 = \mathcal{O}(Fr)$  due to detuning by larger scales advection (see relation (2.32) in chapter 2 for a discussion in the analogue context of inertial waves in rotating flows). As  $u_{\text{rms}}$  scales like  $\beta \lambda_{\text{res}}$ , decreasing  $\beta$  corresponds to decreasing  $Fr$  and therefore to more exact resonances. The only significant change, we believe, is a thinner focusing of the energy along the dispersion relation of internal waves.



# Conclusion

## 1. The saturation of the elliptical instability in planetary cores

### 1.1 Wave-dominated versus geostrophic dominated regimes

In this study targeted at the non-linear fate of the elliptical instability, we have shown the existence of two very different types of saturation with an experiment and an idealised, Cartesian local model. The first regime is dominated by strong geostrophic vortices, it had already been identified by Barker and Lithwick (2013), Grannan et al. (2014) and Favier et al. (2015). This regime bears some similarities with rotating turbulence excited by stochastic forcing: the flow is mostly two-dimensional and the energy accumulates in large-scale condensates. Although the formation of vortices in the local Cartesian model is observed to temporarily inhibit the instability, geometric confinement of vortices in the ellipsoid leads to a quasi-steady state. In this latter case, the spatial structure of resonant modes is modified to account for the persistent vortex.

Because the ellipsoid we have used in our experiment is larger than in any previous set-up, we could draw closer to geophysical regimes of weak dissipation and forcing amplitude. The exploration of these regimes has allowed us to find a second saturation regime which is dominated by a sustained cascade of inertial waves in triadic, resonant interaction, reminiscent of inertial wave turbulence.

Our experiments indicate that the transition between the two types of saturation as a function of the forcing amplitude (or input Rossby number)  $Ro_i$  and dissipation (or Ekman number)  $E$  follows a power law  $Ro_i \propto E^{1/2}$ . This secondary transition could be explained by the existence of a finite Rossby number instability of inertial waves, possibly related to shear instability, giving rise to geostrophic flows. As shown in chapter 4, at high forcing amplitude, the inviscid growth rate of this instability is proportional to the wave amplitude; because in the saturation, the wave amplitude scales like  $Ro_i$  (Grannan et al., 2017), the viscous threshold of the finite Rossby number instability follows a power law  $Ro_i \propto E^{1/2}$ . However, we have found that independently of the viscous damping rate, there exists a minimal wave amplitude below which the flow remains stable. Therefore, the secondary threshold  $Ro_i \propto E^{1/2}$  does not hold as  $Ro_i$  and  $E$  are decrease: there is a minimal Rossby number below which the secondary instability leading to a geostrophic saturation never develops.

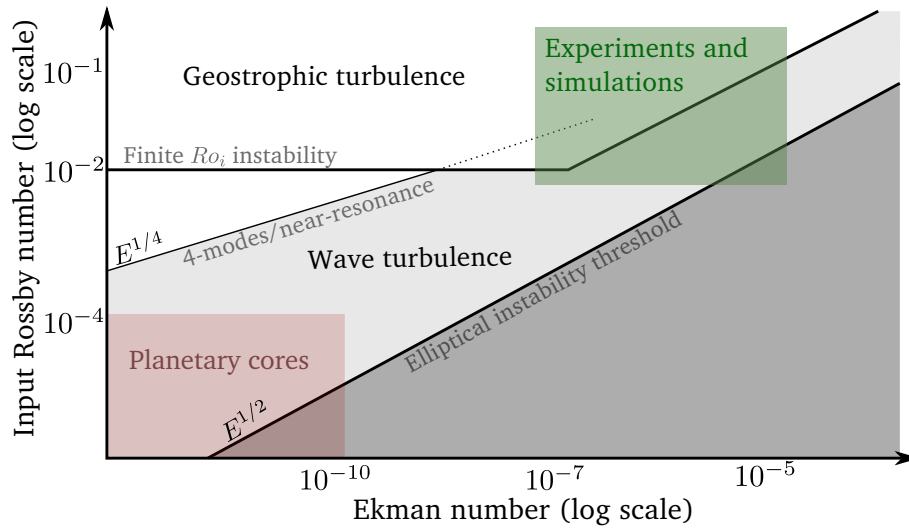


**Figure 7.22:** Schematic regime diagram of the saturation of the elliptical instability as a summary of all the outcomes of the presented work. The two control parameters are the forcing amplitude  $Ro_i$  and the Ekman number  $E$ . We include several lines materialising the threshold of the elliptical instability and of three instabilities featuring geostrophic modes: the four-mode interaction (Kerswell, 1999; Smith and Waleffe, 1999), the near-resonances and the finite wave amplitude instability (“finite  $Ro_i$  instability”). The light shaded area corresponds to the regimes of control parameters where our research indicates that the saturation flow should be dominated by inertial waves in triadic resonant interaction, or inertial wave turbulence. The blank area is where a geostrophic-dominated type of non-linear saturation is expected. We also include the regimes of forcing amplitude and dissipation corresponding to planetary cores, according to Cébron et al. (2012a).

In addition to increasing our understanding of the wave-dominated regime, the idealised simulations of the elliptical instability saturation suggest that the finite wave amplitude secondary instability indeed plays a role in setting the transition between the two regimes, although simulations reaching more extreme regimes in terms of forcing amplitude and dissipation are still needed to confirm it. We have also shown the existence of the two types of saturation for the same values of the control parameters by creating an inertial wave turbulence with a geostrophic-specific friction and then releasing it. Our study thus sheds a new light on rotating turbulence by demonstrating the non-universality of the widely-used stochastic forcing, which systematically leads to bi-dimensionalisation of the flow and to geostrophic vortices dominating the dynamics (see Godeferd and Moisy (2015) for a review). Our results clearly indicate that, in the case of weak forcing and dissipation, a realistic geophysical forcing leads to an inertial wave turbulence free of geostrophic component, a state that had been investigated theoretically and in idealised simulations only (Galtier, 2003; Bellet et al., 2006; Scott, 2014).

## 1.2 A regime diagram to predict the saturation in planetary cores

To conclude, we summarise the outcome of the present work in a schematic regime diagram of the saturation of the elliptical instability shown in figure 7.22. The secondary transition between the wave-dominated regime and the geostrophic-dominated regime is set by instabilities of geostrophic flows building on inertial waves with typical amplitude given by the forcing  $Ro_i$ . We have shown in chapters 4 and 6 the importance of finite wave amplitude insta-

bilities, in agreement with the experimental study presented throughout chapter 3. According to our results, there is a minimal forcing amplitude below which this instability disappears, which is materialised by a horizontal threshold line in the  $(Ro_i, E)$  regime diagram of figure 7.22. Note that direct forcing via viscous boundary layers also drives strong geostrophic flows. We have found in chapter 5 that this mechanism leads to dominant geostrophic modes in the saturation of the elliptical instability only above a finite forcing amplitude, as in the case of finite wave amplitude instability.

Below the threshold of the finite amplitude instability, the remaining instabilities giving rise to geostrophic modes are four-modes interaction and near-resonance. As shown by Kerswell (1999), the inviscid growth rate of the four-mode resonant interaction is proportional to the square of the forcing wave amplitude, here  $Ro_i^2$ . The same  $Ro_i^2$  inviscid growth rate has been theoretically derived in chapter 4 section 5.2 for near-resonances involving geostrophic modes. The viscous threshold of these two instabilities is such that  $Ro_i^2 \propto E^{1/2}$  where the  $E^{1/2}$  corresponds to viscous damping in boundary layers. As a consequence, in figure 7.22, these two secondary instabilities have a  $Ro_i \propto E^{1/4}$  threshold, which is shallower than the elliptical instability threshold  $Ro_i \propto E^{1/2}$ . Below the minimal input Rossby number below which the finite wave amplitude instability vanishes, the transition from the wave-dominated to the geostrophic-dominated regimes is entirely controlled by four-modes or near-resonant interactions.

Note that a last mechanism is missing in figure 7.22 for the formation of geostrophic flows: direct forcing via viscous boundary layers. The latter is not related to an instability and appears without any threshold. Our guess from the study of chapter 5 is that at low  $Ro_i$  and  $E$ , the geostrophic flow driven by direct forcing is of too low amplitude to prevent the emergence of an inertial wave turbulence out of the saturation of the elliptical instability.

We conclude from our work that the wave-dominated saturation regime is relevant to planetary cores unstable to tidal forcing.

### 1.3 Parametric instability in stably-stratified planetary interiors

In addition to exploring the turbulent saturation of the elliptical instability, we have also been interested in the stability of a stably-stratified planetary interior, such as a core or a subsurface ocean, undergoing tidal distortion. We have shown the existence of a parametric subharmonic instability of internal waves, which is very similar to the elliptical instability in rotating fluids.

With an idealised, Cartesian model, we have investigated the turbulent saturation of this parametric instability. We have revealed with spectral methods that it is an internal wave turbulence, a state that had previously been observed in the case of the non-linear collapse of an internal wave attractor (Brouzet et al., 2016; Brouzet et al., 2017). Interestingly, the temporal spectrum of local velocity measurements follows a  $\omega^{-2}$  power law as a function of the frequency  $\omega$  in the range between the resonant wave frequency and the Brunt-Väisälä frequency. Such a power law is sometimes observed in oceanic turbulence in the range of frequency between the tidal forcing and the Brunt-Väisälä frequency and it is interpreted as a signature of internal waves (Garrett and Munk, 1972; Garrett and Munk, 1975; Garrett and Munk, 1979; Levine, 2002). Using pseudo-spectral methods to simulate these flows, we have measured the energy spectrum of the internal wave turbulence and showed how different it

is from a common type of stratified turbulence mostly driven by shear instability (Brethouwer et al., 2007) and which is thought to take place in the Earth's oceans for instance. Moreover, we have quantified the turbulent mixing driven by the internal wave turbulence. Despite the emergence of smaller scale, the mixing efficiency of the overall flow is similar to the mixing efficiency of a single linear internal wave. Therefore, the internal wave turbulence induces almost no enhancement of mixing compared to diffusion.

In the context of planetary cores, our study shows that complex flows arise from tidal excitation of internal waves, which may drive dynamo action despite the stable stratification. It is interesting to note that since very little mixing is induced by the internal wave turbulence, the tidally driven flows should not *a priori* alter the solute stratification of planetary cores that may result from their formation (Landeau et al., 2016).

## 2. Ideas and directions for future works

### 2.1 Dynamo action

The first extension of the present work is to study the consequence of the existence of the two regimes on dynamo action in planetary cores. Reddy et al. (2018) has shown recently that the turbulent flow arising from tidal instabilities drives kinematic dynamo, but their numerical simulations were restrained to moderate forcing amplitude and dissipation. Dynamo action in the wave-dominated regime has remained unexplored but is currently under investigation. Moffatt (1970) has shown theoretically that a random superposition of inertial waves is able to drive a large-scale magnetic field, provided that the wave field is not invariant under reflection, *i.e.* that there is a net global helicity associated to the wave superposition. It remains to be seen whether the inertial wave turbulence forced by the elliptical instability is able to drive a large-scale  $\alpha$  dynamo, that is, a large-scale magnetic field generated from the collective effects of the flow's smaller scales.

Besides, Barker and Lithwick (2014) have shown via numerical simulations that applying a weak background magnetic field to a medium undergoing tidal forcing prevents the emergence of columnar geostrophic vortices in the saturation of the elliptical instability. In the light of the results presented in chapters 4 and 6, the study of Barker and Lithwick (2014) suggests that the threshold of the secondary finite wave amplitude instability is altered, and possibly increased, by the presence of a magnetic field. The influence of a magnetic field, be it self-induced by the saturation flow or in the background, over the existence of the two regimes of non-linear saturation of the elliptical instability remains to be investigated.

### 2.2 Fundamental aspects of wave-vortex interaction

Throughout the study developed in this dissertation, we have touched upon issues related to the interaction between an inertial wave and a vortex, a subject that remains widely unexplored. In the geostrophic-dominated saturation, we revealed with the analysis of bicoherence spectra that although inertial waves are distorted by the strong vortices, persistent triadic interactions between unidentified structures are still occurring. These structures must be inertial modes entangled with the vortex, as the modified resonant modes measured in

chapter 3 figure 3.21. This modified wave shows that in anticyclones, waves with frequencies larger than the local vorticity cannot propagate. It implies that the wave either reflects on the anticyclone or transfers its momentum to the vortex, or both at the same time.

A fundamental investigation of how an inertial wave couples with a vortex, be it a cyclone or an anticyclone, could be an interesting extension of the work presented here. The medium in which the inertial wave propagates is no longer homogeneous, and the amount of energy transferred from the wave to the geostrophic flow is unknown. Such a wave-vortex interaction is yet an ubiquitous and fundamental interaction occurring in rotating turbulence. Carrying out an extensive study of this phenomenon could yield interesting results regarding rotating turbulence and the systematic bi-dimensionalisation observed in the case of stochastic forcing. In addition, despite its importance, the interaction between the inertial waves and the slow geostrophic modes is always neglected in the theories of inertial wave turbulence (Bellet et al., 2006; Scott, 2014).

The investigation of the wave-vortex interaction could be carried out both numerically and experimentally. The experimental set-up could be analogous to the one used by Humbert et al. (2017) to study surface wave interaction with a vortex maintained by a magnetic field and electric currents in a conducting fluid, or to the one used by Afanasyev and Peltier (1998) to study the stability of anticyclones created by a rotating cylinder in a rotating tank. To carry out the numerical study, the SNOOPY code might not be adapted since the imposed geostrophic vortex is a strong inhomogeneity in the system, but the NEK5000 code, used for instance by Favier et al. (2015) and adapted to complex geometries, may be suitable. Diagnostics of the wave-vortex interaction include the incident, reflected and transmitted wave energies and frequencies. These quantities would allow measuring energy exchange as well as detuning induced by the interaction.

## 2.3 Tidal mixing in layered planetary cores

### A layered liquid outer core?

Among the several extensions of the present work that may be envisioned, the one that may demand the largest amount of work is to fully understand the different processes at stake in tidal mixing of a stably stratified liquid core. We have proposed throughout chapter 7 a short analysis of this issue with a very idealised model, with many necessary approximations, in particular the continuous density variation and the strong stratification limit. We believe that, in regard of the recent results of Landeau et al. (2016), a global study of layered planetary core mixing under tidal action is needed.

Landeau et al. (2016) have indeed shown that layering of light elements concentration in the iron core is a natural consequence of its formation process. As mentioned earlier in chapter 7, the formation of a terrestrial planet is an accretion and differentiation process: smaller bodies collide, aggregate and at the same time the metal and silicate phases separate from one another under the action of gravity. In the later stage of planetary formation, the accretion process is dominated by large impacts of partially differentiated bodies on the partially differentiated proto-planets of larger size. The cores of these two bodies do not necessarily have the same light elements (silicon, oxygen, carbon, sulfur, etc.) composition and proportions. After the collision, the iron core of the impactor merges with the core of the proto-planet. As shown by the experiments of Landeau et al. (2016), the merging process does not result in

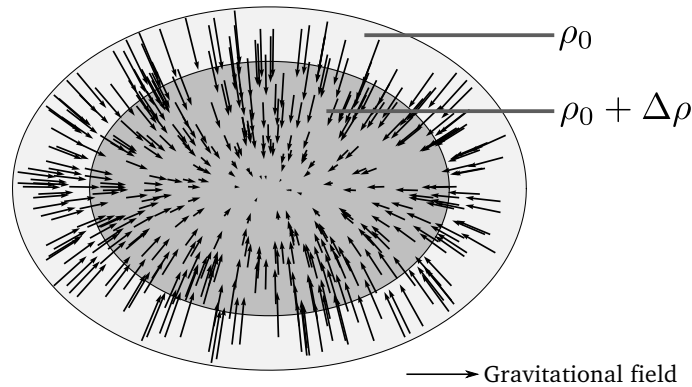


**Figure 7.23:** Picture of a two-layer ellipsoidal core and the gravitational field resulting from the perturbation of the sphere self-gravity by a tidal potential. The densities of the layers are  $\rho_0$  and  $\rho_0 + \Delta\rho$ . We consider the limit where the density contrast  $\Delta\rho$  is small compared to  $\rho_0$  so that the two layer sphere gravity field is approximated by the homogeneous sphere gravity field. The shape of the ellipsoid and the relative strength of the tidal field are related by equation (9) in Barker et al. (2016).

overall homogenisation of the light element composition of the resulting body's core, although some mixing occurs. The impactor's iron rather migrates (with some significant entrainment though) to form a stable superposition of layers with different light elements composition and density. In addition to the evidence presented by Landeau et al. (2016) in their analogue laboratory experiments, seismic and geomagnetic data show that a stable, lighter layer may still persist today, about 4.5 Gy after the last large impact that led to the Earth and Moon formation.

We have shown throughout chapter 7 that tidal forcing couples with waves in a stratified core to drive weak turbulence, but under many approximations that may not be valid. First, we have assumed that the interior of the planet is constantly in barotropic equilibrium, *i.e.* that without instability, the isopycnal surfaces correspond to the equipotential of the gravitational field including the tidal potential. Whether such an assumption still holds in a layered core with small density contrasts is unknown. In addition, we have assumed the stratification to be linear but the analogue experiments of Landeau et al. (2016) rather suggest layering with a sharp density contrast at the interface.

The extension of this work we propose hereafter is a general study of the behaviour of a layered iron core undergoing unsteady tidal distortion. The aim is to find the basic equilibrium of such a configuration, to determine the existence of instabilities at the interface between layers and to quantify the associated mixing, or light element exchanges, between the two miscible layers. It comprises three parts involving global and local simulations, as well as an experimental study.

### Barotropic equilibrium and internal tide

To begin this research project, we first propose to carry out global simulations in order to examine the stability of the two layer configuration presented in figure 7.23. These simulations would feature two layers enclosed in an ellipsoid with a gravitational field that includes both the self-gravity of the unperturbed, spherical fluid body and the tidal field. These simulations may allow studying the excitation of global modes of the interface and probing the stability of the barotropic equilibrium. They would be carried out with the NEK5000 code used for instance in Favier et al. (2015) and Barker et al. (2016).

It is indeed likely that tidal excitation drives perturbation of the shape of the layer separation. To support this assertion, we propose to determine the typical frequency of a gravity wave propagating at the interface between fluids with densities  $\rho_0$  and  $\rho_0 + \Delta\rho$ . Let us call  $h$  the lower layer height and  $g$  the gravitational field intensity at the interface. A typical frequency  $\omega_g$  built upon these quantities and related to the density contrast may be defined as follows:

$$\omega_g = \frac{\Delta\rho}{\rho_0} \sqrt{\frac{g}{h}} \quad (7.49)$$

where we have used a shallow layer height approximation. To evaluate  $\omega_g$  we follow the study of Landeau et al. (2016) who propose that a Moon-forming impact gives rise to a  $\sim 300$  km layer with a density contrast  $\Delta\rho/\rho_0 \sim 10^{-2}$ . As a consequence,  $\omega_g \sim 10^{-4}$  rad.s $^{-1}$  whereas the differential rotation rate between the Earth's rotation and the Moon's orbit  $\gamma$  is about  $7 \times 10^{-5}$  rad.s $^{-1}$ , all the more considering that in the past, orbit and spin rotation rates were larger. We therefore conclude that the typical oscillation frequency of the layer interface is similar to the tidal excitation frequency. This mechanical forcing in a layered core could lead to the propagation of interfacial gravity waves possibly excited by parametric resonance, as well as inertial wave propagation in the bulk of the fluid. These interfacial motions may result in light element mixing as well as dynamo action.

### Local study of the two-layers core under tidal excitation

Although the preceding global study is useful in examining the stability of the two-layers core, it might be limited when it comes to quantifying turbulent mixing driven by the interface instability because of the existence of boundary layers. To study this problem in the regimes of small tidal forcing and small density contrast, the SNOOPY code might be adequate.

Compared to the stably stratified case, it is probably not realistic to maintain a background density profile, since the displacement and blurring of the density interface is an important feature in the dynamics. Instead, it may be useful to follow the numerical work of Horne Iribarne et al. (2017) who study the evolution of an initial stratification undergoing turbulent mixing. A similar approach could be implemented in the present case with an initial—smoothed—density step in a Cartesian box with a background tidal distortion. Note that a two-layers density profile cannot be directly implemented in a Cartesian model with triply periodic boundary conditions. The density profile must be periodic, which can be done without impacting the dynamics by penalisation of the flow over the domain where an artificial density variation is imposed.

With such a model, it may be possible to quantify the mixing produced by the superposition of the classical elliptical instability that should develop in each layer because of the coupling between the tidal forcing and rotation, and the interface gravity waves.

### An analogue laboratory experiment

Implementing tidal distortion with radial stratification and gravity is difficult in the laboratory. In order to study an instability—possibly parametric—of surface waves in a two-layers system, we propose to follow the work of Benielli and Sommeria (1998) and implement a Faraday instability type of set-up. The instability of the interface would be driven by vertical oscillations or, equivalently, harmonic gravity intensity modulation.

Mixing across an interface driven by a Faraday-like instability has been the subject of several studies since the seminal work of Benielli and Sommeria (1998). Zoueshtiagh et al. (2009) and Amiroudine et al. (2012) have carried out experiments of this instability in the regime of very large forcing, so large that the gravity in the referential of the oscillated tank periodically reverses. Gréa and Ebo Adou (2018) and Briard et al. (2019) have simulated the three-dimensional instability of an oscillated two layers system also in the regime of strong forcing. These two numerical studies have focused on the irreversible mixing induced by the strong turbulent flow at the interface.

In the case of small amplitude forcing, which is, again, the relevant limit of geophysical forcing, it is not clear how mixing could be enhanced by the instability. Nevertheless, in the case of weak forcing and dissipation, the non-linear saturation may result in interfacial wave turbulence that could significantly increase the contact surface between the two fluids and thus enhance interfacial mixing.

Mounting this experiment on a turntable could also result in interesting dynamics that could be relevant to interfacial mixing in planetary cores. The density in each layer being constant, they can both sustain inertial waves that are insensitive to the vertical oscillations of the tank, but will depend on the oscillations of the interface. Interaction between the interfacial dynamics and inertial waves could be an interesting feature of the two-layers core dynamics. Note however that rotation induces complications such as inhomogeneous gravity field and bending of the interface into a parabolic shape. These additional features will probably convolute the theoretical analysis, as in the case of the rotating Rayleigh-Taylor instability where the curvature of the interface is an important complication in the stability analysis of the set-up (see for instance the work of Scase et al. (2017)).

Since the seminal work of Malkus (1968), our knowledge of the tidal instabilities and of their relevance to planetary cores has made significant progress. Our conclusion is that indeed, they should lead to specific regimes in planetary cores, involving inertial and internal wave turbulence. These specific regimes could explain the variety of behaviours observed in planets in the solar system and probably in extrasolar ones, beyond the classical Earth model. There still remains a large amount of work to quantify their signature in available data.

## References

- AFANASYEV, Y. D. and PELTIER, W. R. (1998). Three-Dimensional Instability of Anticyclonic Swirling Flow in Rotating Fluid: Laboratory Experiments and Related Theoretical Predictions. *Physics of Fluids* **10**, pp. 3194–3202. DOI: [10.1063/1.869846](https://doi.org/10.1063/1.869846).
- ALEXAKIS, A. (2015). Rotating TaylorGreen Flow. *Journal of Fluid Mechanics* **769**, pp. 46–78. DOI: [10.1017/jfm.2015.82](https://doi.org/10.1017/jfm.2015.82).
- AMIROUDINE, S., ZOUESHTIAGH, F., and NARAYANAN, R. (2012). Mixing Generated by Faraday Instability between Miscible Liquids. *Physical Review E* **85**, p. 016326. DOI: [10.1103/PhysRevE.85.016326](https://doi.org/10.1103/PhysRevE.85.016326).
- ANDRAULT, D. et al. (2016). The Deep Earth May Not Be Cooling Down. *Earth and Planetary Science Letters* **443**, pp. 195–203. DOI: [10.1016/j.epsl.2016.03.020](https://doi.org/10.1016/j.epsl.2016.03.020).
- ASPDEN, J. M. and VANNESTE, J. (2009). Elliptical Instability of a Rapidly Rotating, Strongly Stratified Fluid. *Physics of Fluids* **21**, p. 074104.
- AUBOURG, Q. and MORDANT, N. (2015). Nonlocal Resonances in Weak Turbulence of Gravity-Capillary Waves. *Physical Review Letters* **114**, p. 144501. DOI: [10.1103/PhysRevLett.114.144501](https://doi.org/10.1103/PhysRevLett.114.144501).
- BAJARS, J., FRANK, J., and MAAS, L. R. M. (2013). On the Appearance of Internal Wave Attractors Due to an Initial or Parametrically Excited Disturbance. *Journal of Fluid Mechanics* **714**, pp. 283–311. DOI: [10.1017/jfm.2012.479](https://doi.org/10.1017/jfm.2012.479).
- BAK, P., TANG, C., and WIESENFELD, K. (1987). Self-Organized Criticality: An Explanation of the  $1/f$  Noise. *Physical Review Letters* **59**, pp. 381–384. DOI: [10.1103/PhysRevLett.59.381](https://doi.org/10.1103/PhysRevLett.59.381).
- BARKER, A. J. (2016). Nonlinear Tides in a Homogeneous Rotating Planet or Star: Global Simulations of the Elliptical Instability. *Monthly Notices of the Royal Astronomical Society*, stw702. DOI: [10.1093/mnras/stw702](https://doi.org/10.1093/mnras/stw702).
- BARKER, A. J., BRAVINER, H. J., and OGILVIE, G. I. (2016). Nonlinear Tides in a Homogeneous Rotating Planet or Star: Global Modes and Elliptical Instability. *Monthly Notices of the Royal Astronomical Society* **459**, pp. 924–938. DOI: [10.1093/mnras/stw701](https://doi.org/10.1093/mnras/stw701). arXiv: [1603.06839](https://arxiv.org/abs/1603.06839).
- BARKER, A. J. and LITHWICK, Y. (2014). Non-Linear Evolution of the Elliptical Instability in the Presence of Weak Magnetic Fields. *Monthly Notices of the Royal Astronomical Society* **437**, pp. 305–315. DOI: [10.1093/mnras/stt1884](https://doi.org/10.1093/mnras/stt1884).
- BARKER, A. J. and LITHWICK, Y. (2013). Non-Linear Evolution of the Tidal Elliptical Instability in Gaseous Planets and Stars. *Monthly Notices of the Royal Astronomical Society* **435**, pp. 3614–3626.
- BARTELLO, P. and TOBIAS, S. M. (2013). Sensitivity of Stratified Turbulence to the Buoyancy Reynolds Number. *Journal of Fluid Mechanics* **725**, pp. 1–22. DOI: [10.1017/jfm.2013.170](https://doi.org/10.1017/jfm.2013.170).
- BAYLI, B. J. (1986). Three-Dimensional Instability of Elliptical Flow. *Physical Review Letters* **57**, pp. 2160–2163. DOI: [10.1103/PhysRevLett.57.2160](https://doi.org/10.1103/PhysRevLett.57.2160).
- BELLET, F. et al. (2006). Wave Turbulence in Rapidly Rotating Flows. *Journal of Fluid Mechanics* **562**, pp. 83–121.
- BENDER, C. M. and ORSZAG, S. A. (1978). *Advanced Mathematical Methods for Scientists and Engineers*. McGraw-Hill. 616 pp.
- BENIELLI, D. and SOMMERIA, J. (1996). Excitation of Internal Waves and Stratified Turbulence by Parametric Instability. *Dynamics of Atmospheres and Oceans. Stratified Flows* **23**, pp. 335–343. DOI: [10.1016/0377-0265\(95\)00432-7](https://doi.org/10.1016/0377-0265(95)00432-7).
- BENIELLI, D. and SOMMERIA, J. (1998). Excitation and Breaking of Internal Gravity Waves by Parametric Instability. *Journal of Fluid Mechanics* **374**, pp. 117–144. DOI: [10.1017/S0022112098002602](https://doi.org/10.1017/S0022112098002602).

- BILLANT, P. and CHOMAZ, J.-M. (2001). Self-Similarity of Strongly Stratified Inviscid Flows. *Physics of Fluids* **13**, pp. 1645–1651. DOI: [10.1063/1.1369125](https://doi.org/10.1063/1.1369125).
- BOFFETTA, G. and ECKE, R. E. (2012). Two-Dimensional Turbulence. *Annual Review of Fluid Mechanics* **44**, pp. 427–451. DOI: [10.1146/annurev-fluid-120710-101240](https://doi.org/10.1146/annurev-fluid-120710-101240).
- BONNEFOY, F. et al. (2016). Observation of Resonant Interactions among Surface Gravity Waves. *Journal of Fluid Mechanics* **805**. DOI: [10.1017/jfm.2016.576](https://doi.org/10.1017/jfm.2016.576). arXiv: [1606.09009](https://arxiv.org/abs/1606.09009).
- BORDES, G. et al. (2012). Experimental Evidence of a Triadic Resonance of Plane Inertial Waves in a Rotating Fluid. *Physics of Fluids* **24**, p. 014105. DOI: [10.1063/1.3675627](https://doi.org/10.1063/1.3675627).
- BOURGET, B. et al. (2013). Experimental Study of Parametric Subharmonic Instability for Internal Plane Waves. *Journal of Fluid Mechanics* **723**, pp. 1–20. DOI: [10.1017/jfm.2013.78](https://doi.org/10.1017/jfm.2013.78).
- BRETHOUWER, G. et al. (2007). Scaling Analysis and Simulation of Strongly Stratified Turbulent Flows. *Journal of Fluid Mechanics* **585**, p. 343. DOI: [10.1017/S0022112007006854](https://doi.org/10.1017/S0022112007006854).
- BRIARD, A., GRÉA, B.-J., and GOSTIAUX, L. (2019). Harmonic to Subharmonic Transition of the Faraday Instability in Miscible Fluids. *Physical Review Fluids* **4**, p. 044502. DOI: [10.1103/PhysRevFluids.4.044502](https://doi.org/10.1103/PhysRevFluids.4.044502).
- BROUZET, C. et al. (2016). Energy Cascade in Internal-Wave Attractors. *EPL (Europhysics Letters)* **113**, p. 44001. DOI: [10.1209/0295-5075/113/44001](https://doi.org/10.1209/0295-5075/113/44001).
- BROUZET, C. et al. (2017). Internal Wave Attractors: Different Scenarios of Instability. *Journal of Fluid Mechanics* **811**, pp. 544–568. DOI: [10.1017/jfm.2016.759](https://doi.org/10.1017/jfm.2016.759).
- BROUZET, C. (2016). *Internal Wave Attractors : From Geometrical Focusing to Non-Linear Energy Cascade and Mixing*. PhD thesis. Université de Lyon.
- BUFFETT, B. (2014). Geomagnetic Fluctuations Reveal Stable Stratification at the Top of the Earth's Core. *Nature* **507**, pp. 484–487. DOI: [10.1038/nature13122](https://doi.org/10.1038/nature13122).
- BÜHLER, O. and HOLMES-CERFON, M. (2011). Decay of an Internal Tide Due to Random Topography in the Ocean. *Journal of Fluid Mechanics* **678**, pp. 271–293. DOI: [10.1017/jfm.2011.115](https://doi.org/10.1017/jfm.2011.115).
- BUSSE, F. H. (2010). Mean Zonal Flows Generated by Librations of a Rotating Spherical Cavity. *Journal of Fluid Mechanics* **650**, pp. 505–512. DOI: [10.1017/S0022112010000753](https://doi.org/10.1017/S0022112010000753).
- BUSSE, F. H. (1970). Thermal Instabilities in Rapidly Rotating Systems. *Journal of Fluid Mechanics* **44**, p. 441. DOI: [10.1017/S0022112070001921](https://doi.org/10.1017/S0022112070001921).
- CAMBON, C. (2001). Turbulence and Vortex Structures in Rotating and Stratified Flows. *European Journal of Mechanics - B/Fluids* **20**, pp. 489–510. DOI: [10.1016/S0997-7546\(01\)01126-8](https://doi.org/10.1016/S0997-7546(01)01126-8).
- CAMPAGNE, A. et al. (2014). Direct and Inverse Energy Cascades in a Forced Rotating Turbulence Experiment. *Physics of Fluids* **26**, p. 125112. DOI: [10.1063/1.4904957](https://doi.org/10.1063/1.4904957).
- CAMPAGNE, A. et al. (2015). Disentangling Inertial Waves from Eddy Turbulence in a Forced Rotating-Turbulence Experiment. *Physical Review E* **91**. DOI: [10.1103/PhysRevE.91.043016](https://doi.org/10.1103/PhysRevE.91.043016).
- CÉBRON, D., VANTIEGHEM, S., and HERREMAN, W. (2014). Libration-Driven Multipolar Instabilities. *Journal of Fluid Mechanics* **739**, pp. 502–543. DOI: [10.1017/jfm.2013.623](https://doi.org/10.1017/jfm.2013.623).
- CÉBRON, D. et al. (2010). A Systematic Numerical Study of the Tidal Instability in a Rotating Triaxial Ellipsoid. *Physics of the Earth and Planetary Interiors* **182**, pp. 119–128. DOI: [10.1016/j.pepi.2010.07.003](https://doi.org/10.1016/j.pepi.2010.07.003).
- CÉBRON, D. et al. (2012a). Elliptical Instability in Terrestrial Planets and Moons. *Astronomy & Astrophysics* **539**, A78. DOI: [10.1051/0004-6361/201117741](https://doi.org/10.1051/0004-6361/201117741).
- CÉBRON, D. et al. (2012b). Libration Driven Elliptical Instability. *Physics of Fluids* **24**, p. 061703. DOI: [10.1063/1.4729296](https://doi.org/10.1063/1.4729296).
- CLARK DI LEONI, P. et al. (2014). Quantification of the Strength of Inertial Waves in a Rotating Turbulent Flow. *Physics of Fluids* **26**, p. 035106. DOI: [10.1063/1.4868280](https://doi.org/10.1063/1.4868280).
- CRAYA, A. (1957). Contribution à l'analyse de la turbulence associée à des vitesses moyennes.

- DRAZIN, P. G. and REID, W. H. (2004). *Hydrodynamic Stability*. Cambridge University Press. 630 pp.
- DÜRING, G., JOSSEMAND, C., and RICA, S. (2006). Weak Turbulence for a Vibrating Plate: Can One Hear a Kolmogorov Spectrum? *Physical Review Letters* **97**. DOI: [10.1103/PhysRevLett.97.025503](https://doi.org/10.1103/PhysRevLett.97.025503).
- ELOY, C., LE GAL, P., and LE DIZÈS, S. (2003). Elliptic and Triangular Instabilities in Rotating Cylinders. *Journal of Fluid Mechanics* **476**. DOI: [10.1017/S0022112002002999](https://doi.org/10.1017/S0022112002002999).
- EMBED, P. F. and MAJDA, A. J. (1998). Low Froude Number Limiting Dynamics for Stably Stratified Flow with Small or Finite Rossby Numbers. *Geophysical & Astrophysical Fluid Dynamics* **87**, pp. 1–50. DOI: [10.1080/03091929808208993](https://doi.org/10.1080/03091929808208993).
- FAVIER, B., SILVERS, L. J., and PROCTOR, M. R. E. (2014). Inverse Cascade and Symmetry Breaking in Rapidly-Rotating Boussinesq Convection. *Physics of Fluids* **26**, p. 096605. DOI: [10.1063/1.4895131](https://doi.org/10.1063/1.4895131). arXiv: [1408.6483](https://arxiv.org/abs/1408.6483).
- FAVIER, B. et al. (2015). Generation and Maintenance of Bulk Turbulence by Libration-Driven Elliptical Instability. *Physics of Fluids* **27**, p. 066601. DOI: [10.1063/1.4922085](https://doi.org/10.1063/1.4922085).
- FAVIER, B., CAMBON, C., and GODEFERD, F. (2010). On Space and Time Correlations of Isotropic and Rotating Turbulence. *Physics of Fluids* **22**, p. 015101. DOI: [10.1063/1.3276290](https://doi.org/10.1063/1.3276290).
- GALTIER, S. (2003). Weak Inertial-Wave Turbulence Theory. *Physical Review E* **68**. DOI: [10.1103/PhysRevE.68.015301](https://doi.org/10.1103/PhysRevE.68.015301).
- GAMBA, I. M., SMITH, L. M., and TRAN, M.-B. (2017). On the Wave Turbulence Theory for Stratified Flows in the Ocean. arXiv: [1709.08266](https://arxiv.org/abs/1709.08266) [math-ph, physics:physics].
- GARRETT, C. and MUNK, W. (1972). Space-Time Scales of Internal Waves. *Geophysical Fluid Dynamics* **3**, pp. 225–264. DOI: [10.1080/03091927208236082](https://doi.org/10.1080/03091927208236082).
- GARRETT, C. and MUNK, W. (1975). Space-Time Scales of Internal Waves: A Progress Report. *Journal of Geophysical Research* **80**, pp. 291–297. DOI: [10.1029/JC080i003p00291](https://doi.org/10.1029/JC080i003p00291).
- GARRETT and MUNK, a. W. (1979). Internal Waves in the Ocean. *Annual Review of Fluid Mechanics* **11**, pp. 339–369. DOI: [10.1146/annurev.fl.11.010179.002011](https://doi.org/10.1146/annurev.fl.11.010179.002011).
- GARRICK-BETHELL, I. et al. (2009). Early Lunar Magnetism. *Science* **323**, pp. 356–359. DOI: [10.1126/science.1166804](https://doi.org/10.1126/science.1166804). pmid: [19150839](https://pubmed.ncbi.nlm.nih.gov/19150839/).
- GELASH, A. A., L'VOV, V. S., and ZAKHAROV, V. E. (2017). Complete Hamiltonian Formalism for Inertial Waves in Rotating Fluids. *Journal of Fluid Mechanics* **831**, pp. 128–150. DOI: [10.1017/jfm.2017.611](https://doi.org/10.1017/jfm.2017.611).
- GLATZMAIERS, G. A. and ROBERTS, P. H. (1995). A Three-Dimensional Self-Consistent Computer Simulation of a Geomagnetic Field Reversal. *Nature* **377**, pp. 203–209. DOI: [10.1038/377203a0](https://doi.org/10.1038/377203a0).
- GODEFERD, F. S. and MOISY, F. (2015). Structure and Dynamics of Rotating Turbulence: A Review of Recent Experimental and Numerical Results. *Applied Mechanics Reviews* **67**, pp. 030802–030802. DOI: [10.1115/1.4029006](https://doi.org/10.1115/1.4029006).
- GODOY-DIANA, R., CHOMAZ, J.-M., and BILLANT, P. (2004). Vertical Length Scale Selection for Pancake Vortices in Strongly Stratified Viscous Fluids. *Journal of Fluid Mechanics* **504**, pp. 229–238. DOI: [10.1017/S0022112004008067](https://doi.org/10.1017/S0022112004008067).
- GOODMAN, J. (1993). A Local Tidal Instability of Tidally Distorted Accretion Disks. *The Astrophysical Journal* **406**, p. 596.
- GRANNAN, A. M. et al. (2014). Experimental Study of Global-Scale Turbulence in a Librating Ellipsoid. *Physics of Fluids* **26**, p. 126601. DOI: [10.1063/1.4903003](https://doi.org/10.1063/1.4903003).
- GRANNAN, A. M. et al. (2017). Tidally Forced Turbulence in Planetary Interiors. *Geophysical Journal International* **208**, pp. 1690–1703. DOI: [10.1093/gji/ggw479](https://doi.org/10.1093/gji/ggw479).

- GRÉA, B.-J. and EBO ADOU, A. (2018). What Is the Final Size of Turbulent Mixing Zones Driven by the Faraday Instability? *Journal of Fluid Mechanics* **837**, pp. 293–319. DOI: [10.1017/jfm.2017.837](https://doi.org/10.1017/jfm.2017.837).
- GREENSPAN, H. P. (1969). On the Non-Linear Interaction of Inertial Modes. *Journal of Fluid Mechanics* **36**, pp. 257–264. DOI: [10.1017/S0022112069001649](https://doi.org/10.1017/S0022112069001649).
- GREENSPAN, H. P. (1968). *The Theory of Rotating Fluids*. CUP Archive. 386 pp.
- GUIMBARD, D. et al. (2010). Elliptic Instability of a Stratified Fluid in a Rotating Cylinder. *Journal of Fluid Mechanics* **660**, pp. 240–257. DOI: [10.1017/S0022112010002636](https://doi.org/10.1017/S0022112010002636).
- HERBERT, C. et al. (2016). Waves and Vortices in the Inverse Cascade Regime of Stratified Turbulence with or without Rotation. *Journal of Fluid Mechanics* **806**, pp. 165–204. DOI: [10.1017/jfm.2016.581](https://doi.org/10.1017/jfm.2016.581).
- HERRING, J. R. (1974). Approach of Axisymmetric Turbulence to Isotropy. *Physics of Fluids* **17**, p. 859. DOI: [10.1063/1.1694822](https://doi.org/10.1063/1.1694822).
- HIROSE, K., LABROSSE, S., and HERNLUND, J. (2013). Composition and State of the Core. *Annual Review of Earth and Planetary Sciences* **41**, pp. 657–691. DOI: [10.1146/annurev-earth-050212-124007](https://doi.org/10.1146/annurev-earth-050212-124007).
- HORNE IRIBARNE, E. et al. (2017). “Irreversible Mixing And Energetic Aspects Of Turbulent Stratified Flow”. *16th European Turbulence Conference*. Stockholm, Sweden.
- HOUGH, S. S. (1895). XII. The Oscillations of a Rotating Ellipsoidal Shell Containing Fluid. *Phil. Trans. R. Soc. Lond. A* **186**, pp. 469–506. DOI: [10.1098/rsta.1895.0012](https://doi.org/10.1098/rsta.1895.0012).
- HUMBERT, T., AUMAÎTRE, S., and GALLET, B. (2017). Wave-Induced Vortex Recoil and Nonlinear Refraction. *Physical Review Fluids* **2**, p. 094701. DOI: [10.1103/PhysRevFluids.2.094701](https://doi.org/10.1103/PhysRevFluids.2.094701). arXiv: [1709.08912](https://arxiv.org/abs/1709.08912).
- JONES, E., OLIPHANT, T., PETERSON, P., et al. (2001). *SciPy: Open Source Scientific Tools for Python*.
- JOUBAUD, S. et al. (2012). Experimental Parametric Subharmonic Instability in Stratified Fluids. *Physics of Fluids* **24**, p. 041703. DOI: [10.1063/1.4706183](https://doi.org/10.1063/1.4706183).
- JOUVE, L. and OGILVIE, G. I. (2014). Direct Numerical Simulations of an Inertial Wave Attractor in Linear and Nonlinear Regimes. *Journal of Fluid Mechanics* **745**, pp. 223–250. DOI: [10.1017/jfm.2014.63](https://doi.org/10.1017/jfm.2014.63).
- KARTASHOVA, E. (2009). Discrete Wave Turbulence. *EPL (Europhysics Letters)* **87**, p. 44001. DOI: [10.1209/0295-5075/87/44001](https://doi.org/10.1209/0295-5075/87/44001). arXiv: [0907.4406](https://arxiv.org/abs/0907.4406).
- KERSWELL, R. R. (1993a). Elliptical Instabilities of Stratified, Hydromagnetic Waves. *Geophysical & Astrophysical Fluid Dynamics* **71**, pp. 105–143. DOI: [10.1080/03091929308203599](https://doi.org/10.1080/03091929308203599).
- KERSWELL, R. R. (1999). Secondary Instabilities in Rapidly Rotating Fluids: Inertial Wave Breakdown. *Journal of Fluid Mechanics* **382**, pp. 283–306. DOI: [10.1017/S0022112098003954](https://doi.org/10.1017/S0022112098003954).
- KERSWELL, R. R. (1993b). The Instability of Precessing Flow. *Geophysical & Astrophysical Fluid Dynamics* **72**, pp. 107–144. DOI: [10.1080/03091929308203609](https://doi.org/10.1080/03091929308203609).
- KERSWELL, R. R. (1996). Upper Bounds on the Energy Dissipation in Turbulent Precession. *Journal of Fluid Mechanics* **321**, pp. 335–370. DOI: [10.1017/S0022112096007756](https://doi.org/10.1017/S0022112096007756).
- KERSWELL, R. R. (2002). Elliptical Instability. *Annual Review of Fluid Mechanics* **34**, pp. 83–113. DOI: [10.1146/annurev.fluid.34.081701.171829](https://doi.org/10.1146/annurev.fluid.34.081701.171829).
- KERSWELL, R. R. and MALKUS, W. V. R. (1998). Tidal Instability as the Source for Io’s Magnetic Signature. *Geophysical Research Letters* **25**, pp. 603–606. DOI: [10.1029/98GL00237](https://doi.org/10.1029/98GL00237).
- KIVELSON, M. G. et al. (1996a). Discovery of Ganymede’s Magnetic Field by the Galileo Spacecraft. *Nature* **384**, pp. 537–541. DOI: [10.1038/384537a0](https://doi.org/10.1038/384537a0).
- KIVELSON, M. G. et al. (1996b). Io’s Interaction with the Plasma Torus: Galileo Magnetometer Report. *Science* **274**, pp. 396–398. DOI: [10.1126/science.274.5286.396](https://doi.org/10.1126/science.274.5286.396).

- KIVELSON, M., KHURANA, K., and VOLWERK, M. (2002). The Permanent and Inductive Magnetic Moments of Ganymede. *Icarus* **157**, pp. 507–522. DOI: [10.1006/icar.2002.6834](https://doi.org/10.1006/icar.2002.6834).
- LABROSSE, S. (2015). Thermal Evolution of the Core with a High Thermal Conductivity. *Physics of the Earth and Planetary Interiors*. Transport Properties of the Earth's Core **247**, pp. 36–55. DOI: [10.1016/j.pepi.2015.02.002](https://doi.org/10.1016/j.pepi.2015.02.002).
- LACAZE, L., LE GAL, P., and LE DIZES, S. (2005). Elliptical Instability of the Flow in a Rotating Shell. *Physics of the Earth and Planetary Interiors* **151**, pp. 194–205.
- LAGRANGE, R. et al. (2011). Precessional Instability of a Fluid Cylinder. *Journal of Fluid Mechanics* **666**, pp. 104–145. DOI: [10.1017/S0022112010004040](https://doi.org/10.1017/S0022112010004040).
- LANDEAU, M. et al. (2016). Core Merging and Stratification Following Giant Impact. *Nature Geoscience* **9**, pp. 786–789. DOI: [10.1038/ngeo2808](https://doi.org/10.1038/ngeo2808).
- LARMOR, J. (1919). “How Could a Rotating Body Such as the Sun Become a Magnet?” *Report of the British Association for the Advancement of Science*, pp. 159–160.
- LE BARS, M., LE DIZÈS, S., and LE GAL, P. (2007). Coriolis Effects on the Elliptical Instability in Cylindrical and Spherical Rotating Containers. *Journal of Fluid Mechanics* **585**, p. 323. DOI: [10.1017/S0022112007006866](https://doi.org/10.1017/S0022112007006866).
- LE BARS, M. et al. (2011). An Impact-Driven Dynamo for the Early Moon. *Nature* **479**, pp. 215–218. DOI: [10.1038/nature10565](https://doi.org/10.1038/nature10565).
- LE BARS, M. et al. (2010). Tidal Instability in Stellar and Planetary Binary Systems. *Physics of the Earth and Planetary Interiors* **178**, pp. 48–55. DOI: [10.1016/j.pepi.2009.07.005](https://doi.org/10.1016/j.pepi.2009.07.005).
- LE BARS, M., CÉBRON, D., and LE GAL, P. (2015). Flows Driven by Libration, Precession, and Tides. *Annual Review of Fluid Mechanics* **47**, pp. 163–193. DOI: [10.1146/annurev-fluid-010814-014556](https://doi.org/10.1146/annurev-fluid-010814-014556).
- LE DIZÈS, S. (2000). Three-Dimensional Instability of a Multipolar Vortex in a Rotating Flow. *Physics of Fluids (1994-present)* **12**, pp. 2762–2774.
- LEMASQUERIER, D. et al. (2017). Libration-driven Flows in Ellipsoidal Shells. *Journal of Geophysical Research: Planets* **122**, pp. 1926–1950. DOI: [10.1002/2017JE005340](https://doi.org/10.1002/2017JE005340).
- LESUR, G. and LONGARETTI, P.-Y. (2005). On the Relevance of Subcritical Hydrodynamic Turbulence to Accretion Disk Transport. *Astronomy and Astrophysics* **444**, pp. 25–44. DOI: [10.1051/0004-6361:20053683](https://doi.org/10.1051/0004-6361:20053683). arXiv: [astro-ph/0509541](https://arxiv.org/abs/astro-ph/0509541).
- LEVINE, M. D. (2002). A Modification of the GarrettMunk Internal Wave Spectrum. *Journal of physical oceanography* **32**, pp. 3166–3181.
- LIFSCHITZ, A. and HAMEIRI, E. (1991). Local Stability Conditions in Fluid Dynamics. *Physics of Fluids A: Fluid Dynamics (1989-1993)* **3**, pp. 2644–2651. DOI: [10.1063/1.858153](https://doi.org/10.1063/1.858153).
- LINDBORG, E. and BRETHOUWER, G. (2008). Vertical Dispersion by Stratified Turbulence. *Journal of Fluid Mechanics* **614**, pp. 303–314. DOI: [10.1017/S0022112008003595](https://doi.org/10.1017/S0022112008003595).
- LINDBORG, E. (2006). The Energy Cascade in a Strongly Stratified Fluid. *Journal of Fluid Mechanics* **550**, pp. 207–242. DOI: [10.1017/S0022112005008128](https://doi.org/10.1017/S0022112005008128).
- LIVERMORE, P. W., BAILEY, L. M., and HOLLERBACH, R. (2016). A Comparison of No-Slip, Stress-Free and Inviscid Models of Rapidly Rotating Fluid in a Spherical Shell. *Scientific Reports* **6**, p. 22812. DOI: [10.1038/srep22812](https://doi.org/10.1038/srep22812).
- MAAS, L. R. M. and LAM, F.-P. A. (1995). Geometric Focusing of Internal Waves. *Journal of Fluid Mechanics* **300**, pp. 1–41. DOI: [10.1017/S0022112095003582](https://doi.org/10.1017/S0022112095003582).
- MACKINNON, J. A. and WINTERS, K. B. (2005). Subtropical Catastrophe: Significant Loss of Low-Mode Tidal Energy at 28.9°. *Geophysical Research Letters* **32**, p. L15605. DOI: [10.1029/2005GL023376](https://doi.org/10.1029/2005GL023376).
- MAFFIOLI, A., BRETHOUWER, G., and LINDBORG, E. (2016). Mixing Efficiency in Stratified Turbulence. *Journal of Fluid Mechanics* **794**. DOI: [10.1017/jfm.2016.206](https://doi.org/10.1017/jfm.2016.206).

- MAFFIOLI, A. and DAVIDSON, P. A. (2016). Dynamics of Stratified Turbulence Decaying from a High Buoyancy Reynolds Number. *Journal of Fluid Mechanics* **786**, pp. 210–233. DOI: [10.1017/jfm.2015.667](https://doi.org/10.1017/jfm.2015.667).
- MALKUS, W. V. R. (1968). Precession of the Earth as the Cause of Geomagnetism: Experiments Lend Support to the Proposal That Precessional Torques Drive the Earth's Dynamo. *Science* **160**, pp. 259–264. DOI: [10.1126/science.160.3825.259](https://doi.org/10.1126/science.160.3825.259). pmid: 17788230.
- MALKUS, W. V. R. (1963). Precessional Torques as the Cause of Geomagnetism. *Journal of Geophysical Research* **68**, pp. 2871–2886. DOI: [10.1029/JZ068i010p02871](https://doi.org/10.1029/JZ068i010p02871).
- MALKUS, W. V. R. and WALEFFE, F. A. (1991). “Transition from Order to Disorder in Elliptical Flow: A Direct Path to Shear Flow Turbulence”. *Advances in Turbulence 3*. Ed. by A. V. JOHANSSON and P. H. ALFREDSSON. Springer Berlin Heidelberg, pp. 197–203.
- MALKUS, W. V. R. (1989). An Experimental Study of Global Instabilities Due to the Tidal (Elliptical) Distortion of a Rotating Elastic Cylinder. *Geophysical & Astrophysical Fluid Dynamics* **48**, pp. 123–134. DOI: [10.1080/03091928908219529](https://doi.org/10.1080/03091928908219529).
- MARINO, R. et al. (2013). Inverse Cascades in Rotating Stratified Turbulence: Fast Growth of Large Scales. *EPL (Europhysics Letters)* **102**, p. 44006. DOI: [10.1209/0295-5075/102/44006](https://doi.org/10.1209/0295-5075/102/44006).
- MASON, D. M. and KERSWELL, R. R. (1999). Nonlinear Evolution of the Elliptical Instability: An Example of Inertial Wave Breakdown. *Journal of Fluid Mechanics* **396**, pp. 73–108.
- MCEWAN, A. D. and ROBINSON, R. M. (1975). Parametric Instability of Internal Gravity Waves. *Journal of Fluid Mechanics* **67**, pp. 667–687. DOI: [10.1017/S0022112075000547](https://doi.org/10.1017/S0022112075000547).
- MCWILLIAMS, J. C. and YAVNEH, I. (1998). Fluctuation Growth and Instability Associated with a Singularity of the Balance Equations. *Physics of Fluids* **10**, pp. 2587–2596. DOI: [10.1063/1.869772](https://doi.org/10.1063/1.869772).
- MIQUEL, B. and MORDANT, N. (2011). Nonstationary Wave Turbulence in an Elastic Plate. *Physical Review Letters* **107**. DOI: [10.1103/PhysRevLett.107.034501](https://doi.org/10.1103/PhysRevLett.107.034501).
- MIYAZAKI, T. (1993). Elliptical Instability in a Stably Stratified Rotating Fluid. *Physics of Fluids A: Fluid Dynamics* **5**, pp. 2702–2709. DOI: [10.1063/1.858733](https://doi.org/10.1063/1.858733).
- MIYAZAKI, T. and FUKUMOTO, Y. (1992). Three-Dimensional Instability of Strained Vortices in a Stably Stratified Fluid. *Physics of Fluids A: Fluid Dynamics* **4**, pp. 2515–2522. DOI: [10.1063/1.858438](https://doi.org/10.1063/1.858438).
- MOFFATT, H. K. (1970). Dynamo Action Associated with Random Inertial Waves in a Rotating Conducting Fluid. *Journal of Fluid Mechanics* **44**, pp. 705–719. DOI: [10.1017/S0022112070002100](https://doi.org/10.1017/S0022112070002100).
- MORIZE, C. et al. (2010). Experimental Determination of Zonal Winds Driven by Tides. *Physical Review Letters* **104**. DOI: [10.1103/PhysRevLett.104.214501](https://doi.org/10.1103/PhysRevLett.104.214501).
- NAZARENKO, S. (2011). *Wave Turbulence*. Vol. 825. Lecture Notes in Physics. Springer Berlin Heidelberg: Berlin, Heidelberg.
- NESS, N. F. et al. (1975). Magnetic Field of Mercury Confirmed. *Nature* **255**, pp. 204–205. DOI: [10.1038/255204a0](https://doi.org/10.1038/255204a0).
- NOIR, J. et al. (2009). An Experimental and Numerical Study of Librationally Driven Flow in Planetary Cores and Subsurface Oceans. *Physics of the Earth and Planetary Interiors* **173**, pp. 141–152. DOI: [10.1016/j.pepi.2008.11.012](https://doi.org/10.1016/j.pepi.2008.11.012).
- NOIR, J., JAULT, D., and CARDIN, P. (2001). Numerical Study of the Motions within a Slowly Precessing Sphere at Low Ekman Number. *Journal of Fluid Mechanics* **437**. DOI: [10.1017/S0022112001004311](https://doi.org/10.1017/S0022112001004311).
- NOIR, J. et al. (2012). Experimental Study of Libration-Driven Zonal Flows in Non-Axisymmetric Containers. *Physics of the Earth and Planetary Interiors* **204-205**, pp. 1–10. DOI: [10.1016/j.pepi.2012.05.005](https://doi.org/10.1016/j.pepi.2012.05.005). arXiv: 1301.5303.

- OGILVIE, G. I. (2014). Tidal Dissipation in Stars and Giant Planets. *Annual Review of Astronomy and Astrophysics* **52**, pp. 171–210. DOI: [10.1146/annurev-astro-081913-035941](https://doi.org/10.1146/annurev-astro-081913-035941). arXiv: [1406.2207](https://arxiv.org/abs/1406.2207).
- OGILVIE, G. I. (2005). Wave Attractors and the Asymptotic Dissipation Rate of Tidal Disturbances. *Journal of Fluid Mechanics* **543** (-1), p. 19. DOI: [10.1017/S0022112005006580](https://doi.org/10.1017/S0022112005006580).
- OKS, D. et al. (2017). Inverse Cascades and Resonant Triads in Rotating and Stratified Turbulence. *Physics of Fluids* **29**, p. 111109. DOI: [10.1063/1.5001740](https://doi.org/10.1063/1.5001740).
- OLSON, P. (2015). “8.01 - Core Dynamics: An Introduction and Overview”. *Treatise on Geophysics (Second Edition)*. Ed. by G. SCHUBERT. Elsevier: Oxford, pp. 1–25. DOI: [10.1016/B978-0-444-53802-4.00137-8](https://doi.org/10.1016/B978-0-444-53802-4.00137-8).
- OSBORN, T. R. (1980). Estimates of the Local Rate of Vertical Diffusion from Dissipation Measurements. *Journal of Physical Oceanography* **10**, pp. 83–89. DOI: [10.1175/1520-0485\(1980\)010<0083:EOTLRO>2.0.CO;2](https://doi.org/10.1175/1520-0485(1980)010<0083:EOTLRO>2.0.CO;2).
- PELTIER, W. R. and CAULFIELD, C. P. (2003). Mixing Efficiency in Stratified Shear Flows. *Annual Review of Fluid Mechanics* **35**, pp. 135–167. DOI: [10.1146/annurev.fluid.35.101101.161144](https://doi.org/10.1146/annurev.fluid.35.101101.161144).
- PIERREHUMBERT, R. T. (1986). Universal Short-Wave Instability of Two-Dimensional Eddies in an Inviscid Fluid. *Physical Review Letters* **57**, pp. 2157–2159. DOI: [10.1103/PhysRevLett.57.2157](https://doi.org/10.1103/PhysRevLett.57.2157).
- POINCARÉ, H. (1885). Sur l'équilibre d'une masse fluide animée d'un mouvement de rotation. *Acta Mathematica* **7**, pp. 259–380. DOI: [10.1007/BF02402204](https://doi.org/10.1007/BF02402204).
- RAMBAUX, N. and CASTILLO-ROGEZ, J. (2013). “Tides on Satellites of Giant Planets”. *Tides in Astronomy and Astrophysics*. Lecture Notes in Physics. Springer, Berlin, Heidelberg, pp. 167–200. DOI: [10.1007/978-3-642-32961-6\\_5](https://doi.org/10.1007/978-3-642-32961-6_5).
- REDDY, S. K., FAVIER, B., and LE BARS, M. (2018). Turbulent Kinematic Dynamos in Ellipsoids Driven by Mechanical Forcing. *Geophysical Research Letters* **45**, pp. 1741–1750. DOI: [10.1002/2017GL076542](https://doi.org/10.1002/2017GL076542).
- RIEUTORD, M. and VALDETTARO, L. (1997). Inertial Waves in a Rotating Spherical Shell. *Journal of Fluid Mechanics* **341**, pp. 77–99.
- RIEUTORD, M. (1987). Linear Theory of Rotating Fluids Using Spherical Harmonics Part I: Steady Flows. *Geophysical & Astrophysical Fluid Dynamics* **39**, pp. 163–182. DOI: [10.1080/03091928708208811](https://doi.org/10.1080/03091928708208811).
- RIEUTORD, M. M. (2014). *Une introduction à la dynamique des fluides*. De Boeck Supérieur. 528 pp.
- ROBERTS, P. H. and STEWARTSON, K. (1963). On the Stability of a Maclaurin Spheroid of Small Viscosity. *The Astrophysical Journal* **137**, p. 777. DOI: [10.1086/147555](https://doi.org/10.1086/147555).
- ROBERTS, P. H. (1968). On the Thermal Instability of a Rotating-Fluid Sphere Containing Heat Sources. *Phil. Trans. R. Soc. Lond. A* **263**, pp. 93–117. DOI: [10.1098/rsta.1968.0007](https://doi.org/10.1098/rsta.1968.0007).
- ROGALLO, R. S. (1981). *Numerical Experiments in Homogeneous Turbulence*.
- RORAI, C., MININNI, P. D., and POUQUET, A. (2015). Stably Stratified Turbulence in the Presence of Large-Scale Forcing. *Physical Review E* **92**. DOI: [10.1103/PhysRevE.92.013003](https://doi.org/10.1103/PhysRevE.92.013003).
- SALEHIPOUR, H. et al. (2016). A New Characterization of the Turbulent Diapycnal Diffusivities of Mass and Momentum in the Ocean. *Geophysical Research Letters* **43**, 2016GL068184. DOI: [10.1002/2016GL068184](https://doi.org/10.1002/2016GL068184).
- SALEHIPOUR, H. and PELTIER, W. R. (2015). Diapycnal Diffusivity, Turbulent Prandtl Number and Mixing Efficiency in Boussinesq Stratified Turbulence. *Journal of Fluid Mechanics* **775**, pp. 464–500. DOI: [10.1017/jfm.2015.305](https://doi.org/10.1017/jfm.2015.305).

- SALEHIPOUR, H., PELTIER, W. R., and CAULFIELD, C. P. (2018). Self-Organized Criticality of Turbulence in Strongly Stratified Mixing Layers. *Journal of Fluid Mechanics* **856**, pp. 228–256. DOI: [10.1017/jfm.2018.695](https://doi.org/10.1017/jfm.2018.695). arXiv: [1809.03039](https://arxiv.org/abs/1809.03039).
- SARSON, G. R. et al. (1997). Magnetoconvection Dynamos and the Magnetic Fields of Io and Ganymede. *Science* **276**, pp. 1106–1108. DOI: [10.1126/science.276.5315.1106](https://doi.org/10.1126/science.276.5315.1106).
- SAURET, A. et al. (2010). Experimental and Numerical Study of Mean Zonal Flows Generated by Librations of a Rotating Spherical Cavity. *Journal of Fluid Mechanics* **662**, pp. 260–268. DOI: [10.1017/S0022112010004052](https://doi.org/10.1017/S0022112010004052).
- SAURET, A., LE BARS, M., and LE GAL, P. (2014). Tide-Driven Shear Instability in Planetary Liquid Cores. *Geophysical Research Letters* **41**, pp. 6078–6083. DOI: [10.1002/2014GL061434](https://doi.org/10.1002/2014GL061434).
- SAURET, A. and LE DIZÈS, S. (2013). Libration-Induced Mean Flow in a Spherical Shell. *Journal of Fluid Mechanics* **718**, pp. 181–209. DOI: [10.1017/jfm.2012.604](https://doi.org/10.1017/jfm.2012.604).
- SCASE, M. M., BALDWIN, K. A., and HILL, R. J. A. (2017). Rotating Rayleigh-Taylor Instability. *Physical Review Fluids* **2**, p. 024801. DOI: [10.1103/PhysRevFluids.2.024801](https://doi.org/10.1103/PhysRevFluids.2.024801).
- SCHAEFFER, N. (2013). Efficient Spherical Harmonic Transforms Aimed at Pseudospectral Numerical Simulations. *Geochemistry, Geophysics, Geosystems* **14**, pp. 751–758. DOI: [10.1002/ggge.20071](https://doi.org/10.1002/ggge.20071).
- SCOLAN, H., ERMANYUK, E., and DAUXOIS, T. (2013). Nonlinear Fate of Internal Wave Attractors. *Physical Review Letters* **110**. DOI: [10.1103/PhysRevLett.110.234501](https://doi.org/10.1103/PhysRevLett.110.234501).
- SCOTT, J. F. (2014). Wave Turbulence in a Rotating Channel. *Journal of Fluid Mechanics* **741**, pp. 316–349. DOI: [10.1017/jfm.2013.652](https://doi.org/10.1017/jfm.2013.652).
- SEN, A. et al. (2012). Anisotropy and Non-Universality in Scaling Laws of the Large Scale Energy Spectrum in Rotating Turbulence. *Physical Review E* **86**. DOI: [10.1103/PhysRevE.86.036319](https://doi.org/10.1103/PhysRevE.86.036319). arXiv: [1203.5131](https://arxiv.org/abs/1203.5131).
- SHOWMAN, A. P. and MALHOTRA, a. R. (1999). The Galilean Satellites. *Science* **286**, pp. 77–84. DOI: [10.1126/science.286.5437.77](https://doi.org/10.1126/science.286.5437.77). pmid: [10506564](https://pubmed.ncbi.nlm.nih.gov/10506564/).
- SMITH, L. M. and LEE, Y. (2005). On near Resonances and Symmetry Breaking in Forced Rotating Flows at Moderate Rossby Number. *Journal of Fluid Mechanics* **535**, pp. 111–142.
- SMITH, L. M. and WALEFFE, F. (1999). Transfer of Energy to Two-Dimensional Large Scales in Forced, Rotating Three-Dimensional Turbulence. *Physics of Fluids* **11**, pp. 1608–1622. DOI: [10.1063/1.870022](https://doi.org/10.1063/1.870022).
- SRIDHAR, S. and TREMAINE, S. (1992). Tidal Disruption of Viscous Bodies. *Icarus* **95**, pp. 86–99.
- ST. LAURENT, L. and GARRETT, C. (2002). The Role of Internal Tides in Mixing the Deep Ocean. *Journal of Physical Oceanography* **32**, pp. 2882–2899.
- STANLEY, S. and MOHAMMADI, A. (2008). Effects of an Outer Thin Stably Stratified Layer on Planetary Dynamos. *Physics of the Earth and Planetary Interiors* **168**, pp. 179–190. DOI: [10.1016/j.pepi.2008.06.016](https://doi.org/10.1016/j.pepi.2008.06.016).
- STELLMACH, S. et al. (2014). Approaching the Asymptotic Regime of Rapidly Rotating Convection: Boundary Layers versus Interior Dynamics. *Physical Review Letters* **113**, p. 254501. DOI: [10.1103/PhysRevLett.113.254501](https://doi.org/10.1103/PhysRevLett.113.254501).
- STEVENSON, D. J. (2001). Mars' Core and Magnetism. *Nature* **412**, pp. 214–219.
- TARDUNO, J. A. et al. (2010). Geodynamo, Solar Wind, and Magnetopause 3.4 to 3.45 Billion Years Ago. *Science* **327**, pp. 1238–1240. DOI: [10.1126/science.1183445](https://doi.org/10.1126/science.1183445). pmid: [20203044](https://pubmed.ncbi.nlm.nih.gov/20203044/).
- TILGNER, A. (2007a). “8.07 - Rotational Dynamics of the Core”. *Treatise on Geophysics*. Ed. by G. SCHUBERT. Elsevier: Amsterdam, pp. 207–243.
- TILGNER, A. (2007b). Zonal Wind Driven by Inertial Modes. *Physical Review Letters* **99**, p. 194501. DOI: [10.1103/PhysRevLett.99.194501](https://doi.org/10.1103/PhysRevLett.99.194501).

- VANNESTE, J. (2005). “Wave Interactions”. *Nonlinear Waves in Fluids: Recent Advances and Modern Applications*. Ed. by R. GRIMSHAW. CISM International Centre for Mechanical Sciences. Springer Vienna: Vienna, pp. 69–94. DOI: [10.1007/3-211-38025-6\\_3](https://doi.org/10.1007/3-211-38025-6_3).
- VIDAL, J. and SCHAEFFER, N. (2015). Quasi-Geostrophic Modes in the Earth’s Fluid Core with an Outer Stably Stratified Layer. *Geophysical Journal International* **202**, pp. 2182–2193. DOI: [10.1093/gji/ggv282](https://doi.org/10.1093/gji/ggv282).
- VIDAL, J. and CÉBRON, D. (2017). Inviscid Instabilities in Rotating Ellipsoids on Eccentric Kepler Orbits. *Journal of Fluid Mechanics* **833**, pp. 469–511. DOI: [10.1017/jfm.2017.689](https://doi.org/10.1017/jfm.2017.689).
- VIDAL, J., CÉBRON, D., and SCHAEFFER, N. (2017). Diffusionless Hydromagnetic Modes in Rotating Ellipsoids: A Road to Weakly Nonlinear Models? arXiv: [1702.07198 \[physics\]](https://arxiv.org/abs/1702.07198).
- WALEFFE, F. (1993). Inertial Transfers in the Helical Decomposition. *Physics of Fluids A: Fluid Dynamics* **5**, pp. 677–685. DOI: [10.1063/1.858651](https://doi.org/10.1063/1.858651).
- WALEFFE, F. (1990). On the Three-dimensional Instability of Strained Vortices. *Physics of Fluids A: Fluid Dynamics* **2**, pp. 76–80. DOI: [10.1063/1.857682](https://doi.org/10.1063/1.857682).
- WEBER, M. J. (2018). *Handbook of Optical Materials*. CRC Press. DOI: [10.1201/9781315219615](https://doi.org/10.1201/9781315219615).
- YAROM, E., SALHOV, A., and SHARON, E. (2017). Experimental Quantification of Nonlinear Time Scales in Inertial Wave Rotating Turbulence. *Physical Review Fluids* **2**. DOI: [10.1103/PhysRevFluids.2.122601](https://doi.org/10.1103/PhysRevFluids.2.122601).
- YAROM, E. and SHARON, E. (2014). Experimental Observation of Steady Inertial Wave Turbulence in Deep Rotating Flows. *Nature Physics* **10**, pp. 510–514. DOI: [10.1038/nphys2984](https://doi.org/10.1038/nphys2984).
- YOKOYAMA, N. and TAKAOKA, M. (2017). Hysteretic Transitions between Quasi-Two-Dimensional Flow and Three-Dimensional Flow in Forced Rotating Turbulence. *Physical Review Fluids* **2**. DOI: [10.1103/PhysRevFluids.2.092602](https://doi.org/10.1103/PhysRevFluids.2.092602).
- ZAKHAROV, V. E., L’VOV, V. S., and FALKOVICH, G. (2012). *Kolmogorov Spectra of Turbulence I: Wave Turbulence*. Springer Science & Business Media. 275 pp.
- ZEMAN, O. (1994). A Note on the Spectra and Decay of Rotating Homogeneous Turbulence. *Physics of Fluids* **6**, pp. 3221–3223. DOI: [10.1063/1.868053](https://doi.org/10.1063/1.868053).
- ZHOU, Y. (1995). A Phenomenological Treatment of Rotating Turbulence. *Physics of Fluids* **7**, pp. 2092–2094. DOI: [10.1063/1.868457](https://doi.org/10.1063/1.868457).
- ZOUESHTIAGH, F., AMIROUDINE, S., and NARAYANAN, R. (2009). Experimental and Numerical Study of Miscible Faraday Instability. *Journal of Fluid Mechanics* **628**, p. 43. DOI: [10.1017/S0022112009006156](https://doi.org/10.1017/S0022112009006156).